

**Triple-barrier resonant tunneling diodes  
for mobile THz emission and sensitive zero-bias detection**

Von der Fakultät für Ingenieurwissenschaften,  
Abteilung Elektrotechnik und Informationstechnik  
der Universität Duisburg-Essen

zur Erlangung des akademischen Grades

Doktor der Ingenieurwissenschaften

genehmigte Dissertation

von

Khaled Arzi  
aus  
Petah Tiqva,

Gutachter: Prof. Dr. Franz-Josef Tegude  
Gutachter: Prof. Dr. sc. techn. Daniel Erni  
Tag der mündlichen Prüfung: 08.05.2020

# DuEPublico

Duisburg-Essen Publications online

UNIVERSITÄT  
DUISBURG  
ESSEN

*Offen im Denken*

ub | universitäts  
bibliothek

Diese Dissertation wird über DuEPublico, dem Dokumenten- und Publikationsserver der Universität Duisburg-Essen, zur Verfügung gestellt und liegt auch als Print-Version vor.

**DOI:** 10.17185/duepublico/71829

**URN:** urn:nbn:de:hbz:464-20200708-135420-8



Dieses Werk kann unter einer Creative Commons Namensnennung - Weitergabe unter gleichen Bedingungen 4.0 Lizenz (CC BY-SA 4.0) genutzt werden.

“Für den gläubigen Menschen steht Gott am Anfang, für den Wissenschaftler am Ende aller seiner Überlegungen”

- Max Planck



---

## Acknowledgments

Firstly, I would like to express my sincere gratitude to my advisor Prof. Franz-Josef Tegude who is a great inspiration for me. Because of his passion to physics in general and semiconductor physics in particular, he awakened in me the interest for this field, which led me to change my master's degree to electrical engineering, following then this dissertation. Prof. Daniel Erni I would like to thank you for your continuous support during my PhD studies and related research, for the tips and new ideas which improved my thesis, especially for the injection locking process. Prof. Nils Weimann, thank you for the support during the end phase of my thesis, for the long and fruitful discussions and the opportunity given me to attend a lot of conferences.

My sincere thanks also go to Prof. Masahiro Asada and Prof. Safumi Suzuki, from Tokyo Institute of Technology in Japan, who provided me an opportunity to join their team within my short-term scientific mission, and who gave me access to their laboratory and research facilities. Without this fruitful cooperation it would not be possible to conduct this research.

I would also like to thank Dr. Werner Prost for his constant encouragement and support, for the great trust he placed in me when it came to try out new things. Dr. Wolfgang Brockerhoff, thank you for the technical and non-technical discussions, your support has a direct impact on the success of my thesis. Dr. Artur Poloczek, thank you for your commitment and support, especially in the clean room and sample preparation, your knowledge provided a huge contribution to my thesis.

I would like to thank the rest of my colleagues within the BHE team for the good working atmosphere and helpful discussions and all the fun we have had in the last years: Udo Dork and Horst Barthel thank you both for the support, especially when assembling new, and in some cases, weird and crazy measurement setups and a big thank for your IT support. Ralf Geitmann thank you for the many epitaxial growth of the devices and test layers in the MBE. Andrea Merz and Heike Bobzien, thank you both for the support in the cleanroom and the many tests we did together to get the devices running. Reimund Tilders thank you for providing us secure clean room environment and Wolfgang Molls for the great support, in the background, keeping everything running in the clean room when needed. I would like to thank all my bachelor and master students who joined my project to write their thesis or as assistant student; Their hard work was a significant contribution to the success of this thesis.

A big thank goes also to Dr. Andreas Rennings and Benedikt Sievert from the laboratory of ATE at the University of Duisburg-Essen for the helpful contribution to the antenna design and simulation. This fruitful cooperation led to a great success especially in the integration of the devices within an antenna.

---

Last but not the least, I would like to thank my family: my parents, my brother and sisters for supporting me spiritually throughout this thesis and my life in general. My lovely wife for her support and acceptance, especially during the end phase of the thesis and for her big help by proofreading of the thesis.





---

## Abstract

Coherent, compact design, and battery-operated signal sources and sensitive signal detectors operating in the THz-frequencies are currently subject of intense research. Within this work, a promising solution that is suitable to fulfill these requirements is investigated. Therefore, for a compact design and low power consumption operation, a novel device structure is developed. By enhancing the double barrier resonant tunneling diode material system with a third barrier a new zero-bias detection capability is added, while maintaining the known de-attenuation functionality of a resonant tunneling device. Providing one device that depending on its bias point, can rectify or generate signals in the sub- and THz range. Furthermore, during this work a novel subharmonic signal injection locking method is developed to overcome the major challenge of coherent THz signal source, which is the output signal phase and frequency control. A wireless signal injection approach has been developed to isolate the injection signal source and the THz signal emitter. In addition, the wireless signal injection concept is well suited for heterogeneous integration of both signal sources achieving a compact THz signal source, especially for array-based integration.

Within this work a new material stack design improved the maximum current density from 200 up to 900 kA/cm<sup>2</sup>. The characterization and fabrication flow are established and enhanced. Further, a novel low-cost solution for small-area devices via soft-UV nano-imprint mechanisms is developed. For characterization and modeling of single devices, on-wafer DC and scattering parameter measurements were carried out. Different commercial electromagnetic simulators were used to design and characterize the antennae. Monolithic integration technology of the characterized triple barrier resonant tunneling diode into a slot-antenna for oscillator and detector operation, and the integration into a self-complementary bowtie antenna for broadband detection are developed and successfully operated for the first time in the sub- THz range. Oscillation at 260 GHz with an output power of 92  $\mu$ W were measured, achieving a competitive value for internal DC-to-RF conversion efficiency of  $\eta_{\text{DC-RF}} \cong 1.5\%$ , and a resonant detection maximum at 280 GHz. The broadband detection accomplished a high average internal voltage responsivity of 2000 V/W and noise equivalent power of 1 fW/Hz<sup>0.5</sup> in the frequency range between 220 and 330 GHz. Within this work, the first experimental proof of concept for a successful wireless subharmonic signal injection locking in the THz-range at  $f_0=550$  GHz and an externally injected signal at  $f_{\text{inj}}=f_0/2$  is presented. After locking the THz oscillator an improvement of the full width at half maximum of the output signal from 34.69 MHz to 483 Hz at the carrier frequency  $f_0=550$  GHz is achieved, providing a single-sideband phase noise value of -121 dBc/Hz at an offset frequency of 10 MHz from the carrier frequency.



---

## Kurzfassung

Diese Arbeit beschäftigt sich mit innovativen Ansätzen für die Entwicklung und Optimierung von kompakten Signalquellen mit einer niedrigen Betriebsleistung sowie hoch empfindlichen Signaldetektoren für den Betrieb im THz-Bereich. Hierfür wird eine Drei-Barrieren-Resonanztunneldiode eingesetzt. Durch das asymmetrische Stromspannungsverhalten, sowie den negativen differentiellen Widerstandsbereich eignet sich dieses Bauelement für die Signalerzeugung als auch -Detektion. Des Weiteren wird eine neuartige Methode, basierend auf der Einkopplung eines externen subharmonischen Signals, zur Steuerung der Phase und Frequenz des Ausgangssignals entwickelt. Diese Methode eignet sich auch zur Heterointegration beider Signalquellen, insbesondere für Array-basierte THz-Signalquellen. Ein weiterer Vorteil dieses Ansatzes ist die Isolierung beider Signalquellen durch die drahtlose Signaleinkopplung.

Im Rahmen dieser Arbeit wurde durch systematische Materialschicht-Design-Optimierung der Drei-Barrieren-Resonanztunneldiode die maximale Stromdichte von 200 auf 900 kA/cm<sup>2</sup> erhöht. Der Charakterisierungs- und Fertigungsablauf wurde optimiert und ein neuartiger, kostengünstiger Prozess zur Herstellung von kleinflächigen Bauelementen mittels *Soft-UV-Nanoimprint*-Technologie entwickelt. Zur elektrischen Charakterisierung und Modellierung einzelner Bauelemente wurden *On-Wafer-DC*- und Streuparameter-Messungen durchgeführt. Für die Entwicklung und Verbesserung der Antennen wurden verschiedene kommerzielle elektromagnetische Simulationsprogramme eingesetzt. Die im Rahmen dieser Arbeit entwickelten Drei-Barrieren-Resonanztunneldioden wurden zum einen in eine Slot-Antenne integriert, so dass diese als Oszillator und resonanter Detektor betrieben werden kann. Zum anderen wurde diese in eine selbst komplementäre Bow-Tie Antenne integriert, so dass diese für die Breitband-Detektion eingesetzt werden kann. Für beide Anwendungen werden dadurch erstmals Frequenzen für Oszillation und Detektion im Sub-THz-Bereich erfolgreich erreicht. Es werden Oszillationen bei 260 GHz mit einer Ausgangsleistung von 92  $\mu$ W gemessen. Die Oszillationen weisen einen DC-RF-Wirkungsgrad von  $\eta_{\text{DC-RF}} \cong 1.5\%$  auf und ein resonantes Detektionsmaximum bei 280 GHz. Die breitbandige Signaldetektion zeichnet sich durch eine hohe mittlere interne Spannungsempfindlichkeit von 2000 V/W und eine äquivalente Rauschleistung von 1 fW/Hz<sup>0.5</sup> im Frequenzbereich von 220 bis 330 GHz aus. Desweiteren konnte im Rahmen dieser Arbeit zum ersten Mal experimentell das Ausgangssignal einer Resonanztunneldiode integriert in eine *Slot*-Antenne oszillierend bei  $f_0=550$  GHz mit einem extern eingekoppelten Signal, oszillierend bei  $f_{\text{inj}}=f_0/2$  synchronisiert werden. Dabei wurde eine Verbesserung der Halbwertsbreite des Ausgangssignals von 34,69 MHz auf 483 Hz bei  $f_0=550$  GHz erreicht, wodurch ein Einseitenband-Phasenrauschwert von -121 dBc/Hz, bei einer Offset-Frequenz von 10 MHz zur Trägerfrequenz  $f_0$  bestimmt wird.

---

## List of contents

<b>1</b>	<b>Motivation, state of the art and novelty of this work.....</b>	<b>3</b>
1.1	Overview of the work.....	5
<b>2</b>	<b>Oscillator and detector: fundamental analysis.....</b>	<b>9</b>
2.1	TBRTD operation principle.....	9
2.2	Modeling of resonant tunneling-based devices.....	13
2.3	Principle of NDR-based fundamental oscillator.....	18
2.3.1	TBRTD integration as an oscillator.....	21
2.4	Injection locking of NDR-based oscillator.....	22
2.4.1	Locking process.....	24
2.4.2	Fundamental signal locking.....	25
2.5	Antenna.....	27
2.5.1	Antennae characteristics parameters.....	27
2.5.2	Electromagnetic simulations-software for antennae.....	30
2.5.3	On-Chip THz Antennae.....	32
2.5.4	THz Antenna types and antenna integration in a circuit simulator.....	33
2.6	Principle of resonant tunneling-based rectifier.....	37
2.6.1	Broadband detector approach.....	39
2.6.2	Resonant detector approach.....	40
<b>3</b>	<b>Measurements setups.....</b>	<b>43</b>
3.1	DC-Measurement setup.....	43
3.2	S-parameter measurement setup.....	43
3.2.1	Calibration.....	44
3.2.2	De-embedding.....	44
3.3	Quasi-Optical measurement setup.....	46
3.3.1	Oscillation frequency measurement setup.....	47
3.3.2	Oscillator output power measurement setup.....	49
3.3.3	Detector Measurement setup.....	50
<b>4</b>	<b>Single devices and circuit fabrication process.....</b>	<b>53</b>
4.1	Single TBRTD fabrication.....	53
4.1.1	Device miniaturization.....	58
4.2	Monolithic integration of TBRTD within an antenna.....	66
4.2.1	Slot antenna.....	66
4.2.2	Bowtie antenna.....	72

<b>5</b>	<b>Triple-Barrier-Resonant-Tunneling-Diode: design and characterization .....</b>	<b>75</b>
5.1	Vertical device design .....	76
5.2	Measurement and modeling .....	78
5.2.1	DC measurement results and modeling .....	78
5.2.2	S-parameter measurements and modeling .....	82
<b>6</b>	<b>Free running oscillator and zero bias detector: design and characterization</b>	<b>87</b>
6.1	Oscillator and detector design.....	87
6.1.1	Slot antenna design .....	87
6.1.2	TBRTD integration within a slot antenna.....	90
6.1.3	Self-complementary bowtie antenna design .....	95
6.1.4	TBRTD integration within a bowtie antenna.....	96
6.2	Measurements and characterization .....	96
6.2.1	TBRTD-based oscillator.....	96
6.2.2	TBRTD-based zero-biased detector .....	98
<b>7</b>	<b>Injection locking of a free running sub-THz oscillator .....</b>	<b>103</b>
7.1	Simulation of subharmonic injection locking .....	103
7.2	First experimental proof of concept for subharmonic injection locking .....	106
<b>8</b>	<b>Summary and Outlook.....</b>	<b>113</b>
<b>9</b>	<b>References .....</b>	<b>117</b>
<b>10</b>	<b>Own publication .....</b>	<b>127</b>
<b>Appendix.....</b>		<b>130</b>
A:	Single TBRTD and circuit fabrication instruction.....	130
B:	Layout design for single Test-devices and circuits.....	135
C:	Simulation of a TBRTD slot antenna detector.....	139
<b>List of figures .....</b>		<b>VIII</b>
<b>List of tables.....</b>		<b>XIV</b>
<b>Abbreviations .....</b>		<b>XV</b>
<b>symbol directory .....</b>		<b>XIX</b>



---

# 1 Motivation, state of the art and novelty of this work

THz radiation holds the promise to enable innovative breakthroughs for ultrahigh wireless data-rate transmission [1, 2], non-destructive material analysis [3, 4], and extremely high-resolution images. Moreover, the signal energy is below the thermal energy at room temperature, and hence the exposure to THz emission is considered to be free of harm [5–7]. In the last decade, these advantages pushed the research to investigate and provide novel methods to fill the so-called THz-gap with THz-sources and -detectors. The THz-gap is between the microwave frequencies at the lower side (0.1 THz), and infrared light at the top side (10 THz). Both, optical and electronic devices are potential candidates to operate in this frequency region.

Nowadays, the THz-gap is not a completely empty gap anymore; many real-life application challenges are solved with systems operating in the THz range. However, small, energy-efficient, and battery-driven mobile THz devices, operating at room temperature, are still subject of intense research. On the optical side, Quantum Cascade Lasers (QCL) and Far-Infrared (FIR) gas lasers are still investigated for operation in this frequency range, and under cryogenic cooling conditions, high output power in the mW range is achieved [8, 9]. Further, fast laser pulses are intensively investigated to generate and detect THz radiation and is commonly used in Time-Domain Spectroscopy (TDS), where a large frequency range is covered within a run [10–12]. As electronic devices, two and three-terminal devices are investigated. Impact Ionization Avalanche Transit Time diodes (IMPATT), Gunn diodes [13, 14], and Resonant Tunneling-based devices (RTD) [15] are all promising devices for two-terminal sub- and THz signal generation. Transistors are also demonstrating promising results in the THz range. InP- and SiGe-based Heterostructure Bipolar Transistors (HBTs), High Electron Mobility Transistors (HEMTs), and Si CMOS transistors shows a cut-off frequency and maximum oscillation frequency in the THz regime [16–21].

The use of multiplier chains with a low-frequency source is widely used to achieve the THz range. In this method, the low-frequency source is multiplied in a series chain of devices providing non-linear impedance, generating higher-order harmonic signals. Mainly, a series of frequency doublers and triplers are used with Schottky diodes [22] or Heterostructure Barrier Varactors (HBV) [23]. Frequencies up to 2.55 THz, with an output power of -40 dBm were achieved [24]. However, the input power is attenuated at each multiplication stage due to the conversion efficiency  $< 1$ . This efficiency is further reduced when the operation frequency is increased. Furthermore, this technique depends on the development of solid-state sources.

Among the electronic fundamental mode oscillators, up to now, the RTD-based devices demonstrated the highest oscillation frequency at 1.98 THz [15]. Moreover, the operation at 3 THz is predicted for the very near future [25]. This promising candidate joins essential

properties such as a high current density while maintaining a small area-capacitance in the range of few fF/ $\mu\text{m}^2$ . Furthermore, the RTD is a compact and small device that can be monolithically integrated into an on-chip antenna for in-plane [26] and orthogonal [27, 28] free-space radiation. Theoretically, RTD-based oscillators can achieve a DC-to-RF conversion efficiency of up to 50% [29]. However, the reported RTD-based THz oscillators DC-to-RF conversion is among 1%, mainly due to the lack of matching between the RTD and the radiator.

The first theoretical analysis of a realizable RTD was demonstrated in 1973 [30], with multi-barrier design, and shortly afterward, the experimental proof of a DBRTD was reported in 1974 [31]. Since then, the RTD was further developed and investigated. Its high-frequency operation capability was experimentally demonstrated in 1991 for the first time [32] with an oscillation frequency  $f_0$  at 712 GHz. However, because of the lack of results reproduction, the RTD research was almost turned down. In the years 2010 and 2011, the situation changed as oscillation at 1 and 1.1 THz was demonstrated by two different groups [27] and [26], respectively. Since then, the RTD regained strong attention, and as shown in Figure 1.1, a sharp increase in the oscillation frequency is observable over the last 14 years. At this moment, the RTD is the only electronic device oscillating around 2 THz at room temperature. Further, many approaches were reported to improve its output power [15, 25, 26, 28, 32, 33], almost achieving mW level at the upper sub-THz frequencies [34].

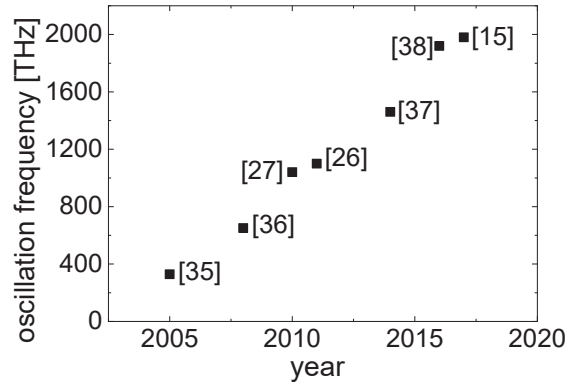


Figure 1.1: Oscillation frequency enhancement of an RTD-based oscillator in recent years: 2005 [35], 2008 [36], 2010 [27], 2011[26], 2014 [37], 2016 [38], 2017 [15].

The main aim of this work is to realize novel functionalities for RTD-based oscillators and detectors in the THz regime. These functionalities shall contribute to a filling of the THz-gap with the required coherent, compact, efficient, and battery-operated devices. In this work, instead of a conventional Double Barrier RTD (DBRTD), the Triple Barrier (TBRTD) devices are developed and improved for operation in the THz range. Due to the third barrier, the TBRTD provides, besides a wide negative differential region for the oscillation operation, a current blocking behaviour in the reverse bias direction [39]. For this reason, this device

---

can be operated as an oscillator, when biased in the NDR region, or as a zero-bias rectifier. While maintaining the advantages of the RTD as an oscillator, the TBRTD can provide a significant improvement in the sensitivity of THz detectors and response time compared to microbolometers, golay cell detectors [40] and to Schottky diode-based detectors. Nowadays, the most used compact device for THz signal detection is the Schottky diode. Different designs are investigated, such as binary and ternary compounds [41] and heterostructure detectors [42]. The non-linearity of these devices is given through the thermal exponent in the current-voltage characteristics and hence, is limited by the thermal energy component with  $kT \sim 25$  meV at room temperature, and consequently, only a maximum achievable current sensitivity of roughly 20 A/W is achievable. The non-linearity in the TBRTD is given by the alignment of the 2D sub-bands in the quantum wells [43] with no thermal exponent limitation, and hence a stronger non-linearity can be achieved which leads to an increasement of the detector responsivity.

To improve the free-running, NDR-based oscillators, a coherent source operation is required. For this purpose, a phase and frequency control of the output signal is needed. In this work, a novel subharmonic injection mechanism is investigated to control the phase and the frequency of THz emission. A subharmonic signal, oscillating at the frequency  $f_0/n$ , with a high signal purity, is injected from an external source master into the THz oscillator. The property of this signal, in terms of signal purity and stability, is then transferred on the output signal of the free running NDR-based oscillator. To circumvent the lack of isolation in a two-terminal device, a wireless injection mechanism is developed. This method holds the promise to overcome the challenge in an array-based oscillator, such as beam steering, or output power enhancement, by tuning the phase of single THz oscillators.

## 1.1 Overview of the work

The presented thesis is structured as follows:

### Chapter 2

The operation principle of the TBRTD is illustrated in this chapter; first, a simple model of charge transport is introduced to define an analytical model for the TBRTD. This model is then used to demonstrate the dependency of the device capacitance and negative differential region on the operation frequency. This analytical model is also used to define the elements of the small-signal equivalent circuit in specific frequency regions. The influence of the parasitic elements on the small-signal equivalent circuit is introduced. A general, NDR-based oscillator, its design parameters, and conditions are discussed. The integration of a TBRTD within a resonator for oscillation operation is presented. The required redesign of the resonator due to the TBRTD impedance is illustrated. Following is the analytical modeling of the subharmonic injection locking of an NDR-based oscillator. Utilizing the van der Pol

---

model and the Adler's equations, an analytical model for the phase and frequency locking mechanism is developed. Before the final section of this chapter, the antennae used to structure the resonator, and THz radiator in this work are briefly introduced. Finally, the TBRTD detection capability, the comparison between broadband and resonant detector, is presented.

### **Chapter 3**

In this chapter, the measurement setups assembled within this work are presented. Starting with the standard characterization setups for single device characterization for the DC and scattering parameters, the measurement setup calibration and the de-embedding of a Device Under Test (DUT) from its surrounding is presented. Then, the quasi-optical measurement setups used to characterize the fabricated oscillator and detectors are introduced.

### **Chapter 4**

A presentation of the fabrication process for a single TBRTD device is demonstrated with a strong coupling to the step-by-step instruction presented in the Appendix A. Further, a detailed presentation of a novel approach, to achieve small area devices, down to nm range is reported. Then the integration of the TBRTD within an antenna for oscillator and detector operation is illustrated. A detailed description of the main challenges is given, and its solution are shown in this chapter.

### **Chapter 5**

The vertical design of the TBRTD and its epitaxial growth strategy is presented in this chapter. Six devices with different quantum well designs were grown. The main goal is first the improvement of the current-voltage characteristics of the TBRTD to mainly increase its current density for high-frequency operation. DC and HF characterization of single devices are then carried out. The results show good agreement to the expected behavior using the presented charge transport model. A promising device is then characterized, and its small-signal equivalent circuit is presented.

### **Chapter 6**

The design of a single antenna for integration with a TBRTD is presented in this chapter. The properties of the antennae are determined with different electro-magnetic based simulators. To integrate the antenna into a circuit simulator, for matching with the TBRTD, a small-signal equivalent circuit of the antennae is developed and characterized. Then the integration for oscillation and resonant detection design is shown, followed by the integration within a broadband antenna for detection operation. The characterization of the fabricated devices is finally reported, where the quasi-optical measurement setups are used.

---

## Chapter 7

In this chapter, the novel approach developed within this work for phase and frequency control of the free running THz oscillator, via subharmonic injection locking, is presented. Simulation results of a locked, RTD-based THz oscillator are reported. Then, for the first an experimental proof of concept for wireless subharmonic injection locking at THz frequencies is presented. The oscillation frequency of the RTD-based oscillator is located at 550 GHz. The injected signal is among  $f_0/2 \sim 275$  GHz.



---

## 2 Oscillator and detector: fundamental analysis

In this chapter, the fundamental analysis of oscillators and detectors is presented. The design techniques, based on the negative conductance oscillator and rectifier detector, will be introduced, starting by presenting the operation principle of a TBRTD utilizing a simple model, as presented in Figure 2.2. Then an analytical model for the TBRTD is developed, which includes the voltage and frequency dependence. Further, for circuit simulation and to simplify the TBRTD modeling, a large and small-signal model is extracted out of the analytical model. In the next section, the numerical relations of the locking mechanism of an NDR-based device will be discussed. In this work, wireless subharmonic injection locking of a free-running oscillator is developed to overcome the main drawback of a free-running oscillator such as output signal phase-noise and frequency instability. The main challenges of the mechanism and the advantage of a wireless injection are then presented. Following in this chapter, the used antennae are briefly introduced with its most important parameters. This chapter is ending with the fundamental analysis of a TBRTD-based rectifier detector. The difference between a resonant and broadband detector approach will be discussed.

### 2.1 TBRTD operation principle

The active device in this work is the TBRTD. This device is an improved DBRTD by adding a third barrier in the material stack. The TBRTD is a two-port device, with a top (emitter electrode) and bottom contact (collector electrode), as shown in Figure 2.1a. In this work, only n-doped devices (i.e., electrons as main charge carriers, hence higher mobility) are used, and therefore, only the shape and influence of the conduction band edge are considered. Stacking materials with low band gaps (quantum well) between materials with a high bandgap (quantum barrier), the internal part of the resonant tunneling based device is structured. Modifying the internal part of the DBRTD, by adding a third barrier, i.e., structuring a second quantum well (compare Figure 2.1b and c) leads to additional functionalities [39] such as current blocking in the backward direction while remaining a large NDR in the forward direction. The main difference and improvement between the DBRTD and TBRTD are presented in Figure 2.1. The internal region of the device defines its functionality. For illustration, the conduction band edges of the internal parts for both devices are presented in Figure 2.1b and c. To demonstrate the functionality difference of the devices and the enhancement caused by the third barrier, typical current-voltage characteristics of the devices are presented. A typical current-voltage characteristic of a DBRTD, as presented in Figure 2.1d, shows a symmetrical current-voltage curve in the forward and reverse direction. A typical current-voltage characteristic of the TBRTD is presented in Figure 2.1e. The third barrier and the asymmetrical design of the quantum wells lead to an asymmetrical current-

voltage curve, i.e., current blocking region in the reverse direction, which is utilized for signal rectification.

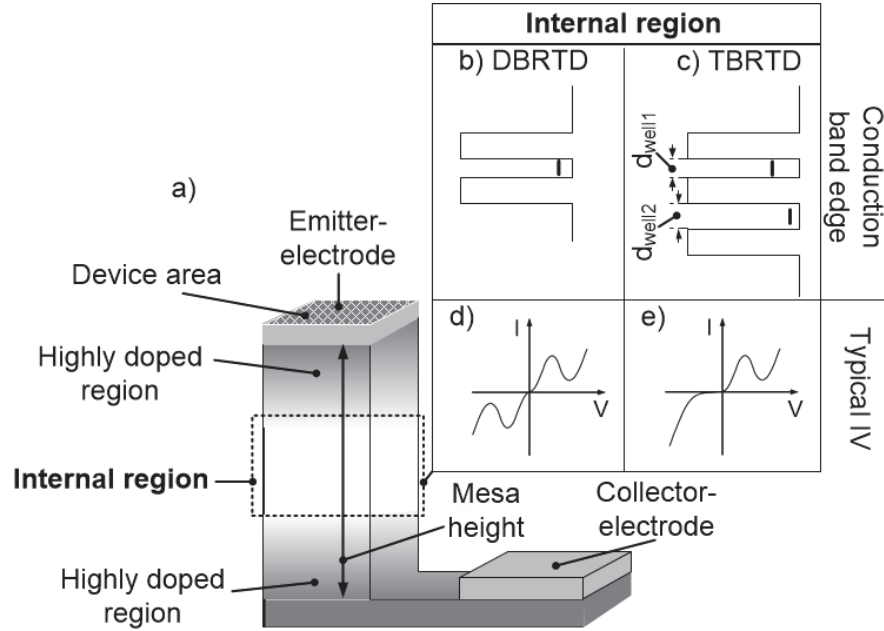


Figure 2.1: a) Schematic setup of a two-port device illustrating the undoped internal part, which defines the functionality of the device, and the device area, which is defined by the top contact area. In the inset, the difference in the current-voltage characteristics for d) DB- and e) TBRTD and their conduction band edges are presented in b) and c), respectively.

The operation principle of a TBRTD is schematically presented in Figure 2.2. The internal part of the device is built by semiconductor heterostructures. Considering an internal part with only one barrier. The thickness of this barrier defines the probability of an electron, with energy smaller than the barrier energy, to tunnel through it. This probability decreases exponentially with the thickness of the barrier, as shown in the following equation [44]:

$$T_p(W_e) = \exp \left[ -2 \cdot d_{\text{bar}} \sqrt{2m_e^* \frac{\Delta W_L - W_e}{\hbar^2}} \right] \quad (2.1)$$

where  $d_{\text{bar}}$  represents the thickness of the barrier,  $m_e^*$  the effective electron mass,  $\Delta W_L$  the discontinuity formed by the barrier and  $\hbar = \frac{h}{2\pi}$ , with  $h$  the Planck's constant. When forming a quantum well (QW), i.e., two undoped material layers with a large bandgap (quantum barrier structure) are surrounding an undoped narrow bandgap material layer (QW structure) where discrete energy levels are formed [31, 45]. The thickness of the QW defines the energy of the discrete levels. When assuming an infinite barriers height, the energy of the discrete energy level, as a function of the thickness of the well is presented as follows:

$$W_\eta = \frac{(\eta\pi\hbar)^2}{2} \cdot \frac{1}{m_e^* d_{\text{well}}^2} \quad (2.2)$$

---

where  $\eta$  denotes the energy level index and is an integer, and  $d_{\text{well}}$  the QW thickness. The TBRTD contains three quantum barriers and two QW in the internal part [46, 47]. The emitter and collector sides, which provide the electrical connection of the TBRTD, are heavily doped to reduce any further materials resistance.

The operation principle of the TBRTD is described by utilizing the model presented in Figure 2.2 as follows: Starting with Figure 2.2a, which represents the steady-state condition, with no voltage applied on the device; Due to the thin QWs, discrete energies are created within the QWs, the energy level of the energies differs because of the different QW thickness, i.e., asymmetrical design of the QW. These design criteria are essential for the function of the device, which should provide resonance between the energy levels and the electrons at the emitter side, in the forward bias direction, and to misalignment between them in the reverse direction for current blocking. Applying bias to the device tilts its conduction band edge and therefore, to a shift of the discrete energy levels in the QWs. At a specific voltage, a resonance between the energy levels in the QWs and the fermi-level, i.e., electron energy at the emitter side, is occurring see Figure 2.2b. At this point, the maximum current is flowing through the device. This operation point is characteristic for the TBRTD: its voltage is defined as the peak voltage ( $V_p$ ) and the corresponding current as peak current ( $I_p$ ). Increasing or decreasing the applied voltage shifts the system out of the resonance, which reduces the current flow. The current-voltage region before the peak voltage is defined as the first Positive Differential Resistance (PDR1) region. The second characteristic operation point of a TBRTD is the valley point with its valley voltage ( $V_v$ ) and its corresponding current ( $I_v$ ). At this voltage, the thermionic current, i.e., charge transport over the barriers, dominates the current flow in the TBRTD. At higher voltages, the second PDR region is reached (PDR2). Between the peak and valley point, the Negative Differential Resistance (NDR) region is located. In the reverse bias direction of a TBRTD, a misalignment between the discrete energy levels leads to a current blocking like behavior (see Figure 2.2d). At higher voltage in the reverse direction, the thermionic current will dominate and current flows. As presented this device can be used not only to de-attenuate a resonator and provide oscillation but also, due to the asymmetric current-voltage characteristics near zero point, as a zero-bias rectifier detector.

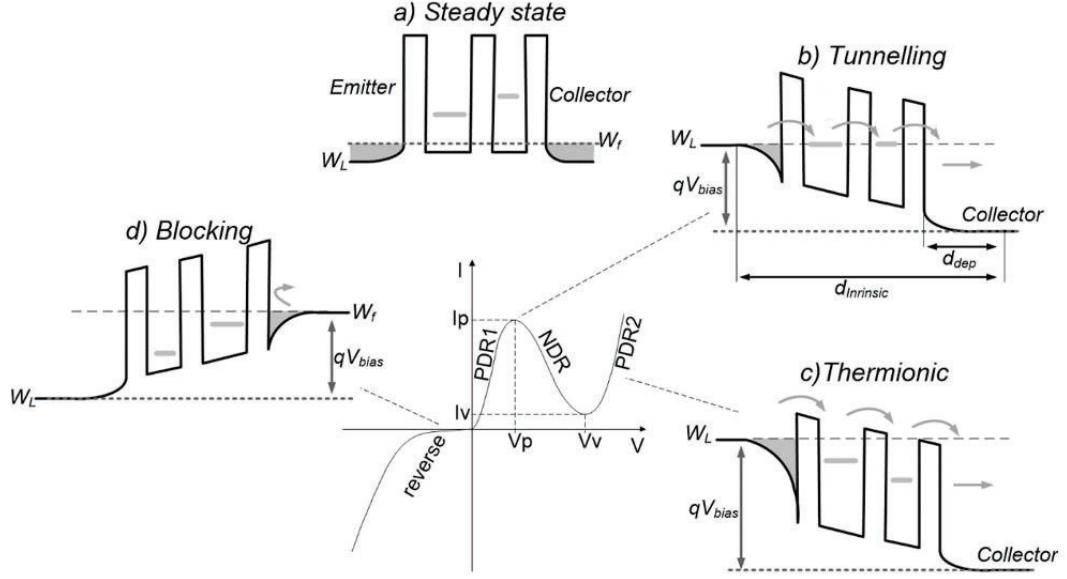


Figure 2.2: Typical IV-curve of a TBRTD with its main parameters and the conduction band edge structure at different bias points: a) at steady state, i.e., no bias is applied. b) Charge transport at the peak-point of the current-voltage characteristics, resonance. c) Applying a voltage higher than the valley point, the thermionic charge transport dominates. d) Blocking region, no resonance between the discrete energy levels. At higher negative voltage, the thermionic current is then dominating.

The current-voltage characteristic of a TBRTD, as presented in Figure 2.2, provides first insights into its main figure of merit parameters that are defined as follows:

- Current density ( $J_p$ ):

$$J_p = \frac{I_p}{\text{device area}} \quad (2.3)$$

the *device area* is the top-contact- and mesa-area (see Figure 2.1a). The current density of a TBRTD provides a first insight look in its high-frequency operation capability, as will be shown later.

- Peak to Valley Current Ratio (*PVCR*):

$$PVCR = \frac{I_p}{I_v} \quad (2.4)$$

- Peak to Valley Voltage Ratio (*PVVR*):

$$PVVR = \frac{V_p}{V_v} \quad (2.5)$$

The *PVCR* and *PVVR* are used to estimate the maximum achievable output power, which is proportional to its negative differential resistance, as will be shown later.

- Rectification Factor  $G$ :

$$G = \frac{|I^+(V^+)|}{|I^-(V^-)|} \quad (2.6)$$

A characteristic parameter of a rectifying device is its rectification factor  $G$ , which determines the factor of current flowing in the forward direction ( $I^+$ ) compared to the current following in the reverse direction ( $I^-$ ) at a specific absolute voltage ( $+V$ ) and ( $-V$ ), respectively.

## 2.2 Modeling of resonant tunneling-based devices

The current-voltage characteristic of the TBRTD is split into two parts for modeling: The NDR region is used for oscillation, the reverse, and the PDR1 region for detection. Starting with an analytical model to describe the device behavior by the use of its conductance and total capacitance for oscillator operation. The DC-characteristic of the TBRTD in the forward direction is investigated. As shown in Figure 2.3a, the forward bias direction of the TBRTD is very similar to the DBRTD. Therefore, the current-voltage modeling is adopted from the DBRTD model presented in [36, 48] and modified in this work, to include the influence of charge tunneling through the second quantum well including the resonance between both energy levels.

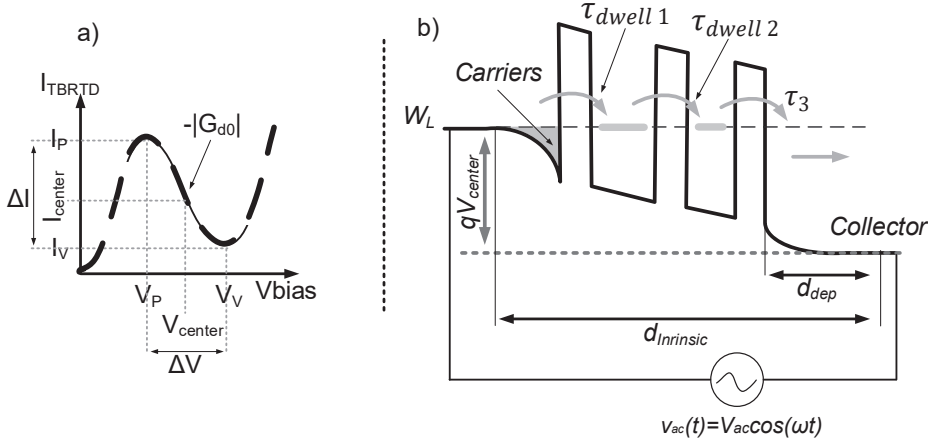


Figure 2.3: a) Current-voltage characteristic of a TBRTD in the forward direction with its characteristic operation points, the dashed line illustrates the measured curve and, the solid line the region the model is covering. b) The conduction band edge illustrating the internal part of a TBRTD presenting the delay times during tunneling.

For the first term analysis, the transit and tunneling times (see Figure 2.3b) are neglected. The TBRTD current  $I_{TBRTD}$  as a function of the bias voltage  $V_{bias}$  is approximated by a cubic polynomial at the center of the NDR region:

$$I_{TBRTD}(V_{bias}) \cong -aV_{bias} + bV_{bias}^3 \quad (2.7)$$

$I_{\text{TBRTD}}$  and  $V_{\text{bias}}$  are the current and voltage at the bias point after shifting the origin of the IV-curve to the center of the NDR region. The fitting terms  $a$  and  $b$  are related to the current-voltage characteristic as follows:  $a = \left(\frac{3}{2}\right) \left(\frac{\Delta I}{\Delta V}\right)$  and  $b = \frac{2\Delta I}{\Delta V^3}$  with  $\Delta I$  and  $\Delta V$  the width of the current- and voltage range of the NDR region, respectively. This modeling provides a good agreement to the current-voltage characteristics of a measured DC behavior of the TBRTD device, as illustrated by the solid line in the current-voltage characteristics in Figure 2.3a, in the NDR region. Out of the current-voltage equation in the NDR region, equation (2.7), the negative conductance of the TBRTD is determined. Considering a voltage  $v_{\text{ac}}(t) = V_{\text{ac}} \cos \omega t$  exciting around the center of the NDR and providing a current  $I_{\text{TBRTD}}(v_{\text{ac}})$ , which includes the fundamental component of the angular frequency at  $\omega$  and the third harmonic at  $3\omega$ , see equation (2.7). The negative differential conductance is determined by including only the fundamental oscillation component as:

$$G_{\text{d0}}(V_{\text{ac}}) = \frac{\partial I_{\text{TBRTD}}(V_{\text{ac}})}{\partial v_{\text{ac}}} = a - 3bV_{\text{ac}}^2 \quad (2.8)$$

the absolute value of the negative differential conductance  $G_{\text{d0}}$ , as given in equation (2.8), is only valid at lower frequencies.

At higher frequencies, the tunneling dwell ( $\tau_{\text{dwell1}}, \tau_{\text{dwell2}}$ ) and transit time, i.e., time after tunneling the third barrier until reaching the collector region ( $\tau_3$ ), as demonstrated in Figure 2.3b, must be included. For this reason, the total current of the TBRTD, including the delay time, is considered. This current is generated by the following mechanism: Electrons tunneling through the barriers have a residence time within the wells. The electron's existence within the quantum wells induces positive charges at the emitter and the collector electrode, depending on the position of the electron within the wells. The induced charges change with the movement of the electron from the emitter to the collector side resulting in current generation between the emitter and the collector external path. For a voltage  $v_{\text{ac}}(t) = V_{\text{ac}} \cos(\omega t)$  vibrating at the center of the NDR region, the total current is derived as shown in [36, 48] and is modified here for the three barrier device as:

$$i(t) = \frac{1}{d_{\text{dep}}} \int_0^{d_{\text{dep}}} I_{\text{TBRTD}} \left[ v_{\text{ac}} \left( t - (\tau_{\text{dwell1}} + \tau_{\text{dwell2}}) - \frac{z}{v_s} \right) \right] dz + \frac{\varepsilon A}{d} \frac{dv_{\text{ac}}(t)}{dt} \quad (2.9)$$

with  $d_{\text{dep}}$  the thickness of the collector depletion layer;  $d$  the total thickness including the emitter accumulation layer, internal device, and depletion layer at the collector side;  $\varepsilon$  the material dielectric constant; and finally, the area of the device  $A$ . The electron injected from the emitter has the time delays  $\tau_{\text{dwell1}}$  and  $\tau_{\text{dwell2}}$  in the first and second QW, respectively.  $v_s$  is the saturation velocity at which the electron moves to the collector through the depletion layer. The change of the depletion layer  $d_{\text{dep}}$  in the collector area with  $v_{\text{ac}}(t) = V_{\text{ac}} \cos(\omega t)$  is neglected. The first term of equation (2.9) represents the induced charges mentioned earlier. The second term is the displacement current. After substituting  $v_{\text{ac}}(t)$  into equation (2.9),

two current components are given.  $i_{c,TBRTD}$  and  $i_{s,TBRTD}$ , where the first is proportional to  $v_{ac}(t)$ , i.e.,  $\cos(\omega t)$ , the latter is phase-shifted, i.e., proportional to  $\sin(\omega t)$ . They are defined as follow:

$$i_{c,TBRTD}(t) = \frac{\omega}{\pi} \int_0^{\frac{2\pi}{\omega}} i(t) \cos(\omega t) dt \quad (2.10)$$

$$i_{s,TBRTD}(t) = \frac{\omega}{\pi} \int_0^{\frac{2\pi}{\omega}} i(t) \sin(\omega t) dt \quad (2.11)$$

The current proportional to  $\cos(\omega t)$  provides direct access to the differential conductance, including the tunneling and transit times at higher frequencies which is determined as:

$$G_{TBRTD}(V_{ac}) = \frac{-i_{c,TBRTD}}{V_{ac}} = \frac{\cos[\omega(\tau_{dwell1} + \tau_{dwell2} + \frac{\tau_3}{2})] \sin \frac{\omega \tau_3}{2}}{\frac{\omega \tau_3}{2}} G_{d0}(V_{ac}), \quad (2.12)$$

at higher frequencies  $G_{TBRTD}(V_{ac})$  decreases even reaching 0 at:

$$f = \frac{\omega}{2\pi} = f_c = \frac{1}{\tau_{dwell} + \frac{\tau_3}{2}}. \quad (2.13)$$

The frequency, defined in equation (2.13), defines the cut-off frequency of the TBRTD. Above this frequency, the TBRTD is no longer able to de-attenuate the circuit. This model is a simplified description of the device behavior, where the Coulomb interaction between charges in the QWs, is not considered. In cases where  $\tau_{dwell1} + \tau_{dwell2} \gg \tau_3$  as presented in [49, 50], the Coulomb interaction must be considered for viable modeling.

To include the frequency dependency of the differential conductance, due to the dwell times ( $\tau_{dwell1}$  and  $\tau_{dwell2}$ ) and relaxation times ( $\tau_3$ ), as shown in equation (2.12), the fitting parameter is modified in the IV-characteristic model of the TBRTD, equation (2.7). This is done by extending the terms of the fitting parameters  $a$  and  $b$  with a frequency-dependent part which is related to the time an electron remains in the well and the time it needs to go through the depletion layer to reach the collectors side [36]:

$$a(\omega) = a(0) \cdot \cos[\omega(\tau_{dwell1} + \tau_{dwell2} + \frac{\tau_3}{2})] \quad (2.14)$$

$$b(\omega) = b(0) \cdot \cos[\omega(\tau_{dwell1} + \tau_{dwell2} + \frac{\tau_3}{2})] \quad (2.15)$$

where  $a(0)$  and  $b(0)$  are the parameters defined at the static point, and  $\tau_{dwell1}$ ,  $\tau_{dwell2}$  are the times the electron remains in the QWs and  $\tau_3$  is the time an electron needs to go from the QW through the depletion layer to the collector side (see Figure 2.3), and the cosine term can be extracted experimentally by measuring devices with different absolute currents but same delay times, i.e., same material stack and fitting the results it to the values extracted from the theory presented in this chapter.

In the next step, the reactance of the TBRTD current is investigated. The reactance due to the tunneling and transit time is extracted from equation (2.9) and (2.11), i.e., the phase-shifted component  $i_{s,\text{TBRTD}}(t)$  of the current  $i(t)$ . This effect is expressed as a negative inductance [51] however, in this work, the model presented in [36, 48] is chosen, where the mentioned negative inductance is described with a parallel positive capacitance, which is somewhat simpler to model and a direct dependency on the applied voltage is given. In this model the reactance is expressed as a parallel capacitance to the TBRTD. The total capacitance of a TBRTD is described as follows:

$$C_{\text{TBRTD}}(V_{\text{ac}}) = C_0 + C_{\text{tunnel}}(V_{\text{ac}}) = \frac{i_{s,\text{TBRTD}}}{\omega V_{\text{ac}}} \quad (2.16)$$

with  $C_0$  the geometrical capacitance and  $C_{\text{tunnel}}$  the additional capacitance caused by the tunneling and delay time, which is called quantum capacitance. The relation between this tunneling capacitance and the delay time is demonstrated and experimentally extracted in [36]. The analogy to this capacitance the tunnel capacitance of the TBRTD is determined:

$$C_{\text{tunnel}}(V_{\text{ac}}) = \frac{\sin[\omega(\tau_{\text{dwell}1} + \tau_{\text{dwell}2} + \tau_3/2)] \sin \frac{\omega\tau_3}{2}}{\omega^2 \tau_3/2} G_{\text{d0}}(V_{\text{ac}}), \quad (2.17)$$

the quantum capacitance  $C_{\text{tunnel}}$ , exhibits a frequency dependency and is mainly dominating when the TBRTD is biased in the NDR region. The carrier accumulation in the QW, which causes the time delay, has been observed and theoretically analyzed in [78-80] for a DBRTD. This effect is expected to be similar in a TBRTD but at different energy levels, i.e., different bias voltages because of the two QWs: At a specific voltage, the first QW will be in resonance with the electrons at the emitter side, but not with the energy level in the second QW, which leads to charge accumulation in the first QW and, therefore, increasing the total quantum capacitance before reaching the NDR region. The geometrical capacitance, i.e., depletion capacitance  $C_0$  depends on the material stack and its doping profile. Due to the band bending, when biasing the device, the depletion capacitance  $C_0$  is bias voltage depended and is defined as follow:

$$C_0(V_{\text{TBRTD}}) = C_0^* A_{\text{TBRTD}} \frac{1}{\left(1 + \frac{V_{\text{TBRTD}}}{\phi_C}\right)^{m_m}} \quad (2.18)$$

where  $C_0^*$  is the capacitance per unit area at zero bias,  $A_{\text{TBRTD}}$  is the TBRTD mesa active area (see *device area* illustrated in Figure 2.1),  $m_m$  and  $\phi_C$  are a unit loss, fitting parameters. Further,  $C_0^*$  can be approximately determined by the dielectric constants and the layer thicknesses of the quantum structure in combination with the undoped internal layer:

$$C_0^* = \frac{\epsilon_{\text{material}} \epsilon_0 A_{\text{TBRTD}}}{d_{\text{b1}} + d_{\text{b2}} + d_{\text{b3}} + d_{\text{QW1}} + d_{\text{QW2}} + d_{\text{dep}}} \Big|_{U=0V} \quad (2.19)$$

where  $d_{b1}$ ,  $d_{b2}$ ,  $d_{b3}$  are the barrier thicknesses,  $d_{QW1}$ ,  $d_{QW2}$  the thicknesses of the wells, and  $d_{dep}$  the thickness of the depletion region, respectively.  $\epsilon_{material}$  contains the average value of the materials dielectric constants within the TBRTD internal part.

To complete the TBRTD modeling and to provide a method for circuit simulation, the small- and large-signal equivalent circuit of the TBRTD are presented. They are extracted mainly from the analytical model presented here and including the parasitic elements of the device. Different models are proposed in the literature to model resonance tunneling based devices [52–55], which, however, can primarily be traced back to the equivalent circuit used here, see Figure 2.4.

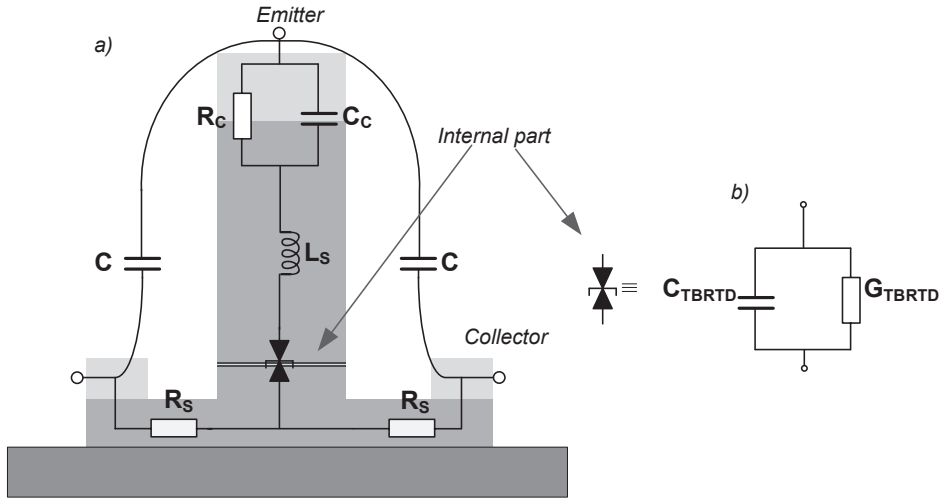


Figure 2.4: Schematic structure of a TBRTD device. a) Illustrating the internal and its connection to the external parasitic elements including the device structure and mesa height. b) internal part corresponding equivalent circuit.

The large-signal equivalent circuit provides a detailed voltage-dependent analysis of the individual components. Because of the frequency dependency of the admittance of the TBRTD, the small-signal equivalent circuit element values are determined for a specific frequency range and are considered to be constant at this range. The series inductance  $L_s$  is mesa dimension and doping dependent. The influence of the contact, i.e., the metal-semiconductor junction is modeled by the capacitance  $C_c$  parallel to the resistance  $R_c$ , which is mainly dependent on the metal and semiconductor material and doping. Furthermore, these parameters give a direct insight into the quality of the device fabrication steps. For example, an increase in the series resistance or inductance implies a fabrication problem. The total impedance of this equivalent circuit, as shown in Figure 2.4, is given as:

$$Z_{TBRTD}(V_{TBRTD}, \omega) = \frac{1}{\frac{1}{R_c} + j\omega C_c} + R_s + j\omega L_s + \frac{1}{G_{TBRTD}(V_{TBRTD}) + j\omega C_{TBRTD}(V_{TBRTD})} \quad (2.20)$$

By combining the capacitance presented in equation (2.17) with the impedance equation (2.20), the quantum capacitance and the negative conductance in the NDR region

can be experimentally determined. Further, a linear dependence of the internal TBRTD equivalent circuit parameter on the device area is given.

### 2.3 Principle of NDR-based fundamental oscillator

Assuming a simple resonator consisting of inductance ( $L$ ), capacitance ( $C$ ) and resistance ( $R$ ), as shown in Figure 2.5 where the inductance and capacitance describe the energy storage, magnetic and electric field energy, respectively, the resonator losses are included by the resistance ( $R$ ).

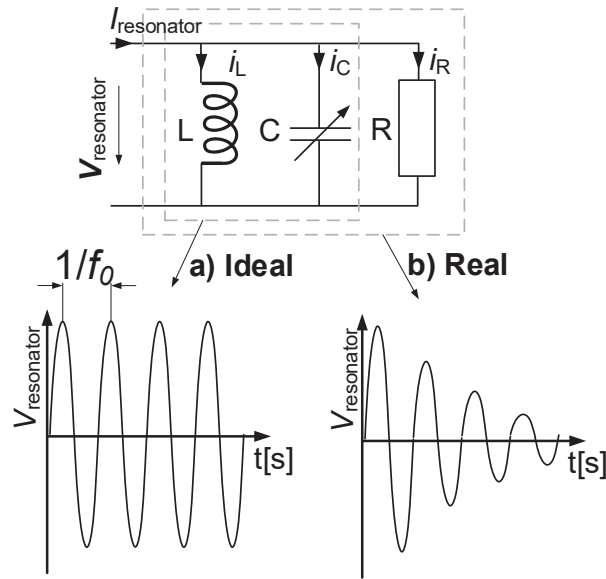


Figure 2.5: Equivalent circuit of a parallel resonator illustrating the output signal in the a) ideal case, where no losses are exciting, and b) a more realistic output signal, where the losses are damping the output signal over time.

The average stored energy is considered to determine the oscillation frequency. The electrical energy  $W_{\text{elec}}$  stored in the capacitance is:

$$W_{\text{elec}} = \frac{1}{4} |V_{\text{resonator}}|^2 C, \quad (2.21)$$

and the average magnetic energy  $W_{\text{mag}}$  stored in the inductor:

$$W_{\text{mag}} = \frac{1}{4} |i_L|^2 L = \frac{1}{4} |V_{\text{resonator}}|^2 \frac{1}{\omega^2 L}. \quad (2.22)$$

In resonance the magnetic energy and the electric energy stored in the system are equal  $W_{\text{elec}} = W_{\text{mag}}$  and therefore the resonance frequency is determined to:

$$\omega_0 = \frac{1}{\sqrt{LC}} \quad (2.23)$$

Another characteristic parameter of a resonator is its quality factor  $Q$ , which defines the ratio of the stored energy, equation (2.21) and equation (2.22), in the system to the lost energy as follows:

$$Q = \omega \frac{W_{\text{elec}} + W_{\text{mag}}}{P_{\text{loss}}}, \quad (2.24)$$

where the loss energy of the resonator is defined as the energy consumed at the loss resistance leading to a quality factor  $Q$  that can be rewritten at resonance as:

$$Q = \frac{R}{\omega_0 L} = \omega_0 RC. \quad (2.25)$$

A higher-quality factor means lower losses in the oscillator, i.e., less oscillation damping, and therefore the oscillation remains for a longer period before it disappears. Furthermore, due to the lower internal losses the oscillation stability at the resonance frequency is enhanced and therefore, the random shift in the phase of the signal is minimized leading to an improvement of the signal phase noise. On the other hand, a higher quality factor affects the oscillation buildup time negatively by increasing it. Next, the impedance of the resonator is investigated. The impedance seen at the input of the resonator is:

$$Z_{\text{in}} = (Y_{\text{in}})^{-1} = \left( \frac{1}{R} + \frac{1}{j\omega L} + j\omega C \right)^{-1}, \quad (2.26)$$

the delivered power to a parallel resonator is given by:

$$P_{\text{in}} = \frac{1}{2} Z_{\text{in}} |I_{\text{resonator}}|^2 = \frac{1}{2} |V_{\text{resonator}}|^2 \frac{1}{Z_{\text{in}}} = \frac{1}{2} |V_{\text{resonator}}|^2 \left( \frac{1}{R} + \frac{1}{j\omega L} + j\omega C \right). \quad (2.27)$$

And the lost power of the resonator is the power dissipated by the loss resistor  $R$  and is determined to:

$$P_{\text{loss}} = \frac{1}{2} \frac{|V_{\text{resonator}}|^2}{R}. \quad (2.28)$$

As shown in equation (2.25) and equation (2.28), the performance of the resonator is coupled to the total resonator losses. Decreasing this parasitic resistance increases the resonator quality factor. As will be shown later, for antennas this resistance includes also a radiation resistance part which defines radiation efficiency of the radiator and therefore, both resistances have to be separated for antenna characterization.

Eliminating the electrical losses of a resonator will provide a resonator without any damping over time. For this purpose, a negative resistor is to be integrated into the resonator. If the negative resistance has a sufficiently low value (high negative conductance), then the total resistance of the resonator is negative. In such a case, the amplitude of the oscillations excited in the resonator will grow over time until a stable large-amplitude of the oscillation is achieved. To illustrate the behavior of a negative differential resistance-based oscillator, the equivalent circuit presented in Figure 2.6 is used. The resonator with the admittance  $Y_{\text{res}}$  is

separated from the active elements, which provide negative resistance with the admittance  $Y_{\text{neg}}$ .

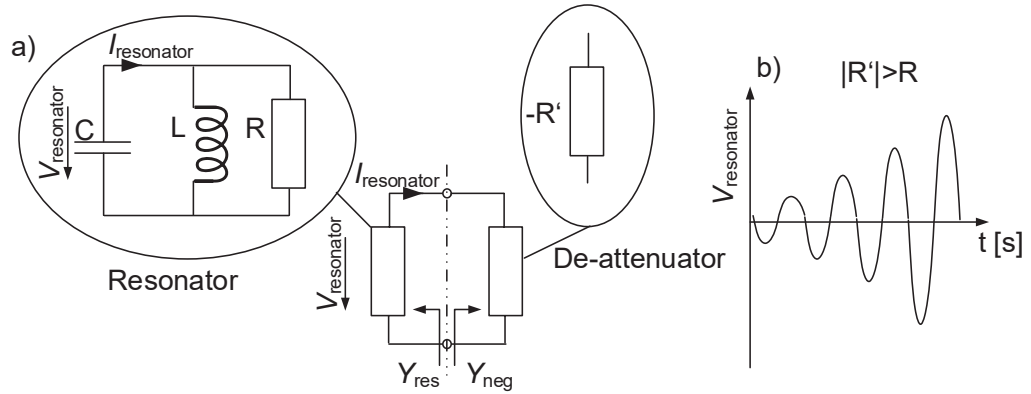


Figure 2.6: a) Equivalent circuit of the negative conductance model: the resonator and negative differential resistance are connected in parallel. b) the output signal of the resonator over time, illustrating the amplification, i.e., gain as a result of the negative resistance.

The admittance of the parts in Figure 2.6 is given as:

$$Y_{\text{res}} = G_{\text{res}}(\omega) + jB_{\text{res}}(\omega) \quad (2.29)$$

$$Y_{\text{neg}} = G_{\text{neg}}(\omega, V_{\text{bias}}) + jB_{\text{neg}}(\omega, V_{\text{bias}}) \quad (2.30)$$

while a total positive conductance of the circuit in Figure 2.6 implies energy dissipation, a total negative conductance implies an energy source. A total negative conductance is given when the negative differential conductance compensates the losses of the resonator, which defines the first oscillation condition:

$$\text{Re}\{Y_{\text{res}}\} + \text{Re}\{Y_{\text{neg}}\} < 0. \quad (2.31)$$

This equation implies that the output power is increasing (energy gain) until a steady-state condition is fulfilled. At this point, the real part of the admittance is equal to zero, and therefore the oscillation is stabilized. The second oscillation condition defines the oscillation frequency, i.e., resonance point. At this point, the total imaginary part of the admittance is equal to zero:

$$\text{Im}\{Y_{\text{res}}\} + \text{Im}\{Y_{\text{neg}}\} = 0 \quad (2.32)$$

These equations: (2.31) and (2.32), provide the first and second oscillation conditions that have to be fulfilled when designing an NDR based oscillation such as a TBRTD-based oscillator, which is the aim of this work.

### 2.3.1 TBRTD integration as an oscillator

The TBRTD is a device that is able to de-attenuate the losses of a resonator (see section 2.1). To utilize the de-attenuation properties of the TBRTD, a resonator re-design is needed. The resonator presented in Figure 2.6 is a simple and idealized equivalent circuit. As was shown earlier in chapter 2.2, the TBRTD has capacitance dominated complex impedance, and hence, to structure a resonator an inductance dominated resonator is required. Furthermore, due to this fact, a shift in the resonance frequency of the resonator is expected after integration.

In Figure 2.7, a more realistic equivalent circuit of a TBRTD integrated into a resonator is presented. The capacitive part of the device is shared between the TBRTD and the resonator but is dominated by the TBRTD. The losses that are to be compensated are not only the resonator but also the internal TBRTD losses, such as the series material stack resistance. The inductive part is provided by the resonator. As will be shown later, the on-chip antennae allows the realization of an equivalent resonator for oscillation application.

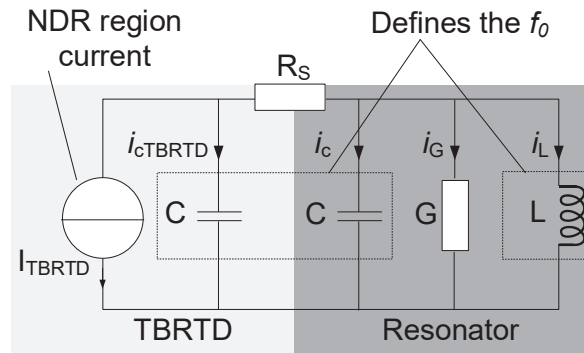


Figure 2.7: A equivalent circuit of a TBRTD integrated into a resonator, neglecting the external parasitic elements at high-frequencies.

A good model to describe an NDR based oscillator is given by the van der Pol equation. This equation is widely used when discussing an NDR based oscillator [56–58]. The van der Pol oscillator, which is an oscillator with a non-linear damping factor, was proposed by Balthasar van der Pol in 1920. The general second-order differential equation of such an oscillator is given as [59]:

$$\frac{d^2x}{dt^2} - \varepsilon_v(1 - x^2)\frac{dx}{dt} + x = 0 \quad (2.33)$$

where  $x$  represents the dynamic variable,  $\varepsilon_v$  defines the waveform of  $x$  versus  $t$ . Positive values for  $\varepsilon_v$  lead to an unstable circuit, and therefore oscillation occurs. Negative values are chosen to suppress the oscillation, where higher negative values indicate faster damping of the oscillation. For small values,  $0 < \varepsilon_v \ll 1$  a sinusoidal waveform is expected and for higher values,  $\varepsilon_v > 1$ , a rectangular-shaped signal.

In this work, the van der Pol model is utilized to determine the oscillating signal-form and to verify the fulfillment of the oscillation condition where  $0 < \varepsilon_v \ll 1$ . Furthermore, this model includes the gain saturation at steady-state operation and hence, is used to determine the maximum output power of an oscillator. Another advantage of this model is the possibility of injecting a second signal with a different frequency than the resonant frequency into the system. This property will be utilized when discussing the injection locking of a free-running oscillator with an external master signal. Considering the oscillator presented in Figure 2.7 under the following assumptions: the series resistance  $R_s$  is neglected and the capacitance of the TBRTD and resonator are summarized in a joint capacitance  $C$ . The currents within the single paths, in the TBRTD  $i_{\text{TBRTD}}$ , the capacitance  $i_C$ , the inductance  $i_L$ , and the resonator conductance  $i_G$  can be written as:

$$i_{\text{TBRTD}} = I_{\text{dc}}(V_{\text{dc}} + v) - I_{\text{dc}}(V_{\text{dc}}), \quad (2.34)$$

$$i_C = C \frac{dv}{dt}, \quad (2.35)$$

$$i_L = \frac{1}{L} \int v dt, \quad (2.36)$$

$$i_G = G_L v, \quad (2.37)$$

with  $I_{\text{dc}}(V_{\text{dc}})$  in equation (2.34) being the TBRTD current at the bias voltage  $V_{\text{dc}}$ . The TBRTD current is approximated using a cubic polynomial fitting [36]:  $I_{\text{TBRTD}}(V_{\text{dc}}) = -a(V_{\text{dc}} - V_{\text{center}}) + b(V_{\text{dc}} - V_{\text{center}})^3 + I_{\text{center}}$  where  $V_{\text{center}}$  and  $I_{\text{center}}$  are the voltage and current at the center of the negative differential conductance (NDC) region, and  $a$  and  $b$  are the fitting constants (see chapter 2.2 for more details). Applying Kirchhoff's current law on the oscillator node presented in Figure 2.7 and substituting equations (2.34)–(2.37) for the currents and differentiating with respect to  $t$ , the following expression is obtained:

$$C_{\text{TBRTD}} \frac{d^2 v}{dt^2} - [a - 3b(V_{\text{dc}} - V_{\text{center}})^2 - G_L - 6b(V_{\text{dc}} - V_{\text{center}}) - 3b] \frac{dv}{dt} + \frac{1}{L} v = 0 \quad (2.38)$$

The second-order differential equation shown here is similar to the van der Pol oscillator model presented in equation (2.33).

## 2.4 Injection locking of NDR-based oscillator

The free-running RTD-based fundamental oscillator is a promising candidate to achieve the highest possible oscillation compared to other electronic devices. Achieving a phase and frequency control of such oscillators will establish new application possibilities in the field of spectroscopy, radar systems, and communication. Phase control of single devices in an array approach can be used to increase the output power. Further, beam steering can be

accomplished by changing the phase of the output signal of single oscillators in the array. Controlling the phase and increasing the stability of the output signal leads to an increase in signal purity and hence, sharp signals.

In Figure 2.8, the developed locking mechanism is illustrated. An external signal oscillating at  $\frac{\omega_0}{n}$  is injected into a free running oscillator, oscillating at  $\omega_0$  (cf. Figure 2.8b). A small locking signal power compared to the power of the free running oscillator is sufficient to lock the oscillator. The multiplication factor  $n$  can be adjusted by changing the biasing point. The multiplied signal is then locking the free running oscillator.

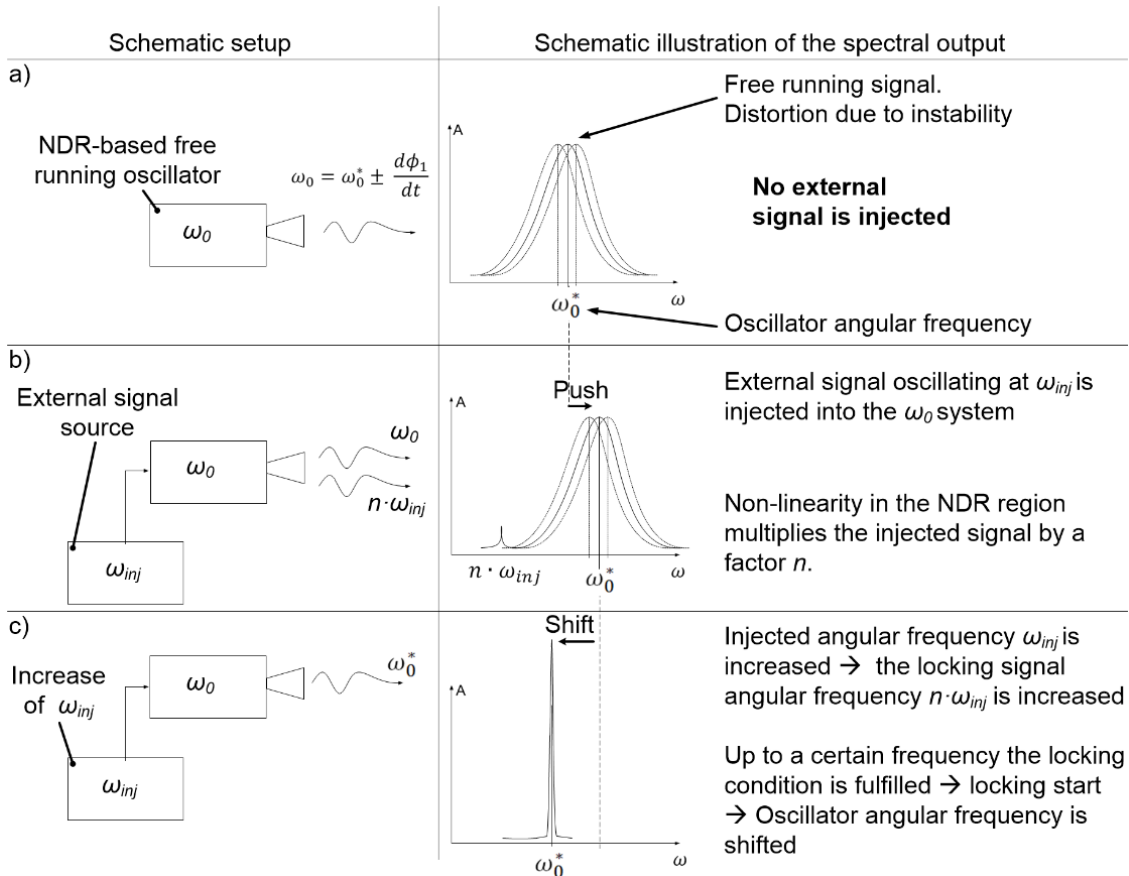


Figure 2.8: Illustration of the subharmonic injection locking mechanism. a) Shows an NDR based oscillator oscillating at  $\omega_0$  with no external injected signal, whereas in b) a signal oscillating at an angular frequency slightly lower than  $\frac{\omega_0}{n}$  is injected into the  $\omega_0$  system. The injected signal is multiplied by a factor  $n$ , and is visible in the spectrum. In c) the locking conditions are fulfilled and locking starts.

Some work was done using an external Phase-Locked-Loop (PLL) system to control the phase and stabilize the oscillation frequency, i.e., a sharp output signal of an RTD-based THz oscillator was presented for gas spectroscopy [60]. In this work, for phase and frequency control, wireless subharmonic signal injection is developed. The main target of this work is to present a proof of concept and demonstrate the capability of this novel process, in terms of frequency control and stability, even at THz frequencies.

### 2.4.1 Locking process

The fundamental numerical analysis presented in this section shall explain the locking mechanism in more detail. These theoretical investigations of injection locking were developed in close collaboration with Prof. Asada and Prof. Suzuki from *Tokyo Institute of Technology* and within their stay in our department as part of the Mercator fellowship and my short-term scientific mission at their laboratory in *Tokyo Institute of Technology*.

To sum up the locking mechanism, this process can be divided into three steps: first, the injected signal at  $\frac{f_0}{n}$  is detected in the  $f_0$  system (step I). Due to the current-voltage non-linearity in the NDR region, the signal is multiplied by a factor  $n$  (step II), where the factor  $n$  is bias voltage-dependent. The multiplied signal  $n\left(\frac{f_0}{n}\right)$  is locking the free-running signal when the locking condition, between the multiplied signal and the free-running signal  $f_0$ , is fulfilled (step III). For the detailed analysis, the circuit used in section 2.3.1 is extended with an external current source for injection locking, as shown in Figure 2.9. In this work, to circumvent the lack of isolation in two-terminal devices such as (TB-)RTD devices, a novel, wireless injection locking is investigated. This technique enables the utilization of architecture for power-scalable integrated THz transmitter arrays.

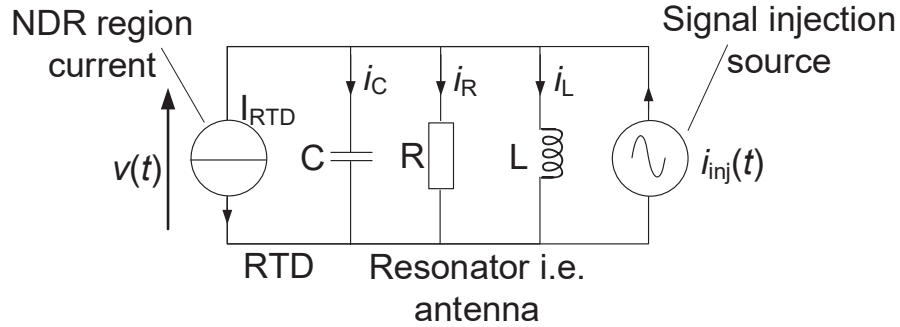


Figure 2.9: Simplified equivalent circuit of an NDR-based oscillator. The RTD device is modeled via a current source providing the negative resistance and the non-linearity.

The current definitions are the same as presented in section 2.3.1, which leads to the following second-order differential equation for this equivalent circuit:

$$\frac{d^2v}{dt^2} - \frac{\alpha - \beta v - \gamma v^2}{C} \frac{dv}{dt} + \omega_0^2 v = -\frac{\omega_1 I_{inj}}{C} \sin(\omega_1 t) \quad (2.39)$$

where  $\alpha = a - \frac{1}{R} - 3b(V_{dc} - V_c)^2$ ,  $\beta = 6b(V_{dc} - V_c)$  and  $\gamma = 3b$ . The second harmonic oscillation component is controlled by  $\beta$  where  $\beta \rightarrow 0$ , when biased at the center of the NDR region.  $\gamma$  controls the third harmonic component and has its maximum when biased at the NDR center.  $I_{inj}$  The current amplitude of the injected signal. The angular frequency of the oscillator without any external injection is defined by the RTD capacitance and the inductance of the resonator:  $\omega_0 = 1/\sqrt{LC}$ .

The subharmonic injection locking process of the NDR-based free running oscillator, oscillating at  $f_0$ , is as follows: A subharmonic signal, oscillating at  $\frac{f_0}{n}$  is wirelessly injected into a free running system, oscillating at  $f_0$ . The detected  $\frac{f_0}{n}$  signal is multiplied by the non-linearity of the device in the NDR-region represented by the factor  $n$ . The factor  $n$  is affected through the bias point in the NDR region. A bias point at the center of the NDR will result in an odd  $n$  factor ( $n = 3, 6$ , etc.), i.e., the odd number harmonic signal power is higher than the even harmonic signal power, whereas a bias point near the peak or valley point gives an even  $n$  factor ( $n = 2, 4$ , etc.). This behavior can be derived from the mentioned factors  $\beta$  and  $\gamma$  within the model. The multiplied signal  $n\left(\frac{f_0}{n}\right)$  is only then locking the free running oscillator when the locking conditions are fulfilled. Therefore, the fundamental locking mechanism is responsible for locking even at a subharmonic signal injection. In the next chapter, the analytical model of the fundamental locking is presented in more detail.

### 2.4.2 Fundamental signal locking

The voltage across the oscillator, including the harmonic components, can be written as:

$$v(t) = \sum_{n=1}^{\infty} V_n \cos(n\omega_1 t + \phi_n) = \frac{1}{2} \sum_{\substack{n=-\infty \\ n \neq 0}}^{\infty} \tilde{V}_n e^{jn\omega_1 t}, \quad (2.40)$$

with  $\tilde{V}_n = V_n e^{j\phi_n}$ . For the fundamental locking, where the injected signal frequency is equal to the resonator frequency, i.e., the oscillator angular frequency is given as  $\omega_0 = \omega_1 + \frac{d\phi_1}{dt}$ , with  $n = 1$ , the equation (2.40) is simplified to

$$v(t) = \frac{1}{2} \tilde{V}_1 e^{j\omega_1 t}. \quad (2.41)$$

Substituting equation (2.41) into (2.39) gives:

$$\begin{aligned} \frac{d\tilde{V}_1}{dt} e^{j\omega_1 t} + \left( j \frac{\omega_1^2 - \omega_0^2}{2\omega_1} - \frac{\alpha}{2C} \right) \tilde{V}_1 e^{j\omega_1 t} + \frac{\beta}{4C} V_1^2 e^{j\omega_1 t} + \frac{\gamma}{8C} V_1^3 e^{j\omega_1 t} \\ = \frac{I_1}{2C} (e^{j\omega_1 t} - e^{-j\omega_1 t}), \end{aligned} \quad (2.42)$$

and the fundamental injection locking ( $\omega_1 \approx \omega_0$ ) it is simplified to:

$$\frac{d\tilde{V}_1}{dt} + \left( j(\omega_1 - \omega_0) - \frac{\alpha}{2C} \right) \tilde{V}_1 + \frac{\beta}{4C} V_1^2 + \frac{\gamma}{8C} V_1^3 = \frac{I_{inj}}{2C}. \quad (2.43)$$

Insert  $\tilde{V}_1 = V_1 e^{j\phi_1}$  into equation (2.43) and separating it into its real and imaginary part, gives:

$$\frac{dV_1}{dt} - \frac{\alpha}{2C} V_1 + \frac{\beta}{4C} V_1^2 + \frac{\gamma}{8C} V_1^3 = \frac{I_{inj}}{2C} \cos(\phi_1), \quad (2.44)$$

$$\frac{d\phi_1}{dt} + (\omega_1 - \omega_0) = -\frac{I_{inj}}{2CV_1} \sin(\phi_1). \quad (2.45)$$

Equation (2.45) is the so-called Adler's equation [61]. For the stationary state  $\frac{d\phi_1}{dt} = 0$ , the angular frequency of the oscillator, is locked to  $\omega_1$ . The possible values of the sine function give the locking range of the oscillator which can be written as:

$$|\omega_1 - \omega_0| \leq \frac{I_{inj}}{2CV_1} \quad (2.46)$$

the voltage  $V_1$  is determined by equation (2.44) and is bias voltage-dependent. At the locking edge (i.e.,  $\phi_1 = \frac{\pi}{2}$ ) equation (2.44) can be rewritten:

$$-\frac{\alpha}{2C}V_1 + \frac{\beta}{4C}V_1^2 + \frac{\gamma}{8C}V_1^3 = 0, \quad (2.47)$$

Biasing at the center of the NDR region, i.e., the quadratic component  $\beta \rightarrow 0$ ,  $V_1$  can be expressed as:

$$V_1 = 2\sqrt{\frac{\alpha}{\gamma}} = \sqrt{R \cdot P_{out}}, \quad (2.48)$$

where  $P_{out}$  is the output power of the free-running oscillator, without locking, and  $R$  is the resistance of the resonator. When biasing the device in the peak or valley region, the quadratic component  $\beta$  increases while the cubic component  $\gamma$  decreases and can be set to 0. In this scenario  $V_1$  is defined as:

$$V_1 = 2\alpha\beta, \quad (2.49)$$

The locking current  $I_{inj}$  in equation (2.46), is defined by the consumed injected power at  $R$ :

$$I_{inj} = \sqrt{\frac{P_{in}}{R}}. \quad (2.50)$$

Substituting equation (2.48) and (2.50) in equation (2.46), the relative locking range, where fundamental locking occurs, is determined as:

$$\frac{|\omega_1 - \omega_0|}{\omega_0} \leq \frac{1}{2CR} \sqrt{\frac{P_{in}}{P_{out}}}. \quad (2.51)$$

From equation (2.45) and (2.51) the phase relation of the angular frequency difference between the locking signal  $\omega_1$  and the free-running signal  $\omega_0$  is given as:

$$\phi_1 = \sin^{-1} \left\{ 2CR \sqrt{\frac{P_{out}}{P_{in}}} \cdot \frac{\omega_0 - \omega_1}{\omega_0} \right\}, \quad (2.52)$$

changing the free-running angular frequency  $\omega_0$  within the locking range, equation (2.51), the phase relation regarding the injected signal changes from  $-\pi/2$  to  $+\pi/2$ . Therefore, this technique provides a mechanism to tune the phase of a single oscillator in an array of oscillators for beam steering in the free space.

---

## 2.5 Antenna

The first-time antenna communication was demonstrated in 1886 by Heinrich Hertz at the *Karlsruhe Institute for Technology* (KIT) [62]. Since then, antennae were improved, and many new designs for different applications were investigated. An antenna transfers energy from an electronic circuit (moving charge) to an electromagnetic wave, which can propagate, and vice versa. With increasing frequency, the size of the antenna shrinks, making them suitable for mobile applications. In this work, on-chip antennae are used to design a resonator for the active elements, to define its frequency and as a radiator for the electromagnetic energy at different frequencies. At UDE, antennae and structures in the microwaves range [63] and also in the sub THz [64] were designed and fabricated.

The presented resonator in chapter 2.2 is made with an embedded antenna. Two different types of antennae were designed in this work: a resonant antenna (slot antenna) and a broadband antenna (bowtie antenna). A resonant antenna provides strong functionality at a specific frequency. The broadband approach covers a large frequency range at the expense of functionality and efficiency. The broadband antennae are mainly used for detection operation, as will be shown later. To describe the antenna performance, its main parameters, such as its radiation pattern, directivity, and antenna efficiency, are briefly described in this chapter, while a more detailed description can be found elsewhere [65–70]. Furthermore, for simplicity, the antennae description is carried out on antennae that are placed in the free space, i.e., surrounded by one medium. Afterwards, the main challenges when operating an antenna in the THz frequencies, are presented. In this work, the antenna performance was determined via an EM-simulation, where co-simulation of the structure was carried out with Advanced Design System (ADS)-momentum, Empire, and Computer Simulation Technology (CST). A short introduction to the simulation tools will be presented. At the end of this chapter, the used antennae and its operation region are shortly introduced. Further, the development of the antenna equivalent circuit, out of its internal current flow is presented. Later the equivalent circuit of the antenna is used for circuit simulation and matching of the antenna to the active element.

### 2.5.1 Antennae characteristics parameters

#### Radiation pattern

The radiation pattern of the antenna shows the behavior, i.e., shape and strength, of the radiated beam. The minimum distance for the far-field pattern is called Fraunhofer distance  $d_f$  [71] with  $d_f = \frac{2O^2}{\lambda}$ , where  $O$  is the largest dimension of the radiator and  $\lambda$  the wavelength. If considering an antenna placed in one medium, e.g., free space, the radiation patterns can be categorized into three groups [71]: isotropic, omnidirectional, and directive, as shown in Figure 2.10. The isotropic antenna (Figure 2.10a) is a hypothetical lossless, i.e., ideal, antenna

which is not realizable. The performance of such an antenna is taken as a reference for expressing the performance of the realistic antenna. The omnidirectional antenna has a directional pattern in one plane and a non-directional pattern in its orthogonal plane (Figure 2.10b). The radiation pattern of the directive antenna shows a pattern focusing on a point in space (Figure 2.10c).

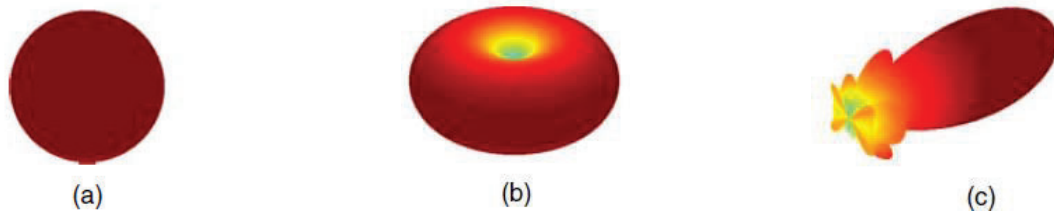


Figure 2.10: 3D-Pattern of the far-field radiation of three antenna types placed in free space. a) isotropic, b) omnidirectional, and c) directive. Adapted from [72]. Reprinted with permission.

The three-dimensional representation provides a simple illustration of the radiated beam pattern. Typically, spherical coordinates are used  $(r, \theta, \varphi)$  with  $r$  the radial distance and  $\theta$  the inclination angle and  $\varphi$  the azimuth angle [72]. For more detailed analyses, two-dimensional section cut out of the radiation patterns, presented in polar or cartesian plots are used. Basic antenna parameters can then be extracted directly out of these diagrams. As an example, a cut-line in the radiation beam of a directive antenna (Figure 2.10c) is presented:

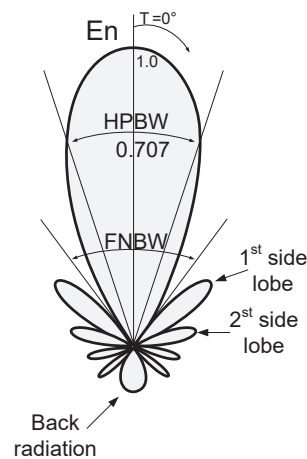


Figure 2.11: 2D cut-line in one angle of the far-field radiation pattern. This figure illustrates the fundamental parameters that can be gathered from the radiation pattern.

The following important antenna parameters are directly extracted from the antenna radiation pattern shown in Figure 2.11:

- 3dB beamwidth or Half Power BeamWidth (HPBW): Angular distance for which the power density radiation pattern is equal to half of its maximum.
- First Null BeamWidth (FNBW) or beamwidth zero: Angular distance of the main lobe minimum.

- 
- Side Lobe Level (SLL): The power difference between the main lobe power to the first side lobe power.
  - Front to back radiation: the relation between the radiation pattern value in the direction of maximum radiation, and the value of the radiation pattern value in its opposite direction.

These parameters are required to determine the properties of an antenna for signal radiation or detection.

### Directivity

The directivity  $D(\theta, \varphi)$  of an antenna specifies the ability to radiate or receive a radiated power density to or from a specific direction. This parameter is a relative quantity and is defined as the relation between the power density emitted in a specific direction at a fixed distance  $P(\theta, \varphi)$  compared to the power density of an isotropic antenna radiating the same power  $\frac{P_r}{(4\pi r^2)}$ :

$$D(\theta, \varphi) = \frac{P(\theta, \varphi)}{\frac{P_r}{(4\pi r^2)}} \quad (2.53)$$

A good approximation of the maximum directivity  $D_{max}$  can be calculated from the radiation pattern of the antenna:

$$D_{max} = \frac{4\pi}{\Delta\theta_1 \cdot \Delta\theta_2} \quad (2.54)$$

Where the angles  $\theta_1$  and  $\theta_2$  are the 3 dB beamwidth in the main plans of the radiation pattern shown in Figure 2.11. The directivity is a fundamental parameter and is required to characterize the performance of the antenna.

### Antenna Gain

The antenna directivity  $D(\theta, \varphi)$  is proportional to the antenna gain,  $Gain(\theta, \varphi)$ . An ideal antenna will radiate all the delivered power into the free space, and therefore its gain is equal to its directivity at any specific location  $Gain(\theta, \varphi) = D(\theta, \varphi)$ . In real scenarios, antennae are lossy, and only a part of the delivered power is radiated into the free space. To include the losses of the antenna, an antenna efficiency parameter  $\epsilon_{rad}$  is introduced. The antenna efficiency value is a number between zero (no power is radiated) and one (all delivered power is radiated, i.e., no losses). The antenna gain:

$$Gain(\theta, \varphi) = \epsilon_{rad} \cdot D(\theta, \varphi), \quad (2.55)$$

provides the exact power transmission capability of an antenna and is proportional to the effective antenna area, as will be illustrated next, see equation (2.57).

---

## Effective area

The area of an antenna is determined first by its aperture size  $A_{\text{aper}}$ . However, due to losses and directivities of the beam the effective antenna area  $A_{\text{eff}}$  differs from its aperture area size. As was mentioned earlier, most of the antenna parameters defined relating to an isotropic radiating ideal antenna, which is applicable for the effective area as well. The area of an ideal isotropic antenna is defined as:

$$A_{\text{iso}} = \frac{\lambda^2}{4\pi}, \quad (2.56)$$

where  $\lambda$  is the wavelength. The ideal isotropic antenna area is proportional to the antenna effective area by a factor of the gain of the antenna. The effective antenna area is determined as:

$$A_{\text{eff}} = A_{\text{iso}} \cdot \text{Gain} = \frac{\lambda^2}{4\pi} \cdot \text{Gain}. \quad (2.57)$$

This leads to another parameter which is the aperture efficiency given by the following formula:

$$\varepsilon_{\text{ape}} = \frac{A_{\text{eff}}}{A_{\text{aper}}} \quad (2.58)$$

The antenna size defines the amount of power that will be received or transmitted through an antenna at a constant power density. For this reason, larger effective antenna areas are required, and hence, the reduction of the antenna losses, such as power dissipation in the form of heat in the antenna metals, un-uniform illumination, to mention some, is pursued.

### 2.5.2 Electromagnetic simulations-software for antennae

A short introduction of the used commercial software for antenna design is presented in this section. The focus point is set on a brief introduction to the used solution methods. In this work, co-simulations of the same structure with different solver techniques were carried out to validate the simulation results. Good agreement between the different simulation techniques was used as a prerequisite to accept the results, else, a more in-depth investigation of the structure and its modeling was done.

In our department, ADS-momentum was used to design the first structure for the antenna. This structure was then co-simulated by CST and Empire in the laboratory of ATE at the University of Duisburg-Essen. Therefore, the usage of ADS-momentum is briefly introduced. Full attention must be paid to feed the same information into different simulation tools. For the antenna structure, the same Graphic Data System File (.GDS-File) containing the geometric shapes of the antenna and its feeding data is used. Further, the material parameter, such as permittivity, conductivity, and losses, must be adjusted. For the designed structure the EM-simulators provide as a result the scattering parameters,

---

admittance and impedance and its radiator characteristics. The scattering and admittance results are used in this work to characterize the electrical properties of the simulated antenna and hence also antenna integration within the circuit simulation mainly for matching application which will be presented later in more detail.

#### **ADS-Momentum:**

This simulator uses the Integral Equations solved by the Method Of Moments (IE-MoM) [73]. This method provides a simulation technique that gives a valid solution at each point in the environment surrounding the object and hence can describe large and arbitrary, multi-layered structures [74]. However, complicated structures result in a substantial memory requirement due to the MoM matrix results.

ADS-momentum EM simulator provides a solver for 2.5 D layouts using the IE-MoM method. A modeling capability for a full 3D structure is limited since finite dielectric volumes are not included in the simulation. Vertical currents per layer and horizontal side-current of a layer are included. The results of this solver are in the frequency domain, i.e., the solution is determined at each frequency point. The simulation results are displayed as the impedances, scattering parameters, and especially for antennae, the radiation pattern, and the basic antenna parameters. After defining the object structure, in our case, the antenna metallization layer, the environment surrounding the antenna is specified. This step is done within a so-called substrate definition step. In this work, the antenna is placed on an InP substrate and is surrounded by air. For accurate modeling of the antenna, and because of the lack of the full 3D structures, an infinitely high InP substrate, at the bottom-side, and air, at the top-side, of the antenna are configured. Then a mesh is structured, which is a function of the frequency. The mesh density is determined through the stimulation frequency and the number of cells per wavelength.

#### **Empire XPU:**

Empire is a 3D full-wave EM solver in the time-domain and is based on the Finite-Difference Time-Domain (FDTD) technique [75]. This technique is a time-domain technique that provides solutions for a wide frequency range with a single run. By approximating a numerical solution for a discretized form of Maxwell's equation, both in space and time provides a powerful method to determine the electric and magnetic field at each point in the simulation area. This is possible due to the nature of Maxwell's differential equation, which describes the time evolution relation of the electric field and magnetic field. The time variation of the electric field is determined through the spatial variation of the magnetic field, and the time variation of the magnetic field is defined by the spatial variation of the electric field [76].

---

## CST studio suite:

This 3D layout simulator is based on the Finite Integration Technique (FIT) [77]. This simulator provides both a time and a frequency domain solvers; however, for our approach here, only the time domain was used. The FIT solving method describes Maxwell's equation on a grid space, the resulting matrix containing the obtained integral quantity equations which include directly some characteristic properties of Maxwell's equation. The FIT can be used for different kinds of grids. The time-domain solver of CST calculates the broadband behavior of the electromagnetic response of a device in one simulation run [78].

### 2.5.3 On-Chip THz Antennae

So far, the introduced antennae are placed in the free space or are surrounded by only one medium with its radiation, when using planar antennae, is radiated equally above and below the antenna planes. At THz frequencies, the antennae are very small and usually monolithically integrated on-chip. They are placed on an isolator or insulating semiconductor, which influences their radiation pattern due to the interface of two different mediums (air on the top side and isolator or semiconductor, on the bottom side).

In this work, only InP-substrates with a static dielectric constant of  $\epsilon_{\text{InP}} = 12.35 - 12.61$  [79, 80] are used. The high dielectric constant of the substrate, results in antenna radiation direction mainly into the substrate [81, 82]. This effect poses several challenges for on-chip antenna design, which will be discussed in this section. Considering sub-THz and THz waves, the substrate thickness is several magnitudes thicker than the wavelength of the radiated beam. Waves with an incident angle larger than the critical angle  $\alpha_{\text{critical}}$  are entirely reflected and trapped as surface waves (see Figure 2.12). This effect negatively influences the radiation and detection efficiency of the device. Besides, standing waves may occur due to Fabry-Perot behavior. The output power over the frequency can vary and has maxima at specific frequencies, as shown in [83].

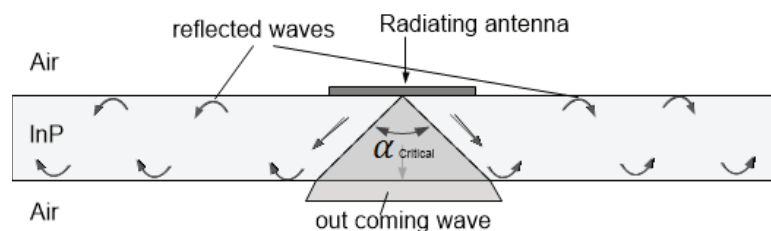


Figure 2.12: Schematical structure of a THz antenna fabricated on an InP-substrate illustrating the reflected wave within the substrate. A substrate wave is formed within the InP-substrate because of the significant height of the InP-substrate, and hence, a small critical angle occurs.

To overcome these challenges, several methods were investigated elsewhere. First, reducing the thickness of the substrate down to some  $\mu\text{m}$  will ensure electromagnetic transparency of

the substrate [84]. Further, an antenna-over-antenna structure was introduced. Thereby the beam was reflected to the top side of the antenna [85, 86], i.e., no beam is traveling through the substrate to the bottom side. These methods provide a good solution, but their realization is very challenging and affects the fabrication yield. A more straightforward approach is to use a Si-lens at the bottom side of the antenna. Si has a similar permittivity value as the InP; hence, the Si-lens acts as an extension of the InP-wafer. As shown in Figure 2.13, the thickness of the lens improves the beam angle of the incident wave to almost normal, and therefore the internal reflection of the beam in the substrate is reduced; additionally, the directivity of the antenna is increased. Disadvantages of the surface lenses are the increased device area and the power losses caused by reflection on the curved surface of the Si-lens, 30% of the incident THz wave is reflected [87].

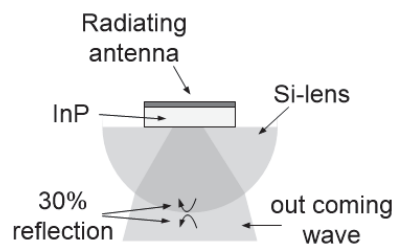


Figure 2.13: A possible solution for the substrate wave — critical angle rises by using a Si-lens at the bottom side of the InP substrate.

#### 2.5.4 THz Antenna types and antenna integration in a circuit simulator

In this work, the THz resonator for the oscillator or detector is structured by monolithic on-chip integration of an antenna on InP-substrate. As shown in chapter 2.1, a TBRTD has a frequency-dependent capacitive impedance. In order to build a resonator with such a TBRTD an antenna with inductive impedance is required. For this kind of operation and an on-chip integration the dipole-, slot- and patch-antennae [88] are the candidates of choice. Within this work, the slot antenna was chosen, mainly because of its smaller size and relatively simple fabrication process even at THz frequencies. Further, as will be shown later, this type of antenna provides the best structure for wireless signal injection for the locking mechanism. As a broadband antenna, the self-complementary bowtie antenna was chosen.

The antenna characterization is mainly performed with EM-simulation (see section 2.5.2). The simulated scattering parameters are utilized to determine the antenna admittance. For circuit simulation and matching of the antenna to an active device, an equivalent electrical circuit for the antenna is developed. The equivalent circuit elements are determined out of the simulated admittance. This approach is briefly introduced for both antennae in this section.

---

## Resonant approach: Slot antenna

The slot antenna consists of a metal plate with a defined slot at its center, which defines its resonance frequency, see Figure 2.14a. Within this slot, a standing electromagnetic wave is formed. Performance tuning is carried out by adjusting the slot dimensions. The radiation pattern of a slot antenna is omnidirectional [71]. If the antenna is placed on an InP-substrate, because of the high permittivity, the radiation is directed towards the InP-substrate. As shown in Figure 2.14a, the feeding point position of the slot antenna applied between its long ends. The electrical field of the standing wave is within the slot opening, and the current flows along the slot opening. Further, Figure 2.14b is illustrating the impedance of a slot antenna. The typical bandwidth of this resonant antenna is among 10 % of its resonance frequency  $f_0$ . Moreover, the slot antenna impedance is dominated by its inductance at frequencies lower than the resonance frequency. At frequencies higher than the resonance frequency, the impedance of the antenna is dominated by its capacitance.

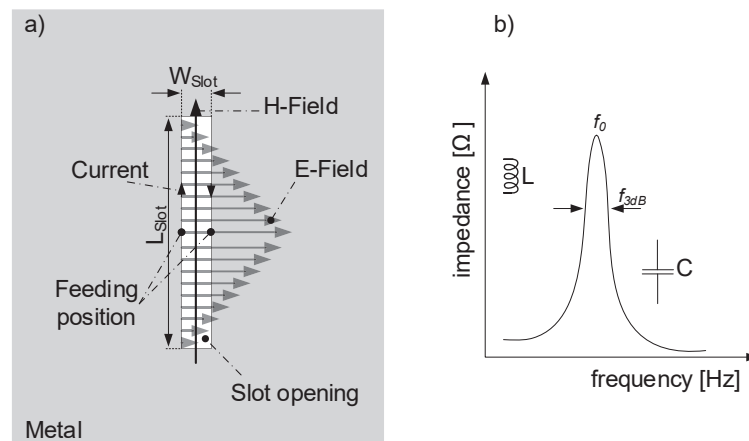


Figure 2.14: a) Schematic structure of a slot antenna illustrating the E-field orientation and the current flow at the slot-edge. In b) The impedance over the frequency of a slot antenna is presented. The inset illustrates the dominating impedance part in the specific frequency region, i.e., before and after the resonance point.

Utilizing the knowledge of the current flow and the standing wave in the slot antenna, the equivalent circuit is developed (see Figure 2.15a), which is valid up to the resonance frequency. This equivalent circuit is used for antenna characterization and integration into the circuit simulators. The equivalent circuit approach provides an effective mechanism for antenna-description.

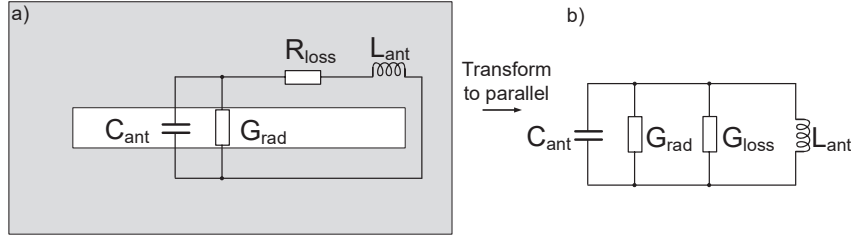


Figure 2.15: a) Extraction of the electrical equivalent circuit of a slot antenna utilizing the current flow-path and b) its simplification to an equivalent parallel circuit.

$C_{\text{ant}}$  and  $L_{\text{ant}}$  are the antennae capacitance and inductance, respectively, defining the antenna resonant frequency.  $G_{\text{rad}}$  is the radiation conductance which quantifies the amount of power radiated or consumed by the antenna. The antenna losses are summed up in  $R_{\text{loss}}$ . To simplify the equivalent circuit approach of the antenna and provide a more straightforward admittance calculation, the series connection is transformed into a parallel connection, as shown in Figure 2.15b. The impedance of the series connection is:

$$Z_{\text{ser}}(\omega) = R_{\text{loss}} + j\omega L_{\text{ant}}. \quad (2.59)$$

Transforming it to its admittance which is equal to  $\frac{1}{Z_{\text{ser}}}$

$$Y_{\text{ser}}(\omega) = \frac{R_{\text{loss}} + j\omega L_{\text{ant}}}{R_{\text{loss}}^2 + (\omega L_{\text{ant}})^2}, \quad (2.60)$$

with  $R_{\text{loss}}^2 \ll \omega^2 L_{\text{ant}}^2$  follows:

$$\text{Re}\{Y_{\text{ser}}(\omega)\} = \frac{R_{\text{loss}}}{(\omega L_{\text{ant}})^2} = G_{\text{loss}}, \quad (2.61)$$

$$\text{Im}\{Y_{\text{ser}}(\omega)\} = \frac{1}{\omega L_{\text{ant}}} = L_{\text{ant}}.$$

Therefore, the total admittance of the antenna can be written as:

$$Y_{\text{ser}}(\omega) = (G_{\text{rad}} + G_{\text{loss}}) + j\omega C_{\text{ant}} + \frac{1}{j\omega L_{\text{ant}}}. \quad (2.62)$$

Using the equivalent circuit presented in Figure 2.15, the radiated or consumed power is determined by:

$$P_{\text{rad}} = \frac{I_{\text{ant}}^2}{G_{\text{rad}}}. \quad (2.63)$$

And the total antenna losses are:

$$P_{\text{loss}} = I_{\text{ant}}^2 R_{\text{loss}}, \quad (2.64)$$

where  $I_{\text{ant}}$  is the current flowing in the antenna. The antenna efficiency is then defined as:

$$\epsilon_{\text{eff}} = \frac{P_{\text{rad}}}{P_{\text{rad}} + P_{\text{loss}}} = \frac{1}{1 + G_{\text{rad}} R_{\text{loss}}}. \quad (2.65)$$

## Broadband approach: Self-complementary bowtie antenna

A broadband antenna is best suited, especially for detector applications, via the self-complementary approach. The advantage of a self-complementary antenna for broadband detector applications is its frequency-independent input impedance [89]. As presented in [90], the impedance of a self-complementary antenna is defined as:

$$Z_{in} = \frac{Z_0}{2} \quad (2.66)$$

Where  $Z_0$  is the impedance of the environmental medium and in free space  $Z_0 = \eta = 120\pi \Omega$  when assuming an infinitely long wing length. However, in reality, a frequency dependency is given since antenna length is limited. The schematic structure of a bowtie antenna is shown in Figure 2.16a. As a design principle of the bowtie antenna, only the angle between the wings is used as a design parameter. Both wings in Figure 2.16a are from the same material system. In this work, only the self-complementary antenna is designed. The antenna angle  $\alpha$  is kept constant at  $90^\circ$ , and the wing width  $W$  corresponds to length  $L$ . The active element is positioned in the gap between the wings, as shown in the inset of Figure 2.16a. As shown in Figure 2.16b, this antenna has a self-resonance point, where the imaginary part of the antenna impedance is equal to zero (see Figure 2.16b). At frequencies higher than the self-resonance point, the impedance of the antenna is almost constant and mainly resistive without any imaginary elements. Tuning the length of the self-complementary antenna tunes its self-resonance point frequency. The equivalent circuit of the bowtie antenna can be extracted out of its shape, as shown in the inset of Figure 2.16a, and gives a good agreement to the antenna impedance for frequencies higher than the self-resonance point.

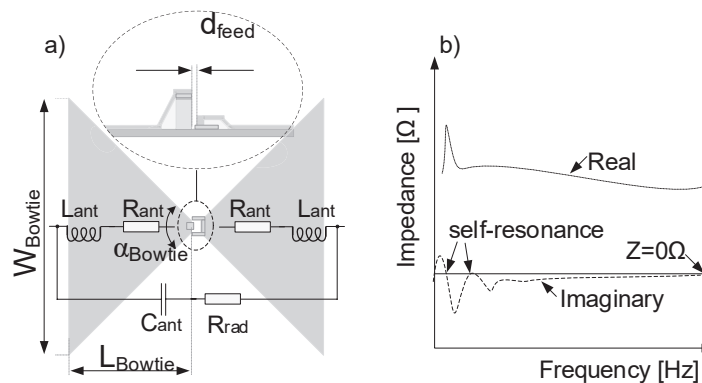


Figure 2.16: a) Schematical structure of a bowtie antenna with its characteristic design parameters. Its equivalent circuit and its metal-structure are presented. b) A typical impedance of a self-complementary bowtie antenna with its self-resonance at low frequencies.

## 2.6 Principle of resonant tunneling-based rectifier

A rectifier detector converts an AC input signal to its DC quantity directly, and therefore, it is also called a direct detector. Utilizing the non-linear current-voltage-characteristics of a device leads to a measured net DC quantity due to the asymmetry. A wide used device for direct rectification is the Schottky diode. These elements utilize the work function difference between a semiconductor and a metal brought into contact to provide a non-linearity in its current-voltage characteristics. Different designs are used, such as binary and ternary compounds [41] and heterostructure detectors [42]. The non-linearity of these devices is given by the thermal exponent in the current-voltage characteristics and hence, is limited through the thermal energy component with  $kT \sim 25$  meV at room temperature, and consequently, only a maximum current sensitivity of roughly 20 A/W is achievable. Whereas, non-linearity in the TBRTD is given by the alignment of the 2D sub-bands in the quantum wells [43]. Therefore, no thermal exponent limitation is given, and hence, a stronger non-linearity can be achieved. Increasing the non-linearity increases the responsivity of the detector.

For signal rectification with a TBRTD, the non-linearity in the current-voltage characteristic at zero bias is used. The operation principle is shown in Figure 2.17. The current blocking behavior in the reverse direction, is used to rectify the signal, i.e., only the positive part of a sinus signal is transmitted. Using a voltmeter to measure the DC voltage drop over the device, the effective voltage value of the transmitted signal can be defined.

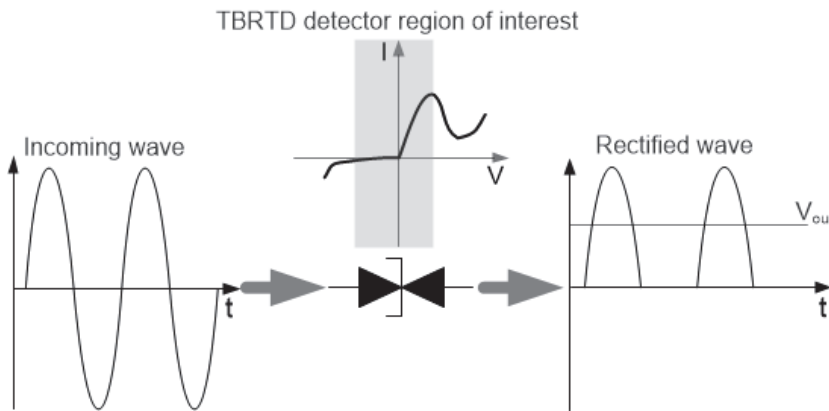


Figure 2.17: Operation principle of a TBRTD biased at zero volts, operating as a rectifier. The inset illustrates the IV-region used for signal rectification.

The main characteristic parameters of a rectifier operating at high frequencies are responsivity and Noise Equivalent Power (*NEP*). The voltage and current responsivity ( $R_v$  and  $R_i$ , respectively) of a detector gives direct information of how much output voltage or current is generated at a particular incoming power as:

$$R_v = \frac{V_{out}}{P_{in}}, \quad (2.67)$$

$$R_i = \frac{I_{\text{out}}}{P_{\text{in}}}, \quad (2.68)$$

with  $P_{\text{in}}$  the power at the input of the detector,  $V_{\text{out}}$  the rectified voltage over the detector and  $I_{\text{out}}$  the rectified current in the detector.

The electrical *NEP*, on the other hand, provides direct access to the detector power-sensitivity and hence, determines the minimum power required to obtain a signal equal to the noise with one Hz bandwidth, i.e., minimum detectable power [91]. Further, it describes the signal to noise ratio. The *NEP* is derived by the noise density  $N$  divided with its responsivity ( $R_v$  or  $R_i$ ). In this work, a zero bias detector is investigated, where the noise density is mainly dominated by the thermal noise arising from the channel resistance. Thus, the Johnson-Nyquist noise relationship with the Rayleigh-Jeans approximation [91] is used. The voltage and current  $NEP_v$  and  $NEP_i$  are defined as follows:

$$NEP_v = \frac{\sqrt{N}}{R_v} = \frac{\sqrt{4k_B T_{\text{temp}} BW R}}{R_v} \quad (2.69)$$

$$NEP_i = \frac{\sqrt{N}}{R_i} = \frac{\sqrt{\frac{4k_B T_{\text{temp}} BW}{G}}}{R_i} \quad (2.70)$$

where  $k_B$  is the Boltzmann constant,  $T$  the temperature in Kelvin,  $BW$  the bandwidth, and  $R$  the channel resistance ( $G$  the conductance =  $\frac{1}{R}$ ).

To characterize the detection capability of a TBRTD integrated into an antenna, the equivalent circuit shown in Figure 2.18 is used.

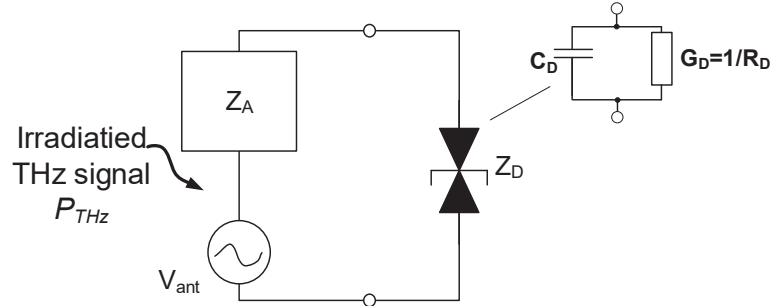


Figure 2.18: Block diagram including the impedance of the antenna as  $Z_A$  and the TBRTD as  $Z_D$  for simulation of the TBRTD antenna device, operating in detection mode.

The rectified current in a non-linear device is given as follow [92]:

$$I_{\text{out}} = \frac{1}{T} \int_0^T i_D(V_{\text{dc}} + V_{\text{ac}} \sin(\omega t)) - I_D(V_{\text{DC}}) dt, \quad (2.71)$$

with  $V_{\text{dc}}$  the operation point,  $V_{\text{ac}}$  the AC voltage amplitude across the diode and  $\omega$  the angular frequency. Setting the operation point at 0 V (zero-bias detector), using the Taylor expansion

for the diode current, neglecting higher-order terms for simplicity and assuming an AC voltage swing over the diode to  $V_{ac} = \frac{V_A Z_D}{Z_A + Z_D}$ , the detected current can be rewritten as:

$$I_{out} \approx \frac{1}{4} \cdot \frac{d^2 I_D}{dV^2} V_{ac}^2 = \frac{1}{4} \cdot \frac{d^2 I_D}{dV^2} \cdot \frac{Z_D^2}{Z_A^2 + Z_D^2} V_A^2. \quad (2.72)$$

Out of equation (2.72), the voltage drop over the diode is determined as follows:

$$V_{out} \approx I_{out} \cdot R_D \approx \frac{1}{4} \cdot \frac{d^2 I_D}{dV^2} V_{ac}^2 \cdot R_D \approx \frac{1}{4} \cdot \gamma_{cc} \cdot V_{ac}^2 = \frac{1}{4} \cdot \gamma_{cc} \cdot \frac{Z_A^2}{Z_A^2 + Z_D^2} V_A^2, \quad (2.73)$$

with the curvature coefficient  $\gamma_{cc} = (d^2 I_D / dV^2) / (dI_D / dV)$  and  $R_D = dV / dI_D$  the differential resistance of the diode at the operation point,  $V_{AC}$  the voltage swing amplitude along the diode,  $Z_A$  and  $Z_D$  the antenna and diode impedance, respectively. The curvature coefficient represents the dominant non-linearity factor, i.e., the AC rectification capability of the device, and is a figure of merit for high-speed switching devices. Irradiating the detector with a signal power  $P_{in}$  excites a voltage within the antenna as follows:

$$V_A = 2 \cdot \sqrt{2 \operatorname{Re}\{Z_A\} P_{in}}. \quad (2.74)$$

Depending on the detector type, i.e., broadband or resonant, the impedance of the antenna is adjusted. A broadband antenna impedance mainly consists of a frequency-independent real part. The resonant antenna mainly provides imaginary impedance and is therefore matched in a narrow frequency range. Summarizing, resonant antennae can be used for detectors with very high responsivities in a narrower frequency range, and broadband antennae for detectors operating in a broad frequency range at the expense of responsivity.

### 2.6.1 Broadband detector approach

Considering the equivalent circuit shown in Figure 2.18 for a broadband detector, i.e., with self-complementary antenna, where the antenna impedance consists only of a real part  $Z_A = R_A$  and including a simplified equivalent circuit for the diode shown in Figure 2.18, the internal voltage drop across the diode is determined as:

$$\begin{aligned} V_D &= \frac{\frac{1}{\frac{1}{R_D} + j\omega C_D}}{R_A + \frac{1}{\frac{1}{R_D} + j\omega C_D}} \cdot V_A & (2.75) \\ &= \frac{1}{1 + \frac{R_A}{R_D}} \cdot \frac{1}{1 + j\omega \frac{(R_A + R_S)C_D}{1 + \frac{R_A + R_S}{R_D}}} \cdot V_A \\ &= \frac{R_D}{R_A + R_D} \cdot \frac{1}{1 + j \frac{\omega}{\omega_C}} \cdot V_A, \end{aligned}$$

with the cut-off angular frequency being:

$$\omega_c = \frac{R_D + R_A}{R_D C_D R_A}, \quad (2.76)$$

and the voltage- and current- responsivity ( $R_v$  and  $R_i$ , respectively) are determined as:

$$R_v = \frac{V_{out}}{P_{in}} = 2 \gamma_{cc} \frac{R_D^2 R_A}{(R_A + R_D)^2} \cdot \frac{1}{1 + \left(\frac{\omega}{\omega_c}\right)^2} = 2 \gamma_{cc} \frac{1}{R_A \omega_c^2 C_D^2} \cdot \frac{1}{1 + \left(\frac{\omega}{\omega_c}\right)^2}, \quad (2.77)$$

$$R_i = \frac{I_{out}}{P_{in}} = 2 \gamma_{cc} \frac{R_D R_A}{(R_A + R_D)^2} \cdot \frac{1}{1 + \left(\frac{\omega}{\omega_c}\right)^2} = 2 \gamma_{cc} R_D \frac{1}{R_A \omega_c^2 C_D^2} \cdot \frac{1}{1 + \left(\frac{\omega}{\omega_c}\right)^2}. \quad (2.78)$$

As shown in equations (2.77) and (2.78), with increasing cut off angular frequency, the detector responsivity is decreasing. The maximum cut-off angular frequency of the device is given under matching condition i.e.  $R_A = R_D$ . Substituting it in equation (2.76), the maximum cut off angular frequency is:

$$\omega_c = \frac{2}{R_D C_D}. \quad (2.79)$$

From equation (2.77), (2.78), and ((2.79), it is clear that there is an anti-proportionality between the responsivity and the bandwidth of the detector leading to a so-called responsivity-bandwidth product.

## 2.6.2 Resonant detector approach

The second detector scenario is a resonant detector approach, i.e., a resonant antenna. In this case, the antenna impedance contains a real and imaginary part. For a resonant detector using a TBRTD, an antenna dominated by its inductance is needed. Changing the impedance of the antenna to a resonant antenna is done by adding an inductive series part to the real part:

$$Z_A = R_A + j\omega L_A \quad (2.80)$$

The voltage across the internal part of the TBRTD  $V_D$  is determined as follows:

$$V_D = \frac{\frac{1}{\frac{1}{R_D} + j\omega C_D}}{R_A + \frac{1}{\omega^2 C_D^2 R_D} + j\omega L_A + \frac{1}{j\omega C_D}} V_A. \quad (2.81)$$

For simplicity, the following assumptions are taken:  $\omega C_D \gg \frac{1}{R_D}$  and in a resonance condition  $\omega_0 L_A = \frac{1}{\omega_0 C_D}$  the voltage drop is simplified to:

---


$$|V_D| = \frac{1}{R_A + \frac{L_A}{R_D C_D}} \sqrt{\frac{L_A}{C_D}} V_A \quad (2.82)$$

The peak responsivity of the voltage responsivity  $R_v$  and current responsivity  $R_i$  under this condition are given as:

$$R_v = \frac{V_{out}}{P_{in}} = \frac{2\gamma_{cc}}{\left(R_A + \frac{L_A}{R_D C_D}\right)^2} \cdot \frac{L_A R_A}{C_D} \quad (2.83)$$

$$R_i = \frac{I_{out}}{P_{in}} = \frac{2\gamma_{cc}}{\left(R_A + \frac{L_A}{R_D C_D}\right)^2} \cdot \frac{L_A R_A}{C_D R_D} \quad (2.84)$$



---

## 3 Measurements setups

A brief introduction to the measurement setups is presented. On-wafer DC- and scattering parameter-measurements are used to determine the performance of single TBRTD and utilize the acquired data for their equivalent circuit modeling (see chapter 0). Finally, the quasi-optical setup is presented, which is used for the characterization of the fabricated oscillator and detector (chapter 6).

### 3.1 DC-Measurement setup

DC-characteristics of a device are fundamentally important for large-signal modeling. In this work, a *Keithley KI 4200 SCS* source with a semi-automated probe chuck (*Karl Süss PA150*) is used to perform the on-wafer measurements. The probe station and source are remotely controlled over a *LabVIEW* program. Each Source Measurement Unit (SMU) offers a force and high input resistance ( $10\text{ M}\Omega$ ) sense line. To perform a precise measurement, the measurements are done with the four points method where a separate probe is connected for each, the force and sense lines of each SMU placed on one device pad. This configuration leads to a very accurate bias voltage adjustment on the device pad by eliminating the voltage drop over the cables and probes. DC current measurements down to single fA are possible with this measurement setup. Further, to reduce leakage currents, the external pre-amplifiers are placed near the measuring probes and are connected with short triaxial cables, to the probes. By increasing the averaging time to high during the DC measurement, the measurement reproducibility is given and hence the measurement error is reduced to under 0.5%, which is sufficient for characterization of the devices.

### 3.2 S-parameter measurement setup

On-wafer S-parameter measurements are carried out to characterize the RF performance of single devices. In this work, a Vector Network Analyzer (VNA) from R&S® *ZVA 67* with an *MPI TS150-THz* probe station setup is used. The network analyzer covers the frequency range from 10 MHz to 67 GHz in its basic measurement setup [93]. For this frequency range, the *MPI T67A* probes in a GSG (Ground-Signal-Ground) configuration are used. The signal power is internally adjustable between -30 dBm and up to +20 dBm [93]. Two external frequency extenders are used to increase the measurement frequency range. The frequency extender *ZVA110* covers the frequency range from 70 to 110 GHz, with a waveguide output of WR10 [94]. An adapter is used to transform the output to a 1 mm coaxial connector, which is then connected to a coaxial 1 mm probes (*MPI T110A*, GSG). The maximum input power of the extender is +10 dBm. The output power of the extender can be adjusted manually by the extender's manipulators. To bias the devices, an external Source

---

Measurement Unit (SMU, 2400 form Keithley) is used, when using frequency extenders with a waveguide output, a so-called bias-tee is used. A bias-tee has two decoupled DC and AC inputs and one output where both signals are coupled on. The power dependency of the S-parameter measurement is caused by the non-linear behavior of the Device Under Test (DUT). For linearization, small signals are needed, but the minimum useable excitation power is limited by the dynamic range of the system.

To increase the accuracy of the measurements a higher averaging and lower measurement bandwidth can be set. The used signal power influences the accuracy as well. A standard signal power for one port measurement of a TBRTD is between -15 and -20 dBm. By setting the averaging between 10 and 20 points and a measurement bandwidth between 100 and 1000 Hz a measurement standard deviation is determined to be lower than 0.2% in the frequency range of up to 67 GHz.

### 3.2.1 Calibration

The ZVA calibration is done using the TOSM standard (Through, Open, Short, and Match) for two-port configuration and OSM (Open, Short, Match) for one-port configuration [93]. Each GSG probe-type has its specific calibration substrate. The structures on the ceramic substrates are designed to provide accurate and known probe tip calibration parameters. The on-wafer measured scattering parameter values of the calibration standard are utilized to calculate an error correction, with the standard classical 12-term error model for the two-port calibration and a four-term error model for one port [95, 96]. This method shifts the reference plane to the probe tips level, eliminating the influence of the probes and cables on the measurement results. To minimize the calibration error, the calibration accuracy is determined by measuring an open structure on the calibration substrate, after calibration. A maximum variation of  $\pm 0.02$  dB of the measured scattering parameter at port 1, i.e.,  $S_{11}$  (and  $S_{22}$  in a two-port calibration) over the measurement frequency range, is sufficient for accurate measurements. To ensure accurate source power level and power reading at the reference plane, power calibration is needed. For this purpose, an external power meter *PM5* from *VDI* is used. The analyzer modifies its source power until the power reading corresponds to the desired source power value. This power calibration is required, especially when using external frequency extenders because there is no direct power adjustment option except the manual tuning of the analog manipulators at the output of the devices.

### 3.2.2 De-embedding

The DUTs are embedded in a coplanar GSG configuration to allow on-wafer measurements, as shown in Figure 3.1a. The influence of these GSG-interconnections is illustrated by the equivalent circuit in Figure 3.1b. The impedance of the DUT is extended with further

elements due to the connection lines. For accurate device characterization, this interconnection must be de-embedded from the measured data.

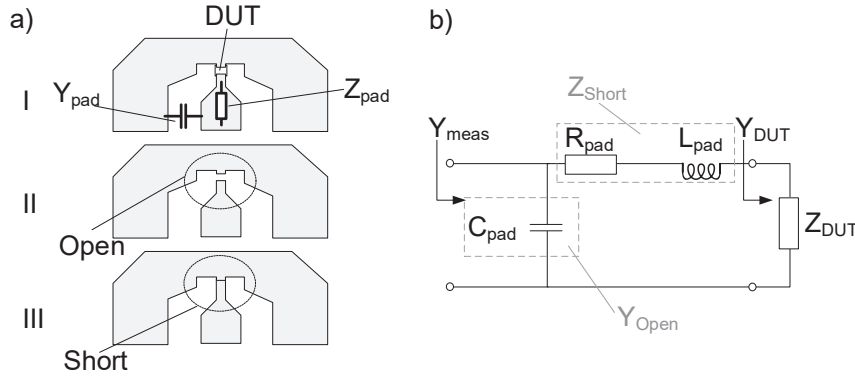


Figure 3.1: a) I: DUT embedded in a GSG-structure for on-wafer measurement, II: open-structure to de-embed the measured data from the capacitance influence of the GSG-structure. III) short-structure to de-embed the measured data from the resistive and inductive influence of the GSG-structure. b) Equivalent circuit of the DUT embedded in a one-port GSG-structure.

Single feeding structures in an open- and short- configuration are fabricated on each substrate to de-embed the feeding structures from the intrinsic device. For a two-port configuration, an additional through-structure is used. The equivalent circuit of the device embedded in the coplanar GSG connection is shown in Figure 3.1b. The open-structure measurement data provides the information of the pad capacitance ( $C_{\text{pad}}$ ), where the short-structure supplies the information regarding the pad resistance ( $R_{\text{pad}}$ ) and the pad inductance ( $L_{\text{pad}}$ ). The total admittance of the measured structure is given by

$$Y_{\text{meas}} = Y_{\text{Open}} + (Z_{\text{Short}} + Z_{\text{DUT}})^{-1}, \quad (3.1)$$

And the intrinsic device characteristics  $Z_{\text{DUT}}$  can be de-embedded as follows:

$$Z_{\text{DUT}} = \frac{1}{Y_{\text{meas}} - Y_{\text{Open}}} - Z_{\text{Short}}. \quad (3.2)$$

To minimize the de-embedding error, which have a direct influence on the s-parameter measurements accuracy, the placing position of the GSG probes on the pads is critical. For accurate measurements, the GSG probes must be placed, as exactly as possible, at the same position during all measurements. A position shift on the pad of  $\pm 30 \mu\text{m}$  between single measurements showed a value difference in the results of over 10%. Therefore, attention must be paid, when placing the probes, however accurate positioning is possible due to the micrometer positioning stage.

---

### 3.3 Quasi-Optical measurement setup

The electromagnetic wave can be treated as an optical beam in terms of focusing, splitting, and scattering. In this chapter, the measurement setups used to characterize the fundamental parameters of oscillators and detectors, such as oscillation frequency  $f_0$ , voltage  $R_V$  and current  $R_i$  responsivities, and noise equivalent power  $NEP$ , will be presented. To minimize the measurements error a precise alignment of the measurement setups is required.

#### Si-lenses:

As was mentioned earlier (see chapter 3), the on-chip antennae are placed on top of an InP-wafer. The permittivity of InP is  $\epsilon_{\text{InP}} \cong 12$ , leading to a beam radiation towards the bottom side of the device ( $>97\%$  of the beam is radiated toward the bottom side) [81]. Furthermore, the InP-wafer thickness is larger than the THz beam wavelength, and the high permittivity discontinuity to air results in a low acceptance angle, which leads to a large beam loss as a result of the THz beam reflection within the substrate building standing wave that remains in the InP-substrate. To overcome this issue, Si-lenses are placed at the bottom side of the devices to collimate the THz radiation (see chapter 2.5.2). The Si-lenses are either hyper-hemispherical or hemispherical lenses, whereby the latter do not change the radiation pattern of the device. The hyper-hemispherical lens, on the other hand, increases the directivity of the device while decreasing the acceptance angle. Accurate placement and lens design are needed, especially when investigating the absolute power radiated or detected at the device on the lens. The incident THz wave reflection on the curved surface of the Si-lens is determined to be among 30 %.

Figure 3.2 illustrates the design parameters of a hyper-hemispherical lens in more detail. Next, the critical relations for a hyper-hemispherical lens will be presented. The virtual focus length, which is a function of the lens material ( $n_{\text{material}}$  material refractive index) and the lens radius ( $r_{\text{lens}}$ ) is given as [97]:

$$L_{\text{lens}} = r_{\text{lens}}(n_{\text{si}} + 1), \quad (3.3)$$

this point defines the acceptance angle of the lens, as shown in Figure 3.2. The beam divergence angle  $\beta_{\text{lens}}$  is defined as follows:

$$\beta_{\text{lens}} = \arcsin\left(\frac{1}{n_{\text{si}}}\right). \quad (3.4)$$

The collection angle from the effective focal point is given as  $\alpha_{\text{lens}}$ :

$$\alpha_{\text{lens}} = \arctan(n_{\text{si}}), \quad (3.5)$$

moreover, the actual focal point-distance  $d_{\text{lens}}$  from the lens edge is defined as follows:

$$d_{\text{lens}} = r_{\text{lens}} \left( \frac{n_{\text{si}} + 1}{n_{\text{si}}} \right). \quad (3.6)$$

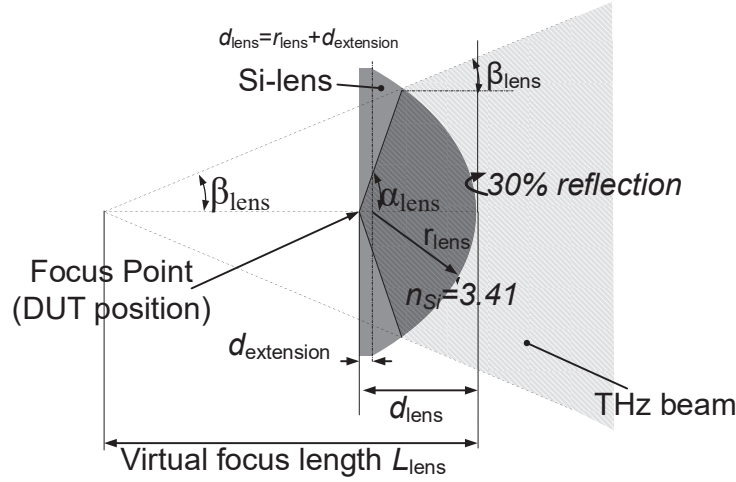


Figure 3.2 Schematic structure of a hyper-hemispherical Si-lens (due to the extension shown as  $d_{\text{extension}}$ , i.e.,  $d_{\text{lens}} > r_{\text{lens}}$ ) illustrating its main design parameters when placing the DUT at the flat lens surface.

### 3.3.1 Oscillation frequency measurement setup

Two different measurement setups were deployed to determine the oscillation frequency of the oscillator. In a Fabry-Perot resonator setup, the intensity of the signal detected at the output of two moveable Si-wafers, as a function of the distance between both Si-wafers determines the wavelength<sup>1</sup> of the incident signal and hence, determines its frequency (Figure 3.3). In a second approach, a Fourier Transform Infrared Spectrometer (FTIR) connected to a helium-cooled bolometer, used as a sensitivity detector<sup>2</sup> (Figure 3.4) determines the signal intensity as a function of the FTIR internal mirror position (Figure 3.4).

#### Fabry-Perot resonator approach<sup>1</sup>

The Fabry-Perot resonator approach for frequency measurement is shown schematically in Figure 3.3. Two partly transparent Si-wafer are placed in the THz beam path to function as a reflector for the THz beam. Standing waves are generated between the reflectors if their distance  $d_x$  fulfills the standing wave conduction:

$$d_x = \frac{m \cdot \lambda}{2}, \quad (3.7)$$

where  $m$  is an integer. As shown in Figure 3.3, a broadband detector is placed on the opposite side of the reflectors. When standing waves are formed between the reflectors, maximum

<sup>1</sup> This setup was devised with Prof. Suzuki during his stay with Mercator fellowship period.

<sup>2</sup> This measurement setup configuration was used in the *Tokyo Institute of Technology* during my short-term scientific mission.

intensity is measured at the detector. By changing the distance between the reflectors, a maximum intensity will be measured, repeatedly each time the condition is fulfilled i.e.  $d' = d + \frac{\lambda}{2}$  as shown in the inset of Figure 3.3

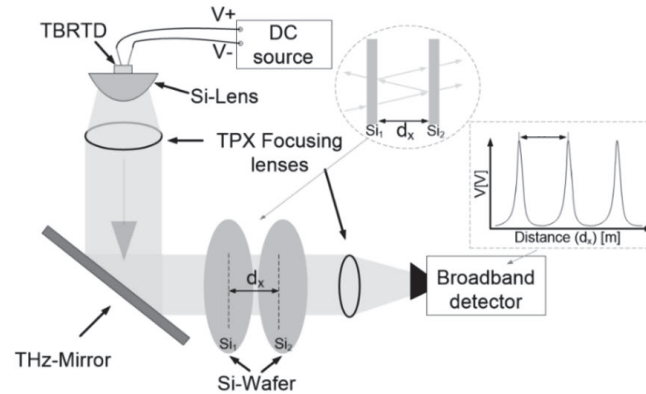


Figure 3.3: Schematic setup of a Fabry-Perot based measurement setup for oscillation frequency determination.

### Fourier Transform Infrared Spectroscopy<sup>2</sup>

Another approach that was used to determine the oscillation frequency is FTIR consisting of two THz mirrors and a signal. The incoming THz signal is split equally to the mirrors, where one of the mirrors is movable. The mirrors reflect both signals, and either constructive or destructive interference is occurring between the reflected beams, depending on the mirror distance. The detector in this setup is a helium-cooled bolometer, however, any other sensitive broadband detector can be deployed to measure the intensity of the reflected beam while moving the mirror position.

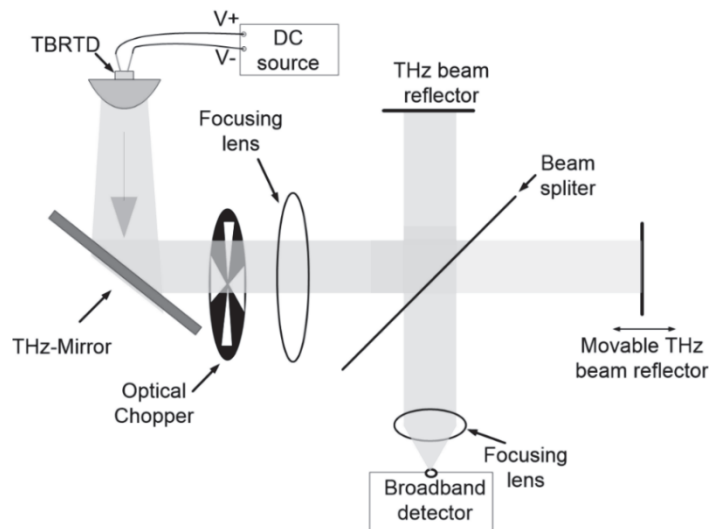


Figure 3.4: Schematic setup of an FTIR measurement setup for oscillation frequency determination.

### 3.3.2 Oscillator output power measurement setup

The measurement of the oscillator output power requires exact knowledge of the THz beam spot area which requires precise placement of the lenses within the beam path. The oscillator is placed on a hemispherical Si-lens. The lens is placed at the focal point of the distance of a parabolic THz reflector. The parallel beam out of the parabolic reflector is focused by a TPX (Polymethylpentene) lens. This lens is placed in the optical focal point from the reflector and the detector, a He-cooled bolometer. The measurement setup and its schematic setup image are shown in Figure 3.5<sup>3</sup>.

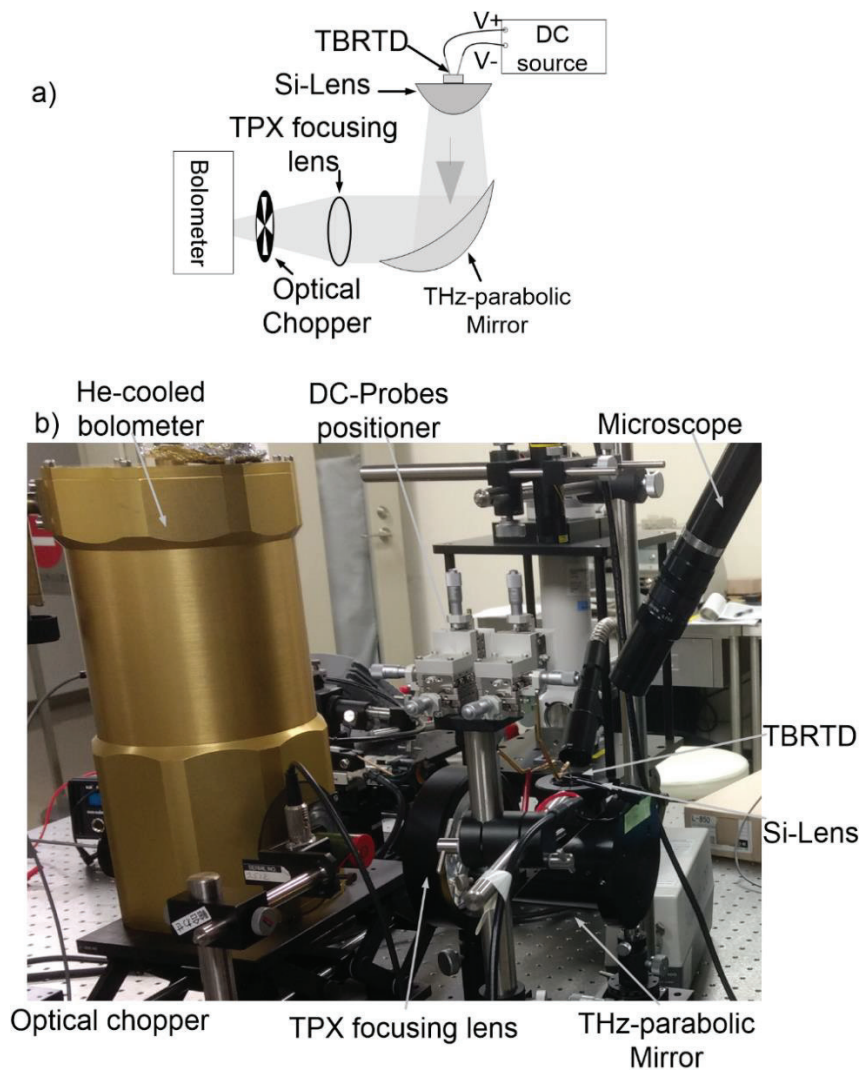


Figure 3.5: a) Schematic setup and b) picture for the used quasi-optical setup for oscillator output power measurement.

After setting this measurement up and placing the lenses at its focal points, the lenses position is finely tuned to achieve the maximum readout power. The determined output

<sup>3</sup> This measurement setup configuration was used in the *Tokyo Institute of Technology* during my short-term scientific mission.

power is corrected by adding the reflected wave on the Si-lens curved surface (30% reflection). Losses on the THz-mirror and TPX-lens are neglectable small.

### 3.3.3 Detector Measurement setup

The detector measurement setup and its schematic are presented in Figure 3.6. A critical point in this setup is power calibration and beam path alignment.

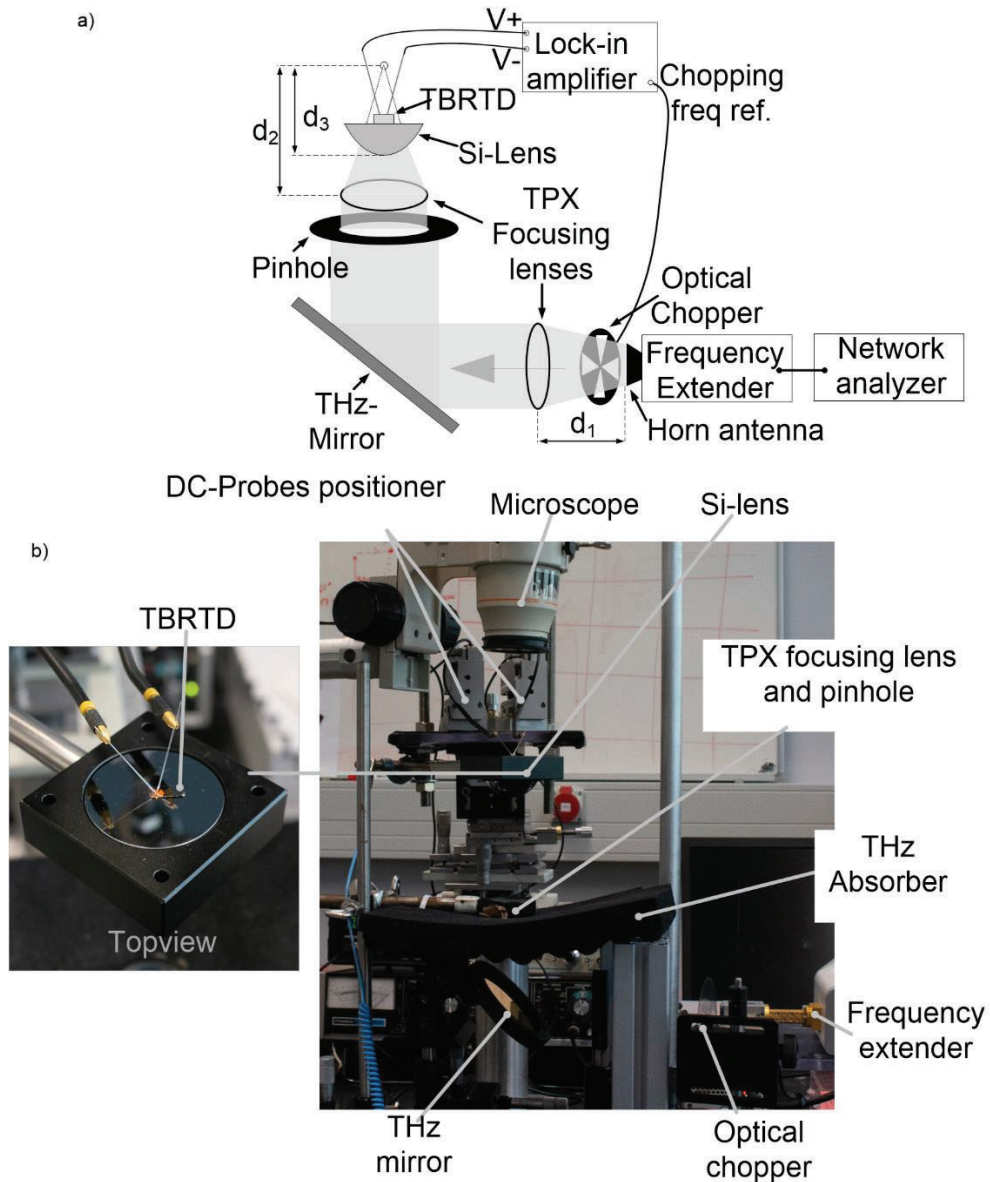


Figure 3.6: a) Schematic setup and b) a picture of a detector characterization measurement setup. In the top-view, the device placed on the Si-lens is presented.

The network analyzer with external frequency extender (see chapter 3.2) is deployed as a THz signal source. The frequency extender ZC 330 from R&S® was used to provide signals in the frequency range from 220 GHz to 330 GHz.

---

The accurate irradiated power value is needed to determine the responsivity of a detector. For this reason, the first step is the power calibration of the setup. The TBRTD detector and the Si-lens are removed. When using a hyper-hemispherical lens, as demonstrated in Figure 3.6, a power-meter (*PM-5 VDI*) is placed with its opening at the distance of the focal point of the second TPX lens (see Figure 3.6 distance  $d_2$ ) to measure the exact output power which is arriving at the Si-lens surface. With equation (3.6), the distance between the focal point and lens bottom (see Figure 3.6 distance  $d_3$ ) is determined. This distance  $d_3$ , defines the amount of radiation within the acceptance angle.

This adjustment is different when using a hemispherical Si-lens instead of hyper-hemispherical Si-lens. Here, after measuring the power at the focal point of the second TPX lens (see Figure 3.6 distance  $d_2$ ), the Si-lens is placed to have its flat surface precisely at the focal point of the second TPX lens, where later the TBRTD will be placed. Independent of the used lens, fine-tuning of the Si-lens is carried out during the measurement to achieve the maximum detected power at the TBRTD. In this way, the setup misalignment can be reduced.



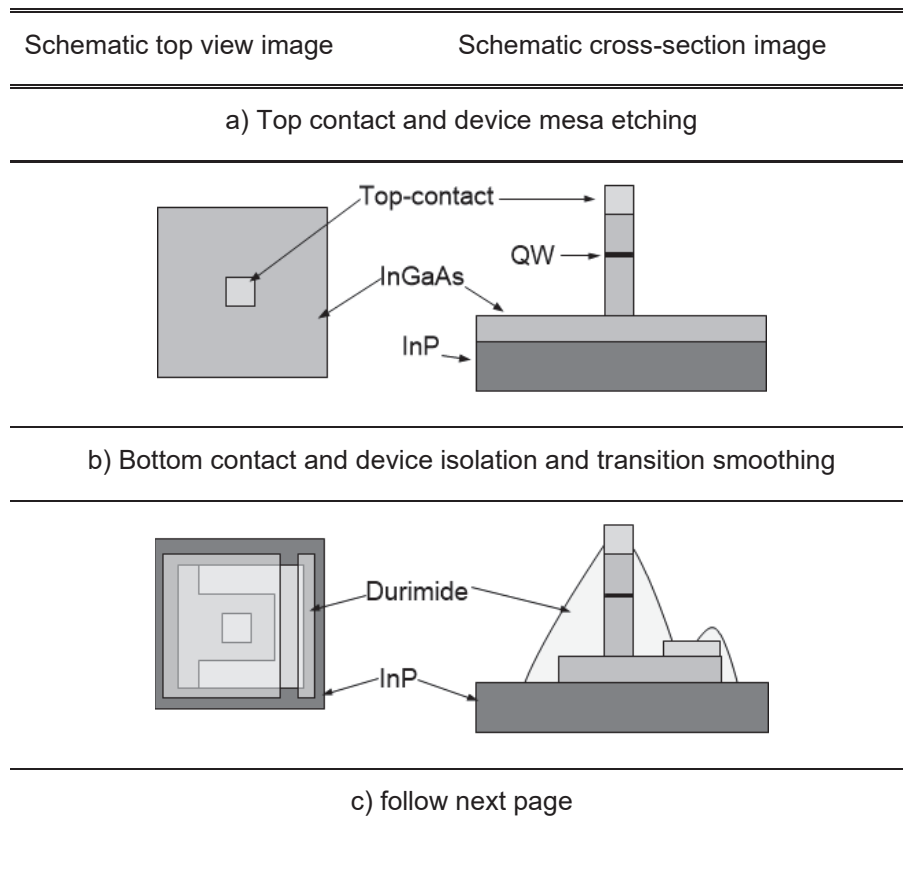
---

## 4 Single devices and circuit fabrication process

In this chapter, a general description of the fabrication steps for THz-device processing is presented, and the most important parameters will be discussed. For more details, see Appendix A, where a step-by-step instruction and detailed processing parameter values are given. Starting with the fabrication of single TBRTD elements that are integrated into GSG interconnection for DC- and S-parameter characterization. Then, a low-cost method to miniaturize the devices down to the nanometer region using nanoimprint is developed and its detailed fabrication steps are presented. Next, the fabrication steps for the TBRTD integration into a slot and bowtie antenna are introduced. The antenna design for the oscillator and detector are carried out based on the results, for the single devices, achieved in chapter 0, and its integration within an antenna in chapter 6.

### 4.1 Single TBRTD fabrication

For the fabrication of the TBRTD, the top-down approach is used, and its fabrication steps are schematically illustrated in Figure 4.1. Detailed information regarding the photomasks for single elements is found in Appendix B.



---

### c) Final metallization

---

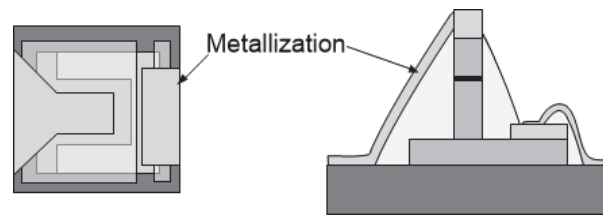


Figure 4.1: Top- and side-view of schematically step-by-step fabrication of single TBRTD devices. a) the deposition of the top-contact and the mesa shape design and structuring, up to the bottom-contact, are demonstrated. b) The deposition of the bottom contact and the isolation of single devices on the substrate are presented. Transition and topology smoothing layer, per *Durimide*<sup>®</sup> deposition, is presented. Finally, in c) the interconnection is illustrated.

After growing the TBRTD materials stack on an InP-substrate, the device fabrication is started. Full attention must be paid to fabricate all devices with the same procedure and hence minimize any fabrication influence on the separated substrates. As shown in Figure 4.1, the fabrication steps will be separated into three groups:

#### a) Top contact and device mesa etching

To ensure an organic-contaminants free substrate surface, the substrate is dipped into acetone for 2 minutes at 56°C, and then is transferred into Iso-Propanol (IPA) for another 2 minutes at 82°C, to remove the acetone from the surface. Due to the high evaporation rate of the IPA, the surface of the substrate is dried when removing it from the IPA solution. This step is controlled with a visual inspection under an optical microscope and is repeated when cleanliness is not adequate. Next, to remove the native oxide on the surface; mainly, to improve the adhesion of photoresist, the substrate is dipped into a dilute hydrochloric acid solution and cleaned with flowing de-ionized (DI) water [98, 99]. These cleaning steps are always used when starting the fabrication to achieve the same starting condition.

For the top contact patterning, a positive photoresist is spin-coated on the substrate. This positive resist is deployed because of its high resolution, which is needed for the top contact design, especially at sub-micro contacts. Spinning the resist with a speed of 4000 rpm, the height of 600 nm is achieved, which is sufficient for the top contact height of 450 nm — followed is then a softbake step on the hotplate. The softbake is needed to dry the photoresist for the next processing steps, i.e., reduce the residual solvent content. Then the photoresist is patterned with a *Carl Suss MA6* mask aligner. The top contact structures and the alignment markers for the next steps are exposed by a dark field quartz glass-chrome mask. Within a dark field of a glass-chrome lithography mask, the patterns structures consist of transparent glass, and the surrounding area on the mask is covered with a chrome-layer and hence blocks the UV-light at the UV exposure step. The needed UV exposure time to pattern the resist

down to the substrate while minimizing the exposure caused by reflection on the substrate surface is determined experimentally, by UV exposure of different test wafers with different times and comparing the results. After exposure, the photoresist is developed. The UV-exposed photoresist part is chemically different compared to the not exposed resist. UV exposure of a positive photoresist results in an increased resist solubility in the developer leading to an opening in the photoresist after development. To remove any photoresist-residues in the openings after development, an O<sub>2</sub>-plasma etch treatment for 1 min at low power of 25 W is carried out. Next, to provide ohmic contacts, an oxidation removal step with an ammonia-water mixture is done. The substrate is placed immediately after this step in the vacuum chamber of the metal deposition system (*Leybold LH560*) to avoid any new native oxide regrows.

The contact material stack of the top contact consists of Titanium, Platin, Gold, and Nickel (Ti/Pt/Au/Ni: 10/10/200/25 nm), whereby the Ti-layer is used as an adhesive layer [100]. Ni layer has a low dry-etch-rate and therefore, the top contact provides an etch mask for the dry-etching step [101]. After the evaporation of the top contact material stack, a lift-off process is performed with acetone and IPA dip. A top view of the fabricated top contacts, after the lift-off step, with a nominal dimension of 1 μm x 3 μm is shown in Figure 4.2. Furthermore, a good patterning of the nominal structure is given, however, diffraction-effects on the sides cause more rounded edges on the shorter part are structured. This effect is reproducible and, is taken into account when designing the top contact.

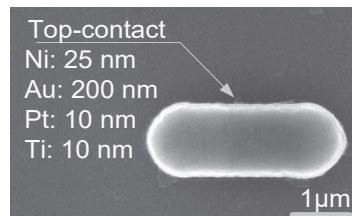


Figure 4.2: Top-view SEM Image of the top contact after the lift-off process. The top metal layer is nickel.

After fabricating the top contact layer stack, an etching step is executed to structure the mesa, i.e., the device area. The etching is carried out up to the material layer of the bottom contact. In this work, wet- and dry-etching were used. For wet-etching, a phosphoric acid, hydrogen peroxide, and DI-water (H<sub>3</sub>PO<sub>4</sub>, H<sub>2</sub>O<sub>2</sub>, H<sub>2</sub>O 1:1:25) solution was applied [102]. The etch-rate control of this solution is given over the water shares and is experimentally<sup>4</sup> determined to 2.8 nm·s<sup>-1</sup>. Depending on the device material stack, an etch depth of 400 to 600 nm was needed to reach the bottom contact layer. A second etching mechanism that was deployed in this work is the dry-etching in an ICP-RIE machine (*Oxford Plasmalab 100 inductively Coupled Plasma 65*). The used parameter values are given in Appendix A and for detailed information

<sup>4</sup> The etch depth was controlled with a profilometer *Bruker DektakXT* to determine the etch-rate.

regarding the dry etching machine and the developed parameter refer to [103]. The etching depth in this system is controlled via time. Therefore, before starting this process, a test piece is etched to determine the etch-rates. After etching the devices for a given time, the etch depth is controlled with a profilometer. In case the depth is not as high as required, and due to the significant change in the dry etching etch-rate when re-etching a substrate, a wet etching was carried out until the required depth is achieved. To determine the effective area of the device, because of the isotropic etching profile of the wet chemical etching and inaccuracies in the lithography patterning of the top contact, an SEM cross-section image of the device is taken, as shown in Figure 4.3. Furthermore, Figure 4.3.a and b present a direct comparison of the wet-etching and its isotropically etch direction, i.e., the etching of the material under the etching mask, and on the other side the dry etching with the ICP-RIE system, i.e., the anisotropic etching profile which is a results of its directed etching process, is visible. ICP-RIE etching provides an etch technique where the etch mask, i.e., top contact, defines the device mesa area. For wet etching, the mesa area is changing depending on the etching time and depth due to its isotropic etching mechanism.

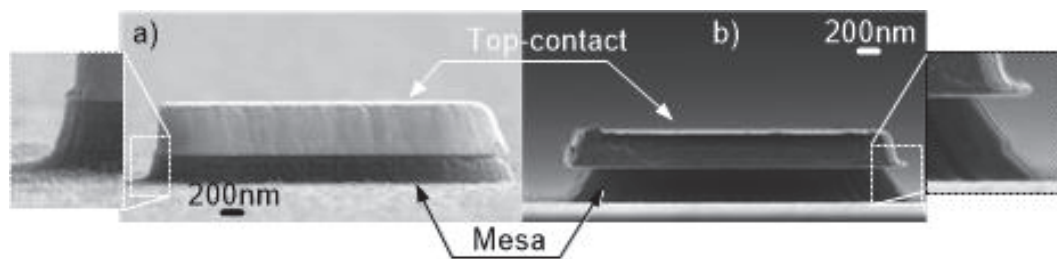


Figure 4.3: SEM side view image of an etched TBRTD mesa a) after ICP-RIE etching step, i.e., anisotropic etching and in b) after a wet-etching step, i.e., isotropic etching. On the sides, a magnification of the mesa-edges shape after etching are presented.

If dry etching is used, then a surface-cleaning step is implemented afterward, for more details see Appendix A.

### **b) Bottom contact and device isolation and transition smoothing**

To pattern the bottom contact, the substrate is spin-coated with a negative photoresist. The negative photoresist is mainly used for the lift-off process, especially when large topologies are present. Since the exposed negative photoresist remains after development, and because of its UV absorption characteristics, a more significant undercut compared to a positive photoresist is expected, which facilitates the lift-off process. After spinning the photoresist on the surface, a softbake step on a hot plate is done, followed by a structured UV exposure. The UV exposure time is determined experimentally<sup>5</sup> to achieve a complete cross-linking up to the substrate without to over-exposure the photoresist. The structures are patterned with

<sup>5</sup> The best UV-exposure time is determined by varying the time on different samples and comparing the results under microscope to the nominal structure dimensions on the mask.

a light-field quartz glass mask, i.e., the structures are UV impermeable. The same cleaning process is done as mentioned at the top contact, including the O<sub>2</sub>-plasma treatment for 1 minute at 25 W to remove the photoresist residual, followed by surface de-oxidation with ammonia-water mixture. The bottom contact material stack is Ti/Pt/Au: 10/10/100 nm. To isolate the devices on the substrate, which are electrically connected through the highly doped InGaAs-layer of the bottom contact, a wet-etching step is executed (with H<sub>3</sub>PO<sub>4</sub>: H<sub>2</sub>O<sub>2</sub>: H<sub>2</sub>O 1:1:25 solution); therefore, the devices are protected with photoresist mesa. This photoresist has high chemical stability, i.e., stable against the etching solution. After spinning the photoresist, a prebake step is carried out. Then, UV exposes- and resist development-steps are executed. An SEM top-view image of the device with its bottom contact is shown in Figure 4.4.

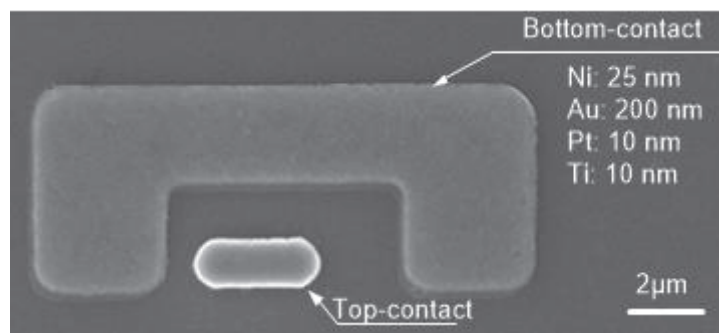


Figure 4.4: SEM top-view image of the TBRTD after depositing the bottom contact.

To isolate the device contacts and to smoothen the vertical transition for the contacts from the InP substrate to the top contact, a spin-on-glass (SOG) is used. This SOG behaves as a negative photoresist and is structured with standard lithography steps. After spin-coating the SOG a prebake is done followed by UV exposure for 10 s and developing step. At this point, the top contact area is covered with the SOG material. To extricate, the top contact an O<sub>2</sub>-plasma etching step [104] is carried out and is controlled every two minutes under the SEM, to stop the etching process as soon as the top contact is free. This step is repeated until the top contact is free of the SOG. Then, a curing step in an oven in an argon atmosphere is performed. After this step, the SOG cannot be etched or removed using developer or O<sub>2</sub>-plasma treatment. Furthermore, it should be kept in mind, that shrinkage of up to 45% of the SOG height after curing is occurring. Figure 4.5 presents the device after the separation and the presented isolation step. As shown, the top contact is free, and a SOG layer (darker material in Figure 4.5) is smoothing the abrupt transitions. This layer is then used as a bridge for the next metallization layer. It also protects the mesa sidewalls from external influences. In Figure 4.5b-c, devices with multi-mesa are presented. The multi-mesa technology provides a method of decreasing the series resistance of a device by separating its area into smaller, parallel-connected areas. This technology is limited up to a certain mesa area, where the total

resistance will start to increase due to the small top contact area of single mesas. The total device area in Figure 4.5a,b, and c is the same but separated into mesas.

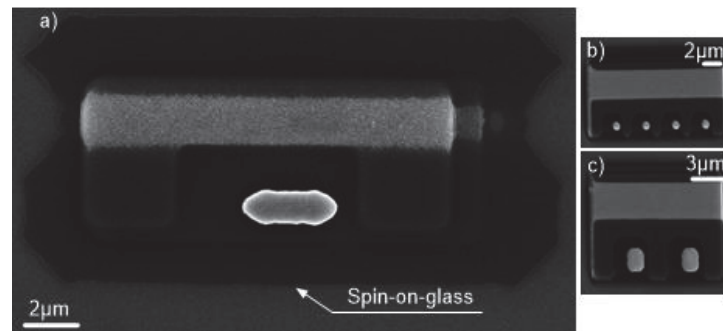


Figure 4.5: SEM top-view image of a TBRTD in a) single and b-c) multi mesa technology after isolating the single devices on the substrate and depositing the *Durimide*® for transaction smoothing.

### c) Final metallization

The last step for processing the TBRTD is by placing the interconnection metals. In this case, the devices are integrated into a GSG structure for on-wafer measurements. Structures for one port and two-port measurement techniques are provided. For this layer, the negative photoresist is structured as described above for the bottom contact. The metallization of the contact structuring consists of Ti/Au: 20/450 nm. After lift-off, the devices are ready for measurement (see Figure 4.6).

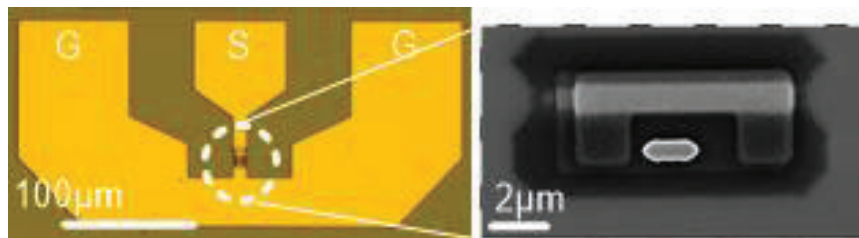


Figure 4.6: Micrograph of a fabricated TBRTD, which is integrated into a one port GSG structure for characterization. The inset shows an SEM top view image of the integrated TBRTD.

#### 4.1.1 Device miniaturization

Downscaling of the devices provides a mechanism to improve high-frequency performance by reducing the device capacitance. For the top-down approach, several techniques are available to miniaturization of the top contact area. First, Electron Beam Lithography (EBL) provides a straightforward method to reduce the size of the structured elements, due to the small spot area of the photoresist structuring beam. This precise structuring mechanism is at the expense of processing time. Second, using the wet chemical etching provides, up to a specific area, a technique for miniaturization by utilizing its isotopically etching mechanism. In Figure 4.7, four different substrates with different wet-etching times after structuring the

top contacts with the EBL parameter, are presented. The combination of both methods shows promising results for downscaling of the devices. An effective contact diameter down to 340 nm is achieved. The EBL parameters are shown in Table 4.1 and are determined by a systematic study of the parameters.

Table 4.1 Experimentally determined EBL parameters for PMMA 671.05 patterning

Photoresist	$V_{ac}$ [kV]	$I_{beam}$ [pA]	$T_{dwell}$ [ $\mu$ s]	$Dose$ [ $\mu$ C/cm <sup>2</sup> ]
AR-P 671.05	20	75	2.4	70

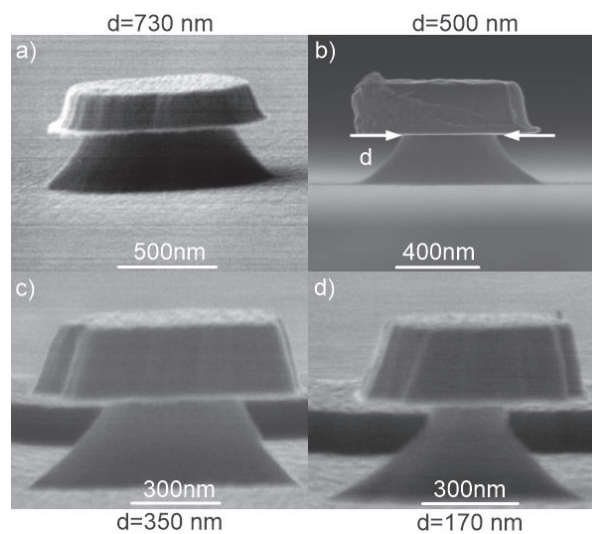


Figure 4.7: SEM side view images of a TBRTD for four different substrates, with the same material stack. The mesa is fabricated by a combination of EBL, for top contact structuring and wet-etching for downscaling of the device area.

Furthermore, an additional way was developed by using a parallel, low-cost, structuring method utilizing the Nanoimprint Lithography (NIL) process. This process is a mechanically imprinting of a surface. Various NIL technologies were investigated [105], and in this work, the soft-UV-NIL is deployed. This method was developed in [106] for a different application such as area selective nano-wire epitaxy and was modified within this work for placing top metal contact at the upper layer to utilize it as an etching mask. This process is developed within this and will be described in more detail in this section including the photoresists and main parameters.

Two photoresists are deployed to structure the surface of the substrate (Figure 4.8a). The resist at the top side is called sol-gel and is used for the mechanical imprinting, and as an etch mask. The sol-gel is a commercial product from Philips's research company, and it is a colloidal solution of TetraMethyl OrthoSilicate (TMOS) MethylTriMethoxySilane (MTMS)

and 2-(2-Butoxyethoxy)ethyl acetate (DBAC) [105]. However, the exact mixture of the elements is not published. At the bottom layer, a strongly dissolved photoresist by a lift-off process is required, and therefore, PMMA (PolyMethyl MethAcrylate, based on chlorobenzene) is used. The height of the PMMA is 650 nm when spin-coated at 2000 rpm and defines the possible metal height. After spinning the PMMA on the substrate, a curing step is carried out by a softbake on the hotplate for 4 minutes at 170°C and followed by a 1 minute O<sub>2</sub>-plasma treatment at a power of 25 W. The low power and short etch time are adjusted to ensure that only the surface roughness of the PMMA is modified, and hence this treatment improves the adhesion to the sol-gel at the top of PMMA [107, 108]. Then the sol-gel is spin-coated over the PMMA, achieving a layer height of around 100 nm. After coating, the curing of the sol-gel starts immediately, i.e., solvent evaporation. To structure the sol-gel surface, a soft PDMS (Polydimethylsiloxane) mold with the form of the negative structures is used. In this work, a mold with mesas is used (see mold in Figure 4.8a). The diameter of the mesa is 400 nm and its height is 100 nm, with a pitch of 2.5 μm (Figure 4.8a). An advantage of the PDMS is its transparency for UV-light and evaporating solvents. The soft PDMS mold is pressed in the surface of the sol-gel while preventing any air traps in between. This step is followed by a UV-expose for 10 minutes to accelerate the curing of the sol-gel, while the mold is pressed into it (Figure 4.8b). After this step, the sol-gel is cross-linked and forms a hard SiO<sub>2</sub> layer [109].

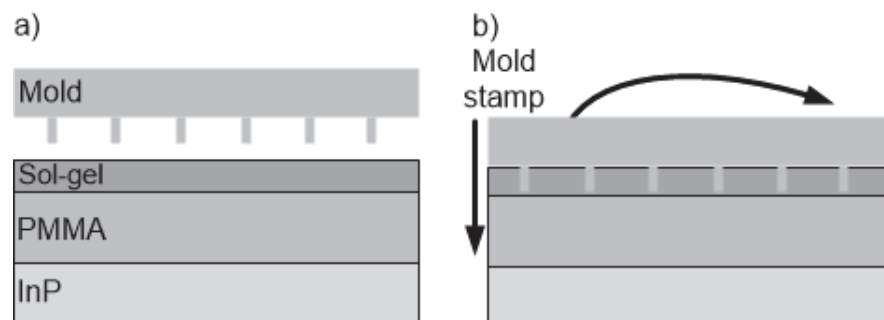


Figure 4.8: Schematic cross-sectional illustration of the substrate a) after spin coating PMMA and sol-gel on the substrate, and at the top the used mold is presented. b) Mold is pressed into the sol-gel.

Next, the PDMS soft mold is released, leaving the UV-curable resist patterned, as shown in Figure 4.9a; however, a sol-gel residual is remaining in the openings. A successful imprint is visible at a visual controlling of the substrate surface, as shown in Figure 4.9b, where the light reflections are visible due to the opening in the photoresist. Further, via the Atomic Force Microscope (AFM), the homogeneity of the successful imprinted surface of the sol-gel on PMMA is visible, as shown in Figure 4.9c,d, where an area of 5 μm x 10 μm is investigated.

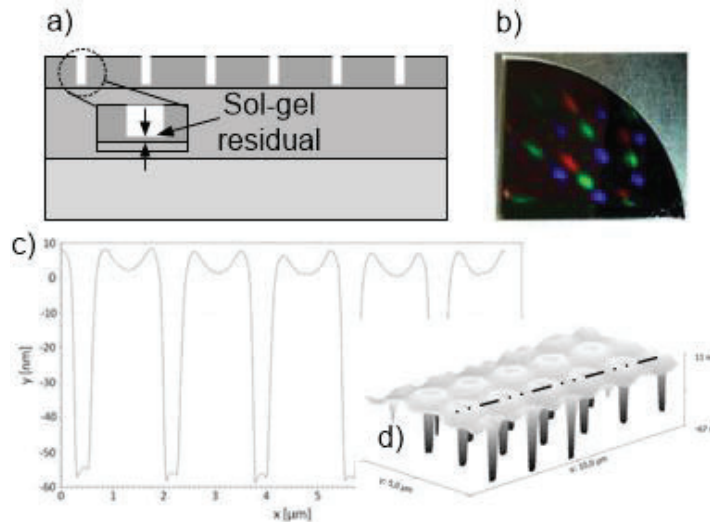


Figure 4.9: a) Schematical cross-sectional illustration of the imprinted substrate, the inset demonstrates the remaining residual layer of sol-gel. b) A successful imprinting result is visible by light diffraction on the substrate surface. c) and d) AFM results of an imprinted surface with a mold of 500 nm mesa diameter and 1.5  $\mu\text{m}$  pitch. A homogeneous imprint depth over an area of 5  $\mu\text{m}$  x 10  $\mu\text{m}$  is presented. Further, the flow of the sol-gel during imprint is visible on the openings-surroundings.

To achieve access to the substrate surface, the residual layer in the sol-gel opening has to be removed. To investigate the Residual Layer Thickness (RLT), SEM images of an imprinted surface cross-section are taken. An RLT of 20 nm is determined. This layer is removed by a dry-etching process (using the *Oxford Plasmalab 100 inductively Coupled Plasma 65*). The following parameters are used:

- $P_{\text{ICP}} = 150 \text{ W}$
- $P_{\text{RF}} = 200 \text{ W}$
- $P_{\text{strike}} = 50 \text{ mTorr}$
- $P_{\text{process}} = 6 \text{ mTorr}$
- $\text{Cl}_2/\text{N}_2 = 3/37 \text{ sccm}$
- $\text{Temperature} = 35^\circ\text{C}$

The initial parameter determination is carried out in [106]. However, a modification for our process was implemented, and the main changes are as follows: lower temperature of 35°C is needed to prevent further curing of the photoresists, then a higher N<sub>2</sub> share in the gas mixture of Cl<sub>2</sub>/N<sub>2</sub>=3/37 sccm is chosen to increase the dry, i.e., physical etching and to reduce the chemical reaction with the sol-gel and Cl<sub>2</sub>. These parameter modifications were determined experimentally, and the introduced combination showed the best performance. With these parameters, a sol-gel etching rate of 0.75 nm·s<sup>-1</sup> and an etching rate of 5.5 nm·s<sup>-1</sup>, for PMMA, is determined. To etch the sol-gel residual layer, an etching process with these parameters, for 20 s is performed. The etching step is stopped at a certain depth in the PMMA layer leading to direct access to the PMMA. To reach an opening down to the

substrate surface, an O<sub>2</sub>-plasma treatment is carried out. O<sub>2</sub>-plasma etches only the PMMA, and therefore the opening dimensions in the sol-gel remain unchanged. The etch-rates of the O<sub>2</sub>-plasma on the PMMA at different power is experimentally determined. An etch-rate of 10, 20, and 50 nm·s<sup>-1</sup> for a power of 25, 50, and 100 W, respectively, is determined. The substrate is etched for 12 minutes to ensure a PMMA removal up to the substrate surface. The O<sub>2</sub>-plasma etching is a quasi-isotropic etching mechanism and an under-etching in the PMMA is expected. Figure 4.10b presents schematically the cross-section of the substrate surface after this step. An SEM image of the cross-section of the fabricated substrate is shown in Figure 4.10c. Clear openings in the upper layer (sol-gel) are shown with a diameter of 500 nm. A successful etching of the PMMA in an O<sub>2</sub>-plasma is done and a perfect structure for the lift-off process, due to the isotropic etching of the O<sub>2</sub>-plasma is achieved.

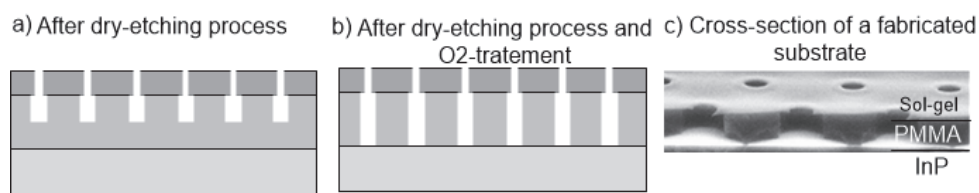


Figure 4.10: a) Schematic illustration of a cross-sectional view of the substrate after dry-etching the sol-gel residuals in the openings and in b) after etching the PMMA residual with an O<sub>2</sub>-plasma treatment. c) SEM cross-section image of the substrate surface after etching.

Then to clean the surface from the oxide, mainly caused by the O<sub>2</sub>-plasma treatment, an oxide cleaning step is implemented. Due to the small opening in the sol-gel where the NH<sub>3</sub>:H<sub>2</sub>O solution must penetrate through to clean the substrate surface and to minimize the surface energy which hinders the penetration, the substrate is dipped for 5 s in an IPA:H<sub>2</sub>O 1:10 mixture and then a dip for 10 s in NH<sub>3</sub>:H<sub>2</sub>O 1:10 followed by drying the substrate with N<sub>2</sub> gas. This step was successfully done, and no etching or dissolving of the used photoresists was visible. As the next step, the metallization of the top contacts is executed, where a metal stack of Ti/Pt/Au/Ni: 10/15/400/25 nm is needed. Then a lift-off process with acetone and IPA is followed (cf. Figure 4.11a-b). As shown in Figure 4.11c, where SEM top view image and in Figure 4.11d, an SEM side view image of the metallized substrate after the lift-off process, a successful modification of the UV-NIL process is accomplished for downscaling of the first metal layer on a substrate. A further downscaling of this method is possible using smaller features in the mold.

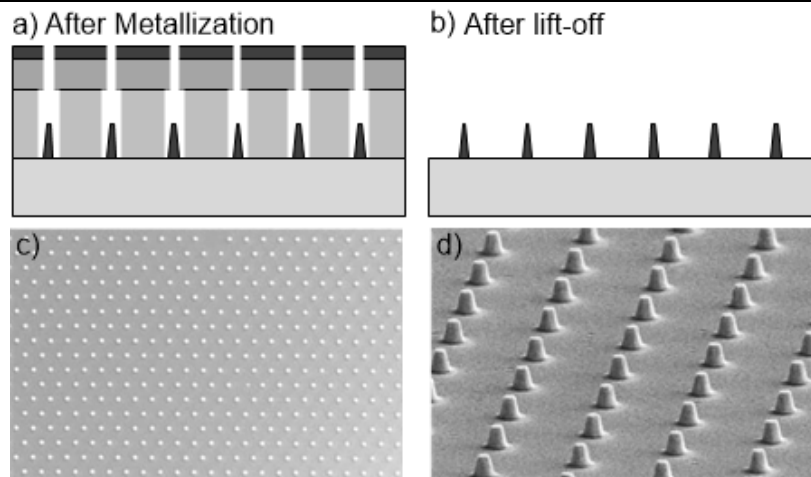


Figure 4.11: a) Schematic illustration of a cross-section of the substrate surface, after metallization and in b) after the lift-off process. c) SEM top-view image and d) SEM side-view image of the fabricated top contacts with a metal diameter of 500 nm and height of 450 nm and a pitch of 2.5  $\mu\text{m}$ .

The NIL technique provides a simple but powerful technology for a low-cost downscaling of devices. Structures smaller than 10 nm were fabricated with this technique [110, 111]. In this work, a downscaling of the devices under 500 nm diameter is aimed and successfully fabricated, as shown in Figure 4.12.

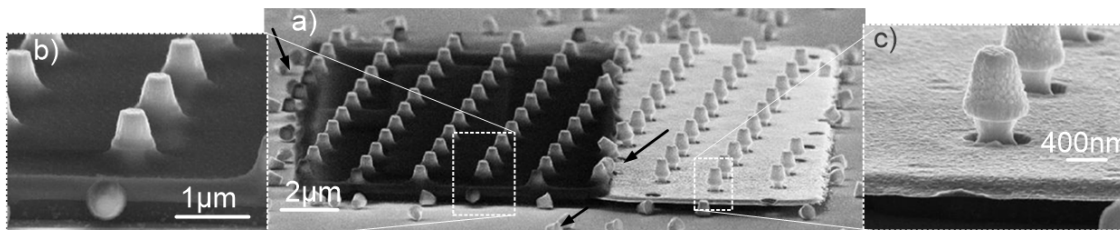


Figure 4.12: a) SEM side view image of a fabricated two electrodes device structured by the introduced NIL-process. b) Magnification of the top contact isolated with *Durimide*® and c) bottom contact is placed with the self-alignment process surrounding the device mesa. Unused top contacts (for illustration, some are marked with a black arrow) are falling on the substrate surface after etching its mesa, causing shorts between device electrodes.

However, as shown in Figure 4.12, structuring the entire substrate surface turned out to be very problematic when implementing further layers. Utilizing this technique for a two-electrode device, the unused top contacts are falling on the substrate surface after etching the mesa under it, caused by Van-der-Waals forces. For illustration, some of these elements are marked with black arrows in Figure 4.12. Ultra-sonic treatment and different cleaning steps did not remove the unused top contacts, which has a diameter of 500 nm and a height of 600 nm. In many situations, these contacts lead to shortening the electrode and hence, damage to the device. To overcome this problem, an area selective NIL process is needed. To structure only areas of interest and to provide a possible alignment method for the next

steps, an improved-NIL-process is developed by integrating a Combined Nanoimprint and Photolithography (CNP) technique. First, alignment markers are brought on the surface of the substrate using a lithography step. Then the standard NIL process, presented in the section before, up to the step after removing the sol-gel residual layer (cf. Figure 4.10a), is used to pre-structure the resist and sol-gel. Then, to selectively cover openings in the resist, a next photoresist layer is deployed, as shown in Figure 4.13a. The sol-gel is spin-coated, with *AZ® 1505* photoresist. This positive photoresist is UV sensitive and has the properties of being quickly resolved during the lift-off process. Further, no mixture between it and the PMMA nor sol-gel was visible after curing. A further advantage for this resist is the lower curing temperatures than the curing temperatures of PMMA, to prevent over-crosslinking of the PMMA. Then to pattern the *AZ®1505* layer a mask is aligned on the available alignment markers, which are visible through the PMMA and sol-gel, and a UV exposure step for 1.7 s is done followed by a developing with an *AZ®*-developer and H<sub>2</sub>O (3:2) mixture for 60 s and then 60 s under flowing DI-water. As shown schematically in Figure 4.13b, the photoresist covers the areas that are not exposed.

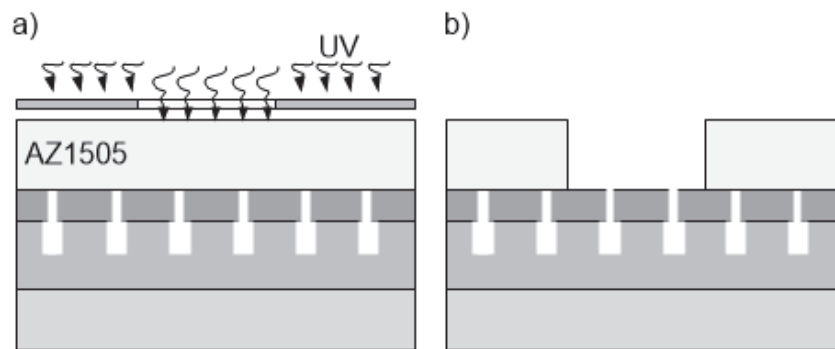


Figure 4.13: a) Schematic illustration of the substrate after the residual layer etching with ICP and spin-coating the third photoresist and at the top, a patterning mask for UV exposure. b) After developing the exposed positive photoresist.

Then as was shown and presented for the standard NIL process, an O<sub>2</sub>-plasma treatment is executed to remove the PMMA in the openings (cf. Figure 4.14a). Furthermore, in Figure 4.14b, an SEM image of such an opening after O<sub>2</sub>-treatment is visible. A successful covering of selectively chosen openings is shown. The height of the covering *AZ® 1505* photoresist is reduced after the O<sub>2</sub>-plasma treatment. Therefore, care is to be taken when choosing the height of the PMMA. After metallization (see standard NIL process), a lift-off process with acetone / IPA is performed. Figure 4.14c shows an SEM side view image of the substrate surface after depositing the metal stack. A successful selective placing of the top contacts with the soft-NIL process is achieved.

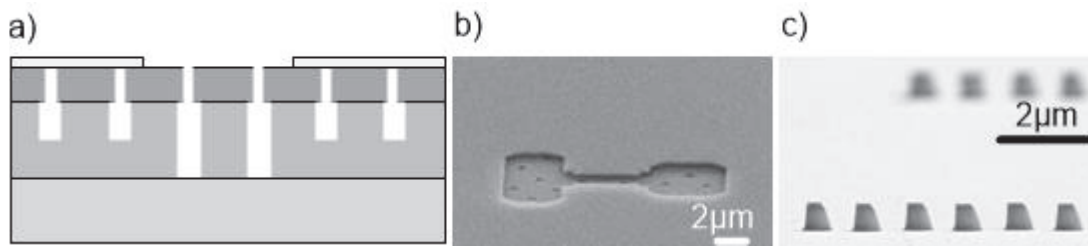


Figure 4.14: a) Schematic illustration after an  $O_2$ -plasma treatment to etch the PMMA in the opening. b) SEM image of the substrate surface after  $O_2$ -plasma treatment. c) SEM side-view image of the substrate surface after metallization and lift-off process.

After structuring the top contact, the next steps are similar, as presented in section 4.1. With the new CNP method, nano-dimensioned-RTDs are successfully fabricated. In Figure 4.15, a top view SEM image of a two-port nanodevice with multi mesa and a side view SEM image of the device mesa after mesa etching is shown. Wet etching is used for mesa structuring to enable a self-alignment of the bottom contact. To control the amount of mesa in one device, additional enhancement of the mask and the mold are needed. By tuning the mask for structuring the third photoresist layer, a pre-estimation of a rough contact number per device is possible. Furthermore, a combination of this method with e-beam lithography will provide a solution for the mesa number and to overcome any throughput limitations of an e-beam lithography in terms of downscaling of devices to sub-nm-range.

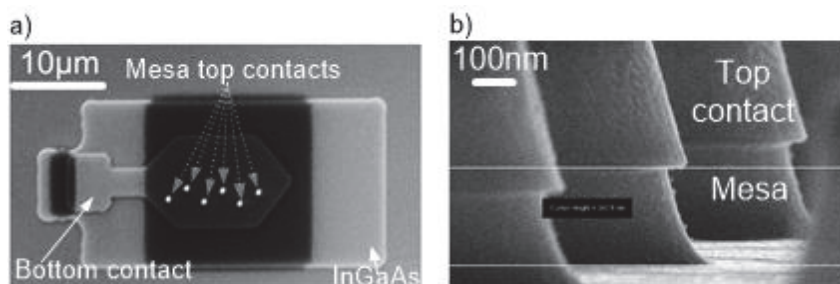


Figure 4.15: SEM images of a fabricated device using the new CNP method whereby in a) the top-view of a device with six mesas is presented, and the bottom contact is placed by the self-alignment method. b) An SEM side-view image to demonstrate the shape of the mesa after ICP and wet-etching.

To test the fabricated devices using the CNP process in terms of current flow, the produced devices are integrated within a GSG connection with the same technique, as presented in Figure 4.6. On-wafer current-voltage-characteristics of devices with different numbers of RTD mesas are successfully carried out, as shown in Figure 4.16. A wide NDR region with low peak voltages indicates a successful fabrication method. Further, with increasing number of mesas, the absolute current is increasing, indicating the increase of the active area.

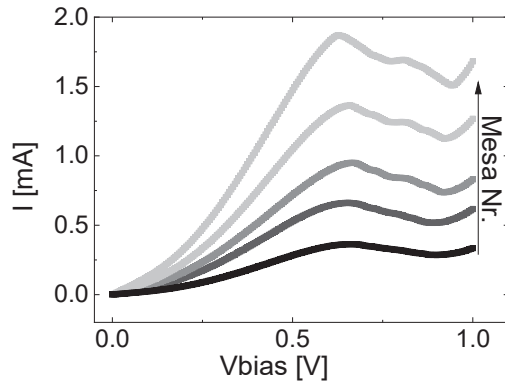


Figure 4.16: Current-voltage characteristics of a fabricated nano-RTD with the new developed CNP-Process.

## 4.2 Monolithic integration of TBRTD within an antenna

### 4.2.1 Slot antenna

A micrographic image of a fabricated slot antenna TBRTD device is shown in Figure 4.17, the insets are SEM images of selected areas to present the challenges during the fabrication and will be presented in more details in this section. The process presented in section 4.1 is used here to fabricate the TBRTD mesa. Then the antenna structures are placed on the substrate surrounding the TBRTD. The fabrication of the slot antenna is realized by starting with structuring of the bottom antenna electrode, which defines the slot dimension. A more detailed step-by-step instruction of the process is given in Appendix A.

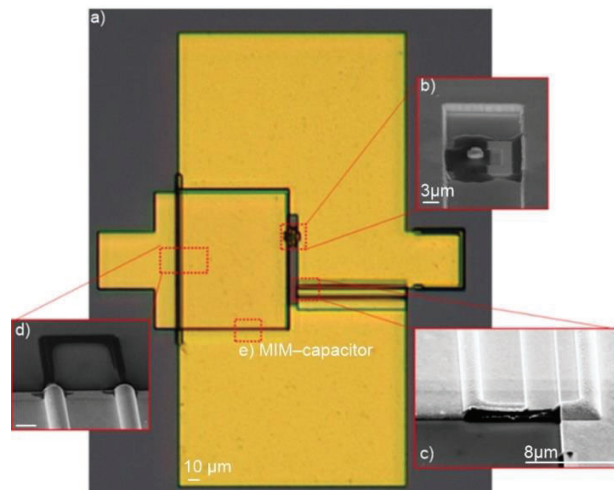


Figure 4.17: a) Micrographic image of the fabricated slot antenna, the SEM images in the inset are presented to illustrate the challenging parts during fabrication. b) Fabricated TBRTD within the slot opening. c) Closing the lift-off-opening with a *Durimide*® bridge and metallization. d) Stabilization resistance under MIM-capacitance. e) The MIM-capacitance structured with SiNx as an isolator.

After fabricating the TBRTD mesa on the substrate, acetone and IPA step is performed, to remove any organic residues, and followed by an oxide cleaning step, with ammonia-water mixture. In Figure 4.18, a simplified schematic, of a top- and cross-section view, for a step-by-step instruction for slot antenna fabrication is presented and is followed with a detailed explanation.

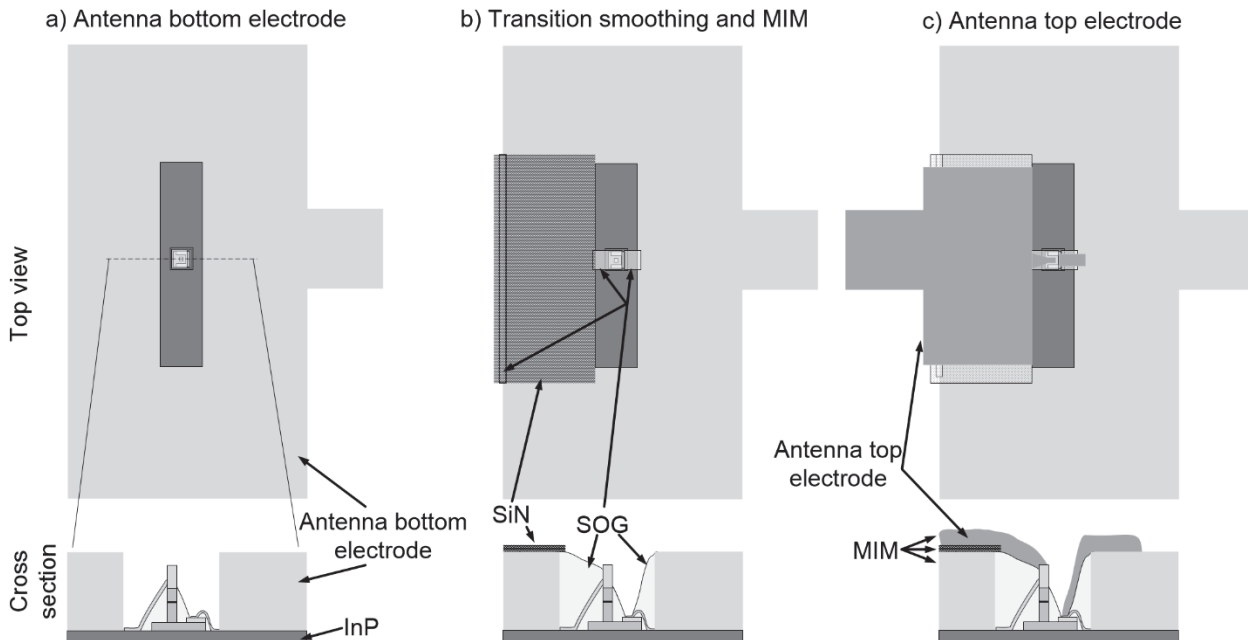


Figure 4.18: Schematic display of the fabrication steps of the TBRTD integration within the slot antenna with a MIM-capacitor for DC-biasing of the TBRTD. a) The lower electrode of the slot antenna is placed, which defines the slot dimensions. b) Transition smoothing by spin-on-glass deposition and the MIM-capacitor isolator (SiNx) is deposited. c) The top and last metallization connecting the TBRTD and forming the MIM is deposited.

#### A- Slot-antenna bottom electrode

As shown in Figure 4.18a, to fabricate the lower electrode, a metal-free closed area must be structured. The starting point of this work was to use standard and established process steps used in our department. Therefore, the photoresist *AZ® nLOF 2020* negative photoresist and a lift-off process with acetone and IPA is used. As shown in Figure 4.19a,b,d, because of the height and sideband-shape of the photoresist, this step was unsuccessful. Metallization-glitter (Figure 4.19c) on the photoresist sidebands prevents the removal of the metallization in this region. After the lift-off with acetone and IPA, the residual metallization is either falling back to the metal-free area or cannot be removed due to the metallization-glitter. Ultrasonic supported lift-off process, and different cleaning steps remained unsuccessful.

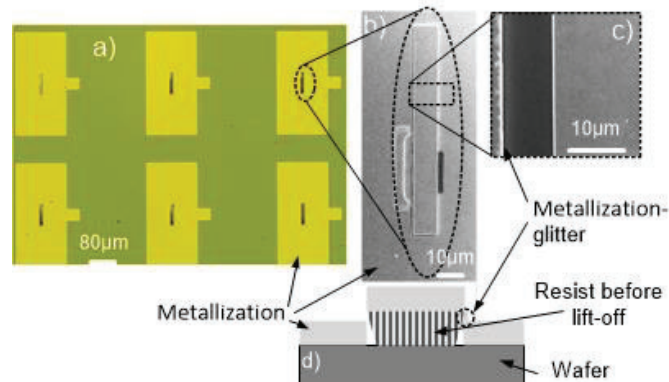


Figure 4.19: Failed lift-off process step because of the photoresist sideband metallization of a metal surrounded, metal-free-area (the slot). a) Micrographic top-view image of the fabricated slot antennae. b) An SEM image of one of the slots, illustrating the metallization falling back on the surface after lift-off. c) SEM Image is illustrating the metallization glitter on the left side of a slot opening. d) A schematical structure illustrating the problem of the lift-off process of such designs.

To overcome this challenge and fabricate the lower electrode using this photoresist, a lift-off-opening is designed (see Figure 4.20a). The simplicity and reproducibility of this method are its advantages; however, two further fabrication steps are needed. After the cleaning step, the substrate is spin-coated with the negative photoresist followed by a softbake step and a structured UV exposure. After UV exposure the photoresist, a post-exposure bake step (PEB) is executed to ensure proper imaging of the photoresist and a developing step. The surface of the substrate is then checked under the microscope to verify a successful development step. An  $O_2$ -plasma treatment for 1 minute at 25 W is followed to remove any residuals in the photoresist openings, and an oxide cleaning step, in an ammonia-water mixture. The next step is placing the substrate in the vacuum chamber of the metal evaporation system for metallization. This step is done as quickly as possible to reduce surface re-oxidation. For the bottom layer, 10 nm titanium and 800 nm gold are evaporated, followed by a lift-off process with acetone dip, until the complete removal of the resist is accomplished, then a dip in IPA to remove the acetone from the substrate surface. After this step, the metallization thickness is measured via a profilometer to verify the thickness. To bridge the lift-off-opening, a spin-on-glass layer (SOG) is used to fill the opening and reduce the topology transitions. In Figure 4.20a-c, a schematic and SEM image of this process is presented. Starting with an oxide cleaning step with dilute hydrochloric acid and water mixture. After spin-coating, the substrate with SOG, and UV exposure, a development step is performed. An  $O_2$ -plasma etching is utilized to etch the SOG height down to be around the metallization height. After reaching the desired height, a post bake is implemented in an oven. Then a metallization step is executed to electrically short the opening and close the slot. To structure this area, the negative resist is used, with the same parameters and steps mentioned before. Following is the evaporation of 10 nm Ti and 800 nm Au and a lift-off

process with acetone and IPA. Figure 4.20c presents an SEM image of a slot antenna electrode after shorten the lift-off opening. Figure 4.20d presents a magnification of the lift-off-opening structure after metallization.

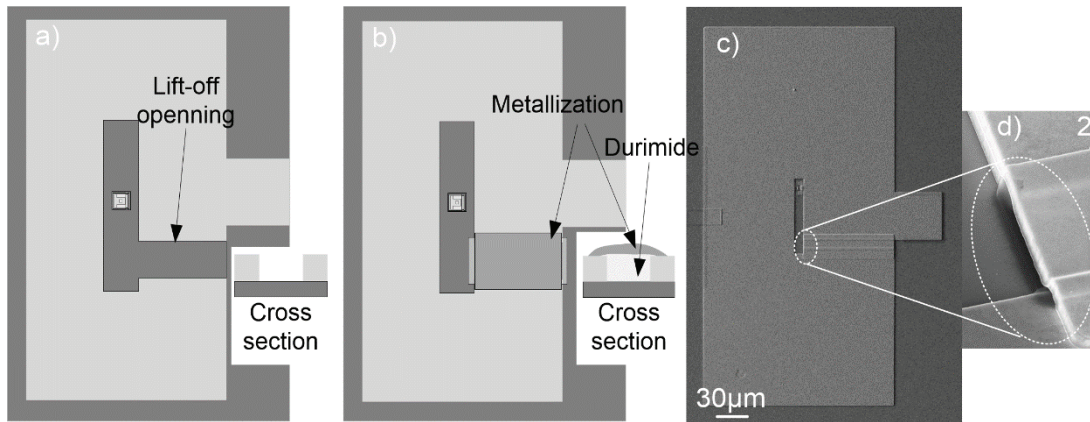


Figure 4.20: Schematic step-by-step of closing the lift-off-opening. a) Depositing the lower metal of the slot antenna with a lift-off-opening. b) SOG layer is used to smooth the transitions at the lift-off-opening and a top metallization to short the opening. c) An SEM image of a fabricated slot antenna with the lift-off-opening method. d) Close lookup of the lift-off-opening structure after metallization.

As presented, this technique causes two further steps to short the opening, which prolongs fabrication time and can distort the slot dimension. To reduce this critical process steps a different method, to structure and fabricate the bottom slot electrode within one lithographic step was developed. For this purpose, a higher photoresist with a stronger cut off profile to prevent metallization-glitter is required. Further, by utilizing a high-boiling solvent, instead of the low-boiling acetone can solve the problem of metal re-deposition on the substrate. Therefore, a new photoresist (*AZ® nLOF 2070*) with a new lift-off medium (DMSO: Dimethylsulfoxide) is introduced. This new photoresist height is 7 µm when spin-coated at the speed of 4000 rpm. The DMSO provides a slow removal of the resist. Due to the high boiling point, compared to acetone, the solvent rate of this media can be adjusted over the temperature. With this resist, the slot antenna is fabricated as follows: after fabricating the TBRTD, an oxide cleaning step with ammonia and water mixture is followed by a spin-coating the *AZ® nLOF 2070*. Then a soft bake step at 110°C for 1 minute and a structured UV expose step for 5 s. Then a PEB step of 1 minute at 110°C is performed for proper imaging (thermally activated chemical amplification). The development is carried out via *AZ®-developer pure* for 90 s and a DI-water cleaning step of 60 s. The fabricated structure using this method is shown in Figure 4.21a-b, where a successful bottom contact deposition of the antenna, with a slot-opening without the lift-off-opening technique, is presented. As shown in Figure 4.21c, this photoresist has a very strong undercut, which prevents the generation of sidewalls during the metal evaporation.

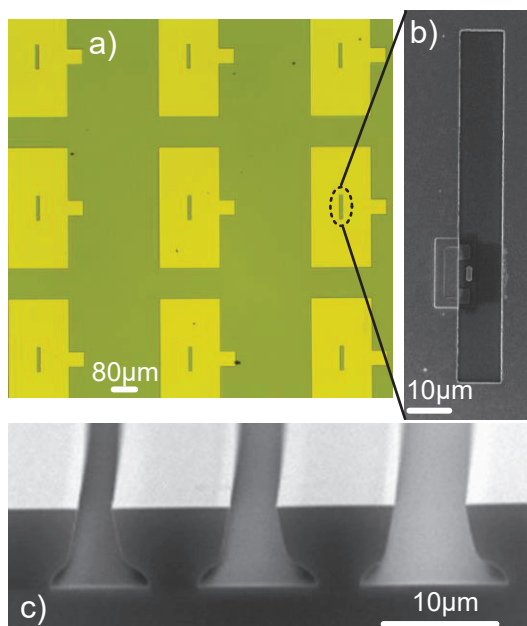


Figure 4.21: The slot antennae fabricated with a higher photoresist. a) Micrographic image of a top-view of the fabricated slot antenna elements on the substrate, a successful metallization lift-off in the slot is shown. b) SEM image of one slot where successful lift-off process was carried out and c) SEM image of a cross-section of the photoresist profile to illustrate its sharp undercut.

The thick photoresist with a strong undercut provides a method for the metallization of a slot in metal plates and a reduction of two steps in the fabrication process while increasing the accuracy of the slot dimension.

### **B- Metal-Isolator-Metal**

To structure the MIM-Capacitance an Electron Cyclotron Resonance Plasma Enhanced Chemical Vapour Deposition (ECR-PECVD) system is deployed [112]. The MIM-Capacitance blocks the DC-currents, i.e., to make a DC biasing of the device at the top and bottom contact possible. For high-frequency signals the MIM is shortened so that the resonator is defined by the slot dimension. One of the advantages of this system is mainly the room temperature deposition of SiN<sub>x</sub>. Therefore, the substrate surface can be structured before the photoresist deposition and using a lift-off process to remove the photoresist with the surplus SiN<sub>x</sub>.

The isotropic deposition of the SiN<sub>x</sub> in the PECVD covers the photoresist side walls as well, despite the photoresist undercut, in Figure 4.22-I a schematic structure of the photoresist sidewall covered by a SiN<sub>x</sub> is illustrated. In most cases, the deposition of the photoresist sidewalls was only some nanometers thick and did not hamper the following process steps. However, occasionally, the SiN<sub>x</sub> sidewalls interrupted the interconnection of the next metallization step (see Figure 4.22). In Figure 4.22IIa-c, an SEM image of a fabricated slot antenna device (a: side view with its inset presenting the SiN<sub>x</sub>-fences in more detail, b: top-

view of a TBRTD integrated into a slot), showing the fences in more detail and the interconnection metallization break which damages the devices.

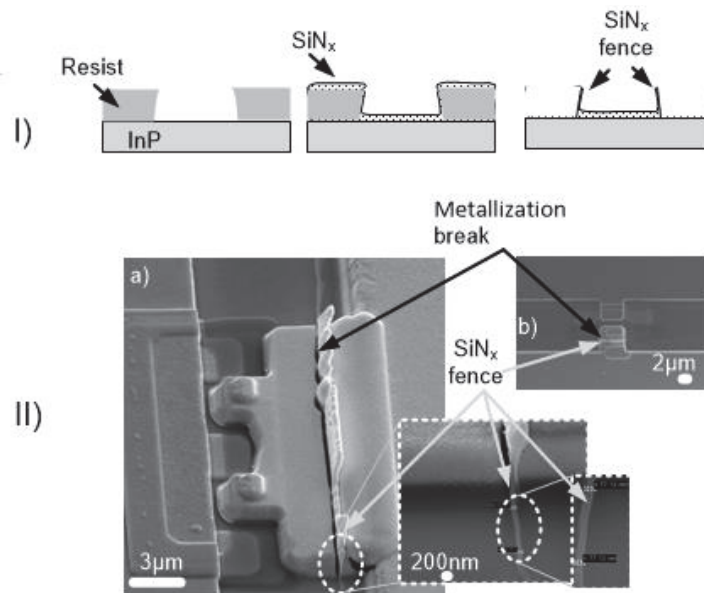


Figure 4.22:  $\text{SiN}_x$  walls caused by the isotropically  $\text{SiN}_x$  deposition in the PECVD. I) Schematic step-by-step of the depositing of the  $\text{SiN}_x$  on a structured substrate surface, starting with the structured photoresist, then the deposition of  $\text{SiN}_x$ , and finally after lift-off process removing the photoresist illustrating the  $\text{SiN}_x$  fences. II) SEM images of a fabricated device utilizing this process showing in a-b) an integrated TBRTD with two mesa in a slot antenna, a metallization break in the last metallization layer is visible due to the  $\text{SiN}_x$  fence, which is presented in more details in the inset.

Consequently, a second method was developed to structure the  $\text{SiN}_x$  layer for the MIM-capacitor to ensure a reliable and reproducible process. In this method, the  $\text{SiN}_x$  is deposited on the whole substrate surface. Then, photoresist-mesa is structured to protected areas where the  $\text{SiN}_x$  should remain. An etching step with hydrofluoric acid (5% HF) is performed to remove the unprotected  $\text{SiN}_x$  from the substrate surface. Figure 4.23 illustrates this  $\text{SiN}_x$  deposition method schematically.

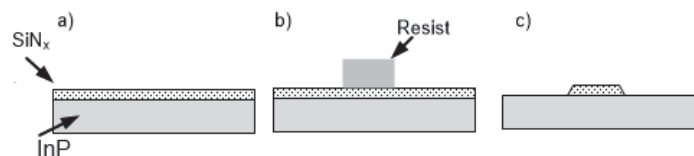


Figure 4.23: Schematic illustration of the processing steps via selective etching to prevent  $\text{SiN}_x$  fences. a) Depositing of  $\text{SiN}_x$  on the whole substrate surface. b) Photoresist mesas structuring to protect the  $\text{SiN}_x$  area. c) 5%-HF etching of the unprotected  $\text{SiN}_x$ .

Furthermore, to determine the permittivity of the deposited material, a MIM structure is fabricated, as shown in Figure 4.24. The MIM-capacitor is integrated into a GSG connection to enable S-parameter measurements for characterization.

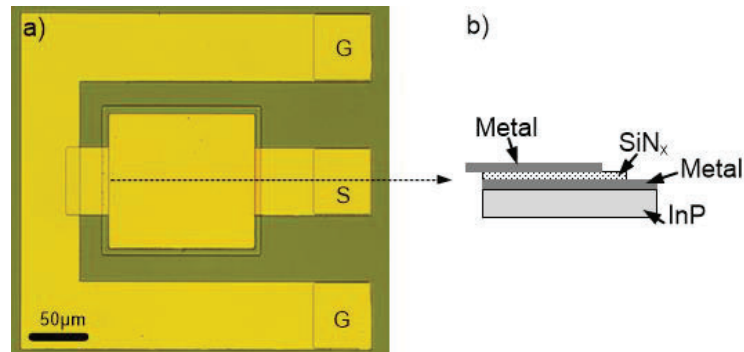


Figure 4.24: a) Micrographic top-view of a fabricated MIM-capacitance for isolator permittivity determination. b) Cross-section of the internal part illustrating the MIM structure in more detail.

### C- Stabilization resistance

The stabilization resistor layer, which is used to suppress any parasitic oscillation at low frequency caused by the external bias line inductance and the capacitance of the device, is structured in the bottom highly doped InGaAs layer in order not to increase the number of fabrication steps and the process complexity. Therefore, during the processing of the TBRTD, the process presented in chapter 4.1, a new step is added. During the wet etching of the remaining InGaAs layer, a pre-defined InGaAs area is structured by deploying a photoresist mesa to protect this area. The thickness of the sheet resistor is  $\sim 300$  nm. To provide a smooth transition for the metallization, a spin-on-glass layer is deposited on the edges of the resistance area. An SEM image of the stabilization resistor after the deposition of the bottom electrode is shown in Figure 4.17d.

### 4.2.2 Bowtie antenna

The fabrication of the bowtie antenna is implemented with the e-beam lithography (*Jeol JSM-6600* SEM, with a *Reith* system for EBL operation). For detectors, a small junction area TBRTD is required (see section 6.1.4). To achieve small area devices, a combination of e-beam lithography and wet chemical etching providing some undercut is used to reduce the device diameter down to 350 nm. After fabricating the TBRTD as presented in section 4.1, the bowtie wings are structured. The substrate is cleaned with acetone and IPA step, to remove any organic residues, followed by an oxide cleaning step in dilute hydrochloric acid which also improves the adhesion of the metal on the substrate. Then the e-beam sensitive resist, PMMA (*AR-P 671.05*) is spin-coated. This resist is cured at 170°C for 10 min reaching a resist thickness of  $\sim 500$  nm. After e-beam exposure (see section 4.1 for EBL parameters), the resist is developed in methyl isobutyl ketone (MIBK) for 60 s. To stop the development,

an IPA dip for 30 s is carried out. Then, a metallization step with Ti/Au 10/400 nm, followed is a standard acetone IPA lift-off process, is executed. A fabricated TBRTD-based bowtie antenna, with a wing length of 400  $\mu\text{m}$  and a metallization height of  $\sim 500$  nm, is shown in Figure 4.25; the inset presents a magnification of the integrated TBRTD device.

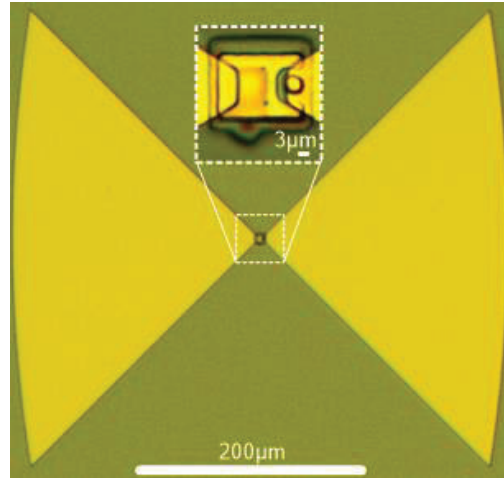


Figure 4.25: Micrographic image of the fabricated TBRTD integrated into a self-complementary bowtie antenna. In the insert, a micrographic image of the TBRTD is visible.



## 5 Triple-Barrier-Resonant-Tunneling-Diode: design and characterization

In this thesis, the TBRTD design was carried out by adopting the model presented in chapter 2.1. Different epitaxial layer designs defining the intrinsic device functionality were realized and tested. For this purpose, the devices based on the layer structures presented in Figure 5.1 are fabricated and characterized. A detailed description of the material stack growth strategy, presented in Figure 5.1, is given in the next section.

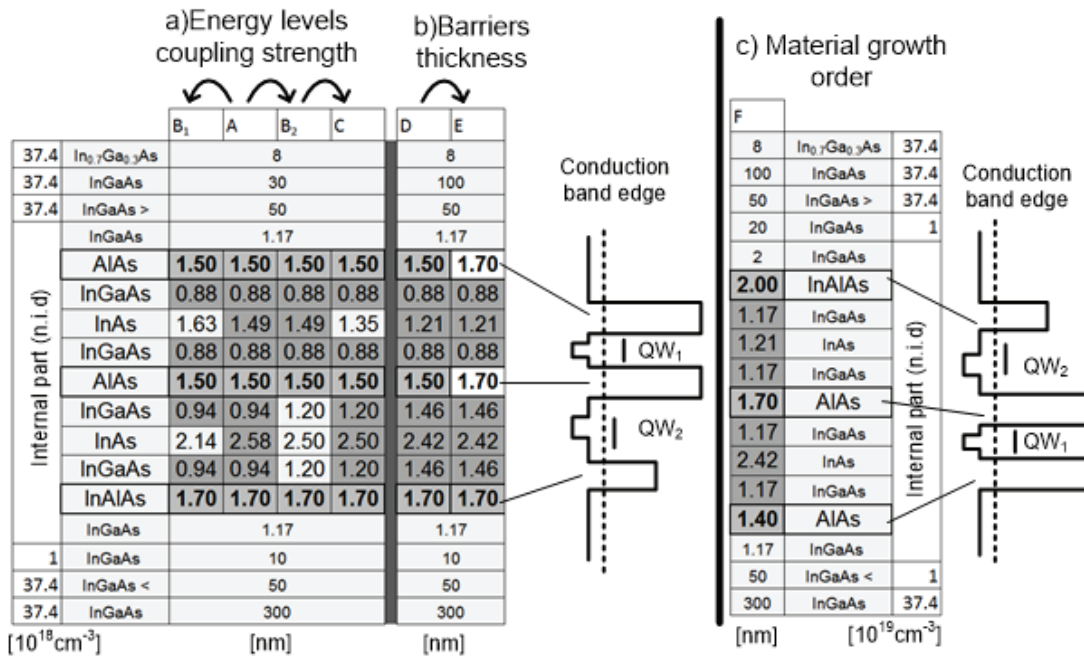


Figure 5.1: Investigated TBRTD layer stack. Further, for simplicity, a conduction band edge is illustrated. a) The energy levels coupling strength is investigated by fine-tuning of the QWs thickness. b) The influence of the slight difference in the AlAs barriers is examined. c) The material growth order is investigated. Bright colored cells in the internal region represent the modified layer. Arrows illustrates the modification direction.

The typical layer stack for the internal region is made of InGaAs/AlAs/InGaAs/InAs epitaxial layers grown on InP-substrate. An excellent junction abruptness between these, mostly only a few nm thick materials, is needed. Thus, growth rate control with monolayer precision is required. Further, a high quality advanced heterostructure design is needed to build up the TBRTD layer stack. In this work, the *device-A* to *F* were grown in a Molecular Beam Epitaxy machine (*Varian-MBE GEN II*). The fabricated TBRTDs are characterized by on-chip DC and scattering-parameter measurements and are modeled to include it into circuit simulation, as will be shown later in this chapter.

Three categories were investigated in this work to develop and investigate the TBRTD model and THz devices. The starting material stack is of *device-A*, all other material stacks (*device-B1*

to  $-F$ ) are grown with modification of the internal part. These TBRTDs have a lower third barrier discontinuity (see Figure 5.1), which turned out to be more efficient for the forward direction current, as shown in [113]. As shown in Figure 5.1, the first group is *a) Energy level coupling strength*. The arrows at the top show the modification direction. The second investigated category is shown in Figure 5.1b), where the influence of the *barrier thickness* is investigated. Category three is under Figure 5.1c) where the *material growth order* is investigated. In this chapter, the investigated categories and design strategy are presented. Then the device characterization and correlation to the model are reported.

## 5.1 Vertical device design

The main goal of the TBRTD design is increasing the non-linearity near zero-volt for detector application and enhancing the NDR region to de-attenuate a resonator for oscillator operation. Further, for efficient mobile THz device, the following aspects are to be considered in the growth strategy:

- High current density
- Large NDR region
- Low time constants
- Low operation voltage
- Strong non-linearity at zero-volt.

To illustrate the growth strategy in more detail, a typical conduction band edge of a TBRTD is presented in Figure 5.2 with its main design parameters.

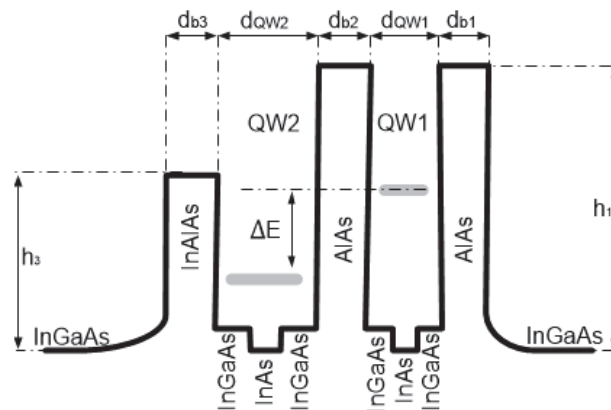


Figure 5.2: Typical conduction band edge of a TBRTD presented with its design parameters.

For large NDR region, high discontinuities are needed to reduce any non-resonant current. Therefore, the AlAs layer is used on InGaAs, which provide a significant discontinuity (see Figure 5.2 parameter  $h_1$ ) of  $\sim 1.5$  eV. The third barrier is formed with  $\text{In}_x\text{Al}_{1-x}\text{As}$ , where the In component defines the height of the barrier (see Figure 5.2 parameter  $h_3$ ). To decrease the time constants, i.e., the time an electron needs from starting the tunneling process until

---

reaching the collector side and increase the current density, the quantum wells and barriers thickness is reduced (see Figure 5.2 parameter  $d_{b1}$ ,  $d_{b2}$ ,  $d_{b3}$ ,  $d_{QW1}$ ,  $d_{QW2}$ ). Reducing the QW thickness ( $d_{QW1}$  and  $d_{QW2}$ ) shifts the discrete energies to a higher level, see equation (2.2). This leads to an increase in the operating voltage caused by the increase of the resonance energy (i.e., peak voltage). To decrease the QWs thickness and still operate at lower voltages, the InAs layer is added in the QWs. InAs material has a low bandgap and hence shifts the discrete energy level back to lower energies. A further important function of the InAs material in the QW is increasing the separation between the first and second discrete energy level in the QW. For strong non-linearity at zero bias, a misalignment, i.e., large  $\Delta E$  (see Figure 5.2) between the discrete energy level in the QW is advisable and will be investigated. Further, to reduce any parasitic resistance in the material stack, the material up to the internal part is highly doped, as shown in Figure 5.1. Further, to improve the contact junction at the top contact, an In-rich (80%) 8 nm InGaAs layer is grown at the top. The higher indium composition in this layer decreases the material bandgap at the metal-semiconductor junction and hence the barrier between the top contact and the device is decreased leading to an improvement of the contact resistance.

Keeping these aspects in mind, the detailed enhancement of the device performance by adjusting its material stack, shown in Figure 5.1, is implemented as follows: Starting with the investigation of the coupling strength (Figure 5.1 group a) by fine-tuning of the QW width ( $d_{QW1}$ ,  $d_{QW2}$ ), i.e., the change in the material stack of *device-A* to *-B1* and to *-B2*. To *device-B1*, the QWs width is tuned to bring the energy levels of the discrete energies to a similar value, hence decreasing the misalignment ( $\Delta E$  decreases, see Figure 5.2). For this purpose, the width of the first well,  $d_{QW1}$ , is increased to reduce the energy level of the discrete energy, and the width of the second well is decreased to increase the discrete energy level in the second QW. The change of the material stack in *device-B2* is done to investigate the influence of increasing the misalignment. This is carried out by increasing the width of the second well  $d_{QW2}$  to reduce the energy level in this QW, while keeping the discrete energy level in the first QW constant. The material stack designed for *Device-C* is to further investigate the coupling strength by tuning the first QW thickness and hence the change from *device-B2* to *-C* is a further increase of the  $\Delta E$ . This is achieved by decreasing the thickness of the first well,  $d_{QW1}$ , hence, increasing the energy level of the discrete level.

In the second group (Figure 5.1 group b, *device-D*, and *-E*), the influence of the barrier thickness is investigated. Therefore, the barrier thickness ( $d_{b1}$  and  $d_{b2}$ ) in the material of *device-E* is slightly increased compared to the barrier material thickness in *device-D* from nominally 1.5 to 1.7 nm. This slight change is chosen because a massive increase in the barrier thickness will influence many parameters concurrently.

Finally, in the third group (see Figure 5.1c), the material stack of *device-F* is grown. In this test, the growth order is changed such that the third barrier (InAlAs-layer) is grown on the

top of the two other barriers. This growth direction is chosen to improve the surface roughness at which the first QW and its AlAs barriers layers are grown. Improving this layer roughness should decrease the overall leakage currents [114, 115] through the double barriers.

## 5.2 Measurement and modeling

In this section, the improvements in the internal material stack, presented in section 5.1, and its influence on the TBRTD performance are first introduced and discussed in terms of DC current density, rectification factor, and curvature factor. In the following section the scattering parameter measurements obtained from a device with promising performance data are used to model its behavior and accomplish its model for circuit simulation.

### 5.2.1 DC measurement results and modeling

The measured current-voltage characterization is used to model and determine the first performance estimation of the TBRTD. In the modeling and for simplicity, the characterization of the TBRTD is split into two regions, as mentioned in chapter 2.1. The first region (diode-like behavior) is for the detection operation, and the second region (NDR region) is for oscillation operation. In Figure 5.3, the current density of three devices over the bias voltage are presented (dots are measured points, and solid lines are fitted by the current-voltage model presented in chapter 2.2). The current density characteristics are modeled separately in each region. The values of the fitting parameters for the NDR region of these three elements are found in Table 5.1.

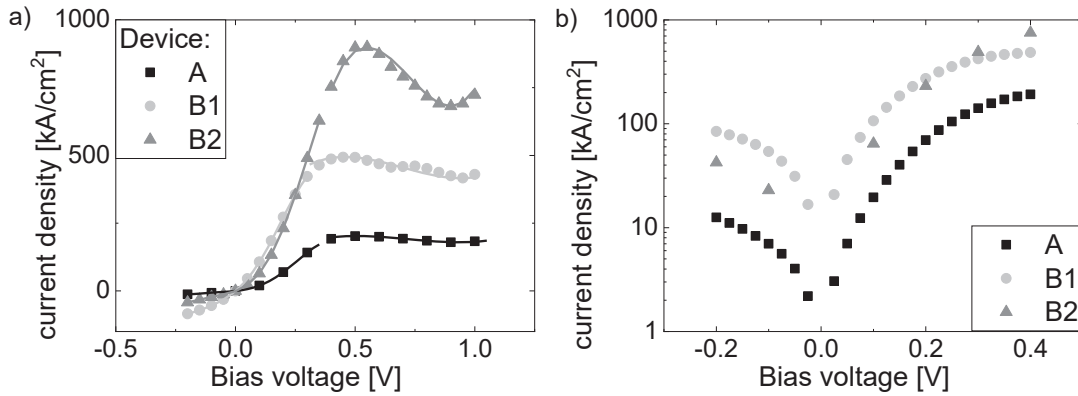


Figure 5.3: a) Measured (dashed) and modeled (solid lines) current-voltage of three devices. b) Half-logarithmical presentation only of the measured current-voltage characteristics in the reverse and PDRI region.

The current-voltage characteristics provide the first figure of merit parameter values of the TBRTD material stack. A comparison of the fabricated devices is shown in Table 5.1.

Table 5.1 first figure of merit parameters of a TBRTD extracted from the DC-characterization

Device	$J_p \left[ \frac{\text{kA}}{\text{cm}^2} \right]$	$V_p [\text{V}]$	$PVCR$	$PVVR$	$G_{V=\pm 0.2\text{V}}$	$\gamma_{V=0\text{V}}$	$P_{out} \left[ \frac{\text{kW}}{\text{cm}^2} \right]$
<b>A</b> -Starting device-	230	0.50	1.13	0.54	5.56	14	2.1
<b>B</b> <sub>1</sub>	494	0.45	1.19	0.49	3.24	-	7.1
<b>B</b> <sub>2</sub>	900	0.55	1.32	0.61	5.45	15.8	14.3
<b>C</b>	746	0.58	1.22	0.58	5.76	29.8	10.6
<b>D</b>	572	0.56	1.34	0.67	-	-	-
<b>E</b>	603	0.74	1.38	0.71	-	-	-
<b>F</b>	549	0.52	1.70	0.52	8.06	12.3	23.0

As shown in Table 5.1, the current density improvement from 230 kA/cm<sup>2</sup> (*device-A*) to 900 kA/cm<sup>2</sup> (*device-B2*) by tuning the internal material stack is achieved. The material stack of *device-B2* provides the best configuration in terms of high current density. It is also shown that the tuning range is limited. Small changes in the QWs thickness have a significant influence on the device properties, especially the NDR region. Further challenging is the fact that this device should be used for both as signal-source and signal-detector by just changing the bias point. This implies a device with a wide NDR region and a strong non-linearity at zero voltage, which is considered with the curvature factor.

Equalizing the energy level in both QWs (changes from *device-A* to *-B1*) improves the coupling strength of the energies, which is visible through the current density increase by a factor larger than two, achieving a maximum current density of 494 kA/cm<sup>2</sup>. This current density enhancement is at the expense of the current rectification factor  $G$ . The factor  $G$  is decreasing as a result of the increase in the current in the reverse bias direction. The changes in *device-B1* equalize the energy level and hence reduces the misalignment of the QWs. Further, reducing the overall energy of the resonance point (reducing the energy level of both discrete energy levels in both QWs), a reduction of the peak voltage is expected and is visible, as shown in Table 5.1. In the next step, the change from *device-A* to *-B2* where the misalignment is increased by increasing the thickness of the second QW ( $d_{\text{QW}2}$ ), while keeping the other material thicknesses constant. As shown in Table 5.1, stronger resonance strength is given over a wider NDR region. A current density increase from 230 to 900 kA/cm<sup>2</sup> is achieved. The increase in the  $PVCR$  and  $PVVR$  from 1.13 to 1.32 and from 0.54 to 0.61, respectively, explains the sharp rise of the possible maximum RF output power from 2.1 kW/cm<sup>2</sup> to 14.3 kW/cm<sup>2</sup>. In terms of the rectification factor and curvature factor, no significant improvement was visible. A further increase in the misalignment between the QWs is investigated at *device-C*. Therefore, the first QW thickness ( $d_{\text{QW}1}$ ) is further reduced

compared to *device-B2*. The curvature factor increases from 14 to 15.8 to 29.8 at *device-C*, which has the strongest misalignment between the QW's. This confirms again the assumption taken at the model description in chapter 2.1, that the misalignment between the QWs is a crucial element for the detector performance of the device.

The main parameters for high output power are the current and voltage in the NDR region. Decreasing the leakage current of the device, increases the NDR region, i.e., increasing the *PVVR* and *PVCR*. This is investigated by changing the epitaxial growth order as shown for *device-F* (see Figure 5.1c). A possible improvement is due to the smoother surface at the AlAs barrier layers, which reduces the leakage currents in the NDR region [114, 115]. *Device-F* has a large NDR region with a *PVCR* and *PVVR* of 1.7 and 0.52. The high *PVCR*, which is the highest in this investigation, indicates a reduction of the leakage current. Non-resonant current in the NDR region leads to *PVCR* reduction and is visible through the increase in the valley current. As shown, *device-F* has a maximum possible output power of 23 kW/cm<sup>2</sup> with a maximum current density of 549 kA/cm<sup>2</sup>. Compared to *device-B2* with an output power of 14.3 kW/cm<sup>2</sup> and a current density of 900 kA/cm<sup>2</sup>. This confirms the assumption that the output power is mainly a function of *PVCR* and *PVVR*, and not of the maximum current density. The effect of the leakage current reduction when flipping the growth direction shows a promising improvement mechanism and, should be investigated in more detail in the future.

Finally, the influence of the barrier thickness on the static behavior of the TBRTD is investigated. The tunneling probability and, therefore, the current density and resonance voltage are directly affected by the barrier thickness. To minimize the change, a limited thickness tuning of the AlAs layer from nominally 1.5 to 1.7 nm was chosen (changes from *device-D* to *-E* see Figure 5.1). As shown in Figure 5.4, the current density of both devices remains at a similar level, but a substantial peak voltage shift of around 180 mV is visible.

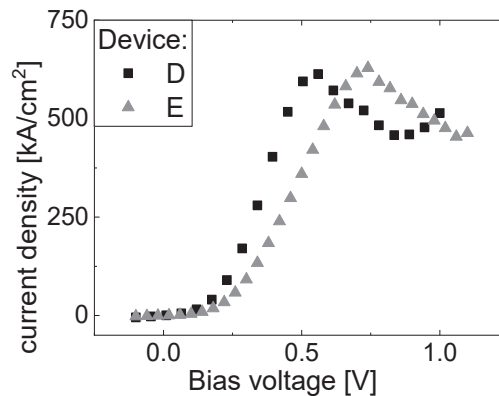


Figure 5.4: Current-voltage characteristics of two devices to illustrate the influence of the barrier thickness on the device performance.

The extracted parameters from the devices by modeling of the NDR region via the model presented in chapter 2.2 are presented in Table 5.2. As was shown in equation (2.8), the static negative differential conductance is proportional to the fitting parameter. As shown in Table 5.2, a direct proportionality is given between the fitting parameter  $a$  and the maximum device current density, where *device-A* shows the lowest  $a$  value of  $8.15e4$  S/cm<sup>2</sup> at a current density of  $230$  kA/cm<sup>2</sup> and *device-B2* exhibits  $a = 9.37e5$  S/cm<sup>2</sup> at the highest current density of  $900$  kA/cm<sup>2</sup>. This means that devices with high current density can de-attenuate resonators with higher losses.

Table 5.2 Model parameters extracted from the DC-characteristics of the TBRTD

Device	$a$ $\left[\frac{\text{S}}{\text{cm}^2}\right]$	$b$ $\left[\frac{\text{Scm}^2}{\text{V}^2}\right]$	$J_0$ $\left[\frac{\text{kA}}{\text{cm}^2}\right]$	$V_0$ [V]
A-Starting device-	8.15e4	6.02e5	191	0.72
B <sub>1</sub>	2.45e5	1.42e6	455	0.70
B <sub>2</sub>	9.37e5	1.02e7	790	0.72
C	4.79e5	3.62e6	680	0.80
<b>F</b>	8.06e5	4.66e6	490	0.76

## 5.2.2 S-parameter measurements and modeling

To extract the internal parameters of the TBRTD, the parameters surrounding the internal part must be deembedded from the measurement results. Therefore, the following extended equivalent circuit, including the internal parasitic elements and contact pads, is introduced in Figure 5.5. This section is starting by presenting and discussing the modeling strategy and parameter extraction methods followed by introducing the measured results and the modeling of a TBRTD single device.

### Equivalent circuit parameter extraction method

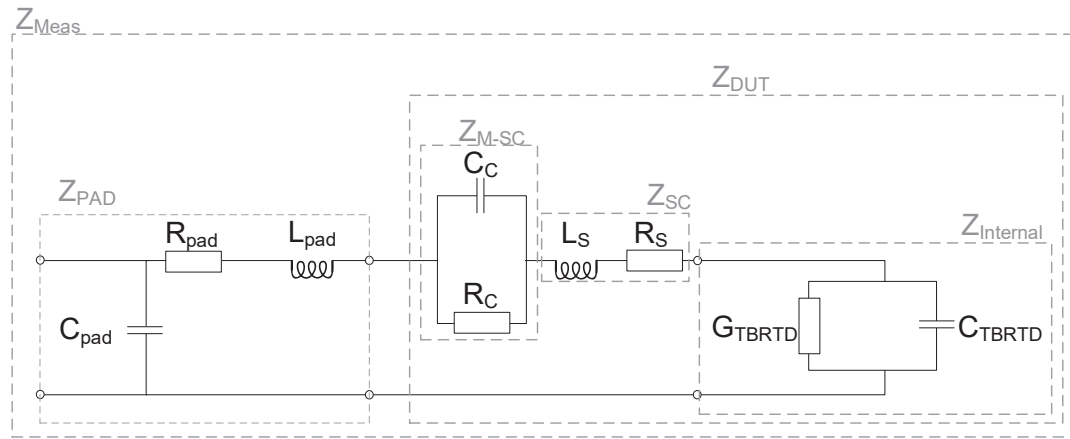


Figure 5.5: Complete equivalent circuit of an on-wafer measured TBRTD device embedded into a one port GSG-structure.

The  $Z_{PAD}$  is the impedance of the contact pads presented in section 3.2.2 and can be excluded by the open and short de-embedding method (see section 3.2). The next element, the  $Z_{M-SC}$  is the impedance which is caused by the metal-semiconductor junction. The resistance of the metal and semiconductor junction  $R_C$  is determined via Transmission Line Measurement (TLM). Due to the similarity of the metal-semiconductor interface at all the investigated devices, its values will be in a similar range at all devices and depends only on the device area. Then an estimation of the contact  $C_C$  capacitance is carried out while including the contact material and material doping. The components of  $Z_{SC}$ , which is due to the device mesa where  $L_S$  is because of the vertical current flow in the device, given by the height of the material stack and the diameter of the device. In this work, the height was sufficiently low to neglect its influence.  $R_S$ , on the other hand, is an essential parameter. An exact determination of the series resistance is mandatory, because of its impact on the maximum achievable frequency. Therefore, in this work  $Z_{SC}$  consist only of the real part given due to the series resistance  $R_S$ . Several methods were published elsewhere to extract the series resistance  $R_S$  of a resonant tunneling diode from its measured current-voltage curve. The most popular and straightforward method is presented in [116], where the static current-voltage characteristics of the diodes are utilized. In [116] the series resistance of the RTD is extracted at very high

voltages, far beyond the valley voltage, where the conductance of the equivalent circuit is very high, and therefore the resistive part measured is contributed to the series resistance. This method is challenging when dealing with high current density devices, as in this work. When biasing the devices at voltages far beyond the valley point, due to the high current flowing through the device, the devices can be thermally damaged. A different method, which utilizes the S-parameter measurements instead of DC, is presented in [117]. Here, use was made of the properties of the internal equivalent circuit at the valley or peak point. At these operating points, the conductance ( $G_{\text{TBRTD}}$ ) is very low (ideally zero), and therefore the impedance of the device is described by the series resistance and a serial connected capacitance. The impedance is then written as:

$$\text{For the real part:} \quad \text{Re}\{Z_{\text{peak,valley}}\} \approx R_s, \quad (5.1)$$

$$\text{and the imaginary part:} \quad \text{Im}\{Z_{\text{peak,valley}}\} \approx \frac{1}{j\omega C_D}. \quad (5.2)$$

This method requires a stable device in terms of oscillation immediately after the peak point or before the valley point. Further, due to the high non-linearity of the RTD, especially at the peak and valley point, small signals are to be used during the measurements ( $P_{\text{in}} < -30$  dBm) to ensure linearity. This method provides a good first estimation of the series resistance for small area RTDs.

Then, after extracting the first estimation of the equivalent circuit elements, the device capacitance, and its parallel conductance are characterized. The parameter extraction is executed with the model presented in chapter 2.2. Starting the parameter extraction of the device conductance, which is extracted firstly from its current-voltage characteristics and equations (2.7), (2.8), and (2.12), its frequency dependence is included.

The next parameter is the device capacitance, which is an overlap of the depletion capacitance, equation (2.19) and the quantum capacitance, equation (2.17). The depletion capacitance is determined by the material stack layers thicknesses, doping, and can be extracted with equation (2.18) and (2.19). The quantum capacitance, on the other hand, is determined by subtracting the depletion capacitance from the capacitance derived from the measurements.

## Measurement and modeling results

Next, the scattering parameters and the equivalent circuit modeling are presented. The scattering parameter measurements are carried out in the whole current-voltage range of *device-F*. As shown in Figure 5.6, where the Smith chart of the measured return loss of *device-F* is presented in the voltage range from the reverse region up to the second PDR region. To ensure linearity during the S-parameter measurement, low power is applied  $P_{\text{out,VNA}} \sim -30$  dBm. From the Smith chart, it is directly visible that the TBRTD shows a capacitively dominated behavior over the whole biasing range, visible as curved lines expanding in the

lower half of the Smith chart. A known problem when measuring an NDR-based device is its affinity for oscillation when biased in the NDR region, due to the resonator comprised of the device capacitance and the inductance of the bias lines. Several methods were presented in the literature to suppress these oscillations [118, 119] during measurement. However, in this work to prevent parasitic oscillation during measurement, devices with small areas are used for the measurements and characterization. These devices have an absolute conductance that cannot compensate the input impedance of the VNA ( $Z_{in,VNA} = 50\Omega$ ), and hence, no oscillation during scattering parameter measurement is occurring. As shown in Figure 5.6 at a specific voltage, the measured curves are indicating a negative resistance value, i.e., operation point in the NDR region. This shows a successful characterization of the TBRTD in the NDR region, without any external stabilization. In the next steps, *device-F* will be characterized and, as will be presented later, integrated into an antenna because of its good expected performance, as shown in Table 5.1.

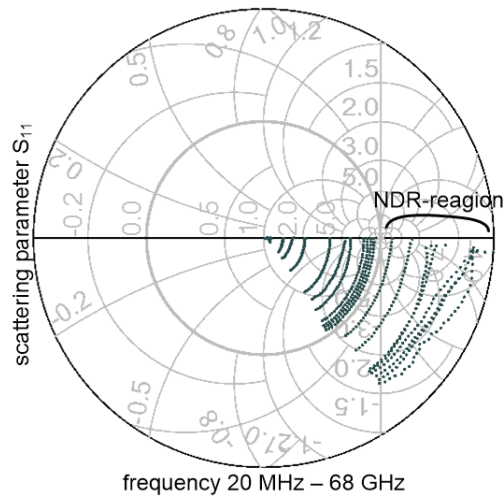


Figure 5.6: Smith-chart diagram of measured scattering parameters of a TBRTD (*device-F*) in the whole voltage range. The capacitive dominating behavior is visible.

Due to the similarity of the contact materials layer stack, including doping (see section 5.1), constant contact property for the used devices was determined  $R_c = 6.2 \cdot 10^{-7} \Omega\mu\text{m}^2$  and  $C_c = \frac{14 fF}{\mu\text{m}^2}$ . Further, as was shown in chapter 2.2, the geometrical capacitance, which is doping and materials stack dependent, is calculated. These data are inserted into the model, shown in Figure 5.5, as a first estimation. Then by fine-tuning of the internal equivalent circuit elements,  $R_s$ ,  $G_{TBRTD}$ , and  $C_{TBRTD}$ , the fitting of the measured and modeled curves is improved. Figure 5.7a-b presents the evaluated real and imaginary part of the measured device impedance at three different operation points in the NDR region, shown due to the negative real part of the impedance. As shown, good agreement between the measured (dotted lines) and modeled (solid lines) impedance is given. This is also given as shown in the PDR1 and reverse voltage region in Figure 5.7c-d

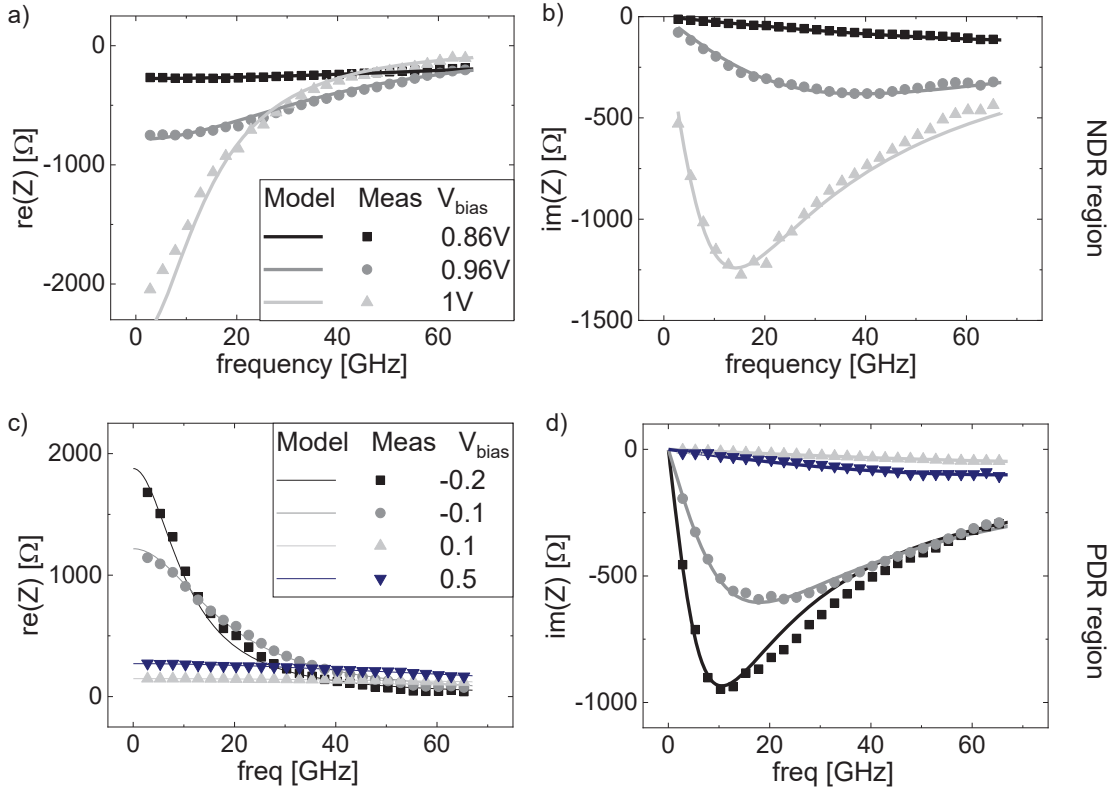


Figure 5.7: Measured (dotted lines) and modeled (solid lines) curves in (a-b) NDR region and (c-d) reverse and PDR region.

After fitting, the influence of the small-signal equivalent circuit elements can be investigated. In Figure 5.8, the main TBRTD equivalent circuit parameters,  $G_{\text{TBRTD}}$  and  $C_{\text{TBRTD}}$ , over the bias voltage are presented. From these data, it is visible that a bias dependency is given, and hence, the response frequency of a TBRTD-based resonator is bias voltage-dependent. The measurement in the NDR region was very challenging because of the self-oscillation; therefore, not all voltage points within the NDR could be characterized. However, it is still obvious that the conductance of the TBRTD has a negative peak point, which will be around the center of the NDR region. An average value of the negative differential conductance in the NDR region can, despite the missing points, be extracted around  $-8 \text{ mS}$ . Further, the capacitance curve shows a capacitance decreasing over the applied voltage, which is typical for a depletion capacitance. However, a capacitance maximum is shown in the PDR1 region. This maximum is expected due to the charge accumulation in the first QW when applying a voltage and tilting the conduction band edge, which leads to a filling of the states in the first QW and hence a decrease in the distance between the non-conducting layers, leading to a capacitance increase. An average capacitance value in the NDR region amounts to  $5 \text{ fF}$ . This device has an area of  $0.68 \mu\text{m}^2$  and hence, the device capacitance and conductance in the NDR region can be given as  $C_{\text{TBRTD,NDR}} = 8.83 \text{ fF}/\mu\text{m}^2$  and  $G_{\text{TBRTD,NDR}} = 11.76 \text{ mS}/\mu\text{m}^2$ .

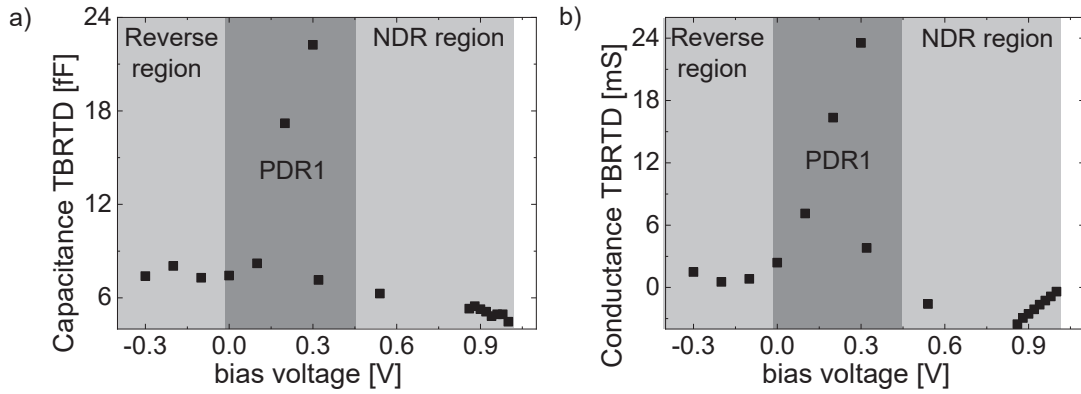


Figure 5.8: Extracted small-signal equivalent circuit of the TBRTD. a) Capacitance and b) conductance, in the whole current-voltage region.

The data obtained from this characterization are used to complete the small- and large-signal equivalent circuit model for later usage in the circuit simulation. By integrating the frequency dependency of the equivalent circuit elements, as was shown in [36, 49, 50] and described in chapter 2.1, this model can estimate the impedance of the device at frequencies beyond the measurement frequency. These are valid up to the transit frequency of the device where the tunneling times cut off the RTD operation.

---

## 6 Free running oscillator and zero bias detector: design and characterization

In this chapter, the design of the slot antenna for the resonant approach and of the self-complementary bowtie antenna for the broadband approach are presented in the form of simulation results. To estimate the antenna characteristics, EM-simulations were performed. Different simulation software, such as CST, Empire, and ADS-Momentum, were deployed to design and predict its performance, see chapter 2.5.2 for more information regarding the simulator-methods and -programs. The aim of the first section is a deeper understanding of the antenna performance, and therefore, the influence of the antenna structure on its performance is investigated. A direct relationship between the antenna structure and its equivalent circuit parameters is then established, for performance tuning. Further, the developed antenna equivalent circuit is integrated within a circuit simulation for matching purposes.

By utilizing the slot-antenna properties, a resonator design at  $f_0 = 260$  GHz is carried out. Depending on the biasing point, this device operates both as a detector or an oscillator. Then, the design of a broadband detector via integration of the TBRTD into a bowtie antenna structure is presented. Finally, the fabricated devices (see chapter 4.2) are characterized in the quasi-optical measurement setup (see chapter 0).

### 6.1 Oscillator and detector design

The circuit design strategy is as follows: first, EM-simulation of the antenna structure is done to determine its scattering parameters and its far-field behavior. Then, using the scattering parameters, the values of its equivalent circuit are extracted and inserted into the equivalent circuit. The advantage of this approach is its simplicity, where the antennae, devices, and parasitic environment can be translated into simple lumped element equivalent circuit. Then utilizing the information regarding the single antennae and the TBRTDs (see chapter 4), the integration for on-chip THz oscillators and detectors is finalized.

#### 6.1.1 Slot antenna design

Figure 6.1 presents a simulated input admittance of a slot antenna with the following geometrical parameters:  $Width_{\text{slot}} = 10 \mu\text{m}$ ,  $Length_{\text{slot}} = 120 \mu\text{m}$ , and feeding point at the center of the slot. The antenna is placed on a lossy InP substrate. From the simulation, it is visible that the antenna series resonance point is at 900 GHz. At this frequency, the antenna radiation conductance is at maximum, meaning that at this frequency, the antenna has its maximum efficiency.

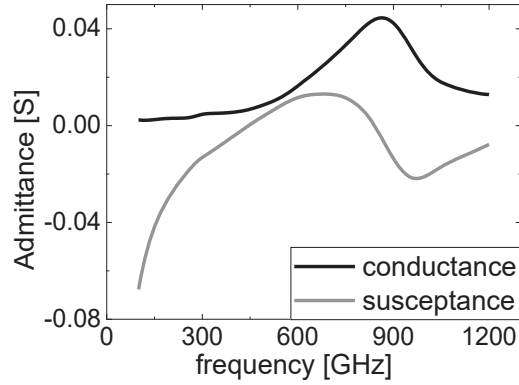


Figure 6.1: Simulated admittance vs. frequency of a slot antenna separated into real (conductance) and imaginary (susceptance) part. The slot dimensions are  $10\ \mu\text{m}$  and  $120\ \mu\text{m}$  width and length, respectively.

Figure 6.2a presents the fitting of the simulated susceptance of the antenna with its equivalent circuit presented in Figure 2.15, and the following parameters are extracted:  $C_{\text{ant}} = 6.5\ \text{fF}$  and  $L_{\text{ant}} = 22\ \text{pH}$ . The conductance of the antenna is frequency-dependent and is presented in impedance form in Figure 6.2b. To determine the radiation conductance of the antenna, a lossless simulation of the setup is carried out. Further, the simulated antenna efficiency provides direct access to the antenna radiation conductance. Figure 6.2b illustrates the difference between the antenna resistance, the antenna losses and the radiation-resistance.

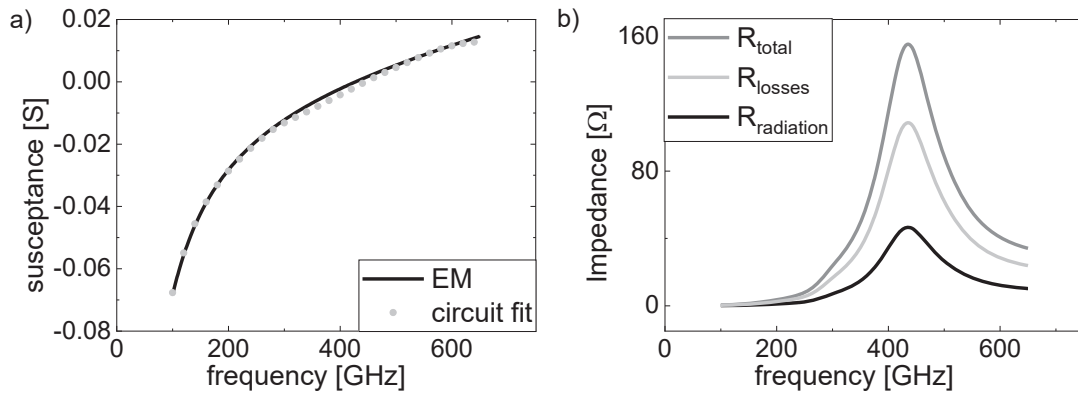


Figure 6.2: a) EM-simulation results of the slot antenna and its curve fitting using the equivalent circuit approach. b) The total resistance and its separation into its losses- and radiation-resistance are presented.

The influence of the dimensions of the slot on the equivalent circuit parameters is investigated in the next step. The parameters used for the environment and substrate, i.e., material losses and conductivity are as follow: substrate permittivity  $\epsilon_{r,\text{InP}} = 12.5$  and loss tangent  $\text{tand}_{\text{InP}} = 0.0004$ . First, the slot length is set to 20, 40, 60, and  $100\ \mu\text{m}$  with a constant width of  $10\ \mu\text{m}$ , as shown in Figure 6.3. Decreasing the slot length increases the resonance frequency of the antenna. The equivalent circuit elements provide an explanation for this behavior. By reducing the length of the slot, the self-capacitance and -inductance of the antenna decreases. The response of the slot antenna is very similar to a slot line with both

ends shortened. Due to the small length of the slot ( $Length_{slot} < \lambda/2$ ), the slot is acting as an inductance. Figure 6.3c illustrates this behavior: By decreasing the slot length, the antenna susceptance increases, caused by the inductance decrease seen from the center of the slot antenna. From Figure 6.3a and Figure 6.3b, the capacitance and inductance pro unit length are determined:  $C_{slot} = 1 \text{ fF pro } 20 \mu\text{m}$  and  $L_{slot} = 0.25 \text{ pH}/\mu\text{m}$ .

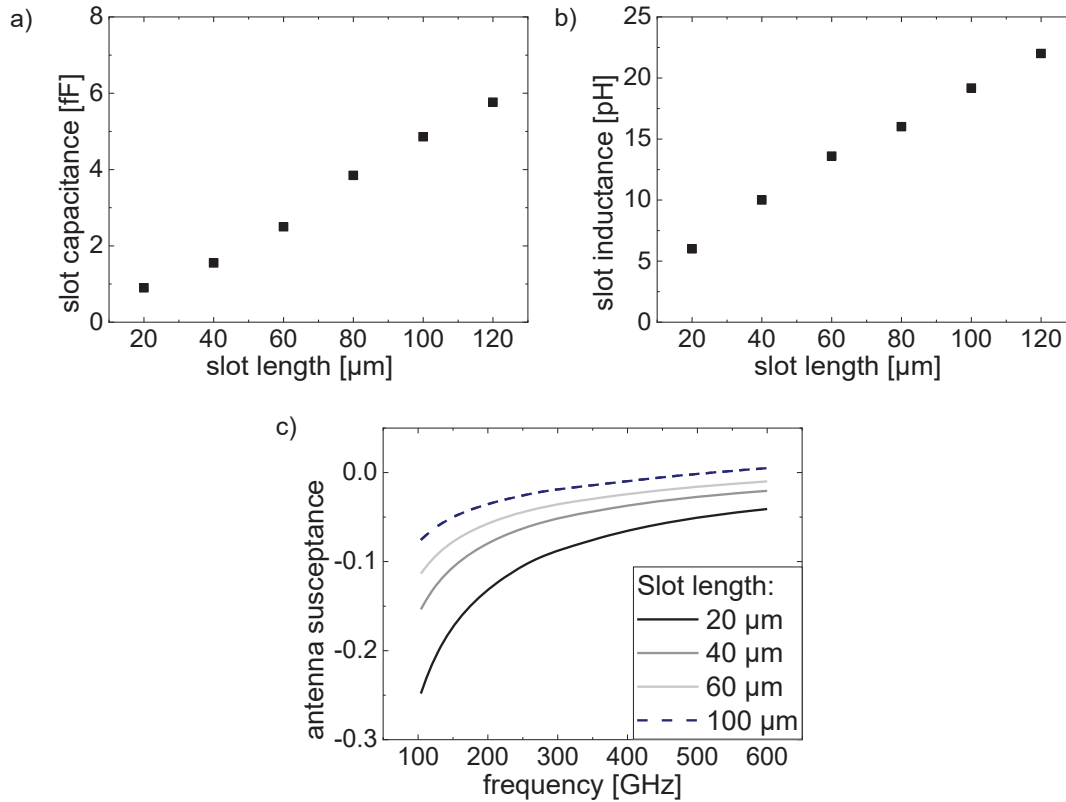


Figure 6.3: Equivalent circuit elements change over the slot length. Slot width is constant at  $10 \mu\text{m}$  and length is tuned from  $20$  to  $100 \mu\text{m}$ . a) And b) illustrates the change of the slot capacitance and inductance, respectively, over the slot length. c) The antenna susceptance change over the frequency at four different antenna lengths is presented.

Decreasing the length of the antenna provides a technique for a direct increase of the resonance frequency due to the reduction of the inductance and capacitance of the structured resonator. The influence of the slot width is simulated in the next step: the length of the antenna is set to a constant value of  $80 \mu\text{m}$ , and its width is set to  $3, 5, 8,$  and  $10 \mu\text{m}$ . It is clear from Figure 6.4 that the antenna susceptance is dependent on the slot width and hence its resonance frequency as well. The slot antenna in this scenario is – as a short-circuited slot line – inductively loaded at the end of the slot. By decreasing the width of the slot, the inductance load is reduced.

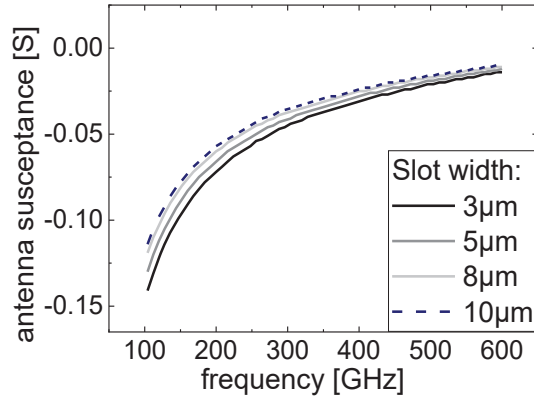


Figure 6.4: Simulated antenna susceptance over the frequency with different slot antenna widths. The length is constant at  $80 \mu\text{m}$  while the width is tuned from 3 to  $10 \mu\text{m}$ .

Due to the small slot length, compared to the wavelength, the radiation pattern of the antenna is almost frequency-independent. Further, the antenna is placed on an InP substrate, and therefore, the radiation direction is to the bottom side (see chapter 2.5.2). In Figure 6.5, a representation of the directivity of the slot antenna at 260 GHz is presented, illustrating its effective area of the antenna and the main lobe radiation direction.

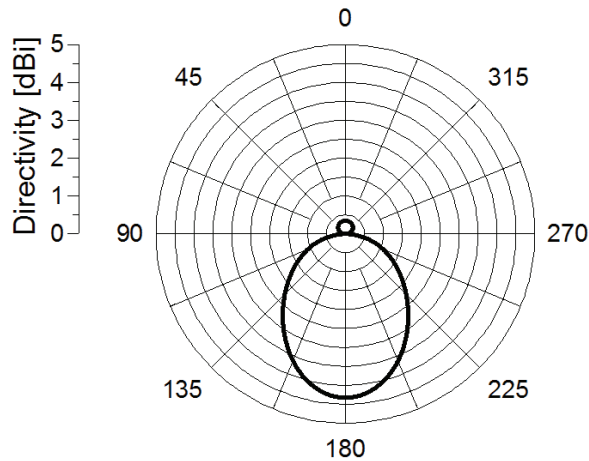


Figure 6.5 Simulated directivity of a slot antenna at 260 GHz with a dimension of 10 and  $80 \mu\text{m}$ , slot width, and length, respectively placed on lossy InP substrate. The main radiation is at the bottom side caused by the high permittivity of the InP substrate.

### 6.1.2 TBRTD integration within a slot antenna

The main part of the slot antenna after radiation of the THz signal is providing an inductive part for the resonator. The TBRTD provides the capacitive part. Designing the slot antenna to be only inductive at specific frequencies detunes its performance, especially the radiation conductance, and hence, low RF output power is expected. Reducing the capacitive part in the antenna is carried out by designing the resonant frequency of the antenna far beyond the

oscillation frequency. In this work, the first run aimed to achieve a THz signal generator at  $f_0 = 260$  GHz. Before integrating the TBRTD into the antenna, a further modification, by adding a MIM-capacitor (Metal Isolator Metal), is needed to make it possible to DC bias the TBRTD, i.e., by separating the top and bottom contact for DC voltages and currents and to form a short for the THz waves. The capacitance value of the MIM-capacitor is to be designed to be shortened at high frequencies, i.e., large capacitance values are required. In our department, as was presented in chapter 4.2, SiN<sub>x</sub> is deposited as an isolator. For the simulation, the material parameters included for the SiN<sub>x</sub> material are determined experimentally by MIM-capacitor integrated into a GSG structure, as shown in chapter 4.2. Further, to suppress the parasitic oscillation at low frequency, caused by the inductance of the bias lines, a resistance, parallel to the MIM-capacitor, is used. In this work, a similar slot antenna structure as the modified slot antenna [120] is developed (cf. Figure 6.6).

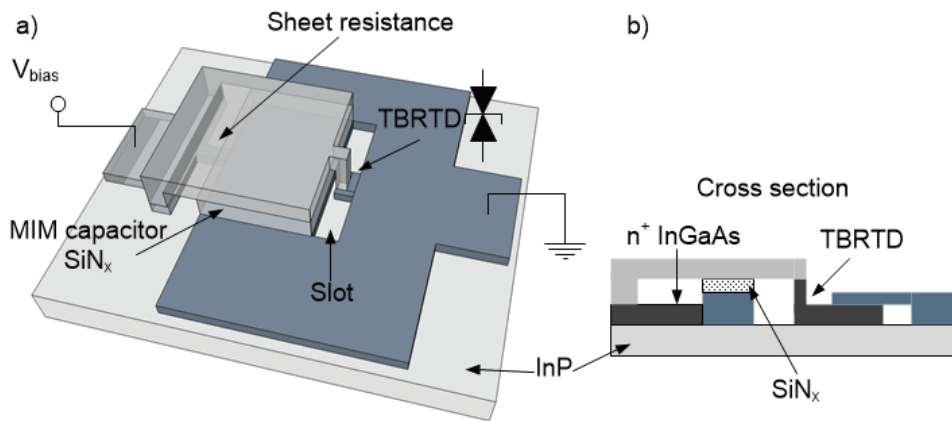


Figure 6.6: a) Schematical structure of the slot antenna and b) a cross-section of the slot antenna at the center point illustrating the position of the TBRTD, MIM-capacitor, and the suppression resistance.

To illustrate the integration of the TBRTD into the slot antenna, the equivalent circuit in Figure 6.7a is presented. At high frequencies, the influences of the structure's parasitic elements are negligible. Therefore, the equivalent circuit for high-frequency operation is simplified to the equivalent circuit shown in Figure 6.7b, where a proper stabilization resistance and large MIM-capacitance is used. The equivalent circuit parameter values are taken from a single device investigation carried out in chapter 3.

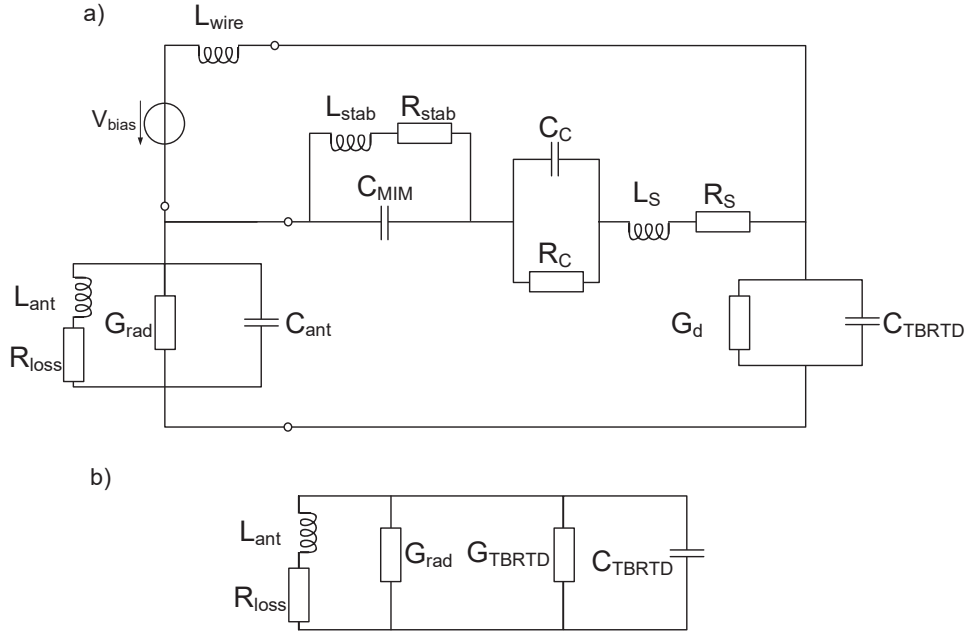


Figure 6.7: Complete equivalent circuit of a TBRTD integrated into a slot antenna a) Equivalent circuit of the whole device b) Equivalent circuit for operating in the THz range. Due to the short device mesa,  $L_S$  can be neglected.

### Oscillator:

For the first antenna, an oscillation frequency of 260 GHz was targeted. To achieve this frequency, the following parameters were deployed for the slot antenna: slot-length  $80 \mu\text{m}$ , slot-width  $10 \mu\text{m}$ . This slot structure provides a slot antenna with a resonance frequency of 832 GHz and hence, inductive behavior around the oscillation frequency of 260 GHz. The extracted equivalent circuit element values are, as shown in Figure 6.3:  $L_{\text{ant}} = 17.33 \text{ pH}$ ,  $C_{\text{ant}} = 2.11 \text{ fF}$ ,  $1/R_{\text{rad}} = 470 \Omega$ ,  $R_{\text{loss}} = 452 \text{ m}\Omega$ .

S-parameter simulations are performed in a circuit simulator (ADS) by integrating the equivalent circuit presented in Figure 6.7b. Then, the area of the integrated TBRTD is tuned (*device F*, see chapter 0), to achieve the targeted frequency of 260 GHz (see Figure 6.8a). The TBRTD area for this oscillator is determined to be  $2.4 \mu\text{m}^2$  with a total capacitance of 21 fF. Then, by integrating a large-signal model of the TBRTD with the equivalent circuit of the antenna, a time-domain simulation is carried out. As shown in Figure 6.8b, the oscillation of the element occurs at the designed frequency of 260 GHz.

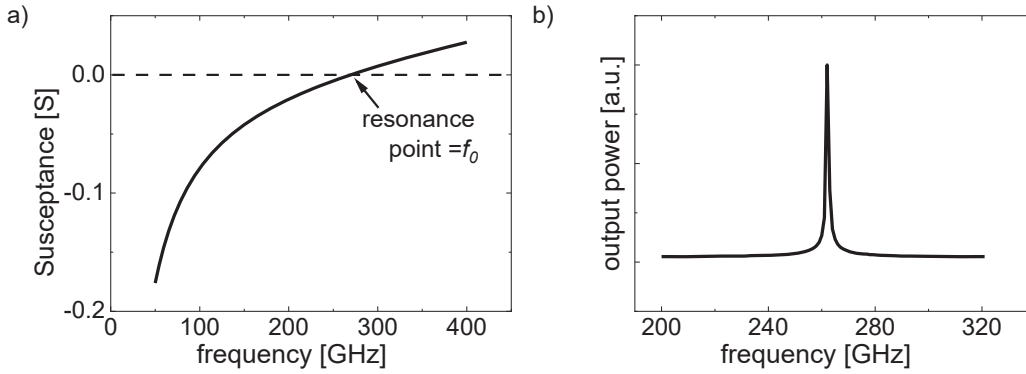


Figure 6.8: a) Simulated susceptance of a TBRTD integrated into a slot antenna. A resonance point is around 260 GHz. b) Fourier transformation of a time-domain simulation result of the output signal of the TBRTD-based oscillator, oscillation frequency peak is around 260 GHz.

### Resonant detector:

The same device is deployed as a direct detector by changing its operation point to 0 V. Further, the resonance frequency of the detector is defined with the capacitance of the TBRTD  $C_{\text{TBRTD}}$  and the inductance of the antenna  $L_{\text{ant}}$ . Therefore, a shift in the resonance frequency is expected due to the TBRTD capacitance dependency over the voltage.

Resonant detectors can achieve high responsivity over a narrow range of frequency, due to the better matching compared to a broadband antenna. In Figure 6.9, the scattering parameter of the antenna, including the TBRTD, is presented. As shown, a resonance point at 280 GHz is given; in this scenario, the TBRTD area is modified to  $1.56 \mu\text{m}^2$ . Further, the -10 dB detection bandwidth (BW) is between 251 GHz and 320 GHz.

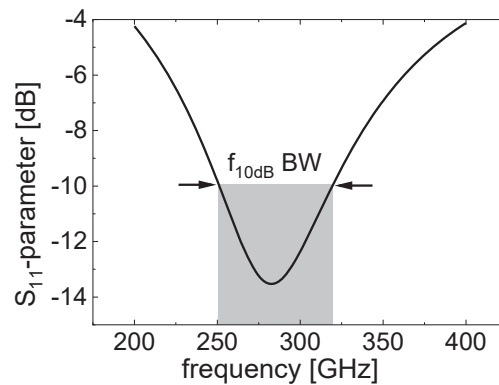


Figure 6.9: Simulated scattering parameter results of a TBRTD integrated into a slot antenna demonstrating the  $f_{10\text{dB}}$  frequency region for detection bandwidth determination.

To illustrate the detection capability of the TBRTD, the equivalent circuit in Figure 6.10 is used. The irradiation source is placed in series to the antenna impedance (see chapter 2.6), and a simplified TBRTD model, consisting of a resistance in series to a parallel connection of capacitance and conductance, is deployed (see section 2.2).

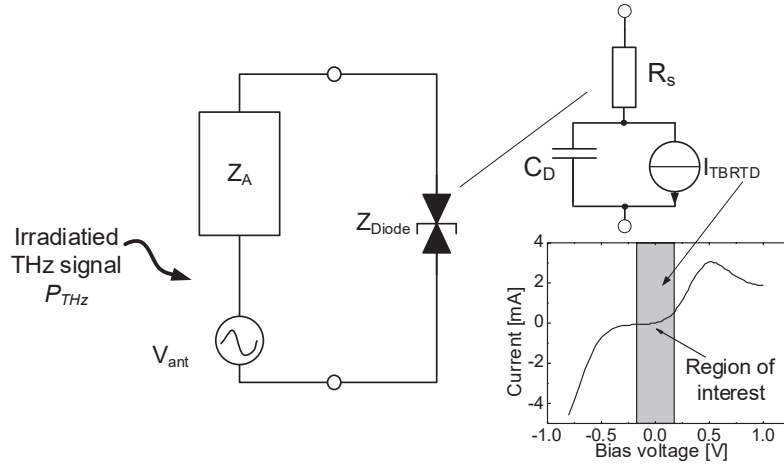


Figure 6.10: A block setup integrated into a circuit simulator for TBRTD detection capability simulation.

In the first step, the rectified voltage of the detector is investigated. For this purpose, transient simulation is carried out by irradiating a signal with constant power ( $P_{THz}$ ) into the antenna, i.e., exciting a voltage swing of  $V_{ant}$  as shown in equation (2.74). The frequency is tuned in the range from 200 GHz to 400 GHz while recording the voltage drop over the device, as shown in Figure 6.11. Integrating one period over time provides the detected DC voltage (see section 2.6). Figure 6.11b presents the detected voltage over the frequency at different nominal input power via Harmonic-Balance (HB) simulation in ADS of the same setup. The HB simulation is a frequency domain simulation that provides a fast simulation of the steady-state response of a non-linear electrical circuit. A good agreement of the resonance frequency is shown, where a detection peak at  $f_0 \sim 280$  GHz is given.

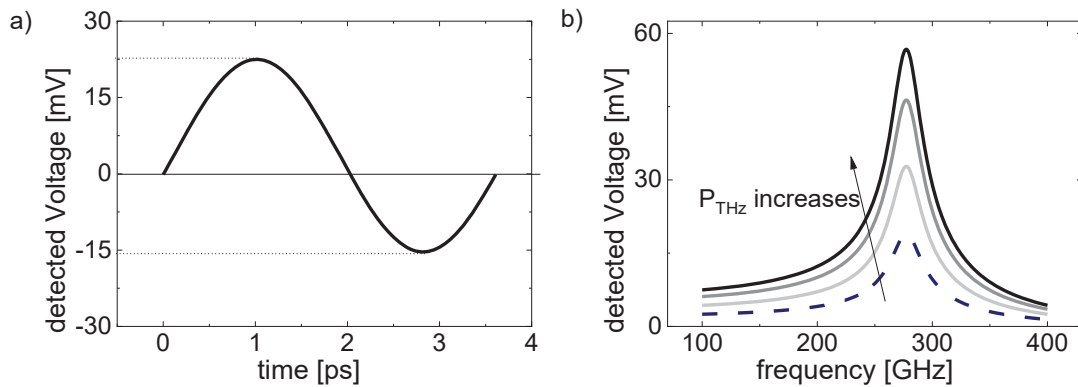


Figure 6.11: a) Transient simulation results of a TBRTD-based resonant detector, whereby the rectification capability is demonstrated by the rectified voltage over the time at the TBRTD when irradiated with a signal with constant power. b) The DC-component over the TBRTD, of an HB simulation, illustrating the detected voltage over the irradiated signal frequency.

### 6.1.3 Self-complementary bowtie antenna design

A self-complementary antenna is known for its large bandwidth [65–67, 71, 89] and is preferred when dealing with broad-band detectors as in this work. The large bandwidth capability of such antennae is given due to the constant input impedance over a wide frequency range. In Figure 6.12a, a schematic structure of the Bowtie antenna, with its typical design parameters, is shown. For a self-complementary bowtie antenna, the angle  $\alpha_{\text{Bowtie}}$  is constant at  $90^\circ$ . The gap between the bowtie wings is defined by the integrated device is kept constant at  $d_{\text{feed}} \sim 5 \mu\text{m}$ . The remaining parameter  $L_{\text{bowtie}}$ , which is the arm length, is the variable tuning parameter. The influence of the antenna length on the admittance of the device is shown in Figure 6.12b,c,d. Susceptance of a self-complementary antenna with wing length between 100, 250, and 400  $\mu\text{m}$  is presented with its self-resonance frequency at 177.5, 70, and 42.5 GHz, respectively. The antenna provides constant behavior at frequencies higher than its internal-resonance frequency. The internal resonance frequency of the antenna is defined by its length. Therefore, for broadband detection starting at very low frequencies, large antennae are needed. A further parameter that must be considered when designing a broadband detector is the antenna efficiency. The larger antenna provides a larger physical area, and hence its detection efficiency is increased

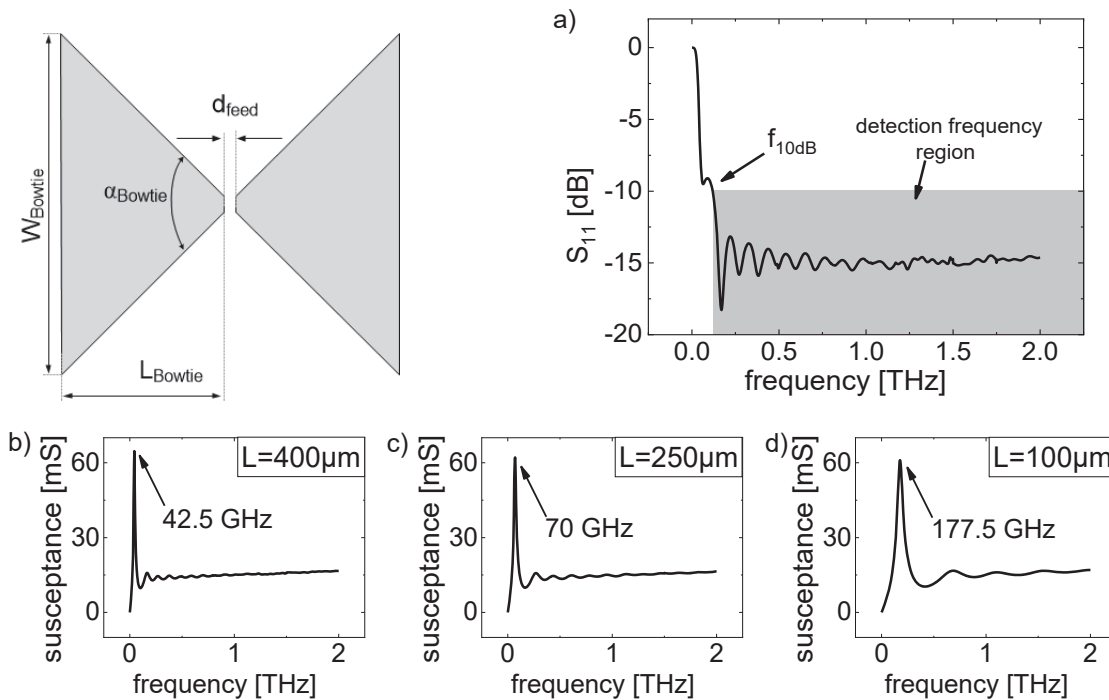


Figure 6.12: Schematic illustration of a bowtie antenna structure with its design parameters. a) Simulation of the scattering parameter of the device with a wing length of  $L_{\text{Bowtie}} = 400 \mu\text{m}$  is shown. b-d) The susceptance of a bowtie antenna at different wing length 100, 250, and 400  $\mu\text{m}$  illustrating the self-resonance of the antenna.

### 6.1.4 TBRTD integration within a bowtie antenna

The pure bowtie antenna is utilized to construct a broadband detector. Starting the detector investigation by integrating the equivalent circuit of the TBRTD (device F see chapter 0) into the circuit simulator with the equivalent circuit of the bowtie antenna with the arm length of  $400\ \mu\text{m}$  (see section 4.2.2). The equivalent circuit components setup used for simulation is similar to the one developed for the slot antenna detector, see Figure 6.10. The first simulation results are shown in Figure 6.13 (solid line). An HB simulation is carried out. As shown, a broadband detection capability in a large frequency range is given. A detection maximum at the lower frequency region is expected which is caused by the self-resonance of the bow antenna, i.e., inductive behavior, see Figure 6.12

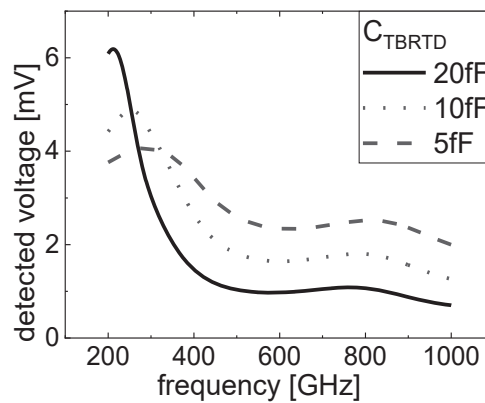


Figure 6.13: HB simulation results of the detected voltage at the TBRTD integrated into a broadband self-complementary antenna. Tuning the TBRTD area (device capacitance) to smaller effective area, improves the detection capability.

In the next step, the influence of the TBRTD area is investigated. Therefore, the equivalent circuit elements of the TBRTD are adjusted, as was shown in chapter 2.2.

The TBRTD area is decreased from  $3$  to  $1\ \mu\text{m}^2$ . The area reduction results in a capacitance reduction, which enhances the detection performance. This behavior is shown in Figure 6.13 (dashed lines). For a broadband detector up to the detection maximum of the device, a self-complementary antenna is the best choice due to its constant impedance, i.e., susceptance. The large detection bandwidth is, however, at the expense of the matching, and hence, maximum possible device responsivity cannot be reached over the whole detection frequency range.

## 6.2 Measurements and characterization

### 6.2.1 TBRTD-based oscillator

Biassing the TBRTD at the center of the NDR region yields an output signal oscillation at  $260\ \text{GHz}$ , see Figure 6.14. The measurement was carried out in pulsed mode with a lock-in

technique to suppress the surrounding noise. The pulse width and repetition rates are 0.3 ms and 300 Hz. As shown, good agreement between the circuit simulation of the oscillation frequency results is achieved.

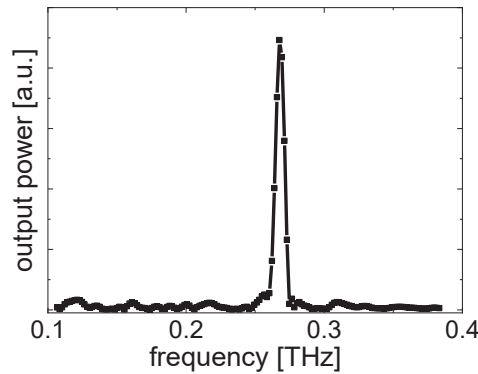


Figure 6.14: FTIR measurement results of a TBRTD-based slot antenna oscillator.

Higher harmonic signals were measured by suppressing the fundamental signal via placing a filter at the opening of the FTIR. Voltage-dependent harmonic signal power was measured, see Figure 6.15. Biasing the TBRTD near the peak or valley point, a stronger second harmonic was measured, while a stronger third harmonic was measured when biasing the TBRTD at the center of the NRD region (cf. Figure 6.15).

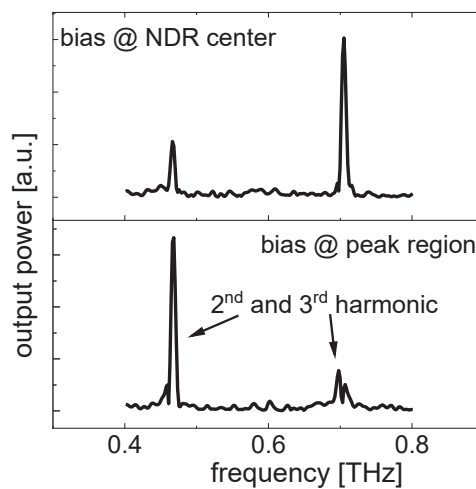


Figure 6.15: Measured harmonic signals of the TBRTD-based oscillator. Harmonic components are bias voltage-dependent.

This behavior is demonstrated and explained in the circuit simulation. To this end, HB simulation, on the equivalent circuit, was carried out. The current-voltage characteristics of the device are fitted, as presented in chapter 2.3. As shown in Figure 6.16, a third harmonic signal part is dominating the harmonic signals when biased at the center of the NDR region. Whereas, biasing the device near the peak or valley point, a stronger second harmonic is visible. This behavior is explainable due to the typical current-voltage characteristics in an

NDR region. For simplicity, in this simulation, the capacitance of the device was set constant, and hence, no frequency change over the bias voltage is visible.

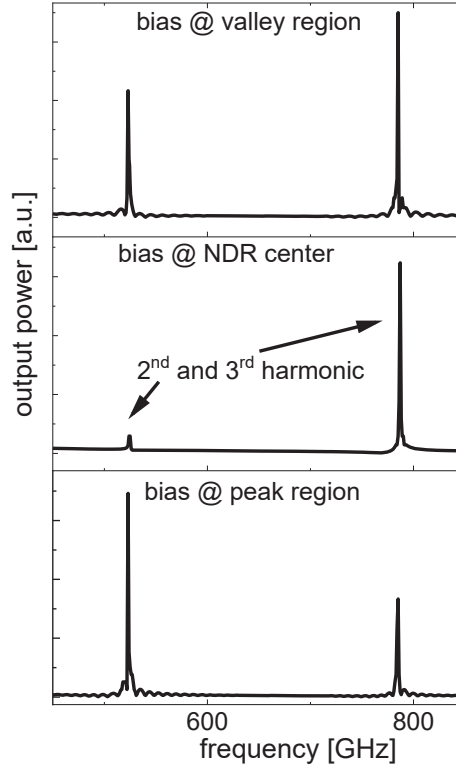


Figure 6.16: HB simulation of the harmonic signals of the TBRTD-based oscillation utilizing the equivalent circuit approach. A voltage-dependent harmonic component power is visible.

The corrected output power of  $92 \mu\text{W}$  was measured in the measurement setup shown in Figure 3.5. An internal DC-to-RF conversion efficiency, when neglecting the stabilization resistance, is around  $\eta_{\text{DC-RF}} \cong 1.5\%$ . For accurate output power simulation, the parasitic elements were included (see chapter 3). Slightly higher output power of  $141 \mu\text{W}$  was simulated in transient simulation of the extended equivalent circuit of the TBRTD and antenna, as presented in Figure 6.7a.

### 6.2.2 TBRTD-based zero-biased detector

To measure the detection capability of the TBRTD, a second measurement setup, as shown in Figure 3.6, is deployed. The output of a signal generator is focused with a THz lens onto a reflector, which reflects the wave toward the lens where the TBRTD is placed. Using DC probes, the voltage drop over the TBRTD is measured. The surrounding noise is minimized in a chopped measurement. In this work, the resonant detector contains a slot antenna, and the broadband detector contains a bowtie antenna. For the resonant detector characterization, a signal generator (*AMC-370* signal source from *VDI*) in the frequency

range from 265 to 297 GHz is used. The output signal of this generator is measured at different attenuation levels, with a power meter (*PM5*, *VDI*) as presented in Figure 6.17.

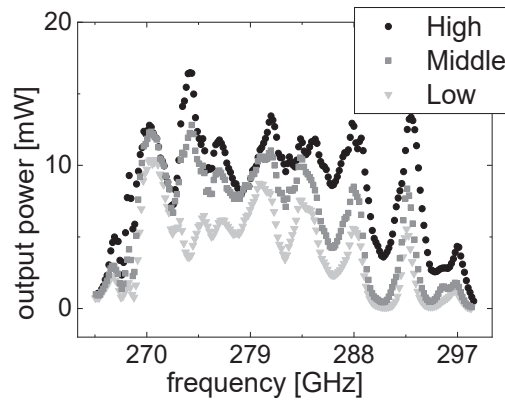


Figure 6.17: Measured output power over the frequency of the signal generator *AMC-370* at different attenuation levels. Measured by *PM5*, *VDI*.

The slot antenna presented as an oscillator in chapter 6.2.1 was operated in this section as a direct detector, by biasing the device at 0 volts. Then the device is irradiated with signals in the frequency range from 265 to 297 GHz and the voltage drop over the TBRTD is measured by a chopped lock-in amplifier. Maximum detection was measured at 280 GHz (see Figure 6.18). These measurements were carried out during my short-term scientific mission at the *Tokyo Institute of Technology*. No power calibration was carried out in this measurement setup, and therefore, no further detector parameters are determined. However, simulation results of this structure, which were done by Prof. Suzuki during his Mercator fellowship in our group are included in Appendix C, showing the capability of a very high responsivity of these devices. A simulated voltage responsivity of 50 kV/W is presented.

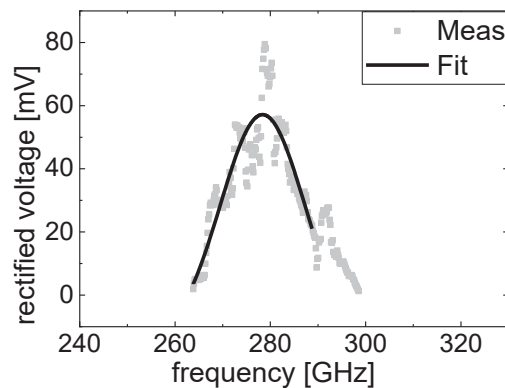


Figure 6.18: Measured rectified voltage over the TBRTD-based resonant detector. The quasi-optical measurement setup presented in chapter 3.3.3 is used.

In the next step, the TBRTD is integrated into a broadband antenna to increase its detection bandwidth. As presented in section 6.1.4, a self-complementary bowtie antenna is used. The measurement of the broadband antenna was done in the frequency range from 75 to 110

GHz by using the *R&S-Z110* extender, and from 220 to 330 GHz by the *R&S-ZC330* extender. To illustrate the broadband detection capability of the device, an uncalibrated measurement in both frequency ranges is carried out. As shown in Figure 6.19, the voltage drop over the diode was measured in both ranges, and hence a broadband detection capability is given.

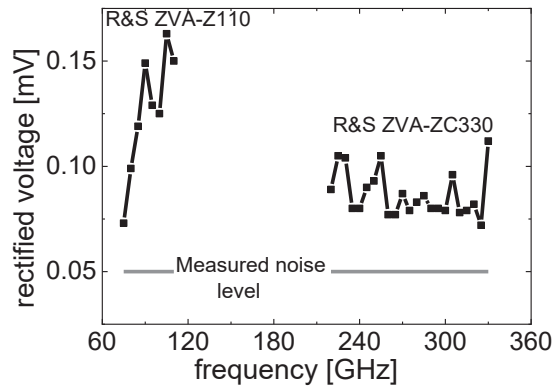


Figure 6.19: Power-uncalibrated measurement of the detected voltage over a wide frequency range of the TBRTD integrated into the self-complementary bowtie antenna.

Then, for accurate determination of the detector properties, the output power of the signal generator, including the beam path losses, is measured with an Erickson *PM5* calibrated detector (see Figure 6.20). The *PM5* is positioned as was presented in section 0. This measurement is used to power-calibrate the setup.

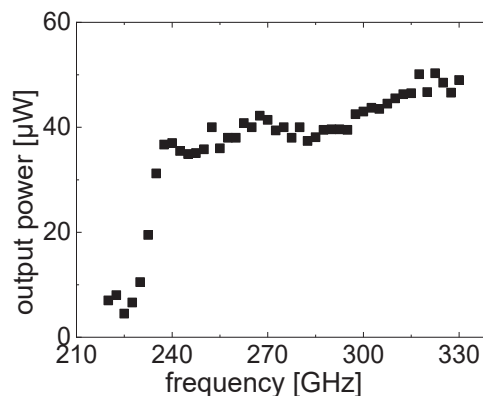


Figure 6.20: Measured output power of the frequency extender ZVA ZC330 from R&S®.

Then, to determine the responsivity of the device, the voltage drop over the device is measured while irradiating the device with the THz signal. The spot size of the irradiated beam is determined to  $7.323 \times 10^{-6} \text{ m}^2$ . An EM-simulation of the receiver antenna directivity with the Si-lens is carried out to determine the effective antenna area in the WR3 frequency range, i.e. from 220 to 330 GHz. Effective antenna size is simulated to  $198.1 \times 10^{-9} \text{ m}^2$ . This information is used to determine the exact power at the device. Further, 50% chopping period and the losses on the Si-lens surface (30% reflection) are included in the

determination. The measured responsivity is presented in Figure 6.21a. An average responsivity of  $2000 \text{ V}\cdot\text{W}^{-1}$  was determined. By integrating the real power over the frequency into the detector model a responsivity average of  $2100 \text{ V}\cdot\text{W}^{-1}$  was simulated. The determined *NEP* values are shown in Figure 6.21b. A minimum value of  $1 \text{ pW}\cdot\text{Hz}^{-0.5}$  is achieved.

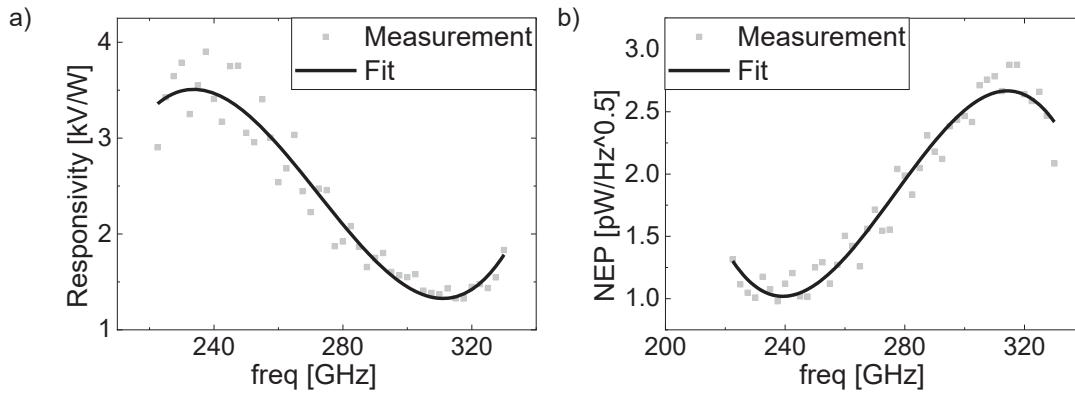


Figure 6.21: Determined responsivity and NEP of the TBRTD integrated into a self-complementary antenna. The quasi-optical measurement setup presented in chapter 3.3.3 is used.



---

## 7 Injection locking of a free running sub-THz oscillator

The investigations of the locking mechanism on a resonant tunneling based THz oscillator were carried out as part of my short-term scientific mission in the *Tokyo Institute of Technology* and the Mercator fellowship collaboration with Prof. Asada and Prof. Suzuki. This work aims to present a proof of concept for this novel method. Resonant tunneling diodes have been demonstrated to oscillate up to 2 THz [15] while operating at room temperature. The instability of the output signal in terms of oscillation frequency, and the fact that no phase control is given, make an array-based operation very challenging. To overcome this problem and to improve the oscillator performance and even to provide new array-based functionalities, an injection locking mechanism is investigated. As was presented in chapter 2.4, a subharmonic signal injection and fundamental locking are used.

In this chapter, first, the simulation of injection locking of a realistic fabricated and packaged RTD-based oscillator is carried out. The THz oscillator is a combination of an RTD integrated into a slot antenna which was designed for oscillation at 550 GHz. No modification for injection locking was implemented. The frequency locking range and performance of a subharmonic injected oscillator will be reported. Then, in the next section, the measurement setup and the deployed RTD will be introduced, followed by the measurement results and its comparison to the simulation results.

### 7.1 Simulation of subharmonic injection locking

Subharmonic injection locking was investigated with a DBRTD device provided to us by Profs. Asada and Suzuki from *Tokyo Institute of Technology*. The same configuration and setup could be used for a TBRTD. The DBRTD is integrated into a slot antenna of width and length of 4  $\mu\text{m}$  and 129  $\mu\text{m}$ , respectively, at the feeding position of 59.5  $\mu\text{m}$  from the center of the slot. This feeding position provided the best matching between the DBRTD and the antenna. A typical current-voltage characteristic of the DBRTD, without stabilization, is shown in Figure 7.1 (dotted line). A maximum current density of 35  $\text{kA}/\mu\text{m}^2$  with a *PVCR* of 2.3 and a peak and valley voltage of 0.39 V and 0.78 V, respectively, is demonstrated. The equivalent circuit of the setup used for the simulation of the locking mechanism is shown in Figure 7.1. For simplicity, the parasitic elements of the DBRTD are neglected, furthermore its capacitance is set to the constant value of  $C_{\text{RTD}} = 7.78$  fF. The current-voltage characteristic of the DBRTD is modeled using the fitting approach shown in equation (2.7) in chapter 2.2. A good agreement between the measured and simulated current-voltage characteristics (see Figure 7.1 solid line) is achieved in the region of interest with the following fitting parameters  $a = 41.1 \cdot 10^{-3} \text{ A} \cdot \text{V}^{-1}$  and  $b = 343.8 \cdot 10^{-3} \text{ A} \cdot \text{V}^{-3}$ . The injected signal source is connected serially to the antenna, to include its detection properties. The antenna

is integrated into the circuit simulation via its scattering parameters. These parameters are retrieved from field simulations (HFSS simulation<sup>6</sup>) of the same antenna structure.

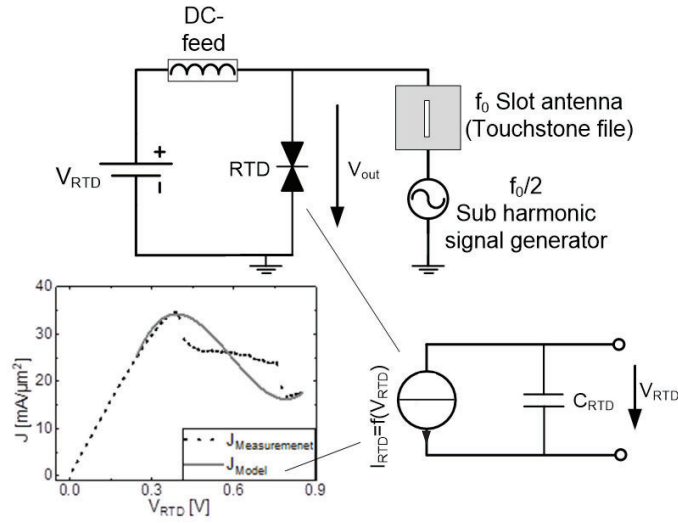


Figure 7.1: Block diagram for circuit simulation of the locking of a free-running oscillator. The slot antenna is integrated using scattering parameters from field simulations. The large-signal RTD equivalent circuit is represented by voltage-controlled current source and constant RTD capacitance for simplicity.

As was mentioned in chapter 2.4, the wireless locking mechanism consists of three steps: First, the injected signal at  $\frac{f_0}{n}$  is detected in the  $f_0$  system. Second, the signal is multiplied by the non-linearity of the current-voltage characteristics up to  $f_0$ , this multiplied signal locks then the free-running oscillator. In this section, the steps of the locking process are investigated separately. In this work, a system designed for  $f_0$  oscillation is used; no further enhancement for  $\frac{f_0}{n}$  detection was carried out. Hence, only a small fraction of the injected signal will arrive at the RTD oscillator, which can be optimized by including suitable antenna-in-antenna structures and should be investigated in the future.

The injection locking simulation is starting with HB simulation to determine the multiplication efficiency of the RTD. For this purpose, the antenna is replaced by a short circuit. Shortening of the antenna is required because the signal multiplication is an internal process within the RTD. A signal is injected into the oscillator while varying the biasing point of the RTD within the NDR region, and recording the power of the multiplied signal (cf. Figure 7.2). Biasing the RTD at the center of the NDR shows damping of around 52 dB for the multiplied signal compared to the amplitude of the fundamental signal. This behavior is attributed to the shape of the current-voltage characteristics in the NDR region.

<sup>6</sup> HFSS simulation of the slot antenna are carried out within the collaboration with the *Tokyo Institute of Technology* and were puten at our disposal in form of scattering parameters for circuit simulation

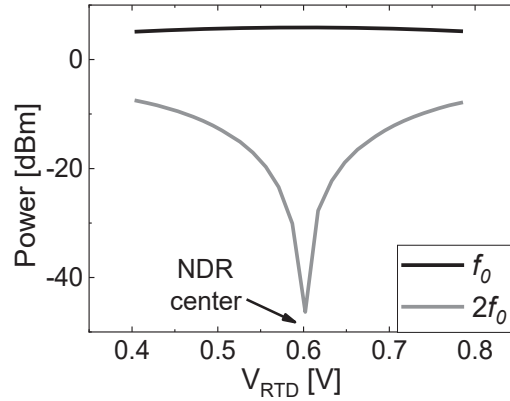


Figure 7.2: HB simulation results of the output power of the doubled signal as a function of biasing point in the NDR region of the RTD

Next, the antenna is reconnected to the DBRTD model, as shown in Figure 7.1. To use the strongest locking signal power, i.e., the multiplied signal, the RTD is biased at  $V_{\text{RTD}} = 0.45$  V. At this bias point, a free-running oscillation is observed at  $f_0 = 560$  GHz (cf. Figure 7.3). Then, a signal with a power of  $-19$  dBm, oscillating at  $f_{\text{inj}} \sim \frac{f_0}{2}$  slightly offset from  $\frac{f_0}{2}$  is injected from the subharmonic signal-generator into the oscillator. This signal is multiplied by the non-linearity of the RTD and results in a locking signal power of  $-2.31$  dBm, which provides a signal power ratio of 4.9 between the free-running signal power and the locking signal power at a frequency offset of 1.1 GHz between both signals. After locking, a frequency shift is visible, as shown in Figure 7.3; furthermore, oscillators synchronization (frequency shift) is visible within the simulation results.

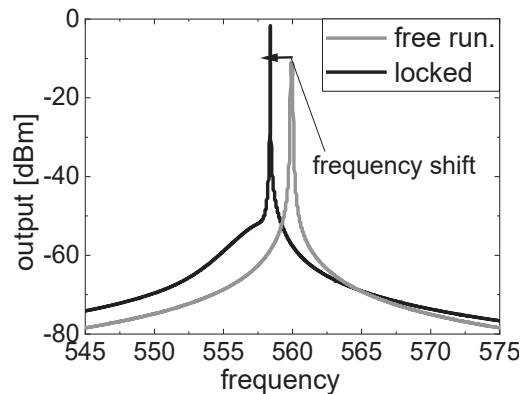


Figure 7.3: Simulated output spectrum of the free running oscillator without locking signals and after locking.

The locking range of the oscillator is investigated by injecting a signal with a frequency that provides a locking signal frequency slightly lower than the frequency of the locking edge. Then, the injected signal frequency is stepwise increased toward the free-running signal frequency. As shown in Figure 7.4 at a particular frequency ( $f_{\text{inj}} = 276$  GHz), the pulling region starts. In this region, the oscillation frequency is decreasing while increasing the

injection signal frequency, i.e., the locking signal frequency. The pulling region ends at the first locking edge ( $f_0 = 556.87$  GHz). The simulated locking range amounts to  $\Delta f_{\text{locking}} = 2.42$  GHz. A second pulling range is visible at the end of the locking range.

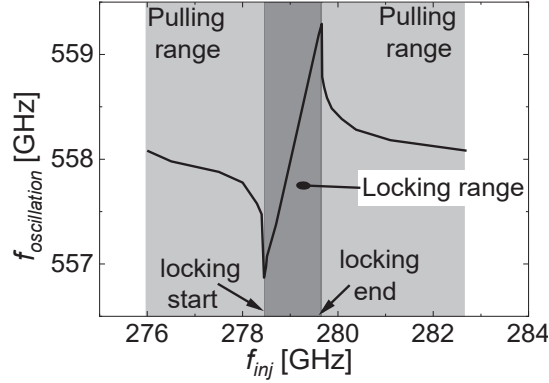


Figure 7.4: Simulated oscillation frequency dependency over the injected signal frequency illustrating the locking range and both locking edges surrounding the locking range.

As was shown numerically in chapter 2.4, when locking a free-running oscillator, i.e., fulfilling Adler's locking condition [61], then no phase change over time is given. The width of the locking range is proportional to the injected power  $P_{\text{in}}$  over the square root of the free-running signal power. The phase change compared between the free-running signal oscillator and the locking signal, i.e., the multiplied signal is between  $\frac{\pi}{2}$  to  $\frac{3\pi}{2}$ , i.e., a phase shift of one  $\pi$  is given.

## 7.2 First experimental proof of concept for subharmonic injection locking

For the proof of concept of the subharmonic injection locking a DBRTD is deployed. The DBRTD-based oscillator is packaged in a quasi-optical arrangement, as shown in Figure 7.5. The oscillator is placed on a Si-hemispherical lens, which collects the output beam at the bottom side of the InP substrate. For DC biasing, the RTD device is wire-bonded to the biasing lines. A typical current-voltage characteristic of the used RTD, without stabilization, is shown in the inset of Figure 7.1. A maximum current density of  $35 \text{ kA}/\mu\text{m}^2$  with a *PVCR* of 2.3 and peak- and valley- voltages of 0.39 V and 0.78 V, respectively, are demonstrated. Biasing the oscillator in different points in the NDR region tunes the oscillation frequency due to the voltage-dependent impedance of the DBRTD, and due to the mismatching, different output power levels were measured (see Figure 7.6c).

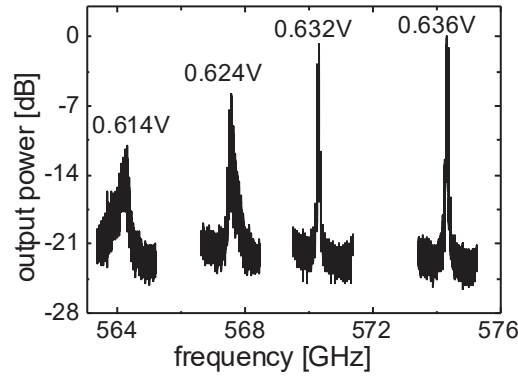


Figure 7.5: Measurement of the output power of the RTD-based resonant antenna oscillating at different bias points, illustrating the frequency and output power dependency over the voltage.

The measurement-setup and its schematic representation for wireless injection and fundamental locking of the free-running oscillator are shown in Figure 7.6a-b. The free-running oscillator is placed at the front side of a signal generator (*AMC-370*, *VDI*), which is connected to a WR3 horn antenna, providing the wireless injected subharmonic signal. The output power over the frequency of the signal generator was measured using a power-meter (*PM5*, *VDI*) and is presented in Figure 7.6c. As shown, a strong variation of the output power over the frequency does exist. At the front side of the free-running oscillator, a heterodyne mixer (*N9029AV*, *VDI*) is placed. The conversion loss of this device is typically around 20 dB. To improve the phase noise, a Low Noise Amplifier (LNA: *BZR-P011800*, *B&Z*) is placed between the mixer and the spectrum analyzer. A typical gain of this LNA is around 38 dB.

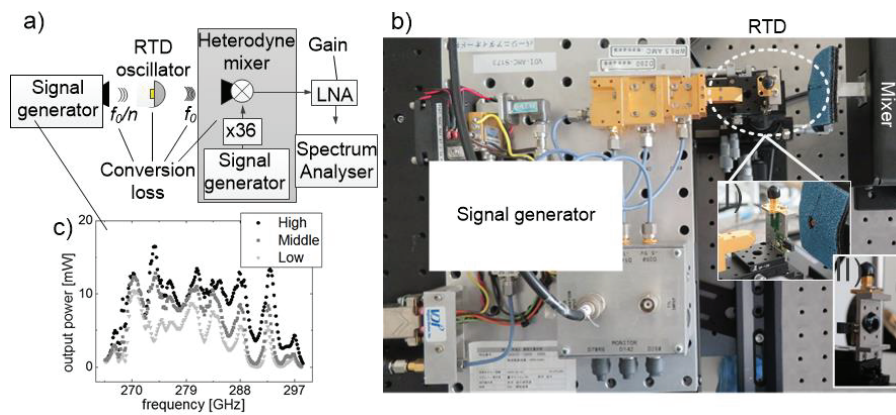


Figure 7.6: a) Schematic and b) a picture of the measurement setup for injection locking investigation. c) the output power of the signal generator is illustrated

To start the locking mechanism investigation, the doubling efficiency of the DBRTD is measured. A quantitative determination of the doubled signal (locking signal) power over the biasing point of the DBRTD in the NDR region is obtained by injecting a signal at a constant frequency of  $f_{inj} = 293$  GHz and tuning the bias point within the NDR region while

recording the power of the doubled signal (i.e., locking signal) at  $f_0 = 586$  GHz. As shown in Figure 7.7, strong attenuation occurs when biasing the RTD at the center of the NDR region. Higher doubling efficiency is observed when biased in the peak or valley regions. Furthermore, good agreement is achieved between the measured and theoretical simulated curve in section 7.1. From the measurement presented in Figure 7.7, biasing the oscillator near the peak or valley point will provide a stronger locked signal when injecting a signal oscillating at  $\frac{f_0}{2}$ .

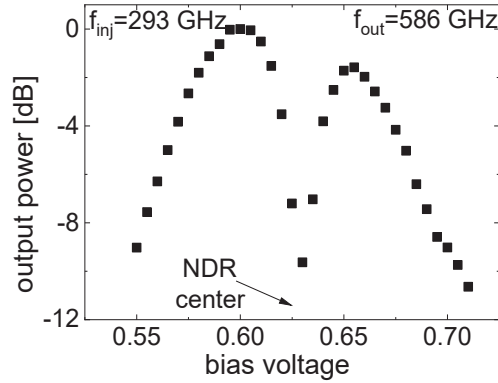


Figure 7.7: Measured doubled signal of the RTD-based oscillator. The frequency of the wireless injected signal is at 293 GHz, and the radiated doubled signal is at  $2 \cdot 293 \text{ GHz} = 586$  GHz. Biasing at the center of the NDR provides the minimum locking signal.

The first experimental proof of concept for frequency locking of a free-running NDR-based THz oscillator is carried out with the maximum locking signal power. During the following measurement, the device is biased at the point in the NDR region, providing the maximum doubled signal. In the next step, the locking range is investigated. A signal oscillating around  $f_{inj} \sim \frac{f_0}{2}$  is wirelessly injected into the system. As shown in Figure 7.8a, in the spectral analysis, two peaks are visible. Then the frequency of the injected signal is stepwise increased (Figure 7.8b) until locking is observed (Figure 7.8c). This point is defined as a locking-start. Further increase of the injected signal frequency shifts the oscillation frequency continuously until arriving at the second locking-edge. Under the locking-condition, the injected signal properties are transformed onto the free-running signal in terms of signal purity and signal stability. In this approach, a locking range of 2 GHz was measured, which shows good agreement with the simulated locking range of 2.42 GHz, as presented in section 7.2. Additional agreement between the measured data and Adler's locking theory is given when considering the numerical investigation presented in chapter 2.4. Inserting the parameters of this oscillator, namely the oscillator's free-running output power  $P_{out, free-running} = 16 \mu\text{W}$  when biased at 0.05 V from the NDR center toward the peak point, an injected power of  $P_{inj} = 20 \text{ mW}$ , an unloaded quality factor of the resonator  $Q = 30$ , and considering back-side irradiation, i.e., an inefficient air-antenna interface, where only 9% of the injected signal is arriving at the RTD, a locking range of 1.8 GHz is calculated. The small deviation between

the circuit simulation, numerical calculation and the measurements results can be explained by the error in estimation of the power arriving at the RTD: only one air-antenna interface is considered, not including reflection within the lens which could increase the power arriving at the RTD.

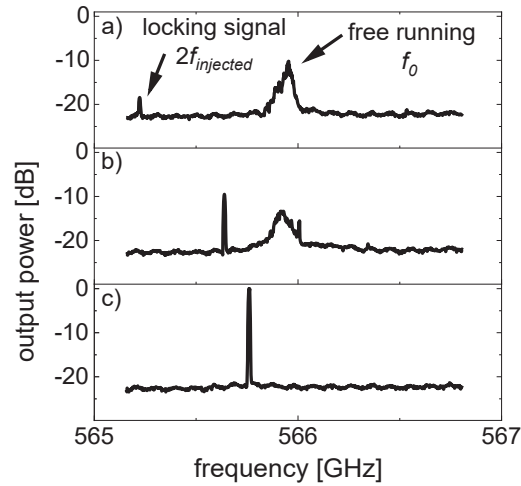


Figure 7.8: Illustration of the locking process. a) Lockin signal frequency has a slight offset from  $f_0/2$ . b) Increasing the frequency of the locking signal. Locking sidebands start appearing. c) Locking condition is fulfilled at locking start frequency.

As a next step, the locking range dependency over the bias point was investigated. As shown in Figure 7.9, the locking range decreases when tuning the bias point, indicating a weaker locking signal (cf. Figure 7.7). Furthermore, biasing the DBRTD at the center of the NDR region raises the free-running signal power, which decreases the locking range as well [61] (cf. Figure 7.5). Then, the locking range dependency over the injected power, at a fixed biasing point  $V_{\text{RTD}} = 0.62 \text{ V}$ , is presented. A locking range between 809 and 1075 MHz is measured with an almost linear dependency, which shows good agreement with Adler's equation [61].

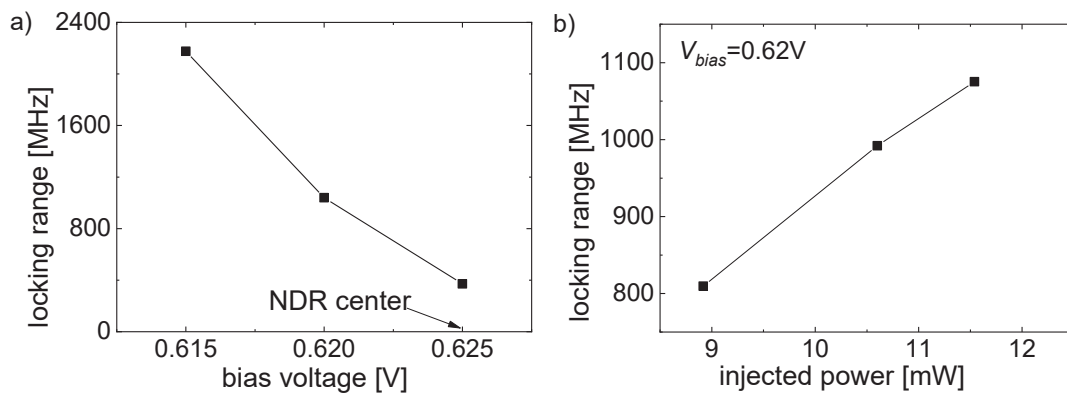


Figure 7.9: Determination of the locking range, a) vs. the bias voltage and b) vs. the injected power.

As was shown in section 7.1, outside the locking range, pushing and pulling regions are expected. These regions are challenging to measure due to the spurious oscillation of the free-running signal. Nevertheless, this behavior is partly presented in Figure 7.10, where a constant frequency signal within the locking range is injected with low power (Figure 7.10a). The injected power is then stepwise increased (Figure 7.10b-e). It is obvious that at a specific power, the locking condition is fulfilled, and the signals are locked (Figure 7.10e). Before this point, a pulling/pushing behavior is visible, with a shift in the oscillation frequency. Furthermore, before locking, sidebands become visible, which is expected from theory when locking strength is low [121]

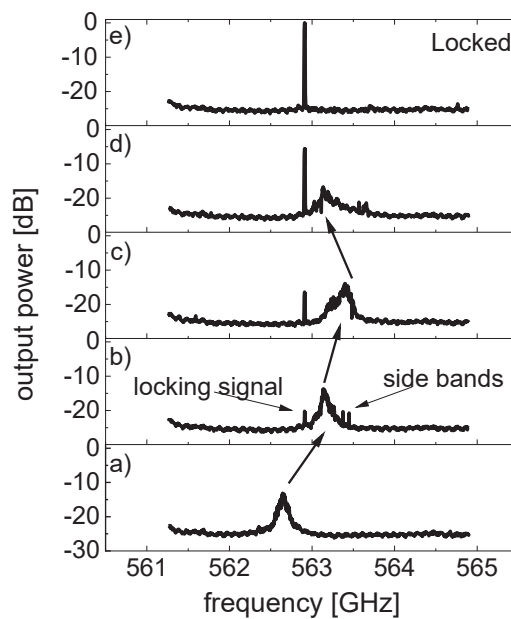


Figure 7.10: Illustration of the injection locking mechanism by presenting the signal push and pull. The injected signal power is increased step-by-step. At b) and d) the locking sidebands are visible. At b) the locking signal peak is at the left of the free-running signal, which is shifted to higher frequency.

Locking the free-running signal with a low noise signal source improves its spectral linewidth [121]. This behavior is shown in Figure 7.11. The free-running signal is adopting the signal properties of the locking signal also in terms of signal purity. To quantify the signal purity enhancement, the peak's Full-Width at Half-Maximum (FWHM) is investigated. An *FWHM* value of the free-running oscillator of 34.69 MHz was determined before locking. After locking an *FWHM* value of 483 Hz was achieved at  $f_0 > 565$  GHz. Which corresponds to a calculated [122], single-sideband phase noise value improvement from -78.6 dBc/Hz to -121 dBc/Hz, at an offset frequency of 10 MHz.

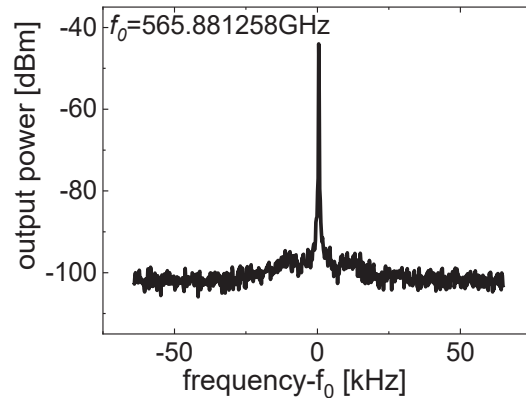


Figure 7.11: Close lookup of the locked output signal. A resolution-bandwidth (RBW) of 100 Hz is set.

The presented subharmonic injection locking method shows good agreement between the measured, the simulated, and the numerically determined data, as well as the theory presented by Adler [61], which confirms the successful locking of a THz oscillator.

Furthermore, Adler's equation claims that within the locking range, the phase relation between the locking signal and the free-running signal remains constant. This indicates phase control of the output signal within the locking range. Tuning the frequency of the locking signal tunes the output signal frequency. Tuning the phase of the locking signal will tune the phase of the output signal (Adler's equation [61]). But how is the change when tuning the frequency of the free-running signal? To investigate this, the bias point of the TBRTD is slightly tuned to tune the oscillation frequency (see Figure 7.5) while keeping the generated signal oscillation frequency within the locking range. After locking, tuning the bias point, while keeping the generated signal frequency within the locking range, didn't alter the oscillation frequency. Conversely, this must lead to a relative phase change of the output signal. Integrating this method in an oscillator array, beam-steering of a multi-element THz oscillator becomes possible. Furthermore, when phase control is given, the spatial output power combination of oscillator elements in an array, all oscillating at one frequency, becomes possible, i.e., output power levels at THz frequencies beyond mW should be attainable.



---

## 8 Summary and Outlook

The aim of this thesis is to add new and novel functionalities to contribute to the efficient filling of the THz-gap with the focus on mobile and battery-operated devices. For this purpose, the TBRTD is investigated. This thesis comprehends the tuning of the TBRTD epitaxial layer design, and the optimizing of its fabrication process, providing an ultra-high-speed device with a wide NDR region in the forward direction and current blocking behavior in the reverse direction. Depending on the bias point, this device can be used for both operation modes, signal generation and detection. The monolithic integration into on-chip resonant- and broadband- antennae for free space operation is elaborated. Furthermore, for coherent signal generation, the phase and frequency control of a single free running oscillator are required. This is achieved by a new method via subharmonic injection locking.

The first step in this work was the enhancement of the maximum current density of the TBRTD. The current density provides the first estimation of the high-frequency operation capability of the device. The current density enhancement is realized by adjusting the internal part of the TBRTD, using a charge transport model. The new design decreased the internal time constants and hence, increased the current density due to the enhancement of the discrete energy level coupling at resonance. A current density improvement from 230 to 900 kA/cm<sup>2</sup> is achieved.

For circuit simulation, a large- and small-signal equivalent circuit is developed. To this end, a DBRTD analytical model was enhanced and extended for the TBRTD structure. This model was then used to describe the equivalent circuit elements. To feed the models with data, on-wafer DC and scattering-parameter measurements were performed. Good agreement between the modeled and measured data is achieved. The new devices show low area capacitance  $C_{\text{TBRTD}}$  of 5-8 fF/ $\mu\text{m}^2$ .

For free-space operation, the TBRTD integration into an antenna is investigated. For the oscillator and resonant detector, the slot antenna is employed, and for broadband detection, the self-complementary bowtie antenna. The antenna design is carried out in different EM-simulators to confirm the results. Matching the TBRTD to the antenna is executed then in a circuit simulator. For this purpose, small-signal equivalent circuits for the antennae were developed. By fitting the equivalent circuit elements to the EM-simulation results, the antenna is characterized. This approach provides a proper estimation of the oscillation frequency. The first design of the TBRTD/slot antenna was implemented for operation at 260 GHz. The TBRTD integration into the bowtie antenna is designed for broadband operation.

Then, the fabrication process for monolithic integration of the TBRTD into an antenna is investigated and successfully developed for THz operation. The main fabrication challenges and their solutions are discussed and presented. The fabricated devices are characterized in

quasi-optical measurement setups, assembled during this work. Biasing the TBRTD/slot antenna device, in the NDR region, a signal with oscillation frequency at  $\sim 260$  GHz was measured with a corrected output power of  $92 \mu\text{W}$  leading to a competitive internal DC-to-RF conversion efficiency of  $\eta_{\text{DC-RF}} \cong 1.5\%$ , when neglecting the current flowing over the stabilization resistance. The detector side of the device also shows promising data as a zero-bias rectifier. The simulation of the resonant detector with a TBRTD device showed a responsivity of over  $50 \text{ kV/W}$ . The power-uncalibrated measurement showed detection capability and a maximum peak at  $280 \text{ GHz}$ . Good agreement between the simulated and measured resonance frequency is given. The shift of the resonance frequency between the oscillator operation and the detection is caused by the voltage dependence of the impedance of the TBRTD. The integration of the TBRTD in a broadband bowtie is at the expense of the responsivity. The broadband detection capability was shown in a power-uncalibrated measurement, where its detection capability in the frequency bands between  $75$  to  $110 \text{ GHz}$  and  $210$  to  $330 \text{ GHz}$  was demonstrated. A power-calibrated measurement showed internal responsivity with an average of  $2000 \text{ V/W}$  in the frequency range between  $210$  and  $330 \text{ GHz}$ . A determined internal *NEP* minimum of  $\frac{1 \text{ pW}}{\sqrt{\text{Hz}}}$  is achieved. The responsivity values are comparable to a Schottky-diode rectifier connected with a WR3.4 flange [123] with  $1500 \text{ V/W}$  (without antenna integration).

To provide coherent fundamental oscillators, the subharmonic injection locking mechanism is developed in this work. An efficient solution to circumvent the lack of isolation in a two-terminal device is given with wirelessly injecting the subharmonic locking signal into the oscillator. The wireless injection concept is well suited for compact heterogeneous integration in arrayed configurations. Circuit simulation could precisely predict the behavior of the locking mechanism. Furthermore, in this work, the first experimental proof-of-concept for subharmonic injection locking of an RTD-based oscillator in the THz frequency range is reported at  $f_0 = 550 \text{ GHz}$ . The used oscillator system, consisting of an RTD integrated into a slot antenna, was not modified for the injection locking experiment. Hence, only a small amount of the injected signal was detected and converted for locking. Nevertheless, a locking range of two GHz was determined in this experiment. Analytical analysis of the method shows that a phase shift of one  $\pi$  is given in this locking range. The *FWHM* of the output signal is improved from  $34.69 \text{ MHz}$  to  $483 \text{ Hz}$ , where the locked linewidth was determined by the phase noise of the locking signal source.

## Outlook

As presented, the TBRTD is a promising device for signal generation and detection and is well suited to provide a wideband solution for efficient and mobile THz devices. The low capacitance and high current densities presented here indicate well that the operation frequency limit is still not achieved. Furthermore, its high responsivity and low *NEP* values also in a broadband approach show its potential for further contributions in the THz range.

---

During this work, the basis for TBRTD THz oscillators and highly sensitive detectors is established. The working flow, starting with single device design, its modeling, integrating into an antenna and its characterization is adopted and improved. Using this technique, higher frequencies will be achievable by a simple modification of the slot antenna length, which reduces the inductive part of the resonator. Further improvement smaller area devices, for example via the developed CNP process, will lead to higher cutoff frequencies. Regarding the detector, adjusting the design, according to the presented charge transport model, a higher responsivity is achievable. A further interesting and promising investigation-field is at the subsystem-level, where matching network between the TBRTD and the antenna can be investigated. A TBRTD-pair can provide further improvement for differential oscillator operation. The non-linear properties of the TBRTD for mixer operation can provide very interesting results and facilitate efficient THz mixers, both as an injection-locked and a self-heterodyne mixer.

The introduced proof of concept for wireless locking mechanism decouples the locking master signal from the RTD oscillator, thus enabling architecture of phase-coupled RTD oscillator cores suitable for power-scalable integrated THz transmitter arrays. Controlling the phase of single elements in an array, THz beam steering becomes possible. Utilizing one lower-frequency subharmonic master signal facilitates its distribution to control and lock the arrayed THz-source.



---

## 9 References

- [1] T. Kleine-Ostmann, K. Pierz, G. Hein, P. Dawson, M. Koch, "Audio signal transmission over THz communication channel using semiconductor modulator", *Electronics Letters*, Vol. 40, No. 2, p. 124, 2004.
- [2] C. M. Mann, "Towards Terahertz Communications Systems", R. E. Miles, P. Harrison, D. Lippens (Eds.), *Terahertz Sources and Systems*, Springer, Dordrecht, pp. 261–267, 2001.
- [3] J. Federici, B. Schulkin, F. Huang, D. Gary, R. Barat, F. Oliveira, D. Zimdars, "THz imaging and sensing for security applications—explosives, weapons and drugs", *Chemical Physics Letters*, Vol. 20, No. 7, S266-S280, 2005.
- [4] H. Liu, Y. Chen, Y. Deng, D. Schauki, M. J. Fitch, R. Osiander, C. Dodson, J. B. Spicer, M. Shur, X.-C. Zhang, "THz spectroscopic investigation of 2,4-dinitrotoluene", *Chemical Physics Letters*, Vol. 400, 4-6, pp. 357–361, 2004.
- [5] R. H. Clothier, N. Bourne, "Effects of THz Exposure on Human Primary Keratinocyte Differentiation and Viability", *Journal of biological physics*, Vol. 29, 2-3, pp. 179–185, 2003.
- [6] T. Löffler, K. Siebert, S. Czasch, T. Bauer, H. G. Roskos, "Visualization and classification in biomedical terahertz pulsed imaging", *Physics in medicine and biology*, Vol. 47, No. 21, pp. 3847–3852, 2002.
- [7] M. R. Scarfì, M. Romanò, R. Di Pietro, O. Zeni, A. Doria, G. P. Gallerano, E. Giovenale, G. Messina, A. Lai, G. Campurra, D. Coniglio, M. D'Arienzo, "THz Exposure of Whole Blood for the Study of Biological Effects on Human Lymphocytes", *Journal of biological physics*, Vol. 29, No. 2, pp. 171–176, 2003.
- [8] A. M. Melo, M. A. P. Toledo, F. C. B. Maia, A. Rocha, M. B. Plotegher, D. Pereira, F. C. Cruz, "Imaging at 0.2 and 2.5 terahertz", In *Terahertz, RF, Millimeter, and Submillimeter-Wave Technology and Applications VI*, SPIE OPTO, San Francisco, California, USA, 2 Feb., SPIE, 86240E, 2013.
- [9] A. Valavanis, Jingxuan Zhu, J. Freeman, Lianhe Li, Li Chen, A. G. Davies, E. H. Linfield, P. Dean, "Terahertz quantum cascade lasers with >1 W output powers", *Electronics Letters*, Vol. 50, No. 4, pp. 309–311, 2014.
- [10] I. Amenabar, F. Lopez, A. Mendikute, "In Introductory Review to THz Non-Destructive Testing of Composite Mater", *J Infrared Milli Terahz Waves*, Vol. 34, No. 2, pp. 152–169, 2013.
- [11] G.Kh. Kitaeva, "Terahertz generation by means of optical lasers", *Laser Physics Letters*, Vol. 5, No. 8, pp. 559–576, 2008.

- 
- [12] A. G. Davies, E. H. Linfield, M. B. Johnston, "The development of terahertz sources and their applications", *Physics in medicine and biology*, Vol. 47, No. 21, pp. 3679–3689, 2002.
- [13] H. Eisele, "480 GHz oscillator with an InP Gunn device", *Electronics Letters*, Vol. 46, No. 6, p. 422, 2010.
- [14] H. Eisele, "State of the art and future of electronic sources at terahertz frequencies", *Electronics Letters*, Vol. 46, No. 26, S8, 2010.
- [15] R. Izumi, S. Suzuki, M. Asada (Eds.), "1.98 THz resonant-tunneling-diode oscillator with reduced conduction loss by thick antenna electrode", *42nd Int. Conf. on Infrared, Millimeter, and Terahertz Waves*, 2017.
- [16] M. Hossain, N. Weimann, V. Krozer, W. Heinrich, "A 315 GHz reflection-type push-push oscillator in InP-DHBT technology", *European Microwave Conference, IEEE Antennas and Propagation Society et al.* 2016, 485–488, 2016.
- [17] M. Hossain, N. Weimann, O. Krueger, V. Krozer, W. Heinrich, "A 270 GHz push-push oscillator in InP-DHBT-on-BiCMOS technology", *European Microwave Conference EuMC*, 588–591, 2014.
- [18] A. Fox, B. Heinemann, H. Rucker, R. Barth, G. G. Fischer, C. Wipf, S. Marschmeyer, K. Aufinger, J. Bock, S. Boguth, H. Knapp, R. Lachner, W. Liebl, D. Manger, T. F. Meister, A. Pribil, J. Wursthorn, "Advanced Heterojunction Bipolar Transistor for Half-THz SiGe BiCMOS Technology", *IEEE Electron Device Lett.*, Vol. 36, No. 7, pp. 642–644, 2015.
- [19] X. Mei, W. Yoshida, M. Lange, J. Lee, J. Zhou, P. Liu, K. Leong, A. Zamora, J. Padilla, S. Sarkozy, R. Lai, W. R. Deal, "First Demonstration of Amplification at 1 THz Using 25-nm InP High Electron Mobility Transistor Process", *IEEE Electron Device Lett.*, Vol. 36, No. 4, pp. 327–329, 2015.
- [20] M. Schroter, T. Rosenbaum, P. Chevalier, B. Heinemann, S. P. Voinigescu, E. Preisler, J. Bock, A. Mukherjee, "SiGe HBT Technology: Future Trends and TCAD-Based Roadmap", *Proc. IEEE*, Vol. 105, No. 6, pp. 1068–1086, 2017.
- [21] M. Urteaga, Z. Griffith, M. Seo, J. Hacker, M. J. W. Rodwell, "InP HBT Technologies for THz Integrated Circuits", *Proc. IEEE*, Vol. 105, No. 6, pp. 1051–1067, 2017.
- [22] T. W. Crowe, "GaAs Schottky barrier mixer diodes for the frequency range 1–10 THz", *Int. J. of Infrared and Millimeter Waves*, Vol. 10, No. 7, pp. 765–777, 1989.
- [23] E. Kollberg, A. Rydberg, "Quantum-barrier-varactor diodes for high-efficiency millimetre-wave multipliers", *Electron. Lett.*, Vol. 25, No. 25, p. 1696, 1989.

- 
- [24] F. Maiwald, S. Martin, J. Bruston, A. Maestrini, T. Crawford, P. H. Siegel, "2.7 THz waveguide tripler using monolithic membrane diodes", *IEEE Microwave Theory and Techniques*, 1637–1640, 2001.
- [25] Ryunosuke Izumi, Takumi Sato, Safumi Suzuki, Masahiro Asada, "Resonant-tunneling-diode terahertz oscillator with a cylindrical cavity for high-frequency oscillation", *AIP Advances*, Vol. 9, No. 8, p. 85020, 2019.
- [26] M. Feiginov, C. Sydlo, O. Cojocari, P. Meissner, "Resonant-tunnelling-diode oscillators operating at frequencies above 1.1 THz", *Appl. Phys. Lett.*, Vol. 99, No. 23, p. 233506, 2011.
- [27] S. Suzuki, M. Asada, A. Teranishi, H. Sugiyama, H. Yokoyama, "Fundamental oscillation of resonant tunneling diodes above 1 THz at room temperature", *Appl. Phys. Lett.*, Vol. 97, No. 24, p. 242102, 2010.
- [28] H. Kanaya, R. Sogabe, T. Maekawa, S. Suzuki, M. Asada, "Fundamental Oscillation up to 1.42 THz in Resonant Tunneling Diodes by Optimized Collector Spacer Thickness", *J. Infrared Milli. Terahz. Waves*, Vol. 35, No. 5, pp. 425–431, 2014.
- [29] S. Javalagi, V. Reddy, K. Gullapalli, D. Neikirk, "High efficiency microwave diode oscillators", *Electron. Lett.*, Vol. 28, No. 18, p. 1699, 1992.
- [30] R. Tsu, L. Esaki, "Tunneling in a finite superlattice", *Appl. Phys. Lett.*, Vol. 22, No. 11, pp. 562–564, 1973.
- [31] L. L. Chang, L. Esaki, R. Tsu, "Resonant tunneling in semiconductor double barriers", *Appl. Phys. Lett.*, Vol. 24, No. 12, pp. 593–595, 1974.
- [32] E. R. Brown, J. R. Söderström, C. D. Parker, L. J. Mahoney, K. M. Molvar, T. C. McGill, "Oscillations up to 712 GHz in InAs/AlSb resonant-tunneling diodes", *Appl. Phys. Lett.*, Vol. 58, No. 20, pp. 2291–2293, 1991.
- [33] R. Sekiguchi, Y. Koyama, T. Ouchi, "Subterahertz oscillations from triple-barrier resonant tunneling diodes with integrated patch antennas", *Appl. Phys. Lett.*, Vol. 96, No. 6, p. 62115, 2010.
- [34] K. Kasagi, S. Suzuki, M. Asada, "Large-scale array of resonant-tunneling-diode terahertz oscillators for high output power at 1 THz", *J. of Appl. Phys.*, Vol. 125, No. 15, p. 151601, 2019.
- [35] N. Orihashi, S. Suzuki, M. Asada, "One THz harmonic oscillation of resonant tunneling diodes", *Appl. Phys. Lett.*, Vol. 87, No. 23, p. 233501, 2005.
- [36] M. Asada, S. Suzuki, and N. Kishimoto, "Resonant Tunneling Diodes for Sub-Terahertz and Terahertz Oscillators", *Jpn. J. of Appl. Phys.*, Vol. 47. No. 6, pp. 4375–4384, 2008.

- 
- [37] M. Feiginov, H. Kanaya, S. Suzuki, M. Asada, "Operation of resonant-tunneling diodes with strong back injection from the collector at frequencies up to 1.46 THz", *Appl. Phys. Lett.*, Vol. 104, No. 24, p. 243509, 2014.
- [38] T. Maekawa, H. Kanaya, S. Suzuki, M. Asada, "Oscillation up to 1.92 THz in resonant tunneling diode by reduced conduction loss", *Appl. Phys. Express*, Vol. 9, No. 2, p. 24101, 2016.
- [39] M. Suhara, S. Takahagi, K. Asakawa, T. Okazaki, M. Nakamura, S. Yamashita, Y. Itagaki, M. Saito, A. Tchegho, G. Keller, A. Poloczek, W. Prost, F.J. Tegude, "Analysis of terahertz zero bias detectors by using a triple-barrier resonant tunneling diode integrated with a self-complementary bow-tie antenna", 70th (DRC), University Park, PA, USA, IEEE, pp. 77–78, 2012.
- [40] F. J. González, M. A. Gritz, C. Fumeaux, G. D. Boreman, "Two Dimensional Array of Antenna-Coupled Microbolometers", *Int. J. of Infrared and Millimeter Waves*, Vol. 23, No. 5, pp. 785–797, 2002.
- [41] E. R. Brown, A. C. Young, J. Zimmerman, H. Kazerni, A. C. Gossard, "Advances in schottky rectifier performance", *IEEE Microwave Magazine*, Vol. 8, No. 3, pp. 54–59, 2007.
- [42] R. G. Meyers, P. Fay, J. N. Schulman, S. Thomas, D. H. Chow, J. Zinck, Y. K. Boegeman, P. Deelman, "Bias and Temperature Dependence of Sb-Based Heterostructure Millimeter-Wave Detectors With Improved Sensitivity", *IEEE Electron Device Lett.*, Vol. 25, No. 1, pp. 4–6, 2004.
- [43] M. Feiginov, "Frequency Limitations of Resonant-Tunnelling Diodes in Sub-THz and THz Oscillators and Detectors", *J. Infrared Milli. Terahz. Waves*, Vol. 40, No. 4, pp. 365–394, 2019.
- [44] L. Esaki, "Long journey into tunneling", *Science (New York, N.Y.)*, Vol. 183, No. 4130, pp. 1149–1155, 1974.
- [45] John H. Davies, "The physics of low-dimensional semiconductors: An introduction", Cambridge University Press, Cambridge, 1998.
- [46] T. Nakagawa, H. Imamoto, T. Kojima, K. Ohta, "Observation of resonant tunneling in AlGaAs/GaAs triple barrier diodes", *Appl. Phys. Lett.*, Vol. 49, No. 2, pp. 73–75, 1986.
- [47] N. Tadashi, F. Takahiro, M. Yutaka, K. Takeshi and O. Kimihiro, "Sharp Resonance Characteristics in Triple-Barrier Diodes with a Thin Undoped Spacer Layer", *Jpn. J. of Appl. Phys.*, Vol- 26, No. 6, L980-L982, 1987.

- 
- [48] N. Orihashi, S. Hattori, S. Suzuki and M. Asada, "Experimental and Theoretical Characteristics of Sub-Terahertz and Terahertz Oscillations of Resonant Tunneling Diodes Integrated with Slot Antennas", *Jpn. J. of Appl. Phys.*, Vol. 44, No. 11, pp. 7809–7815, 2005.
- [49] M. N. Feiginov, "Effect of the Coulomb interaction on the response time and impedance of the resonant-tunneling diodes", *Appl. Phys. Lett.*, Vol. 76, No. 20, pp. 2904–2906, 2000.
- [50] M. N. Feiginov, "Does the quasibound-state lifetime restrict the high-frequency operation of resonant-tunnelling diodes?", *Nanotechnology*, No. 11, pp. 359–364, 2000.
- [51] E. R. Brown, T. C. L. G. Sollner, C. D. Parker, W. D. Goodhue, C. L. Chen, "Oscillations up to 420 GHz in GaAs/AlAs resonant tunneling diodes", *Appl. Phys. Lett.*, Vol. 55, No. 17, pp. 1777–1779, 1989.
- [52] Jian P. Sun, G. I. Haddad, P. Mazumder, J. N. Schulman, "Resonant tunneling diodes: models and properties", *Proceedings of the IEEE*, Vol. 86, No. 4, pp. 641–660, 1998.
- [53] Q. Liu, A. Seabaugh, P. Chahal, F. J. Morris, "Unified AC model for the resonant tunneling diode", *IEEE Trans. Electron Devices*, Vol. 51, No. 5, pp. 653–657, 2004.
- [54] E. R. Brown, O. B. McMahon, L. J. Mahoney, K. M. Molvar, "SPICE model of the resonant-tunnelling diode", *Electron. Lett.*, Vol. 32, No. 10, p. 938, 1996.
- [55] M. I. Lepsa, J.J.M. Kwaspen, T. G. van de Roer, W. van der Vleuten, L.M.F. Kaufmann, "Microwave analysis of double barrier resonant tunneling diodes", *International Semiconductor Conference, 20th Edition. CAS '97 Proceedings, Sinaia, Romania, 7-11 Oct.*, IEEE, Piscataway, pp. 341–344, 1997.
- [56] T. J. Slight, B. Romeira, L. Wang, J. M. L. Figueiredo, E. Wasige, C. N. Ironside, "A LiÉnard Oscillator Resonant Tunnelling Diode-Laser Diode Hybrid Integrated Circuit: Model and Experiment", *IEEE J. Quantum Electron.*, Vol. 44, No. 12, pp. 1158–1163, 2008.
- [57] Z. Z. Sun, Sun Yin, X. R. Wang, J. P. Cao, Y. P. Wang, Y. Q. Wang, "Self-sustained current oscillations in superlattices and the van der Pol equation", *Appl. Phys. Lett.*, Vol. 87, No. 18, p. 182110, 2005.
- [58] L. Wang, J. M. L. Figueiredo, C. N. Ironside, E. Wasige, "DC Characterization of Tunnel Diodes Under Stable Non-Oscillatory Circuit Conditions", *IEEE Trans. Electron Devices*, Vol. 58, No. 2, pp. 343–347, 2011.
- [59] B. van der Pol, "The Nonlinear Theory of Electric Oscillations", *Proceedings of the IRE*, Vol. 22, No. 9, pp. 1051–1086, 1934.

- 
- [60] K. Ogino, S. Suzuki, M. Asada, "Spectral Narrowing of a Varactor-Integrated Resonant-Tunneling-Diode Terahertz Oscillator by Phase-Locked Loop", *J. Infrared Milli. Terahz. Waves*, Vol. 38, No. 12, pp. 1477–1486, 2017.
- [61] R. Adler, "A Study of Locking Phenomena in Oscillators", *Proceedings of the IRE*, Vol. 34, No. 6, pp. 351–357, 1946.
- [62] D. M. Pozar, "Microwave engineering", Wiley, fourth. ed., Hoboken, NJ, 2012.
- [63] K. Arzi, G. Keller, A. Rennings, D. Erni, F.-J. Tegude, W. Prost, "Frequency locking of a free running resonant tunneling diode oscillator by wire-less sub-harmonic injection locking", 10th UK-Europe-China Workshop on Millimetre, 1–4, 2017.
- [64] K. Arzi, S. Suzuki, Andreas Rennings, Daniel Erni, Nils Weimann, M. Asada, W. Prost, "Triple barrier RTD integrated in a slot antenna for mm-wave signal generation and detection", CSW, MIT, Cambridge, MA, USA, 2018.
- [65] K. Fujimoto, H. Morishita, "Modern small antennas", Cambridge University Press, Cambridge, 2013.
- [66] K. R. Jha, G. Singh, "Terahertz Planar Antennas for Next Generation Communication", Springer International Publishing, Cham, s.l., 2014.
- [67] J. D. Kraus, R. J. Marhefka, "Antennas for all applications", McGraw-Hill, third. ed., internat. ed., Boston, Mass., 2003.
- [68] R. E. Collin, "Antennas and radiowave propagation", McGraw-Hill, Internat. ed., New York, NY, 1985.
- [69] W. L. Stutzman, G. A. Thiele, "Antenna theory and design", Wiley, third. ed., Hoboken, NJ, 2013.
- [70] J. L. Volakis, "Antenna engineering handbook", McGraw-Hill, fourth. ed., New York, NY, 2007.
- [71] C. A. Balanis, "Antenna theory: Analysis and design", Wiley, Fourth edition, Hoboken, New Jersey, 2016.
- [72] G. Carpintero, L. E. García Muñoz, H. L. Hartnagel, S. Preu, A. V. Räsänen (Eds.), "Semiconductor terahertz technology: Devices and systems at room temperature operation", Wiley IEEE Press, Chichester, West Sussex, 2015.
- [73] Agilent Technologies, "Electromagnetic Advanced Design System", User manual, 2012.

- 
- [74] Y. Schols, G. A. E. Vandenbosch, "Separation of Horizontal and Vertical Dependencies in a Surface/Volume Integral Equation Approach to Model Quasi 3-D Structures in Multilayered Media", *IEEE Transactions on Antennas and Propagation*, Vol. 55, No. 4, pp. 1086–1094, 2007.
- [75] IMST GmbH, "EMPIRE XPU™ Getting Started", v7.7, 2018.
- [76] D. M. Sullivan, "Electromagnetic Simulation Using the FDTD Method", Wiley, secondnd ed., Hoboken, 2013.
- [77] CST MICROWAVE STUDIO, "Workflow & Solver Overview", 2010.
- [78] P. Monk, C. Carstensen, S. Funken, W. Hackbusch, R. H. W. Hoppe, T. Weiland (Eds.), "Finite Integration Method and Discrete Electromagnetism: Computational Electromagnetics", Berlin, Heidelberg, Springer Berlin Heidelberg, 2003.
- [79] E. F. Schubert, "Doping in III-V semiconductors", Cambridge University Press, Cambridge, 1993.
- [80] T. G. Sanchez, J. E. V. Perez, P. M. G. Conde, D. P. Collantes, "Electron transport in InP under high electric field conditions", *Semicond. Sci. Technol.*, Vol. 7, No. 1, pp. 31–36, 1992.
- [81] R. Compton, R. McPhedran, Z. Popovic, G. Rebeiz, P. Tong, D. Rutledge, "Bow-tie antennas on a dielectric half-space: Theory and experiment", *IEEE Trans. Antennas Propagat.*, Vol. 35, No. 6, pp. 622–631, 1987.
- [82] K. J. Button, "Infrared and Millimeter Waves V10: Millimeter Components and Techniques, Part II", Elsevier Science, Oxford, 1983.
- [83] S. R. J. Brueck, "Radiation from a dipole embedded in a dielectric slab", *IEEE Journal of Selected Topics in Quantum Electronics*, Vol. 6, No. 6, pp. 899–910, 2000.
- [84] K. Urayama, S. Aoki, S. Suzuki, M. Asada, H. Sugiyama, H. Yokoyama, "Sub-Terahertz Resonant Tunneling Diode Oscillators Integrated with Tapered Slot Antennas for Horizontal Radiation", *Appl. Phys. Express*, Vol. 2, p. 44501, 2009.
- [85] K. Kasagi, S. Fukuma, S. Suzuki, M. Asada, "Proposal and fabrication of dipole array antenna structure in resonant-tunneling-diode terahertz oscillator array", 41st International Conference on Infrared, Millimeter, and Terahertz waves (IRMMW-THz), Copenhagen, Denmark, 25.09 - 30.09, IEEE, pp. 1–2, 2016.
- [86] K. Okada, K. Kasagi, N. Oshima, S. Suzuki, M. Asada, "Resonant-Tunneling-Diode Terahertz Oscillator Using Patch Antenna Integrated on Slot Resonator for Power Radiation", *IEEE Trans. THz Sci. Technol.*, Vol. 5, No. 4, pp. 613–618, 2015.

- 
- [87] G. M. Rebeiz, "Millimeter-wave and terahertz integrated circuit antennas", Proc. IEEE, Vol. 80, No. 11, pp. 1748–1770, 1992.
- [88] M. Feiginov, "Frequency Limitations of Resonant-Tunnelling Diodes in Sub-THz and THz Oscillators and Detectors", J. Infrared Milli. Terahz. Waves, Vol. 40, No. 4, pp. 365–394, 2019.
- [89] Y. Mushiake, "Self-Complementary Antennas: Principle of Self-Complementarity for Constant Impedance", Springer London, London, 1996.
- [90] Y. Mushiake, "Self-complementary antennas", IEEE Antennas Propag. Mag., Vol. 34, No. 6, pp. 23–29, 1992.
- [91] P. L. Richards, "Bolometers for infrared and millimeter waves", J. of Appl. Phys., Vol. 76, No. 1, pp. 1–24, 1994.
- [92] N. Inoue, Y. Yasuoka, "Infrared laser detection by antenna-coupled point-contact schottky diodes", Electron. commun. Jpn., Vol. 67, No. 6, pp. 114–121, 1984.
- [93] Rohde & Schwarz GmbH & Co. KG, "R&S ZVA/R&S ZVB/R&S ZVT Operating Manual 31 (FW V4.0)", 2018.
- [94] Rohde & Schwarz GmbH & Co. KG, "R&S®ZVA-Zxx Millimeter-Wave Converters", Vol. 2014.
- [95] Rohde & Schwarz GmbH & Co. KG, "R&S ZVA/R&S ZVB/R&S ZVT Operating Manual".
- [96] A. Rumiantsev, N. Ridler, "VNA calibration", IEEE Microwave Magazine, Vol. 9, No. 3, pp. 86–99, 2008.
- [97] BATOP optoelectronics (Ed.), "hyperhemispherical silicon lens HSL-12-7.1: data sheet", 2019.
- [98] Y. Sun, P. Pianetta, P. Chen, M. Kobayashi, Y. Nishi, N. Goel, M. Garner, W. Tsai, "Arsenic-dominated chemistry in the acid cleaning of InGaAs and InAlAs surfaces", Appl. Phys. Lett., Vol. 93, No. 19, p. 194103, 2008.
- [99] R. Vos, S. Arnauts, T. Conard, A. Moussa, H. Struyf, P. W. Mertens, "Wet Chemical Cleaning of InP and InGaAs", Solid State Phenomena, Vol. 187, pp. 27–31, 2012.
- [100] M. Todeschini, Bastos da Silva Fanta, A., F. Jensen, J. B. Wagner, A. Han, "Influence of Ti and Cr Adhesion Layers on Ultrathin Au Films", ACS applied materials & interfaces, Vol. 9, No. 42, pp. 37374–37385, 2017.
- [101] S. Tanaka, K. Rajanna, T. Abe, M. Esashi, "Deep reactive ion etching of silicon carbide", J. Vac. Sci. Technol. B, Vol. 19, No. 6, p. 2173, 2001.

- 
- [102] R. Moug, A. Alfaro-Martinez, L. Peng, T. Garcia, V. Deligiannakis, A. Shen, M. Tamargo, "Selective etching of InGaAs/InP substrates from II-VI multilayer heterostructures", *Phys. Status Solidi (c)*, Vol. 9, 8-9, pp. 1728–1731, 2012.
- [103] S. Topaloglu, "Process Technology for High Speed InP Based Process Technology for High Speed InP Based Heterojunction Transistors", in *der Fakultät fuer Ingenieurwissenschaften: Universitaet Duisburg-Essen, Duisburg*, 2006.
- [104] F. D. Egitto, "Plasma etching and modification of organic polymers", *Pure and Applied Chemistry*, Vol. 62, No. 9, pp. 1699–1708, 1990.
- [105] M. A. Verschuuren, "Substrate conformal imprint lithography for nanophotonics", Ph.D. at the University Utrecht, The Netherlands, 2010.
- [106] C. Blumberg, S. Grosse, N. Weimann, F.-J. Tegude, W. Prost, "Polarity- and Site-Controlled Metal Organic Vapor Phase Epitaxy of 3D-GaN on Si(111)", *Phys. Status Solidi B*, Vol. 255, No. 5, p. 1700485, 2018.
- [107] N. V. Bhat, D. J. Upadhyay, "Plasma-induced surface modification and adhesion enhancement of polypropylene surface", *J. Appl. Polym. Sci.*, Vol. 86, No. 4, pp. 925–936, 2002.
- [108] S. L. Kaplan, P. W. Rose, "Plasma surface treatment of plastics to enhance adhesion", *Int. J. of Adhesion and Adhesives*, Vol. 11, No. 2, pp. 109–113, 1991.
- [109] H. D. Rowland, A. C. Sun, P. R. Schunk, W. P. King, "Impact of polymer film thickness and cavity size on polymer flow during embossing: toward process design rules for nanoimprint lithography", *J. Micromech. Microeng.*, Vol. 15, No. 12, p. 2414, 2005.
- [110] S. Y. Chou, "Sub-10 nm imprint lithography and applications", *J. Vac. Sci. Technol. B*, Vol. 15, No. 6, p. 2897, 1997.
- [111] S. Y. Chou, P. R. Krauss, P. J. Renstrom, "Imprint of sub-25 nm vias and trenches in polymers", *Appl. Phys. Lett.*, Vol. 67, No. 21, pp. 3114–3116, 1995.
- [112] W. Prost, "Technologie der III/V-Halbleiter: III/V-Heterostrukturen und elektronische Höchstfrequenz-Bauelemente", Springer Berlin Heidelberg, Berlin, Heidelberg, 1997.
- [113] G. Keller, A. Tchegho, B. Münstermann, W. Prost, F.-J. Tegude, "Sensitive high frequency envelope detectors based on triple barrier resonant tunneling diodes", *Int. Conf. on Indium Phosphide and Related Materials*, Santa Barbara, CA, pp. 36–39, 2013.

- 
- [114] W. Prost, P. Keily, A. Guttzeit, V. Khorenko, E. Khorenko, A. Matiss, J. Driesen, A.-C. Mofor, A. Bakin, A. Poloczek, S. Neumann, A. Stohr, D. Jager, M. McGinnity, A. Schlachetzki, F.-J. Tegude, "Design and modelling of a III/V mobile-gate with optical input on a silicon substrate", *Int. Conf. on indium phosphide*, p.p 17–20, 2005.
- [115] W. Prost, V. Khorenko, A.-C. Mofor, S. Neumann, A. Poloczek, A. Matiss, A. Bakin, A. Schlachetzki, F.-J. Tegude, "High performance III/V RTD and PIN diode on a silicon (001) substrate", *Applied Physics A*, Vol. 87, No. 3, pp. 539–544, 2007.
- [116] M. J. Deen, "Simple method to determine series resistance and its temperature dependence in AlAs/GaAs/AlAs double", *Electron. Lett.*, Vol. 28 No. 13, pp. 1195–1197, 1992.
- [117] A. Matiss, "Entwurf und Realisierung neuartiger Schaltungskonzepte mit Resonanztunneldioden", Cuvillier Verlag, first ed., Göttingen, 2008.
- [118] A. C. Cornescu, R. Morariu, A. Ofiare, A. Al-Khalidi, J. Wang, J. M. L. Figueiredo, E. Wasige, "High-Efficiency Bias Stabilization for Resonant Tunneling Diode Oscillators", *IEEE Trans. Microwave Theory Techn.*, pp. 1–6, 2019.
- [119] L. Wang, J. M. L. Figueiredo, C. N. Ironside, E. Wasige, "DC Characterization of Tunnel Diodes Under Stable Non-Oscillatory Circuit Conditions", *IEEE Trans. Electron Devices*, Vol. 58, No. 2, pp. 343–347, 2011.
- [120] Y. Ikeda, S. Kitagawa, K. Okada, S. Suzuki, M. Asada, "Direct intensity modulation of resonant-tunneling-diode terahertz oscillator up to ~30 GHz", *IEICE Electron. Express*, Vol. 12, No. 3, p. 20141161, 2015.
- [121] B. Razavi, "A study of injection locking and pulling in oscillators", *IEEE Journal of Solid-State Circuits*, Vol. 39, No. 9, pp. 1415–1424, 2004.
- [122] A. Demir, A. Mehrotra, J. Roychowdhury, "Phase noise in oscillators: a unifying theory and numerical methods for characterization", *IEEE Transactions on Circuits and Systems I: Fundamental Theory and Applications*, Vol. 47, No. 5, pp. 655–674, 2000.
- [123] Virginia Diodes Inc., "Zero-Bias Detector Operational Manual (ZBD, ZBD-F, QOD)", Rev. March 15, 2017.

---

## 10 Own publication

- 1- “Sub-harmonic injection locking for phase and frequency control of RTD based THz oscillator”  
**K. Arzi**, S. Suzuki, A. Rennings, D. Erni, N. Weimann, M. Asada, and W. Prost  
In: IEEE Terahertz Science and Technology Letters Dec. 2019
- 2- “Toward Mobile Integrated Electronic Systems at THz Frequencies”  
P. Hillger, M. van Delden, U. Sampath M. Thanthrige, A. Mustafa, I. Ahmed, J. Wittmeier, **K. Arzi**, M. Andre, B. Sievert, W. Prost, A. Rennings, D. Erni, T. Much, N. Weimann, A. Sezgin, N. Pohl, U. R. Pfeiffer  
In: Springer THz Journal. Submitted Nov. 2019
- 3- “Experimental evidence for the separation of thermally excited bipolar charge carries within a p-n junction : A new approach to thermoelectric materials and generators”  
F. Maculewicz, T. Wagner, **K. Arzi**, N. Hartmann, N. Weimann, R. Schmechel  
In: Journal of Applied Physics Jg. 125 (2019) Nr. 18, S. 184502 ISSN: 1089-7550; 0021-8979
- 4- “Toward Nanowire HBT : Reverse Current Reduction in Coaxial GaAs/InGaP n(i)p and n(i)pn Core-Multishell Nanowires”  
L. Liborius, F. Heyer, **K. Arzi**, C. Speich, W. Prost, F. -J Tegude, N. Weimann, A. Poloczek  
In: Physica Status Solidi (A): Applications and Materials Science Jg. 216 (2019) Nr. 1, S. 1800562 ISSN: 1862-6319; 1862-6300
- 5- “Electrical characterization and transport model of n-gallium nitride nanowires”  
O. Benner, C. Blumberg, **K. Arzi**, A. Poloczek, W. Prost, F. -J. Tegude,  
In: Applied Physics Letters Jg. 108 (2016) Nr. 4, S. 049901 ISSN: 0003-6951; 1077-3118

- 
- 6- “Triple-Barrier Resonant-Tunnelling Diode THz Detectors with on-chip antenna”  
**K. Arzi**, S. Clochiatti, S. Suzuki, A. Rennings, D. Erni, N. Weimann, M. Asada, W. Prost  
In: German Microwave Conference / 12th German Microwave Conference, GeMiC 2019; Stuttgart; Germany; 25 - 27 March 2019 / 2019 S. 17 - 19  
ISBN: 9783982039701
  - 7- “Broadband millimeter-wave detector based on triple-barrier resonant tunneling diode and tailored Archimedean spiral antenna”  
A. Rennings, B. Sievert, W. Lui, **K. Arzi**, W. Prost, D. Erni  
In: Proceedings of 2017 Asia-Pacific Microwave Conference (APMC) / APMC 2017, 13. - 16. November 2017, Kuala Lumpur, Malaysia; / Pasya, Idris; Seman, Fauziahanim Che (Hrsg.), 2018 S. 775 – 778 ISBN: 978-1-5386-0640-7
  - 8- “Millimeter-wave Signal Generation and Detection via the same Triple Barrier RTD and on-chip Antenna”  
**K. Arzi**, A. Rennings, D. Erni, N. Weimann, W. Prost, S. Suzuki, M. Asada  
In: 2018 1st International Workshop on Mobile Terahertz Systems, IWMTS 2018, Duisburg, Germany, 2 July 2018 through 4 July 2018 / 2018  
ISBN: 978-1-5386-1221-7; 978-1-5386-1220-0; 978-1-5386-1222-4
  - 9- „Broadband detection capability of triple barrier resonant tunneling diodes”  
**K. Arzi**, S. Clochiatti, E. Mutlu, A. Kowaljow, B. Sievert, D. Erni, N. Weimann, W. Prost  
In: Proceedings of the 2nd International Workshop on Mobile THz Systems (IWMTS 2019) / IWMTS 2019; 01 - 03 July 2019; Bad Neuenahr, Germany / 2019
  - 10- “On the sensitivity of triple-barrier resonant-tunneling (sub-) mm-wave detectors”  
**K. Arzi**, S. Suzuki, A. Rennings, D. Erni, N. Weimann, M. Asada, W. Prost  
In: Progress in Electromagnetics Research Symposium (PIERS 2018) / 2018 S. 1247

- 
- 11- “Triple barrier RTD integrated in a slot antenna for mm-wave signal generation and detection”  
**K. Arzi**, S. Suzuki, A. Rennings, D. Erni, N. Weimann, M. Asada, W. Prost  
In: Compound Semiconductor Week (CSW 2018) / 14th Int. Symposium on Compound Semiconductors (ISCS), and the 30th Int. Conference on Indium Phosphide and Related Materials (IPRM), May 29 – June 1, 2018, Massachusetts Institute of Technology (MIT), Cambridge, MA, USA / 2018 S. 54
- 12- “Frequency locking of a free running resonant tunneling diode oscillator by wire-less sub-harmonic injection locking”  
**K. Arzi**, G. Keller, A. Rennings, D. Erni, F.-J. Tegude, W. Prost  
In: 10th UK-Europe-China Workshop on Millimetre Waves and Terahertz Technologies, UCMMT 2017 / UCMMT 2017; Liverpool; United Kingdom; 11 September 2017 through 13 September 2017 / 2017 S. 8068485 ISBN: 9781538627204
- 13- “Antenna design for subharmonic injection-locked triple barrier RTD oscillator in the 300 GHz band”  
M. Zhang, S. Clochiatti, A. Rennings, **K. Arzi**, W. Prost, N. Weimann, D. Erni  
In: Proceedings of the 2nd International Workshop on Mobile THz Systems (IWMTS 2019) / IWMTS 2019; 01 - 03 July 2019; Bad Neuenahr, Germany / 2019
- 14- “Transmitarray element design for subharmonic injection-locked RTD oscillators in THz band”  
M. Zhang, A. Rennings, S. Clochiatti, **K. Arzi**, W. Prost, N. Weimann, and D. Erni  
In: Photonics & Electromagnetics Research Symposium (PIERS 2019)/ December 17–20, 2019 Xiamen, CHINA
- 15- “Theoretically oriented studies about triple-barrier resonant tunneling diodes and integrated structures towards a realization of terahertz wireless communication as terminal devices of RoF systems”  
K. Aikawa, M. Nakanishi, S. Kitakado, M. Suhara, K. Asakawa,  
**K. Arzi**, N. Weimann, W. Prost  
In: Asia-Pacific Workshop on Fundamentals and Applications of Advanced Semiconductor Devices (AWAD 2019)/ July 1 – 3, 2019 Busan, Korea

- 
- 16- “Characterization of the Effective Tunneling Time and Phase Relaxation Time in TripleBarrier Resonant Tunneling Diodes”  
K. Aikawa, M. Suhara, K. Asakawa,  
**K. Arzi**, N. Weimann, and W. Prost  
In: Compound Semiconductor Week 2019 (CSW2019)/ 15th Int. Symposium on Compound Semiconductors (ISCS), and the 31th Int. Conference on Indium Phosphide and Related Materials (IPRM), May 19-23, 2019  
Kasugano International Forum, Nara, Japan
- 17- “Subharmonic Signal Generation and Injection Locking in Resonant-Tunneling-Diode Terahertz Oscillator”  
**K. Arzi**, S. Suzuki, A. Rennings, D. Erni, N. Weimann, M. Asada, W. Prost  
In: The 79th JSAP Autumn Meeting 2018, Nagoya Congress Center 18-21. September
- 18- “Towards Nanowire HBT: Minority Charge Carrier Transition Through Npn Core-Multishell Nanowires”  
L. Liborius, **K. Arzi**, C. Speich, W. Prost, F.-J Tegude, A. Poloczek and N. Weimann  
In: Compound Semiconductor Week (CSW 2018) / 14th Int. Symposium on Compound Semiconductors (ISCS), and the 30th Int. Conference on Indium Phosphide and Related Materials (IPRM), May 29 – June 1, 2018,  
Massachusetts Institute of Technology (MIT), Cambridge, MA, USA
- 19- “Indium phosphide resonant tunneling diodes for THz applications”  
N. Weimann, **K. Arzi**, S. Clochiatti, W. Prost  
In: Mikrosystemtechnik Kongress 2019
- 20- “Wireless injection locking of a free running RTD-based THz oscillator”  
**K. Arzi**, S. Suzuki\*, A. Rennings, D. Erni, N. Weimann, M. Asada\*, W. Prost  
In: Optical Workshop on Heterostructure Microelectronics 2019 (TWHM 2019)/ August 26-29, 2019, Toyama, Japan.

---

## Appendix

### A: Single TBRTD and circuit fabrication instruction

In this section, the step-by-step instruction used and developed for the fabrication of single TBRTD elements and of its integration into the slot antenna is presented.

#### A.1 Single devices

##### Structuring the top contact:

- Surface cleaning:
  - Cleaning organic-contaminants: Acetone at 56°C for 2 minutes and IPA at 82°C for 2 minutes
  - Native oxide cleaning: a dip in an HCl:H<sub>2</sub>O 1:4 mixture for 40 s and cleaning with flowing DI-Water for 60 s
  -
- Photoresist structuring
  - A positive resist is used (AZ® 1505), with the following spin coating parameters: 1000 rpm<sup>2</sup> /30 s/4000 rpm.
  - Bake at the hotplate for 1 minute at 110°C
  - UV-Exposure for 3 s with a dark field photomask
  - Photoresist development.
- Metallization
  - Surface cleaning after development with O<sub>2</sub>-plasma at 25W for 1 minute
  - Surface oxide cleaning step before metal deposition with NH<sub>3</sub>:H<sub>2</sub>O 1:10 for 10 s
  - Metallization in a vacuum chamber: Ti/Pt/Au/Ni: 10/10/400/10nm
  - Lift-off with Acetone step at 56°C until the resist is removed and IPA at 82°C

##### Structuring of the device mesa

- ICP-RIE: First, a test substrate is etched to determine the etching rates with the following parameter.
  - ICP power: Starting with 300W downregulating to 150W
  - RF power: Starting with 150W downregulating to 70W
  - Strike: 50mTorr
  - Pressure: 6 mTorr
  - Gas mixture Cl<sub>2</sub>/N<sub>2</sub>:4/36 sccm
  - Chuck temperature: 170 °C
  - Etch depth determination with a profilometer
  - Etch rate determination and adjust etch time for device mesa etching
- Surface cleaning after etching (repeat this step twice)
  - Acetone 1 minute at 56°C then IPA at 82°C for 1 minute
  - Dip into HCl:H<sub>2</sub>O 1:4 for 40 s and flowing DI-water for 60 s followed by NH<sub>3</sub>:H<sub>2</sub>O 1:10 for 20 s
- Control

- 
- Using a profilometer the etch depth is controlled. If the depth is not sufficient a wet etching in 1:1:25 H<sub>3</sub>PO<sub>4</sub>:H<sub>2</sub>O<sub>2</sub> : H<sub>2</sub>O mixture is carried out.

### Structuring the bottom contact

- Surface cleaning:
  - Native oxide cleaning: a dip in an HCl:H<sub>2</sub>O 1:4 mixture for 40 s and cleaning with DI-Water for 60 s
- Photoresist structuring
  - A negative resist is used (AZ® nLOF 2020), with the following spin coating parameter: 1000 rpm<sup>2</sup>/30 s/4000 rpm.
  - Bake at the hotplate for 1 minute at 110°C
  - acclimatization for 5 minutes in room temperature
  - UV-Exposure for 1.7 s with a light field photomask
  - Post-exposure bake (PEB) step for 1 minute at 110°C
  - Photoresist development
- Metallization
  - Surface cleaning after development with O<sub>2</sub>-plasma at 25W for 1 minute
  - Surface oxide cleaning step before metal deposition with NH<sub>3</sub>:H<sub>2</sub>O 1:10 for 10 s
  - Metallization in a vacuum chamber: Ti/Pt/Au: 10/10/400 nm
  - Lift-off with Acetone step at 56°C until the resist is removed and IPA at 82°C

### Single devices separation and isolation

- separation

- Surface cleaning:
  - Native oxide cleaning: a dip in an HCl:H<sub>2</sub>O 1:4 mixture for 40 s and cleaning with flowing DI-Water for 60 s
- Photoresist structuring
  - A positive resist is used (AZ® 6632), with the following spin coating parameter: 3000 rpm<sup>2</sup>/30 s/3000 rpm.
  - Bake at the hotplate for 10 minutes at 120°C
  - UV-Exposure for 25 s with a light field photomask
  - Post-exposure bake (PEB) step for 30 minutes at 120°C
  - Photoresist development.
- Etching of the InGaAs
  - Using H<sub>3</sub>PO<sub>4</sub>:H<sub>2</sub>O<sub>2</sub>:H<sub>2</sub>O 1:1:25 at room temperature until a surface color change is visible
  - Lift-off with Acetone step at 56°C until the resist is removed and IPA at 82°C

- isolation

- SOG structuring
  - A spin-on-glass is used (Durimide® (1:1)), with the following spin coating parameters: 1000 rpm<sup>2</sup>/150 s/5000 rpm.
  - Bake at the hotplate for 3 minutes at 95°C
  - UV-Exposure for 10 s with a light field photomask
  - Photoresist development with a dip in HTRD2 for 30 s followed by a dip for 30 s in RER600
- Adjusting the resist height

- 
- O<sub>2</sub>-plasma etching for 2 minutes
  - Resist height control in the SEM to ensure that the top contact is free of the resist
  - Repeat the steps until achieving a resist free top contact
  - Bake in an oven at 200°C for 2 hours

## GSG-Pads

- Surface cleaning:
  - Native oxide cleaning: a dip in an HCl:H<sub>2</sub>O 1:4 mixture for 40 s and cleaning with flowing DI-Water for 60 s
- Photoresist structuring
  - A negative resist is used (AZ® nLOF 2020), with the following spin coating parameter: 1000 rpm<sup>2</sup>/30 s/4000 rpm.
  - Bake at the hotplate for 1 minute at 110°C
  - acclimatization for 5 minutes in room temperature
  - UV-Exposure for 1.7 s with a light field photomask
  - Post-exposure bake (PEB) step for 1 minute at 110°C
  - Photoresist development
- Metallization
  - Surface cleaning after development with O<sub>2</sub>-plasma at 25W for 1 minute
  - Surface oxide cleaning step before metal deposition with NH<sub>3</sub>:H<sub>2</sub>O 1:10 for 10 s
  - Metallization in a vacuum chamber: Ti/Pt/Au: 10/10/400 nm
  - Lift-off with Acetone step at 56°C until the resist is removed and IPA at 82°C

## A.2 In antenna integration

The same fabrication steps are done as described in 10.1.2 for single device processing, up to the GSG-Pads integration which is replaced by integration within an antenna. In this step-by-step instruction the integration within the slot antenna is presented:

### Slot antenna bottom contact:

- Surface cleaning:
  - Native oxide cleaning: a dip in an HCl:H<sub>2</sub>O 1:4 mixture for 40 s and cleaning with flowing DI-Water for 60 s
- Photoresist structuring
  - A negative resist is used (AZ® nLOF 2020), with the following spin coating parameter: 1000 rpm<sup>2</sup>/30 s/4000 rpm.
  - Bake at the hotplate for 1 minute at 110°C
  - acclimatization for 5 minutes in room temperature
  - UV-Exposure for 1.7 s with a light field photomask
  - Post-exposure bake (PEB) step for 1 minute at 110°C
  - Photoresist development
- Metallization
  - Surface cleaning after development with O<sub>2</sub>-plasma at 25 W for 1 minute
  - Surface oxide cleaning step before metal deposition with NH<sub>3</sub>:H<sub>2</sub>O 1:10 for 10 s
  - Metallization in a vacuum chamber: Ti/Au: 10/400 nm
  - Lift-off with Acetone step at 56°C until the resist is removed and IPA at 82°C

---

## Isolation and transitions smoothing

- Surface cleaning:
  - Native oxide cleaning: a dip in an HCl:H<sub>2</sub>O 1:4 mixture for 40 s and cleaning with flowing DI-Water for 60 s
- SOG structuring
  - A spin-on-glass is used (Durimide® (1:1)), with the following spin coating parameters: 1000 rpm<sup>2</sup>/150 s/5000 rpm.
  - Bake at the hotplate for 3 minutes at 95°C
  - UV-Exposure for 10 s with a light field photomask
  - Photoresist development with a dip in HTRD2 for 30 s followed by a dip for 30 s in RER600
- Adjusting the resist height
  - (Only if needed) O<sub>2</sub>-plasma etching for 2 minutes
  - (Only if needed) Resist height control in the SEM
  - (Only if needed) Repeat the steps until achieving a required height
  - Bake in an oven at 200°C for 2 hours

### (Only if a “lift-off opening” is used) Closing the lift-off opening:

- Surface cleaning:
  - Native oxide cleaning: a dip in an HCl:H<sub>2</sub>O 1:4 mixture for 40 s and cleaning with flowing DI-Water for 60 s
- Photoresist structuring
  - A negative resist is used (AZ® nLOF 2020), with the following spin coating parameter: 1000 rpm<sup>2</sup>/30 s/4000 rpm.
  - Bake at the hotplate for 1 minute at 110°C
  - acclimatization for 5 minutes in room temperature
  - UV-Exposure for 1.7 s with a light field photomask
  - Post-exposure bake (PEB) step for 1 minute at 110°C
  - Photoresist development
- Metallization
  - Surface cleaning after development with O<sub>2</sub>-plasma at 25W for 1 minute
  - Surface oxide cleaning step before metal deposition with NH<sub>3</sub>:H<sub>2</sub>O 1:10 for 10 s
  - Metallization in a vacuum chamber: Ti/Au: 10/400 nm
  - Lift-off with Acetone step at 56°C until the resist is removed and IPA at 82°C

### Structuring the MIM-Capacitor:

- Surface cleaning:
  - Native oxide cleaning: a dip in an HCl:H<sub>2</sub>O 1:4 mixture for 40 s and cleaning with flowing DI-Water for 60 s

#### - Pre structuring isolator deposition

- Photoresist structuring
  - A positive resist is spin-coated (AZ® 5214) with the following spin coating parameters: 3000 rpm<sup>2</sup>/30 s/3000 rpm
  - Bake at the hotplate for 5 minutes at 95°C
  - Flood exposure for 1.4 s
  - Bake at the hotplate for 4 minutes at 110°C

- 
- UV-Exposure for 40 s with a dark field photomask
  - Photoresist development.
  - Isolator deposition
    - Surface cleaning after development with O<sub>2</sub>-plasma at 25 W for 1 minute
    - Surface oxide cleaning step before metal deposition with NH<sub>3</sub>:H<sub>2</sub>O 1:10 for 10 s
    - Metallization in a vacuum chamber: Ti: 1 nm
    - 110nm SiN deposition in the PECVD
    - Lift-off with Acetone step at 56°C until the resist is removed and IPA at 82°C

#### - Post structuring isolator deposition

- Isolator deposition
  - 110nm SiN deposition in the PECVD
- Photoresist structuring
  - A positive resist is spin-coated (AZ® 5214), with the following spin coating parameters: 3000 rpm<sup>2</sup>/30 s/3000 rpm
  - Bake at the hotplate for 5 minutes at 95°C
  - Flood exposure for 1.4 s
  - Bake at the hotplate for 4 minutes at 110°C
  - UV-Exposure for 40 s with a dark field photomask
  - Photoresist development.
- SiN etching
  - A dip in 5% HF (hydrofluoric acid) water mixture is used to etch the SiN isolator from the areas which are not protected by the resist mesas.

#### Slot antenna top contact

- Surface cleaning:
  - Native oxide cleaning: a dip in an HCl:H<sub>2</sub>O 1:4 mixture for 40 s and cleaning with flowing DI-Water for 60 s
- Photoresist structuring
  - A negative resist is used (AZ® nLOF 2020), with the following spin coating parameter: 1000 rpm<sup>2</sup>/30 s/4000 rpm.
  - Bake at the hotplate for 1 minute at 110°C
  - acclimatization for 5 minutes in room temperature
  - UV-Exposure for 1.7 s with a light field photomask
  - Post-exposure bake (PEB) step for 1 minute at 110°C
  - Photoresist development
- Metallization
  - Surface cleaning after development with O<sub>2</sub>-plasma at 25W for 1 minute
  - Surface oxide cleaning step before metal deposition with NH<sub>3</sub>:H<sub>2</sub>O 1:10 for 10 s
  - Metallization in a vacuum chamber: Ti/Au: 10/400 nm
  - Lift-off with Acetone step at 56°C until the resist is removed and IPA at 82°C

## B. Layout design for single Test-devices and circuits

This appendix section introduces the used masks for photolithography. The test mask is an established mask, which is design during different work in our department. The second mask for the slot antenna THz oscillator and detector is designed and developed during this work.

### B.1 I: Single device test (*Test-RTD* mask):

This mask provides single TBRTD for test and modeling purposes. The mask is designed for the fabrication of  $\frac{1}{4}$  of a 2-inch substrate. Figure B.1 presents the floorplan of the mask. Overall there are 32 cells, and each contains 48 elements. The cells are structured in a checkerboard pattern. The cells differ mainly by the GSG-interconnection structure. A one- and two-port GSG structure with a pitch of  $150\ \mu\text{m}$  is designed. Devices with different areas are structured, starting from the smallest with an area of  $0.56\ \mu\text{m}^2$  and the largest with  $9\ \mu\text{m}^2$ . For mapping purposes within a cell, the rows are grouped together (see Figure B.2). Each cell has an ICPI group that contains two rows, one as a *nsa* row, and the second is a *sa* row. Material and contact characterization elements such as TLM, CBRK are also included in each cell. Further, for scattering parameter measurement, calibration structures, such as open and short for one port and for two-port measurement, an extra through is designed.

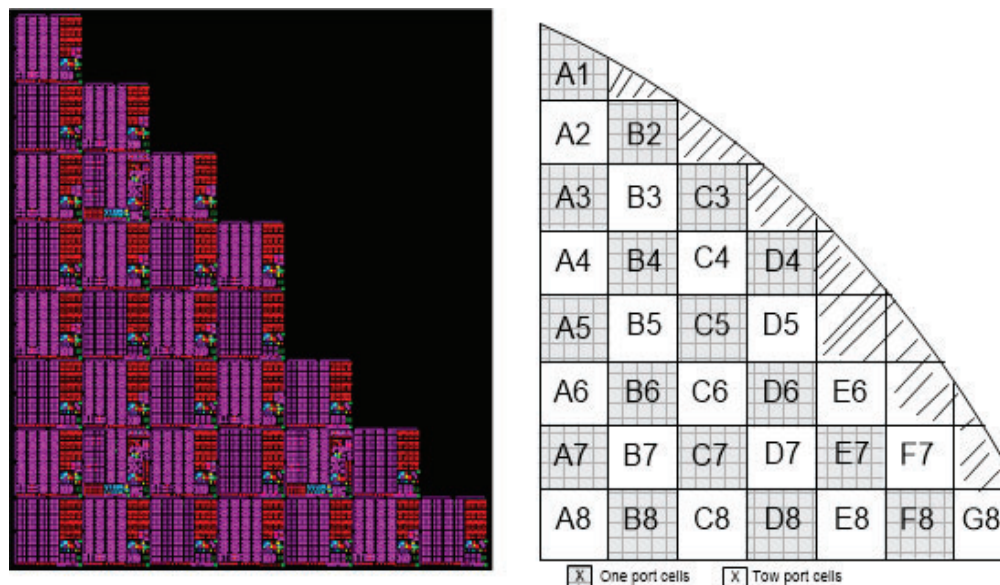


Figure B.1: Floorplan of the used layout for single test elements

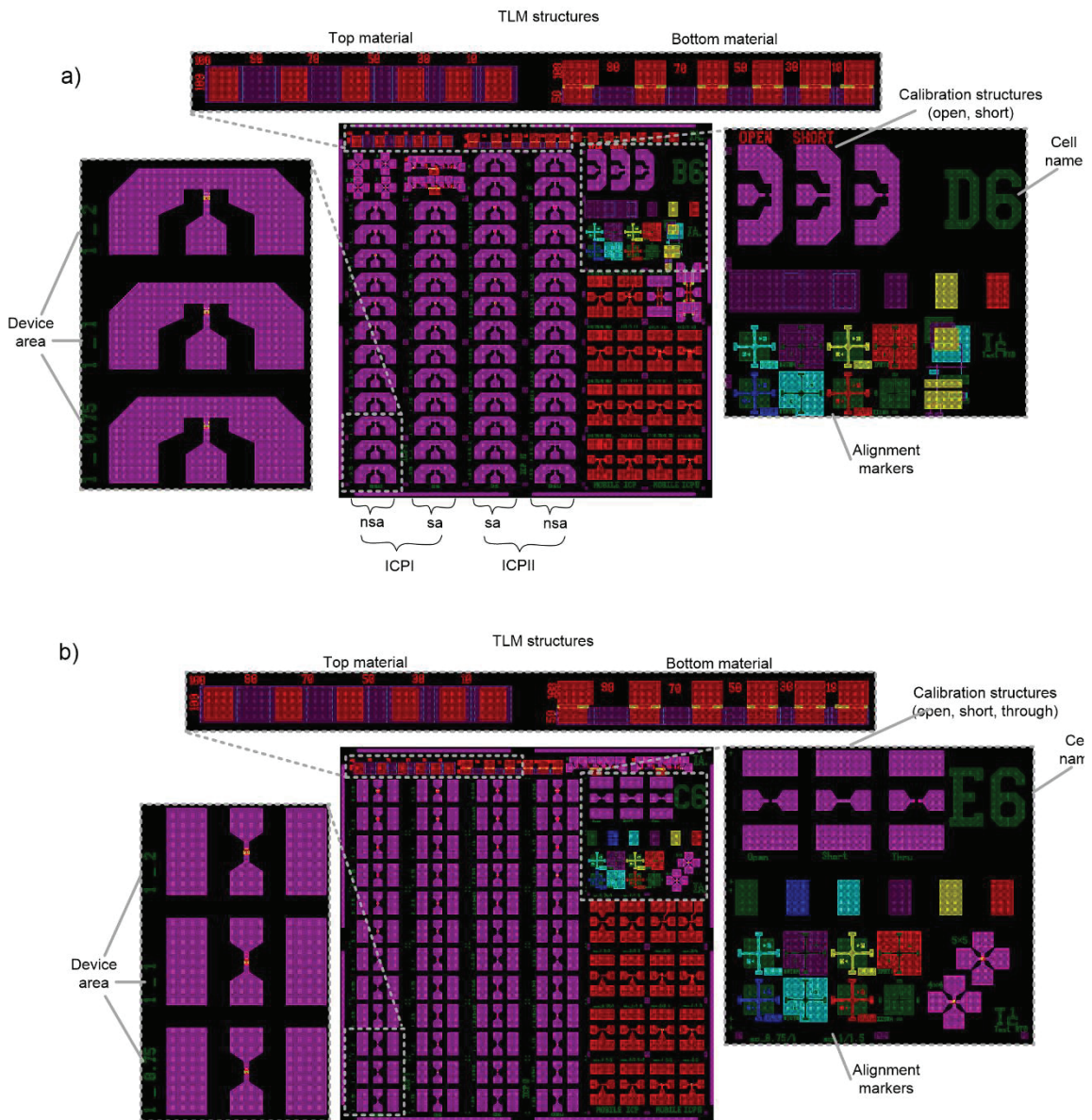


Figure B.2: a) one port cell layout. b) Two-port cell layout

## B.2 TBRTD Slot antenna integration

The mask was designed during this work to provide the first interaction with THz oscillators and detectors within our department. The design consists mainly of three different cells, as shown in Figure B.3. *Test elements* cells: mainly, different fabrication structures are investigated. *Array cells*: in this cell, a metallization layer that connects four elements, with the same TBRTDs and antenna, parallel to each other. The *device and feed point sweep* cells: In this cell, the area of the TBRTD is separated into two, three, and four mesas. Further, the position within the slot is swept from the center toward the upper edge of the slot. Further, an *XXL* cell is also given. Here the slot antennae are larger but with the same slot dimensions.

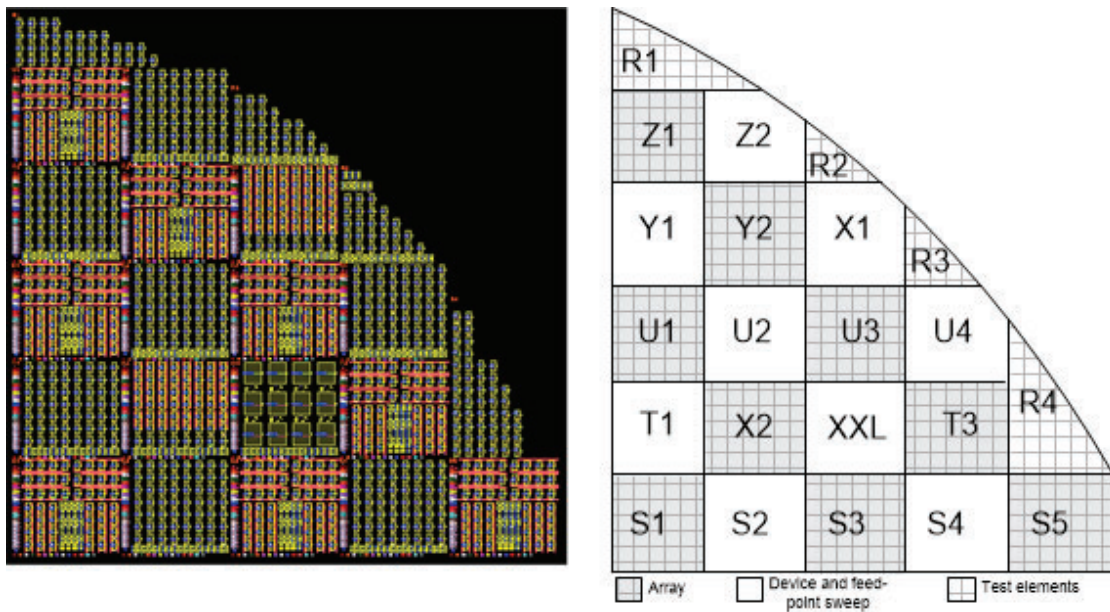


Figure B.3: Floorplan of the used layout for TBRTD integrated into a slot antenna

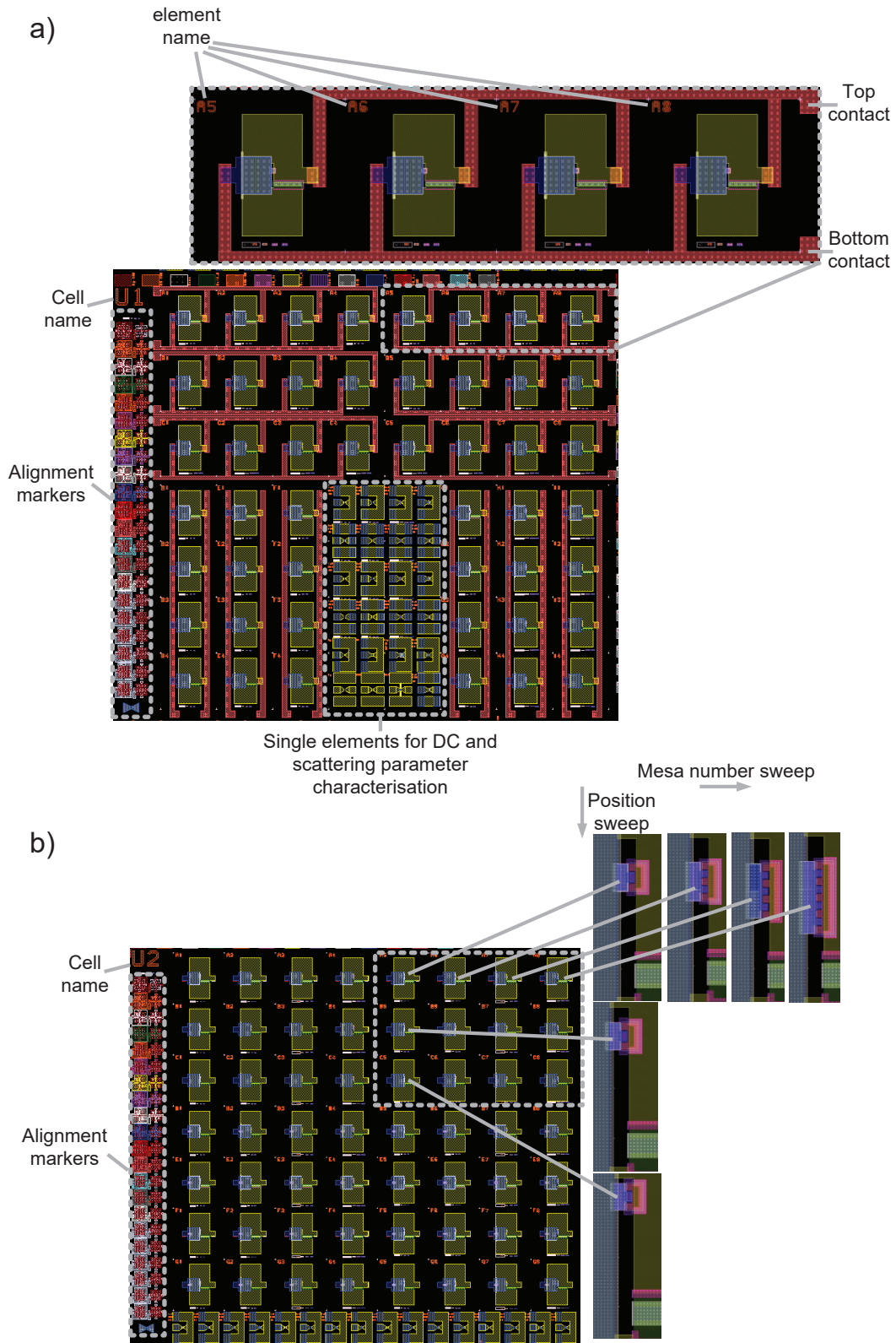


Figure B.4: The main designed cells for TBRTD into antenna integration. a) *Array cells*. b) *Device and feed point sweep cells*

## C. Simulation of a TBRTD slot antenna detector

These Simulation were carried out during the stay of Prof. Suzuki, from *Tokyo Institute of Technology* within the Mercator fellowship. Therefore, only the results are presented.

Figure C.1 presents the small-signal equivalent circuit utilized to characterize the detector. The TBRTD conductance and capacitance were determined by on-wafer scattering parameter measurements, while the antenna equivalent circuit is extracted from EM-simulation of the slot antenna structure.

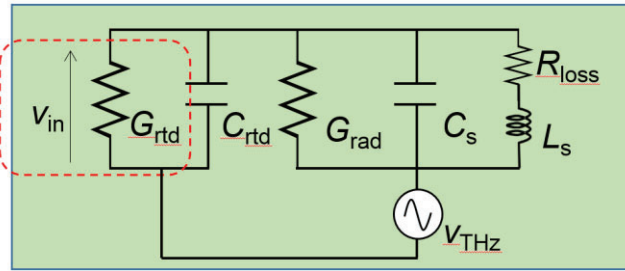


Figure C.1: Small-signal equivalent circuit used for the detector simulation

For rectification simulation, the current-voltage characteristics of the user device are fitted as shown in Figure C.2

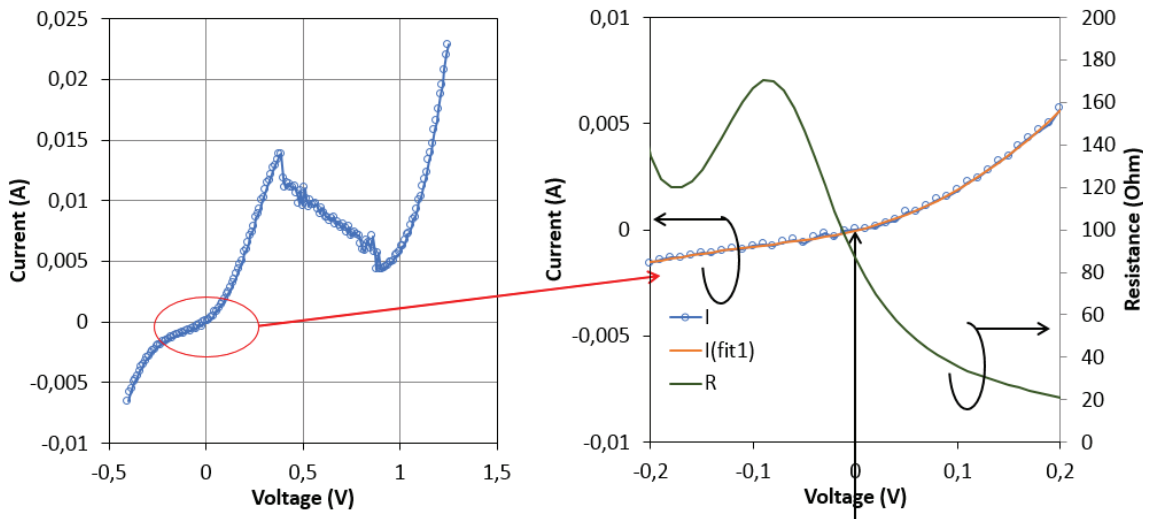


Figure C.2: Measured current-voltage characteristics of the TBRTD and its polynomial fitting for circuit simulation integration.

A rectification is given and shown in Figure C.3, where one period of the rectified signal is shown.

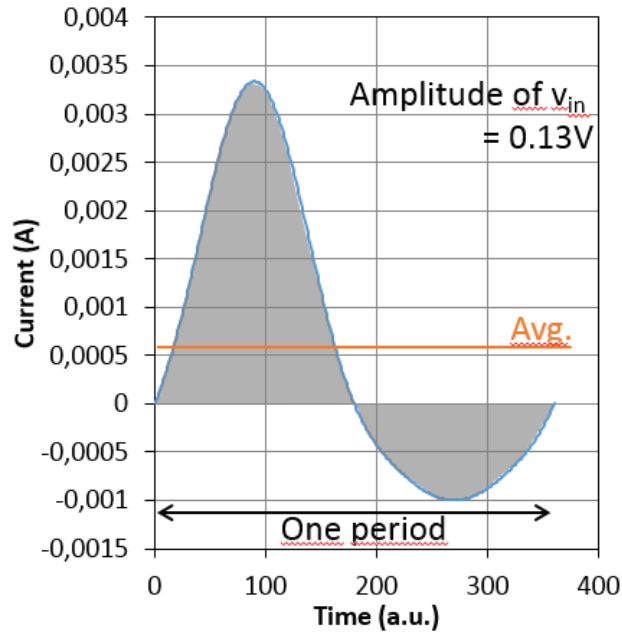


Figure C.3: One period of rectified current by the diode

The voltage and current responsivity of the detector was determined as follow:

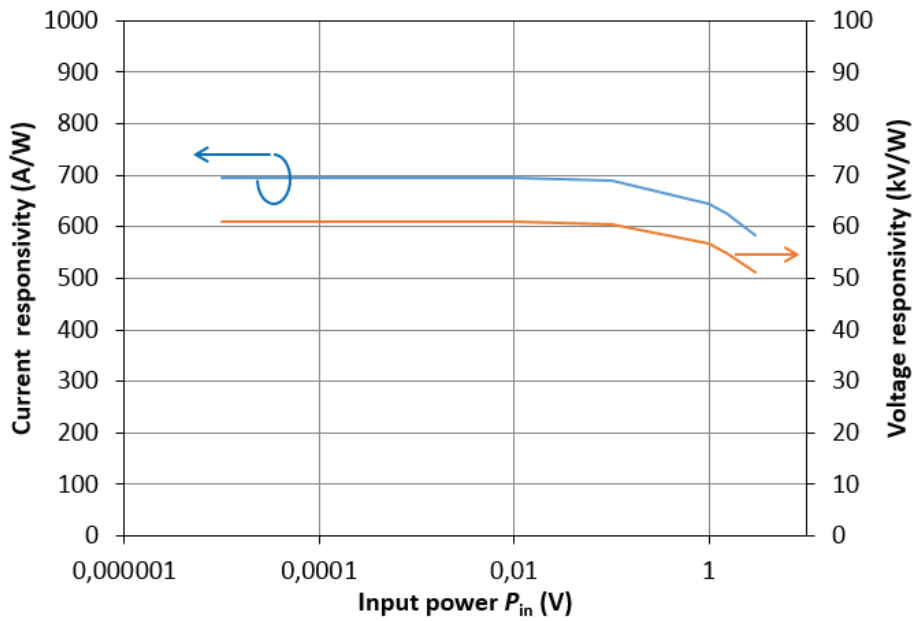


Figure C.4: Current and voltage responsivity of the TBRTD at different incoming power.



---

## List of figures

Figure 1.1: Oscillation frequency enhancement of an RTD-based oscillator in recent years: 2005 [35], 2008 [36], 2010 [27], 2011[26], 2014 [37], 2016 [38], 2017 [15].....	3
Figure 2.1: a) Schematic setup of a two-port device illustrating the undoped internal part, which defines the functionality of the device, and the device area, which is defined by the top contact area. In the inset, the difference in the current-voltage characteristics for d) DB- and e) TBRTD and their conduction band edges are presented in b) and c), respectively. ....	9
Figure 2.2: Typical IV-curve of a TBRTD with its main parameters and the conduction band edge structure at different bias points: a) at steady state, i.e., no bias is applied. b) Charge transport at the peak-point of the current-voltage characteristics, resonance. c) Applying a voltage higher than the valley point, the thermionic charge transport dominates. d) Blocking region, no resonance between the discrete energy levels. At higher negative voltage, the thermionic current is then dominating. ....	11
Figure 2.3: a) Current-voltage characteristic of a TBRTD in the forward direction with its characteristic operation points, the dashed line illustrates the measured curve and, the solid line the region the model is covering. b) The conduction band edge illustrating the internal part of a TBRTD presenting the delay times during tunneling. ....	12
Figure 2.4: Schematic structure of a TBRTD device. a) Illustrating the internal and its connection to the external parasitic elements including the device structure and mesa height. b) internal part corresponding equivalent circuit. ....	16
Figure 2.5: Equivalent circuit of a parallel resonator illustrating the output signal in the a) ideal case, where no losses are exciting, and b) a more realistic output signal, where the losses are damping the output signal over time. ....	17
Figure 2.6: a) Equivalent circuit of the negative conductance model: the resonator and negative differential resistance are connected in parallel. b) the output signal of the resonator over time, illustrating the amplification, i.e., gain as a result of the negative resistance. ....	19
Figure 2.7: A equivalent circuit of a TBRTD integrated into a resonator, neglecting the external parasitic elements at high-frequencies.....	20
Figure 2.8: Illustration of the subharmonic injection locking mechanism. a) Shows an NDR based oscillator oscillating at $\omega_0$ with no external injected signal, whereas in b) a signal oscillating at an angular frequency slightly lower than $\omega_0 n$ is injected into the $\omega_0$ system. The injected signal is multiplied by a factor $n$ , and is visible in the spectrum. In c) the locking conditions are fulfilled and locking starts. ....	22
Figure 2.9: Simplified equivalent circuit of an NDR-based oscillator. The RTD device is modeled via a current source providing the negative resistance and the non-linearity. ....	23
Figure 2.10: 3D-Pattern of the far-field radiation of three antenna types placed in free space. a) isotropic, b) omnidirectional, and c) directive. Adapted from [72]. Reprinted with permission.....	27
Figure 2.11: 2D cut-line in one angle of the far-field radiation pattern. This figure illustrates the fundamental parameters that can be gathered from the radiation pattern. ....	27
Figure 2.12: Schematical structure of a THz antenna fabricated on an InP-substrate illustrating the reflected wave within the substrate. A substrate wave is formed within the InP-substrate because of the significant height of the InP-substrate, and hence, a small critical angle occurs. ....	31
Figure 2.13: A possible solution for the substate wave — critical angle rises by using a Si-lens at the bottom side of the InP substrate.....	32
Figure 2.14: a) Schematic structure of a slot antenna illustrating the E-field orientation and the current flow at the slot-edge. In b) The impedance over the frequency of a slot antenna	

---

is presented. The inset illustrates the dominating impedance part in the specific frequency region, i.e., before and after the resonance point.....	33
Figure 2.15: a) Extraction of the electrical equivalent circuit of a slot antenna utilizing the current flow-path and b) its simplification to an equivalent parallel circuit. ....	34
Figure 2.16: a) Schematical structure of a bowtie antenna with its characteristic design parameters. Its equivalent circuit and its metal-structure are presented. b) A typical impedance of a self-complementary bowtie antenna with its self-resonance at low frequencies. ....	35
Figure 2.17: Operation principle of a TBRTD biased at zero volts, operating as a rectifier. The inset illustrates the IV-region used for signal rectification. ....	36
Figure 2.18: Block diagram including the impedance of the antenna as $Z_A$ and the TBRTD as $Z_D$ for simulation of the TBRTD antenna device, operating in detection mode. ....	37
Figure 3.1: a) I: DUT embedded in a GSG-structure for on-wafer measurement, II: open-structure to de-embed the measured data from the capacitance influence of the GSG-structure. III) short-structure to de-embed the measured data from the resistive and inductive influence of the GSG-structure. b) Equivalent circuit of the DUT embedded in a one-port GSG-structure. ....	44
Figure 3.2 Schematic structure of a hyper-hemispherical Si-lens illustrating its main design parameters when placing the radiating or detecting device at the flat lens surface. ....	46
Figure 3.3: Schematic setup of a Fabry-Perot based measurement setup for oscillation frequency determination. ....	47
Figure 3.4: Schematic setup of an FTIR measurement setup for oscillation frequency determination. ....	47
Figure 3.5: a) Schematic setup and b) picture for the used quasi-optical setup for oscillator output power measurement. ....	48
Figure 3.6: a) Schematic setup and b) a picture of a detector characterization measurement setup. In the top-view, the device placed on the Si-lens is presented. ....	49
Figure 4.1: Top- and side-view of schematically step-by-step fabrication of single TBRTD devices. a) the deposition of the top-contact and the mesa shape design and structuring, up to the bottom-contact, are demonstrated. b) The deposition of the bottom contact and the isolation of single devices on the substrate are presented. Transition and topology smoothing layer, per <i>Durimide</i> ® deposition, is presented. Finally, in c) the interconnection is illustrated. ....	53
Figure 4.2: Top-view SEM Image of the top contact after the lift-off process. The top metal layer is nickel. ....	54
Figure 4.3: SEM side view image of an etched TBRTD mesa a) after ICP-RIE etching step, i.e., anisotropic etching and in b) after a wet-etching step, i.e., isotropic etching. On the sides, a magnification of the mesa-edges shape after etching are presented. ....	55
Figure 4.4: SEM top-view image of the TBRTD after depositing the bottom contact. ....	56
Figure 4.5: SEM top-view image of a TBRTD in a) single and b-c) multi mesa technology after isolating the single devices on the substrate and depositing the <i>Durimide</i> ® for transition smoothing. ....	57
Figure 4.6: Micrograph image of a fabricated TBRTD, which is integrated into a one port GSG structure for characterization. The inset shows an SEM top view image of the integrated TBRTD. ....	57
Figure 4.7: SEM side view images of a TBRTD for four different substrates, with the same material stack. The mesa is fabricated by a combination of EBL, for top contact structuring and wet-etching for downscaling of the device area. ....	58
Figure 4.8: Schematic cross-sectional illustration of the substrate a) after spin coating PMMA and sol-gel on the substrate, and at the top the used mold is presented. b) Mold is pressed into the sol-gel. ....	59

Figure 4.9: a) Schematical cross-sectional illustration of the imprinted substrate, the inset demonstrates the remaining residual layer of sol-gel. b) A successful imprinting result is visible by light diffraction on the substrate surface. c) and d) AFM results of an imprinted surface with a mold of 500 nm mesa diameter and 1.5 $\mu\text{m}$ pitch. A homogeneous imprint depth over an area of 5 $\mu\text{m}$ x 10 $\mu\text{m}$ is presented. Further, the flow of the sol-gel during imprint is visible on the openings-surroundings. ....	60
Figure 4.10: a) Schematic illustration of a cross-sectional view of the substrate after dry-etching the sol-gel residuals in the openings and in b) after etching the PMMA residual with an O <sub>2</sub> -plasma treatment. c) SEM cross-section image of the substrate surface after etching. ....	61
Figure 4.11: a) Schematic illustration of a cross-section of the substrate surface, after metallization and in b) after the lift-off process. c) SEM top-view image and d) SEM side-view image of the fabricated top contacts with a metal diameter of 500 nm and height of 450 nm and a pitch of 2.5 $\mu\text{m}$ . ....	62
Figure 4.12: a) SEM side view image of a fabricated two electrodes device structured by the introduced NIL-process. b) Magnification of the top contact isolated with <i>Durimide</i> ® and c) bottom contact is placed with the self-alignment process surrounding the device mesa. Unused top contacts (for illustration, some are marked with a black arrow) are falling on the substrate surface after etching its mesa, causing shorts between device electrodes. ....	62
Figure 4.13: a) Schematic illustration of the substrate after the residual layer etching with ICP and spin-coating the third photoresist and at the top, a patterning mask for UV exposure. b) After developing the exposed positive photoresist. ....	63
Figure 4.14: a) Schematic illustration after an O <sub>2</sub> -plasma treatment to etch the PMMA in the opening. b) SEM image of the substrate surface after O <sub>2</sub> -plasma treatment. c) SEM side-view image of the substrate surface after metallization and lift-off process. ....	64
Figure 4.15: SEM images of a fabricated device using the new CNP method whereby in a) the top-view of a device with six mesas is presented, and the bottom contact is placed by the self-alignment method. b) An SEM side-view image to demonstrate the shape of the mesa after ICP and wet-etching. ....	64
Figure 4.16: Current-voltage characteristics of a fabricated nano-RTD with the new developed CNP-Process. ....	65
Figure 4.17: a) Micrographic image of the fabricated slot antenna, the SEM images in the inset are presented to illustrate the challenging parts during fabrication. b) Fabricated TBRTD within the slot opening. c) Closing the lift-off-opening with a <i>Durimide</i> ® bridge and metallization. d) Stabilization resistance under MIM-capacitance. e) The MIM-capacitance structured with SiN <sub>x</sub> as an isolator. ....	65
Figure 4.18: Schematic display of the fabrication steps of the TBRTD integration within the slot antenna with a MIM-capacitor for DC-biasing of the TBRTD. a) The lower electrode of the slot antenna is placed, which defines the slot dimensions. b) Transition smoothing by spin-on-glass deposition and the MIM-capacitor isolator (SiN <sub>x</sub> ) is deposited. c) The top and last metallization connecting the TBRTD and forming the MIM is deposited. ....	66
Figure 4.19: Failed lift-off process step because of the photoresist sideband metallization of a metal surrounded, metal-free-area (the slot). a) Micrographic top-view image of the fabricated slot antennae. b) An SEM image of one of the slots, illustrating the metallization falling back on the surface after lift-off. c) SEM Image is illustrating the metallization glitter on the left side of a slot opening. d) A schematical structure illustrating the problem of the lift-off process of such designs. ....	67
Figure 4.20: Schematic step-by-step of closing the lift-off-opening. a) Depositing the lower metal of the slot antenna with a lift-off-opening. b) SOG layer is used to smooth the transitions at the lift-off-opening and a top metallization to short the opening. c) An	

---

	SEM image of a fabricated slot antenna with the lift-off-opening method. d) Close look-up of the lift-off-opening structure after metallization.....	68
Figure 4.21:	The slot antennae fabricated with a higher photoresist. a) Micrographic image of a top-view of the fabricated slot antenna elements on the substrate, a successful metallization lift-off in the slot is shown. b) SEM image of one slot where successful lift-off process was carried out and c) SEM image of a cross-section of the photoresist profile to illustrate its sharp undercut.....	69
Figure 4.22:	SiN <sub>x</sub> walls caused by the isotropically SiN <sub>x</sub> deposition in the PECVD. I) Schematical step-by-step of the depositing of the SiN <sub>x</sub> on a structured substrate surface, starting with the structured photoresist, then the deposition of SiN <sub>x</sub> , and finally after lift-off process removing the photoresist illustrating the SiN <sub>x</sub> fences. II) SEM images of a fabricated device utilizing this process showing in a-b) an integrated TBRTD with two mesa in a slot antenna, a metallization break in the last metallization layer is visible due to the SiN <sub>x</sub> fence, which is presented in more details in the inset.....	70
Figure 4.23:	Schematical illustration of the processing steps via selective etching to prevent SiN <sub>x</sub> fences. a) Depositing of SiN <sub>x</sub> on the whole substrate surface. b) Photoresist mesas structuring to protect the SiN <sub>x</sub> area. c) 5%-HF etching of the unprotected SiN <sub>x</sub> .....	70
Figure 4.24:	a) Micrographic top-view of a fabricated MIM-capacitance for isolator permittivity determination. b) Cross-section of the internal part illustrating the MIM structure in more detail. ....	71
Figure 4.25:	Micrographic image of the fabricated TBRTD integrated into a self-complementary bowtie antenna. In the insert, a micrographic image of the TBRTD is visible. ....	72
Figure 5.1:	Investigated TBRTD layer stack. Further, for simplicity, a conduction band edge is illustrated. a) The energy levels coupling strength is investigated by fine-tuning of the QWs thickness. b) The influence of the slight difference in the AIAs barriers is examined. c) The material growth order is investigated. Bright colored cells in the internal region represent the modified layer. Arrows illustrates the modification direction.....	74
Figure 5.2:	Typical conduction band edge of a TBRTD presented with its design parameters.	75
Figure 5.3:	a) Measured (dashed) and modeled (solid lines) current-voltage of three devices. b) Half-logarithmical presentation only of the measured current-voltage characteristics in the reverse and PDRI region. ....	77
Figure 5.4:	Current-voltage characteristics of two devices to illustrate the influence of the barrier thickness on the device performance. ....	79
Figure 5.5:	Complete equivalent circuit of an on-wafer measured TBRTD device embedded into a one port GSG-structure.....	81
Figure 5.6:	Smith-chart diagram of measured scattering parameters of a TBRTD ( <i>device-F</i> ) in the whole voltage range. The capacitive dominating behavior is visible. ....	83
Figure 5.7:	Measured (dotted lines) and modeled (solid lines) curves in (a-b) NDR region and (c-d) reverse and PDR region. ....	84
Figure 5.8:	Extracted small-signal equivalent circuit of the TBRTD. a) Capacitance and b) conductance, in the whole current-voltage region. ....	85
Figure 6.1:	Simulated admittance vs. frequency of a slot antenna separated into real (conductance) and imaginary (susceptance) part. The slot dimensions are 10 μm and 120 μm width and length, respectively. ....	87
Figure 6.2:	a) EM-simulation results of the slot antenna and its curve fitting using the equivalent circuit approach. b) The total resistance and its separation into its losses- and radiation- resistance are presented. ....	87
Figure 6.3:	Equivalent circuit elements change over the slot length. Slot width is constant at 10 μm and length is tuned from 20 to 100 μm. a) And b) illustrates the change of the slot capacitance and inductance, respectively, over the slot length. c) The antenna	

---

susceptance change over the frequency at four different antenna lengths is presented. .....	88
Figure 6.4: Simulated antenna susceptance over the frequency with different slot antenna widths. The length is constant at 80 $\mu\text{m}$ while the width is tuned from 3 to 10 $\mu\text{m}$ . .....	89
Figure 6.5 Simulated directivity of a slot antenna at 260 GHz with a dimension of 10 and 80 $\mu\text{m}$ , slot width, and length, respectively placed on lossy InP substrate. The main radiation is at the bottom side caused by the high permittivity of the InP substrate.....	89
Figure 6.6: a) Schematic structure of the slot antenna and b) a cross-section of the slot antenna at the center point illustrating the position of the TBRTD, MIM-capacitor, and the suppression resistance.....	90
Figure 6.7: Complete equivalent circuit of a TBRTD integrated into a slot antenna a) Equivalent circuit of the whole device b) Equivalent circuit for operating in the THz range. Due to the short device mesa, $L_s$ can be neglected.....	91
Figure 6.8: a) Simulated susceptance of a TBRTD integrated into a slot antenna. A resonance point is around 260 GHz. b) Fourier transformation of a time-domain simulation result of the output signal of the TBRTD-based oscillator, oscillation frequency peak is around 260 GHz.....	92
Figure 6.9: Simulated scattering parameter results of a TBRTD integrated into a slot antenna demonstrating the $f_{10dB}$ frequency region for detection bandwidth determination. ....	92
Figure 6.10: A block setup integrated into a circuit simulator for TBRTD detection capability simulation.....	93
Figure 6.11: a) Transient simulation results of a TBRTD-based resonant detector, whereby the rectification capability is demonstrated by the rectified voltage over the time at the TBRTD when irradiated with a signal with constant power. b) The DC-component over the TBRTD, of an HB simulation, illustrating the detected voltage over the irradiated signal frequency.....	93
Figure 6.12: Schematic illustration of a bowtie antenna structure with its design parameters. a) Simulation of the scattering parameter of the device with a wing length of $L_{\text{Bowtie}} = 400 \mu\text{m}$ is shown. b-d) The susceptance of a bowtie antenna at different wing length 100, 250, and 400 $\mu\text{m}$ illustrating the self-resonance of the antenna. ....	94
Figure 6.13: HB simulation results of the detected voltage at the TBRTD integrated into a broadband self-complementary antenna. Tuning the TBRTD area (device capacitance) to smaller effective area, improves the detection capability. ....	95
Figure 6.14: FTIR measurement results of a TBRTD-based slot antenna oscillator. ....	96
Figure 6.15: Measured harmonic signals of the TBRTD-based oscillator. Harmonic components are bias voltage-dependent. ....	96
Figure 6.16: HB simulation of the harmonic signals of the TBRTD-based oscillation utilizing the equivalent circuit approach. A voltage-dependent harmonic component power is visible.....	97
Figure 6.17: Measured output power over the frequency of the signal generator <i>AMC-370</i> at different attenuation levels. Measured by <i>PM5</i> , <i>VDI</i> .....	98
Figure 6.18: Measured rectified voltage over the TBRTD-based resonant detector. The quasi- optical measurement setup presented in chapter 3.3.3 is used.....	98
Figure 6.19: Power-uncalibrated measurement of the detected voltage over a wide frequency range of the TBRTD integrated into the self-complementary bowtie antenna.....	99
Figure 6.20: Measured output power of the frequency extender <i>ZVA ZC330</i> from <i>R&amp;S</i> ®.....	99
Figure 6.21: Determined responsivity and NEP of the TBRTD integrated into a self- complementary antenna. The quasi-optical measurement setup presented in chapter 3.3.3 is used.....	100

---

Figure 7.1: Block diagram for circuit simulation of the locking of a free-running oscillator. The slot antenna is integrated using scattering parameters from field simulations. The large-signal RTD equivalent circuit is represented by voltage-controlled current source and constant RTD capacitance for simplicity. ....	103
Figure 7.2: HB simulation results of the output power of the doubled signal as a function of biasing point in the NDR region of the RTD.....	104
Figure 7.3: Simulated output spectrum of the free running oscillator without locking signals and after locking. ....	104
Figure 7.4: Simulated oscillation frequency dependency over the injected signal frequency illustrating the locking range and both locking edges surrounding the locking range. ....	105
Figure 7.5: Measurement of the output power of the RTD-based resonant antenna oscillating at different bias points, illustrating the frequency and output power dependency over the voltage.....	106
Figure 7.6: a) Schematic and b) a picture of the measurement setup for injection locking investigation. c) the output power of the signal generator is illustrated .....	106
Figure 7.7: Measured doubled signal of the RTD-based oscillator. The frequency of the wireless injected signal is at 293 GHz, and the radiated doubled signal is at $2 \cdot 293 \text{GHz} = 586 \text{GHz}$ . Biasing at the center of the NDR provides the minimum locking signal.....	107
Figure 7.8: Illustration of the locking process. a) Lockin signal frequency has a slight offset from $f_0/2$ . b) Increasing the frequency of the locking signal. Locking sidebands start appearing. c) Locking condition is fulfilled at locking start frequency.....	108
Figure 7.9: Determination of the locking range, a) vs. the bias voltage and b) vs. the injected power. ....	108
Figure 7.10: Illustration of the injection locking mechanism by presenting the signal push and pull. The injected signal power is increased step-by-step. At b) and d) the locking sidebands are visible. At b) the locking signal peak is at the left of the free-running signal, which is shifted to higher frequency.....	109
Figure 7.11: Close lookup of the locked output signal. A resolution-bandwidth (RBW) of 100 Hz is set.....	110

---

## List of tables

Table 4.1 Experimentally determined EBL parameters for PMMA 671.05 patterning .....	58
Table 5.1 first figure of merit parameters of a TBRTD extracted from the DC-characterization .....	78
Table 5.2 Model parameters extracted from the DC-characteristics of the TBRTD.....	80

---

## Abbreviations

5% HF:	5% Hydrofluoric Acid
n.i.d:	not intentionally doped
AC:	Alternating Current
ADS:	Advanced Design System
AFM:	Atomic Force Microscope
AlAs:	Aluminum arsenide
Au:	Gold
BW:	BandWidth
Cl <sub>2</sub> :	Chlorine
CMOS:	Complementary Metal-Oxide-Semiconductor
CNP:	Combined Nanoimprint and Photolithography
CST:	Computer Simulation Technology
DBAC:	2-(2-Butoxyethoxy)ethyl acetate
DBRTD:	Double Barrier Resonant tunneling Diode
DC:	Direct Current
DI:	De-Ionized
DMSO:	Dimethylsulfoxide
DUT:	Device Under Test
EBL:	Electron Beam Lithography
ECR- PECVD:	Electron Cyclotron Resonance Plasma Enhanced Chemical Vapor Deposition
EM:	Electro-Magnetic
FDTD:	Finite-Difference Time-Domain
FIR	Far InfraRed
FIT:	Finite Integration Technique
FNBW:	First Null Beam Width
FTIR:	Fourier Transform Infrared Spectrometer
FWHM:	Full-Width at Half-Maximum

---

GDS-File:	Graphic Data System File
GSG:	Ground Signal Ground
HB	Harmonic-Balance
H <sub>2</sub> O:	Water
H <sub>2</sub> O <sub>2</sub> :	hydrogen peroxide
H <sub>3</sub> PO <sub>4</sub> :	phosphoric acid
HBTs:	Heterostructure Bipolar Transistors
HBV	Heterostructure Barrier Varactor
HCl:	hydrochloric acid
HEMTs:	High Electron Mobility Transistors
HF:	High Frequency
HFSS :	High-Frequency Structure Simulator
HPBW:	3dB beamwidth or also called Half Power Beam Width
ICP :	Inductively Coupled Plasma
RIE:	Reactive-ion etching
IE-MoM:	Integral Equations Solved by the Method Of Moments
IMPATT:	Impact Ionization Avalanche Transit-Time diodes
InAs:	Indium Arsenide
InGaAs:	Indium Gallium Arsenide
InP:	Indium Phosphide
IPA:	Iso-Propanol
IV:	Current Voltage
KIT:	Karlsruhe Institute for Technology
LNA:	Low Noise Amplifier
MBE:	Molecular Beam Epitaxy
MIBK:	Methyl IsoButyl Ketone
MIM:	Metal-Insulator-Metal
MOCVD:	Metal-Organic Chemical Vapour Deposition
MTMS:	MethylTriMethoxySilane

---

N <sub>2</sub> :	Nitrogen
NDC:	Negative Differential Conductance
NDR:	Negative differential resistance
NEP:	Noise Equivalent Power
NH <sub>3</sub> :	Ammonia
Ni:	Nickel
NIL:	Nanoimprint Lithography
O <sub>2</sub> :	Oxygen
OSM:	Open/ Short/ Match
PDMS:	Polydimethylsiloxane
PEB:	Post-Exposure Bake step
PLL:	Phase-Locked-Loop
PM:	Power Meter
PMMA:	PolyMethyl MethAcrylate
Pt:	Platin
PVCR:	Peak To Valley Current Ratio
PVVR:	Peak To Valley Current Ratio
QCL	Quantum Cascade Laser
QW:	Quantum Well
RF:	Radio Frequency
RLT:	Residual Layer Thickness
RTD:	Resonant Tunneling Diode
SEM:	Scanning Electron Microscope
Si:	Silicon
SiN <sub>x</sub> :	Silicon Nitride
SLL:	Side Lobe Level
SMU:	Source Measurement Unit
SOG	Spin-On-Glass
TBRTD:	Triple Barrier Resonant Tunneling Diode

---

TDS	Time-domain spectroscopy
THz:	Tera Herz
Ti:	Titanium
TLM:	Transmission-Line-Measurement
TMOS:	TetraMethyl OrthoSilicate
TOSM:	Through/ Open/ Short/ Match
TPX:	Polymethylpentene
UHV:	Ultra-High Vacuum
UV light:	Ultra- Violet light
VDI:	Virginia Diodes
VNA:	Vector Network Analyzer
WR:	Waveguide

---

## symbol directory

$a$	Fitting parameter for the IV-curve. of the TBRTD in the NDR region	[A/V]
$A$	Effective area of a TBRTD	[m <sup>2</sup> ]
$A_{\text{eff}}$	Effective antenna area	[m <sup>2</sup> ]
$A_{\text{iso}}$	Antenna area when an isotropic radiator is assumed	[m <sup>2</sup> ]
$A_{\text{aper}}$	Aperture area	[m <sup>2</sup> ]
$A_{\text{TBRTD}}$	Effective area of a TBRTD device	[m <sup>2</sup> ]
$b$	Fitting parameter for the IV-curve. of the TBRTD in the NDR region	[A/V <sup>3</sup> ]
$BW$	Bandwidth	[Hz]
$B_{\text{neg}}$	Negative-resistance device susceptance	[S]
$B_{\text{res}}$	Resonator susceptance	[S]
$C$	Capacitance	[F]
$C_0$	Depletion capacitance	[F]
$C_0^*$	Depletion capacitance at steady state condition	[F]
$C_{\text{ant}}$	Antenna capacitance	[F]
$C_c$	Contact capacitance formed due to the metal semiconductor junction at the top contact of the TBRTD	[F]
$C_D$	Diode capacitance	[F]
$C_{\text{MIM}}$	Metal isolator metal capacitance	[F]
$C_{\text{pad}}$	Capacitance due to the embedding pad structure	[F]
$C_{\text{RTD}}$	RTD capacitance	[F]
$C_{\text{TBRTD}}$	TBRTD overall capacitance	[F]
$C_{\text{tunnel}}$	Tunnel capacitance	[F]
$d$	The distance between the top and bottom contact metallization	[m]
$D$	Antenna directivity	[-]
$d_{\text{bar}}$	Barrier thickness	[m]
$d_{\text{b1}}$	Thickness of the 1 <sup>st</sup> barrier	[m]
$d_{\text{b2}}$	Thickness of the 2 <sup>nd</sup> barrier	[m]

---

$d_{b3}$	Thickness of the 3 <sup>rd</sup> barrier	[m]
$d_{dep}$	Depletion layer thickness	[m]
$d_{extension}$	Lens extension at the flat lens surface, i.e., hyper-hemispherical lens	[m]
<i>device area</i>	Nominal device mesa area	[m <sup>2</sup> ]
$d_f$	Fraunhofer distance, i.e., far field starting point	[m]
$d_{feed}$	Distance between the antenna wings	[m]
$d_{intrinsic}$	Thickness of the intrinsic part of the device	[m]
$D_{max}$	Maximum antenna directivity	[-]
$d_{lens}$	Lens focus point	[m]
$d_{well}$	Quantum well width	[m]
$d_{QW1}$	Width of the 1 <sup>st</sup> quantum well	[m]
$d_{QW2}$	Width of the 2 <sup>nd</sup> quantum well	[m]
$d_x$	Distance between two Si-reflection layers	[m]
$f_0$	Oscillation frequency of the resonator	[Hz]
$f_{10dB}$	Frequency at which the S11 is equal to -10 dB	[Hz]
$f$	Frequency	[Hz]
$f_c$	Cut-off frequency	[Hz]
$f_{inj}$	Frequency of the injected signal	[Hz]
$f_{out}$	Frequency of the output signal	[Hz]
$G$	Rectification factor	[-]
<i>Gain</i>	Antenna Gain	[-]
$G_{d0}$	TBRTD conductance at DC	[S]
$G_L$	Load conductance	[S]
$G_{loss}$	Antenna loss conductance	[S]
$G_{neg}$	Negative differential conductance	[S]
$G_{rad}$	Antenna radiation conductance	[S]
$G_{res}$	Resonator conductance	[S]

---

$G_{\text{TBRTD}}$	TBRTD conductance with frequency dependency	[S]
$h$	Planck's constant	$[\sim 6.626 \times 10^{-34}] \text{s}$
$i$	Total current within a TBRTD for a voltage $v_{\text{ac}}(t)$	[A]
$i_{\text{C}}$	Current flowing at the capacitance of a resonator	[A]
$I_{\text{Center}}$	DC-Current at the center of the NDR region	[A]
$i_{\text{C,TBRTD}}$	Current flowing at the capacitance of a TBRTD	[A]
$i_{\text{D}}$	AC current within a diode	[A]
$I_{\text{D}}$	Amplitude of the current flowing through a diode	[A]
$i_{\text{G}}$	Current flowing through the conductance of a resonator	[A]
$i_{\text{inj}}$	Injected signal current	[A]
$I_{\text{inj}}$	Amplitude of the injected signal current	[A]
$i_{\text{L}}$	Current flowing through the inductance of a resonator	[A]
$I_{\text{out}}$	Rectified current	[A]
$I_{\text{p}}$	Current value at the peak point	[A]
$I_{\text{resonator}}$	Current flowing through a resonator	[A]
$i_{\text{S,TBRTD}}$	Current component of $i(t)$ that is proportional to sine the voltage	[A]
$I_{\text{TBRTD}}$	Amplitude of the current flowing through a TBRTD	[A]
$i_{\text{TBRTD}}$	AC current within the TBRTD	[A]
$I_{\text{v}}$	Valley current	[A]
$I^{+}$	Current at positive bias voltage $V^{+}$	[A]
$I^{-}$	Current at negative bias voltage $V^{-}$	[A]
$J_0$	Current density at the center of the NDR region	$[\text{A}/\text{m}^2]$
$J_{\text{p}}$	Current density at the peak point of a (TB-)RTD IV-curve	$[\text{A}/\text{m}^2]$
$k_{\text{B}}$	Boltzmann-constant	$[1.380649 \times 10^{-23}] / \text{K}$
$L$	Inductance	[H]
$L_{\text{Bowtie}}$	Wing length of a bowtie antenna	[m]
$L_{\text{lens}}$	Virtual focus point of a Si-lens	[m]

---

$L_{\text{ant}}$	Antenna inductance	[H]
$L_{\text{pad}}$	Inductance due to the embedding pad structure	[H]
$L_s$	Series inductance of the TBRTD formed due to the device mesa	[H]
$L_{\text{slot}}$	Slot length in a slot antenna	[m]
$L_{\text{stab}}$	Inductance due to the stabilization resistance structure	[H]
$L_{\text{wire}}$	DC-biasing wires inductance	[H]
$m$	Index	[-]
$m_e^*$	Effective electron mass	$[9.11 \times 10^{-31} \text{ kg}]$
$m_m$	Fitting parameter	[-]
$N$	Noise voltage variance	[V]
$n$	Subharmonic injection signal factor	[-]
$n_{\text{air}}$	Refractive index air	[1]
$NEP_i$	Detector current noise equivalent power	$\text{W/Hz}^{0.5}$
$NEP_v$	Detector voltage noise equivalent power	$\text{W/Hz}^{0.5}$
$n_{\text{si}}$	Refractive index silicon	[3.41]
$O$	Largest dimension of a radiator	[m]
$P$	Absolute power	[W]
$P_{\text{in}}$	Incoming power	[W]
$P_{\text{injection}}$	Power of the injected signal	[W]
$P_{\text{loss}}$	Power loss of a resonator	[W]
$P_{\text{out}}$	Output power of a free running oscillator	[W]
$P_r$	Absolute output power of an isotropic antenna	[W]
$P_{\text{rad}}$	Radiated antenna power	[W]
$PVCR$	Peak to valley current ratio	[-]
$PVVR$	Peak to valley voltage ratio	[-]
$q$	Electrical charge	$[1.6 \times 10^{-19} \text{ C}]$
$Q$	Quality factor of an LC resonator	[-]
$R$	Resonator resistance	$[\Omega]$

---

$R'$	Negative resistance	[ $\Omega$ ]
$r$	Spherical coordinates parameter: radial distance	[m]
$r_{\text{lens}}$	Lens radius	[m]
$R_c$	Contact resistance due to the metal semiconductor junction at the top contact of the TBRTD	[ $\Omega$ ]
$R_D$	Diode differential resistance at operation point	[ $\Omega$ ]
$R_i$	Detector current responsivity	[A/W]
$R_{\text{loss}}$	Antenna loss resistance	[ $\Omega$ ]
$R_{\text{pad}}$	Resistance due to the embedding pad structure	[ $\Omega$ ]
$R_S$	Series resistance of a TBRTD	[ $\Omega$ ]
$R_{\text{stab}}$	Stabilization resistance	[ $\Omega$ ]
$R_v$	Detector voltage responsivity	[V/W]
$t$	Time	[s]
$T_{\text{Temp}}$	Temperature	[K]
$T$	Time period	[s]
$T_p$	Tunnel probability	[-]
$V_0$	Voltage at the center of the NDR region	[V]
$V_1$	Injected signal amplitude	[V]
$V_A$	Antenna internal excites voltage due to an irradiated power	[V]
$v_{\text{ac}}$	AC voltage signal	[V]
$V_{\text{AC}}$	Amplitude of the oscillating AC Voltage	[V]
$V_{\text{bias}}$	External applied bias voltage	[V]
$V_{\text{center}}$	Bias voltage at the center of the NDR region	[V]
$V_D$	Voltage across a diode	[V]
$V_{dc}$	Applied DC voltage	[V]
$V_n$	Injected n-th subharmonic signal amplitude	[V]
$V_{\text{out}}$	Rectified voltage	[V]
$V_p$	Voltage at the peak point of the (TB-)RTD IV-characteristics	[V]

---

$V_{\text{resonator}}$	Voltage across an LC resonator	[V]
$V_{\text{RTD}}$	Voltage across an RTD device	[V]
$v_s$	Saturation velocity of electrons	[m/s]
$V_{\text{TBRTD}}$	Voltage across a TBRTD device	[V]
$V_v$	Voltage at the valley point of the (TB-)RTD IV-characteristics	[V]
$V^+$	Bias voltage in the forward direction	[V]
$V^-$	Bias voltage in the reverse direction	[V]
$W_{\text{Bowtie}}$	Bowtie antenna wing width	[m]
$W_e$	Electron energy level	[eV]
$W_{\text{elec}}$	Stored electrical energy in an LC resonator	[W]
$W_f$	Fermi energy level	[eV]
$W_L$	Conduction band edge energy level	[eV]
$W_{\text{mag}}$	Stored magnetic energy in an LC resonator	[W]
$W_{\text{slot}}$	Slot width in a slot antenna	[m]
$W_\eta$	Energy level of $n^{\text{th}}$ discrete energy level	[W]
$x$	Dynamical variable of van der Pol equation	[-]
$Y_{\text{in}}$	Input Admittance	[S]
$Y_{\text{meas}}$	Measured embedded device admittance	[S]
$Y_{\text{neg}}$	Negative-resistance input admittance	[S]
$Y_{\text{Open}}$	Measured open-structure admittance	[S]
$Y_{\text{pad}}$	Admittance of the embedding pad	[S]
$Y_{\text{res}}$	Resonator input admittance	[S]
$Y_{\text{ser}}$	Admittance of series-connected elements	[S]
$Z_0$	Impedance of the environmental medium	[ $\Omega$ ]
$Z_A$	Antenna impedance	[ $\Omega$ ]
$Z_D$	Diode impedance	[ $\Omega$ ]
$Z_{\text{DUT}}$	De-embedded DUT impedance	[ $\Omega$ ]

---

$Z_{in}$	Input impedance	[ $\Omega$ ]
$Z_{internal}$	Internal impedance	[ $\Omega$ ]
$Z_{meas}$	Measured impedance	[ $\Omega$ ]
$Z_{M-SC}$	Impedance of the metal semiconductor junction	[ $\Omega$ ]
$Z_{pad}$	Impedance due to the embedding pad structure	[ $\Omega$ ]
$Z_{peak,valley}$	TBRTD impedance at the peak or valley point	[ $\Omega$ ]
$Z_{SC}$	Impedance of the semi-conductor mesa	[ $\Omega$ ]
$Z_{ser}$	Impedance of series contacted elements	[ $\Omega$ ]
$Z_{Short}$	Measured short-structure impedance	[ $\Omega$ ]
$Z_{TBRTD}$	Impedance of the TBRTD seen at its input nodes	[ $\Omega$ ]
$\alpha$	Fundamental component amplitude parameter for van der Pol model for NDR-based oscillator.	[-]
$\alpha_{Bowtie}$	Angle of the bowtie antenna wings	[deg]
$\alpha_{critical}$	Critical of incident wave	[deg]
$\alpha_{lens}$	Beam collection angel of a Si-lens	[deg]
$\beta$	Van der Pol model for NDR-based oscillator. 2 <sup>nd</sup> harmonic component amplitude parameter	[-]
$\beta_{lens}$	Beam divergence angle $\beta$ of a Si-lens	[deg]
$\gamma$	Van der Pol model for NDR-based oscillator. 3 <sup>rd</sup> harmonic component amplitude parameter	[-]
$\gamma_{cc}$	Curvature coefficient	[V <sup>-1</sup> ]
$\Delta I$	Current difference between peak and valley current	[A]
$\Delta V$	Voltage difference between peak and valley voltage	[V]
$\Delta W_L$	Conductance band edge discontinuity	[eV]
$\epsilon$	Product of permittivity of free space and permittivity of a material	[As/Vm]
$\epsilon_{material}$	Material relative permittivity	[-]
$\epsilon_0$	Permittivity of free space	[8,854187x10 <sup>-12</sup> As/Vm]
$\epsilon_v$	Constant and defines the form of the output signal of a van der Pol oscillator	[-]

---

$\epsilon_{\text{rad}}$	Radiation efficiency	[-]
$\epsilon_{\text{ape}}$	Antenna aperture efficiency	[-]
$\eta$	Energy level index	[-]
$\eta_{\text{DC-to-RF}}$	DC to RF conversion efficiency	[%]
$\theta$	Spherical coordinates parameter: inclination angle	[deg]
$\tau_{\text{dwell1}}$	Dwell time of charges tunneling from emitter side through the first quantum well to the second quantum well	[s]
$\tau_{\text{dwell2}}$	Dwell time of charges tunneling from the first quantum well through the second quantum well to the collector side	[s]
$\tau_3$	Transit time for an electron to arrive at the collector side after tunneling through both quantum wells	[s]
$\phi_{\text{C}}$	Fitting parameter	[-]
$\phi_{\text{n}}$	Injected n-th subharmonic signal phase	[deg]
$\varphi$	Spherical coordinates parameter: azimuth angle	[deg]
$\omega$	Output signal angular frequency	[Hz]
$\omega_0$	Angular frequency of a free running oscillator	[Hz]
$\omega_1$	Angular frequency of an injected signal for fundamental locking	[Hz]
$\omega_{\text{C}}$	Cut-off angular frequency	[Hz]
$\omega_{\text{inj}}$	Angular frequency of an injected signal	[Hz]
$\lambda$	Wavelength	[m]
$\hbar$	h-bar: reduced Planck constant = $h/2\pi$	$\sim 6.582 \times 10^{-16} \text{eVs}$

